Entangling electrons and nuclei in a four-qubit, two-atom device in silicon

Holly Georgina Stemp

A thesis in fulfilment of the requirements for the degree of

Doctor of Philosophy

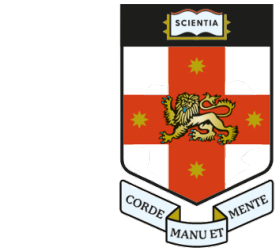

UNSW
SYDNEY

School of Electrical Engineering and Telecommunications

Faculty of Engineering

The University of New South Wales

September 2023

Supervisor: Professor Andrea Morello

Co-supervisor: Dr Vincent Mourik

Thesis accepted upon recommendation of:

- Professor Mete Atatüre, University of Cambridge, United Kingdom
- Professor Dominik Zumbühl, University of Basel, Switzerland

Declaration

ORIGINALITY STATEMENT

☑ I hereby declare that this submission is my own work and to the best of my knowledge it contains no materials previously published or written by another person, or substantial proportions of material which have been accepted for the award of any other degree or diploma at UNSW or any other educational institution, except where due acknowledgement is made in the thesis. Any contribution made to the research by others, with whom I have worked at UNSW or elsewhere, is explicitly acknowledged in the thesis. I also declare that the intellectual content of this thesis is the product of my own work, except to the extent that assistance from others in the project's design and conception or in style, presentation and linguistic expression is acknowledged.

COPYRIGHT STATEMENT

☑ I hereby grant the University of New South Wales or its agents a non-exclusive licence to archive and to make available (including to members of the public) my thesis or dissertation in whole or part in the University libraries in all forms of media, now or here after known. I acknowledge that I retain all intellectual property rights which subsist in my thesis or dissertation, such as copyright and patent rights, subject to applicable law. I also retain the right to use all or part of my thesis or dissertation in future works (such as articles or books).

For any substantial portions of copyright material used in this thesis, written permission for use has been obtained, or the copyright material is removed from the final public version of the thesis.

AUTHENTICITY STATEMENT

☑ I certify that the Library deposit digital copy is a direct equivalent of the final officially approved version of my thesis.

Publications statement

UNSW is supportive of candidates publishing their research results during their candidature as detailed in the UNSW Thesis Examination Procedure.

Publications can be used in the candidate's thesis in lieu of a Chapter provided:

- The candidate contributed **greater than 50%** of the content in the publication and are the "primary author", i.e. they were responsible primarily for the planning, execution and preparation of the work for publication.
- The candidate has obtained approval to include the publication in their thesis in lieu of a Chapter from their Supervisor and Postgraduate Coordinator.
- The publication is not subject to any obligations or contractual agreements with a third party that would constrain its inclusion in the thesis.

☑ The candidate has declared that **some of the work described in their thesis has been published and has been documented in the relevant Chapters with acknowledgement**.

A short statement on where this work appears in the thesis and how this work is acknowledged within chapter/s:

> At the beginning of every chapter I have acknowledged any work that has been published.
>
> Section 3.6 contains results from the publication for which I am a co-author: C. Adambukulam, et.al. "An ultra-stable 1.5 T permanent magnet assembly for qubit experiments at cryogenic temperatures," Review of Scientific Instruments, vol. 92, no. 8, 2021
>
> Chapter 5 contains results from the publication for which I am the primary author: H. G. Stemp, et.al. "Tomography of universal two-qubit logic operations in exchange-coupled donor electron spin qubits" arXiv preprint arXiv:2309.15463, 2023.
>
> Section 5.9 contains results from the publication for which I am a co-author: B. Joecker et.al. "Error channels in quantum nondemolition measurements on spin systems" arXiv preprint arXiv:2307.14103, 2023

Candidate's Declaration

I declare that I have complied with the Thesis Examination Procedure.

Abstract

The nuclear spins of ion-implanted donor spins in silicon have demonstrated record-breaking coherence times of over 30-seconds, along with high fidelity (>99%) single and two-qubit operations, approaching the fidelity required to perform fault-tolerant quantum computation. The considerable coherence times observed for the nuclei are owing to the fact that the nuclear spin interacts very weakly with its environment. This property of the nucleus, although a desirable advantage from the perspective of noise resilience, results in nuclear qubits only weakly coupling to one another, presenting a challenge for performing scalable, multi-qubit operations. Fortunately, donor atoms have the additional resource of the donor-bound electron, which can be utilised as a means of coupling nuclei over larger distance scales.

In this thesis, we focus on a system of two ^{31}P nuclei, each possessing their own bound electron. These electrons are exchange-coupled to one another with a strength of 12 MHz. We begin by experimentally demonstrating high fidelity operation of the electrons in this always-on exchange coupled system. In the regime of weak exchange coupling, defined as the regime for which the qubit coupling is much weaker than the detuning, every native operation on the electrons represents either a conditional rotation (CROT) or zero-conditional rotation (zCROT) gate; rotating one electron conditional on the state of the other electron. We benchmark these native gates using gate set tomography (GST), obtaining single-qubit fidelities of >99.63 $\pm$ 0.07% for both electrons. Additionally, we benchmark the native gates in a two-qubit subspace using phase reversal tomography, obtaining a Bell state fidelity of 92.5 $\pm$ 4.5%. Moreover, we assess the coherence times of the electrons both with and without the presence of the exchange interaction and find that the presence of the weak exchange interaction has no discernible impact on the electron's coherence.

We then benchmark the fidelity of the single qubit gates on the nucleus using single-qubit GST, obtaining a fidelity above 99.82 $\pm$ 0.09% and above 99.5 $\pm$ 0.1% for nucleus 1 and 2 respectively. Using these single-qubit rotations to initialise a superposition state of the nuclei, we utilise an electron in the exchange-coupled pair in order to perform a two-qubit nuclear geometric controlled-Z (CZ) gate between the two nuclei. This is achieved by rotating the electron by 2π, conditional one of the states of the two nuclei that make up the superposition, in order to impart a geometric phase of π on the nuclear state upon which the rotation was conditioned. Finally, we demonstrate the generation of a three-qubit entangled state between the electron and the two-nuclei, by performing a π pulse on the electron, conditional on the state of the two nuclei.

Acknowledgement

Four years ago I came to Australia, without knowing anyone or having ever set foot in this continent before, to embark on a PhD. I could not be more glad that I made that decision. The last four years have been some of the most incredible and formative years of my life and I firmly believe they have left me both a better scientist and a better person. This is all thanks to the incredible people that I have had the fortune of spending time with throughout this journey.

Andrea, it has been an absolute honour to be your student. The passion and integrity with which you approach science is completely inspiring. At times, when the daily challenges associated with bringing an experiment to fruition seemed mundane, you always served as the utmost reminder of the excitement and awe I feel towards the physics that brought me into this field in the first place. Your mantra, whenever any of your group ask if you have time for a question, of 'I'll make time' is a testament to the genuine care you have for your people. Thank you for the time and care you have spent in fostering my scientific career and I only hope that one day I can become a fraction of the scientist that you are.

Serwan, I started my PhD just as you were finishing writing up yours. Since then you have acted as the most incredible mentor, dedicating a huge amount of time to teaching me the fundamentals of measurements. I never cease to be inspired not only by your immense knowledge but, also your work ethic and approach to life in general. Thank you so much for always finding the time for me.

To all the people in the Morello group, what an absolute adventure it has been! I have had such incredible fortune in meeting all of you and have made friendships that will last a lifetime. I could write far too many pages thanking everyone so, I will try to keep it as brief as possible but, please know that I value and thank each and every one of you from the bottom of my heart. Vincent, you have an enormous impact on everyone you meet and I am no exception. Thank you for teaching me everything I know in the cleanroom and for teaching me the importance of keeping everyone's drink topped up at parties. I take this role very seriously now. Mark, on my very first day at UNSW I drilled holes in a breakout box with you and you have helped me so much in the lab ever since, thank you. You are one of the most knowledgeable people I know and the greatest conference buddy anyone could ask for. Big Benni, thank you for all the incredible adventures, from hiking through waist deep water, to camping in the sand dunes, to numerous water park trips. I look forward to many more adventures still to come! Wyatt, you were the one emailing with me before I arrived in Sydney. I thought you were the nicest person then and I think

it even more so now. Thank you for all the fun times over the last few years, from games nights to overnight kayaking. I endeavour to ride a tiny bike as well as you. Irene, you are one of the most caring people I know, thank you for being my desk buddy, taking care of me when I first arrived and for all the BBQs and fun evenings. Rosty, your work ethic is amazing and I hope we can meet up for archery again one day. Hannes, thank you for the liquid nitrogen photoshoots and for keeping me phase coherent. Lil' Benni, thank you for being my swimming and running buddy. I can't wait to tick off all the outdoor pools in Sydney with you. Thank you to you and Mel for injecting so much dog and käsespätzle pizza shaped joy into my life. Daniel Switchback, thank you for all the hiking and camping adventures and for inspiring me to get my cycling lycra act together... Danni, my fellow citizen of Great Britain and Northern Ireland, thank you for so many fun activities. Hiking through snow together at the Grand Canyon was definitely a highlight so far. Arjen, your stories and your handstands are legendary. Chris, thank you for all the movie nights, even the more questionable ones... Mark, Anders, Steve, Gözde, Laura and Brandon, it has been amazing getting to know you all, thank you for all the fun both inside the office and out.

To the members of the Diraq team, thank you to everyone who made my time in Sydney so much richer. If anyone can reach one billion qubits, it's you guys. Arne, thank you for so many fun adventures and ensuring my bike chain is always well-oiled, without me even asking. Santiago, thank you for being my fellow Gloomhaven tank. Amanda, thank you for being my conference wine buddy and for giving me a bouldering role model to aspire to. Alex, thank you for introducing me to Popchops, I will never be the same. Nard, Will, Tuomo, Steve, you are all amazing and my time in Sydney would not have been the same without you.

To all the non-physicists in my life... Thank you to my fellow surf lifesavers, I have met so many people from so many walks of life and you have all had some part in shaping me into the person I am today. Helen, thank you for the many hours spent blowing whistles at people and watching them pick up blue bottles with their bare hands together. To all my friends back home in the UK, thank you for all the support you have given me from afar, you have been my absolute rock.

Thank you to my family, for providing so much support and encouragement throughout this endeavour. Despite not coming from an academic background, you have always encouraged me to follow my scientific dreams and aspirations, right from the start. I wouldn't be the person I am without you. Mum, Dad, Grandad, Issy and Oscar, I love you all.

And finally, thank you to Anatoli; the silicon chip with an attitude. We've had our ups and downs but, the work in this thesis wouldn't have been possible without you...

This research was funded by the Australian Research Council Centre of Excellence for Quantum Computation and Communication Technology (CE170100012) and the US Army Research Office (Contracts no. W911NF-17-1-0200 and W911NF-23-1-0113). I acknowledge support by the Sydney Quantum Academy through the SQA PhD Experience Program. We acknowledge the facilities, and the scientific and technical assistance provided by the UNSW node of the Australian National Fabrication Facility (ANFF), and the Heavy Ion Accelerators (HIA) nodes at the University of Melbourne and the Australian National University. ANFF and HIA are supported by the Australian Government through the National Collaborative Research Infrastructure Strategy (NCRIS) program.

Publications and Presentations

Peer reviewed journal articles

C. Adambukulam, V. Sewani, **H. Stemp**, S. Asaad, M. Mądzik, A. Morello, and A. Laucht, **"An ultra-stable 1.5 T permanent magnet assembly for qubit experiments at cryogenic temperatures,"** Review of Scientific Instruments, vol. 92, no. 8, 2021

Articles submitted for publication

H. G. Stemp, S. Asaad, M. van Blankenstein, A. Vaartjes, M. A. I. Johnson, M. T. Mądzik, A. J. A. Heskes, H.R. Firgau, Y.Su, C.H. Yang, A. Laucht, K. M. Rudinger, R. Blume-Kohout, F. E. Hudson, A. S. Dzurak, K. M. Itoh, A. M. Jakob, B.C. Johnson, D. N. Jamieson, and A. Morello, **"Tomography of universal two-qubit logic operations in exchange-coupled donor electron spin qubits"** arXiv preprint arXiv:2309.15463, 2023

B. Joecker, **H. G. Stemp**, I. Fernandez De Fuentes, M. A. I. Johnson, and A. Morello, **"Error channels in quantum nondemolition measurements on spin systems"** arXiv preprint arXiv:2307.14103, 2023.

Articles in preparation for submission

H. G. Stemp, S. Asaad, M. van Blankenstein, A. Vaartjes, M. A. I. Johnson, M. T. Mądzik, A. J. A. Heskes, A. Laucht, K. M. Rudinger, R. Blume-Kohout, F. E. Hudson, A. S. Dzurak, K. M. Itoh, A. M. Jakob, B.C. Johnson, D. N. Jamieson, and A. Morello, **"Universal nuclear two-qubit logic operations in an exchange-coupled donor system"**.

List of Presentations

Oral presentations:

2020

- Sydney Quantum Academy (SQA) Student Conference - Sydney, NSW, Australia - Talk **(1st place talk award)**

2021

- Silicon Quantum Electronics Workshop, virtual - Talk
- Australian Institute of Physics (AIP) Summer Meeting, virtual - Talk
- Centre for Quantum Computation and Communication Technilogies (CQC2T) Annual Workshop, virtual - Talk

2022

- American Physical Society (APS) March Meeting, Chicago, IL, USA - Talk
- Sydney Quantum Academy research talk - Sydney, NSW, Australia - Talk
- Materials Research Society (MRS), Honolulu, Hawaii, USA - **Invited talk**
- Natalia Ares research group seminar, University of Oxford, UK - Invited seminar
- Scaling of Spin Qubits, University of Copenhagen, Denmark - **Invited talk**
- Quantum Non-Markovianity (QuNoMa), Newcastle, NSW, Australia - **Invited talk**

2023

- APS March Meeting, Las Vegas, NV, USA - Talk
- CQC2T Annual Workshop, Hunter Valley, NSW, Australia - Talk **(1st place talk award)**
- Gordon Godfrey Workshop, Sydney, NSW, Australia - **Invited talk**
- IBS Conference on Quantum Nanoscience (ICQNS), Seoul, South Korea - Talk

Poster presentations:

- 2022 - Spin Qubit 5, Pontresina, Switzerland
- 2022 - CQC2T Annual Workshop, Hobart, TAS, Australia
- 2023 - Quantum Australia, Sydney, NSW, Australia
- 2023 - CQC2T Annual Workshop, Hunter Valley NSW, Australia (highly commended award)

Contents

List of Figures

List of Tables

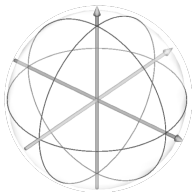

1.

Introduction

Remember to look up at the stars and not down at your feet.

Stephen Hawking

The laws that govern the universe appear to be approximately divided into the laws that govern the macroscopic world, and the laws that govern the microscopic. The nature of the boundary between these worlds, as well as how the laws of the macroscopic world emerge from those dictating the behaviour at the smallest length scales, remains a fiercely studied, open question. Although the physics that governs the large-scale, namely classical physics and, more recently, relativistic mechanics [4, 5], has been studied for at least the last five centuries, the study of quantum mechanics began with the discovery by Max Planck in 1900 that light is absorbed in discrete packets of energy; which Planck denoted as quanta [6]. This discovery sparked the quantum revolution, which took hold in the 1920s with the likes of Niels Bohr, Werner Heisenberg, Erwin Schrödinger, Paul Dirac and many others [7–10]. Although initially dismissed by many in the physics community, as a result of the discrepancy between its physical implications and humanity's classically trained intuition, quantum mechanics now represents one of the most experimentally verified theories ever established.

The two quantum phenomena that are most commonly regarded as defying classical intuition are the concepts of quantum superposition and entanglement. Superposition refers to the ability for quantum states to exist in a linear combination of distinct possible states, until a measurement is performed on the system. Correspondingly, entanglement between quantum particles describes the situation in which an individual particle loses the ability to be described as its own distinct entity and, instead, may only be fully described in relation to the other particles in the entangled pair or group. It is these properties that lead Yuri Manin and Richard Feynman to propose in the 1980s that certain computational problems could benefit from the unique behaviour observed in the quantum world [11, 12]. Both Manin and Feynman noted the potential for enormous amounts of information to be stored in the superposition state of a quantum particle, with a superposition state of N quantum particles, capable of encoding up to 2^N bits of information. Additionally, it was noted that these superposition states could offer the potential for significant parallelisation of certain computational tasks. These postulations spawned an endeavour to build a machine that utilises the laws of the microscopic, instead of the laws of the macroscopic,

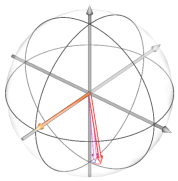

to solve certain computational problems with far greater efficiency than possible with the laws of classical physics alone; thus marking the birth of the field of quantum computing.

Since the 1980s, a prodigious amount of research and progress has been made, developing both the quantum hardware upon which the constituent bits, or qubits, of a quantum computer will be built, along with the development of intelligent algorithms that attempt to bring to bear the full benefit of quantum properties on problems useful to humanity. Although in 2023 we still do not have a quantum computer in every household, the idea of a quantum computer has almost certainly become a household term. With the prevalence of quantum computing in popular news and culture, it is easy to forget that, on the front lines of quantum computing research, even the physical platform upon which a large-scale quantum computer should be ultimately constructed, is still a hotly contended subject. Some of the most promising physical platforms to host a quantum computer, that exist today, include: superconducting qubits [13], trapped-ions [14], photons [15], quantum dots [16, 17] and solid-state nuclear spins [18]; with each platform possessing a unique set of advantages and challenges. Consequently, a widely-held view within the research community is that, ultimately, a combination of multiple physical qubit platforms may be required, in order to realise the full potential of a quantum computer.

One of the outstanding challenges of quantum computing from the perspective of hardware, is in the minimisation of unwanted interactions between qubits and their environment, which offers a pathway through which the sensitive information encoded in the qubit state can be lost to its surroundings. Nuclear spins in the solid state have long been considered a promising candidate for hosting quantum information, as a result of the weak interaction between nuclear spins and their environment; which make the spins extremely resilient to noise in their surroundings [19]. The most well-studied examples of nuclear spins in the solid state, within the context of quantum information, include color-centres in diamond [20–22], magnetic molecules [23] and dopant atoms in silicon [24–26]. It is the latter of this list that forms the basis of the work presented in this thesis.

1.1 Donor spins as qubits

Colloquially, the most basic requirements necessitated by a scalable quantum processor are [27]:

- A well-defined qubit or qudit system.
- The capacity to initialise and read out the state of the qubits with the levels of fidelity required for fault-tolerant quantum computation.
- The capacity to implement a universal set of quantum gates consisting of both single-qubit operations and two-qubit entangling operations.

In 1998, Bruce Kane published a seminal paper in Nature, detailing how the requirements laid out above could be met using the spins of donor atoms in silicon [25]. In this proposal, Kane envisioned utilising the spin of the nucleus, in the presence of a strong magnetic field, as the foundation of the qubit, with the Zeeman-split spin states, $|\Uparrow\rangle$, $|\Downarrow\rangle$ being used to encode the qubit $|0\rangle$ and $|1\rangle$ states respectively.

Upon fabricating an array of donor atoms, Kane envisioned controlling these donor spins through the application of a globally applied field, which acts to rotate all the qubits simultaneously. Within this scheme, individual qubits would be addressed by using the voltages applied to local gates to DC Stark shift the qubits in and out of resonance with the globally applied field [28]. Furthermore, Kane proposed to mediate the coupling between neighbouring nuclei via their electrons, with the exchange coupling between the electrons being controlled by intermediate gates fabricated between the donor atoms.

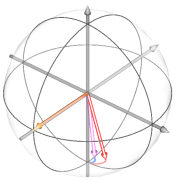

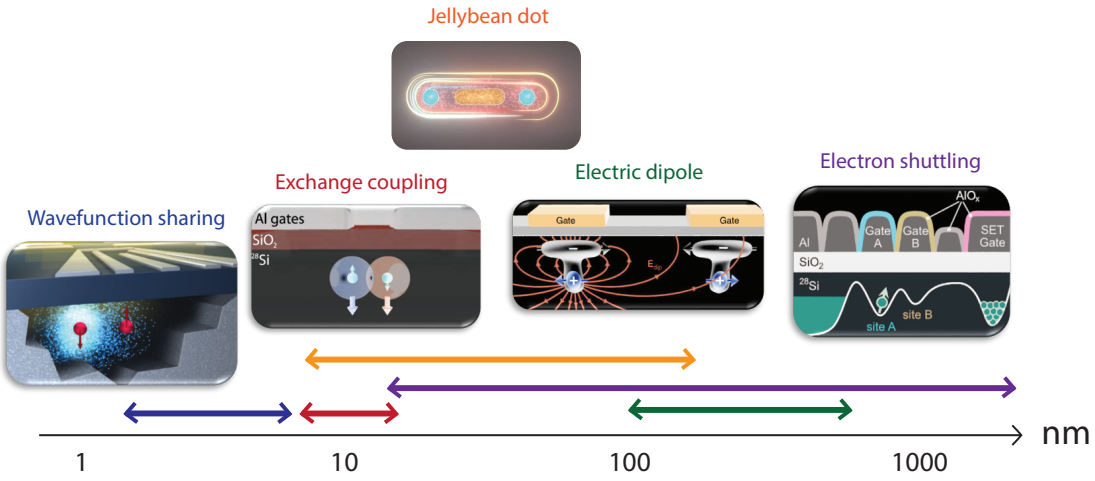

Figure 1.1: **Donor coupling length scales.** Diagram of the approximate length scales of different coupling mechanisms in silicon [29–33]

Significant progress has been made towards Kane's vision over the last 25 years, with many of the capabilities proposed being successfully demonstrated , [19, 26, 28, 34–36]. The work in this thesis focuses primarily on the multi-qubit aspect of Kane's proposal, using the spin of the electron to mediate the coupling between neighbouring donor nuclei. Since 1998 however, the toolbox for coupling nuclei in silicon has expanded considerably, with numerous coupling mechanisms being demonstrated, over a range of different length scales. Figure 1.1 details some of these coupling mechanisms and the length scales at which they operate [29–32]. Crucially, a number of these coupling mechanisms are agnostic to the exact distance between the donors, allowing the flexibility necessary for the placement of ion-implanted donor atom arrays [37]. The two coupling mechanisms most pertinent to this thesis are: wave-function sharing and exchange-coupling.

Wave-function sharing is a coupling mechanism that exists between donor nuclei at the smallest length-scales. When nuclei are very close together, of order < 10 nm, the wave-function of the donor-bound electron is no longer localised to one individual donor but, instead can be spread out over both nuclei. This results in the electron Hamiltonian pos-

sessing two hyperfine coupling terms, one for each of the nuclei, and thus the transition frequency of the electron is conditional on the state of both the nuclei. This condition allows for the performance of nuclear geometric controlled-Z (CZ) gates [29].

Moving from wavefunction sharing to larger distance coupling mechanisms, neighbouring nuclei with a distance of approximately 10-30 nm, can be coupled together via an intermediary exchange interaction [30]. This coupling mechanism forms the foundation for the work carried out in this thesis.

With a means of controlling, initialising and reading out the state of individual nuclear and electron spins, as well as coupling nuclei together using the donor-bound electrons, these capabilities complete the most fundamental checklist for building a scalable donor quantum processor within this physical platform.

1.2 Thesis outline

Chapter 2 - Theory of donor spin qubits in silicon

This chapter begins by detailing the terms in the Hamiltonian of a ^{31}P donor atom in silicon before describing the theory behind the coherent control of the donor nucleus and electron. Coherence of the spins, and the role this plays in mapping out the noise environment of the donors, is also discussed.

Chapter 3 - Donor spin qubit device

The chapter begins by describing the fabrication and experimental design of the devices used in the remainder of this thesis. The basic principles behind the readout and coherent control of the donor electron and nuclear spin are outlined in detail. Finally, the machine learning techniques that have been implemented for electron readout optimisation are

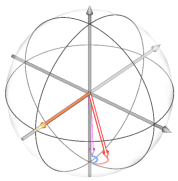

described.

Chapter 4 - Theory of exchange coupled ^{31}P donors

This chapter describes the fundamental theory behind the exchange interaction between neighbouring donor electrons, detailing the eigenstates of the Hamiltonian of the exchange-coupled donor system for different regimes of exchange coupling. The basic theory behind entanglement and how it is quantified experimentally in donor systems is then explained.

Chapter 5 - Two-qubit electron conditional rotation gates in a J-coupled system

This chapter outlines the experimental results associated with benchmarking the first experimental demonstration of exchange-based, entangling two-qubit logic gates between electrons bound to individual ^{31}P donors in silicon. The system consists of two ^{31}P donor nuclei, each with a bound electron that are coupled together with an exchange interaction. Gate set tomography (GST) is performed to assess the performance of the electron two-qubit conditional rotation (CROT) gate native to this system. The limitations of the quantum-non demolition (QND) readout technique used to read out the state of an electron in the J-coupled pair are also discussed.

Chapter 6 - Two-qubit nuclear geometric controlled-Z gates in a J-coupled system

This chapter discusses the experimental implementation of a nuclear geometric controlled-Z (CZ) gate on the nuclei of a pair of exchange-coupled ^{31}P donors by using the conditional rotation of the donor-bound electron to impart a geometric phase on the nuclei. The operations on the nuclei are benchmarked with single-qubit GST.

Chapter 7 - Conclusion and future directions

This chapter summarises the key results presented in this thesis and presents the future outlook of this work.

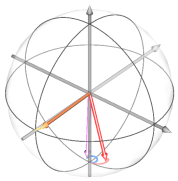

2.

Theory of donor spin qubits in silicon

The scientist does not defy the universe. He accepts it... It is wonderful both in the small and in the large.

Isidor Isaac Rabi

2.1 Donors in silicon

Doping is the process of introducing impurity atoms into a semiconductor crystal. Semiconductor crystals are a class of crystalline solids, whose electrical conductivity lies somewhere in the intermediate regime, between that of a conductor and that of an insulator. The introduction of impurities into these crystals, allows for the conductivity of the crystal to be significantly modified, making these materials extremely valuable for the construction of a number of instrumental devices, within the computer and photovoltaic industries [38]. Some examples of the most prevalent semiconductors used in these industries are: silicon, germanium and gallium arsenide. In our group, we utilise silicon as the host crystal for our dopant atom qubits, as this element is the material of choice for classical computer chip manufacturing [39]; thus offering the possibility of utilising the pre-existing technological developments of this mature industry.

Silicon possesses a diamond cubic crystal structure, with a face-centred cubic lattice and a basis of two silicon atoms. The bandgap of silicon is 1.1 eV, with the Fermi level lying almost in the centre of the bandgap, between the valence and conduction bands [38]. Consequently, at 300 K, thermal excitations cause some electrons to be excited into the conduction band and holes to be created in the valence band, resulting in silicon being conductive at room temperature. When silicon is cooled down to cryogenic temperatures however, the electrons no longer possess sufficient thermal energy to be excited into the conduction band, and thus silicon becomes an insulator.

There are two types of doping that can be used to alter the conductive properties of silicon: positive (p)- type doping and negative (n) - type doping. P-type doping involves introducing an additional positive charge to the silicon lattice, while conversely, n-type doping involves the introduction of an additional negative charge to the crystal. N-type doping can be achieved, by introducing an impurity atom from group V of the periodic table into the silicon lattice. The group V element has 5 electrons in its outer shell, com-

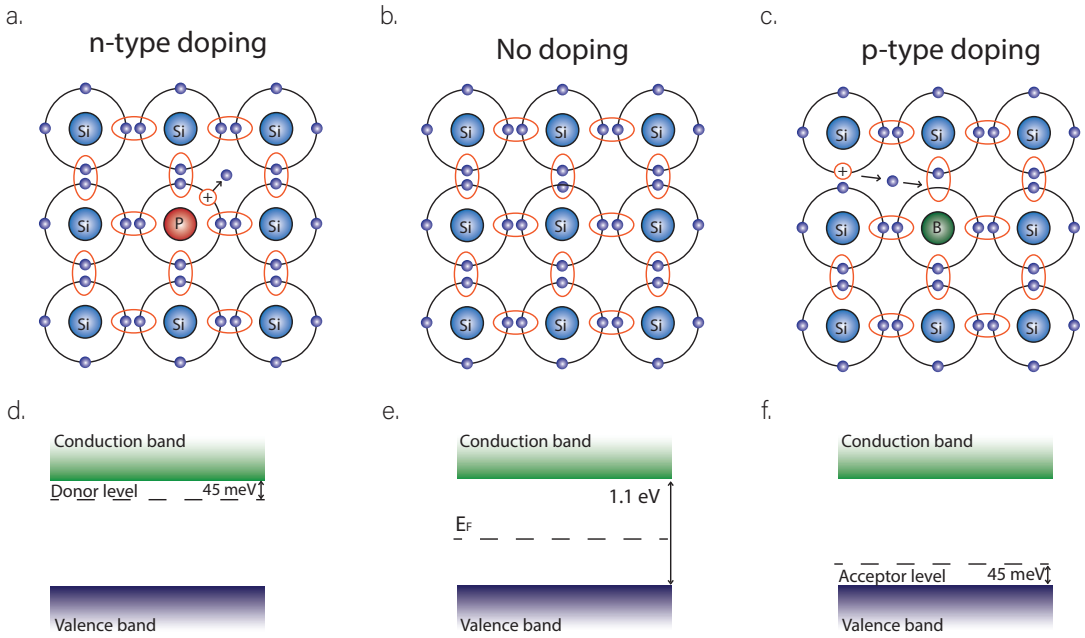

Figure 2.1: **Doping in silicon**. The top row shows a representation of the silicon crystal with negative (n)-type doping using phosphorus atoms (**a.**), no doping (**b.**) and positive (p)-type doping using boron atoms (**c.**). The bottom row (**d.**,**e.**,**f.**) shows the corresponding bandgap for each of these doping regimes. The Fermi level (E_F) in silicon shifts towards either the valence or conduction band, according to the atomic species of the doping impurities [40].

pared to the 4 electrons in the outer shell of the group IV silicon. Thus, when incorporated into the lattice, 4 electrons in the outer shell of the impurity atom form strong covalent bonds with an electron in the outer shell of 4 neighbouring silicon atoms. The remaining unpaired electron from the group V impurity serves as an additional negative charge, which is weakly coupled to the impurity atom. As the impurity has contributed an extra electron to the lattice, these impurities are known as donor atoms. The extra electron weakly bound to the donor atom requires less energy to be excited into the conduction band, compared to the electrons in strong covalent bonds, and thus, for the example of a phosphorus donor atom, the donor energy level lies only 45 meV from the conduction band edge [41].

In contrast, p-type doping can be achieved by introducing a group III impurity atom into the silicon lattice, thus attracting an additional electron from the silicon atoms and leaving behind a positively charged hole in its place. Consequently, group III impurity atoms are known as acceptors, with the acceptor atom energy level, for the example of the acceptor atom boron, lying 45 meV above the valence band. Figure 2.1 shows the silicon lattice and band structure in the presence of both n and p type doping. In the work described in this thesis we make use of donor atoms, introducing a group V impurity nucleus, with a weakly coupled bound electron, into the silicon lattice, to form the basic building blocks of our quantum processors.

Table 2.1 shows some key properties of the group V donors in silicon. One property particularly pertinent to quantum computation is the value of the nuclear spin, as this is the degree of freedom in which we encode our quantum information. Although for a number of purposes, a higher nuclear spin number is desirable, as it gives access to a larger number of states on which to encode our quantum information, in this thesis we will focus primarily on the phosphorus donor atom, ^{31}P, with a nuclear spin of 1/2.

Element	Nuclear spin	Ground state binding energy (meV)	Hyperfine coupling, A (MHz)	Nuclear gyromagnetic ratio, γ_n (MHz/T)
^{31}P	1/2	45.59	117.53	17.26
^{75}As	3/2	53.76	198.35	7.31
^{123}Sb	7/2	42.74	101.52	5.55
^{209}Bi	9/2	70.98	1475.4	6.96

Table 2.1: **Group V donors in silicon.** Parameters of group V donors in silicon. The values in this table were obtained from [1–3]

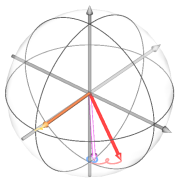

2.2 The spin of the electron and nucleus

The concept of spin was first experimentally demonstrated in 1921, by Otto Stern and Walter Gerlach [42]. In this experiment, Stern and Gerlach heated silver atoms in an oven possessing a small aperture, through which a beam of energetic atoms could escape. A series of magnets were positioned such that a magnetic field gradient was created in a direction perpendicular to the atoms' trajectory. The beam was then detected using a photographic plate. The purpose of the experiment was to detect the angular momentum of the single outer shell electron of the silver atom, by observing the deflection of the atom in the inhomogeneous magnetic field. The results of this experiment were utterly unexpected to the physics community at the time. If the angular momentum of the electron was classically distributed, then the expected outcome of the experiment would be a continuous distribution of deflection angles of the beam, resulting in a smeared smudge observed on the photographic plate. Instead, two discrete lines, were observed, indicating that the angular momentum of the electron must be quantised. This result was also incompatible with the prevailing knowledge of the time that orbital angular momentum, $\hat{\mathbf{L}}$, was responsible for the angular momentum of a particle, as $\hat{\mathbf{L}}$ is quantised according to $2L+1$, where L must take an integer value [43]. Thus, if the orbital angular momentum were responsible for this quantisation, an odd number of discrete trajectories should have been observed. This led researchers to postulate the idea of an intrinsic angular momentum, $\hat{\mathbf{S}}$, independent of the orbital angular momentum, which instead possesses $2S+1$ quantised levels, where S can take a non-integer value. This intrinsic angular momentum is what we now refer to as the spin and, like mass or charge, it is a property inherent to every particle.

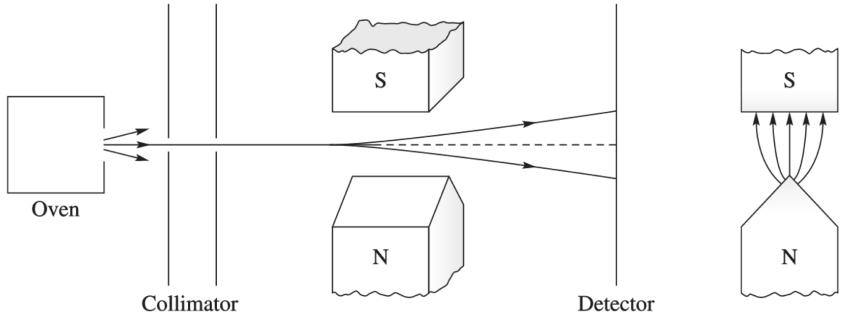

Figure 2.2: **Stern Gerlach experimental apparatus.** Experimental setup to test the angular momentum of a single electron. Silver atoms were heated in an oven before travelling in a beam through an inhomogeneous magnetic field towards a photographic detector plate. The trajectories of the atoms displaced by the field revealed that the electron possesses a quantised intrinsic angular momentum. Image taken from [44].

The overall angular momentum, $\hat{\mathbf{J}}$,of a given particle is made up of contributions from both its orbital angular momentum and its spin. The total magnitude of angular momentum is therefore given by

$$\hat{\mathbf{J}} = \hat{\mathbf{L}} + \hat{\mathbf{S}}. \tag{2.1}$$

The angular momentum of a single electron in the s-orbital consists of only contributions from the intrinsic spin angular momentum. For a nucleus however, the overall angular momentum consists of contributions from all of its constituent protons and neutrons, which themselves can possess both spin and orbital angular momentum. The spin of a nucleus can therefore take both integer or half-integer values, depending on its constituent nucleons [45].

For simplicity, for the remainder of this section, we will refer only to a generic spin, $\hat{\mathbf{S}}$, however, although this notation typically refers to the electron spin, the same mathematics can be applied to both the spin of the electron and of the nucleus (which is typically denoted by $\hat{\mathbf{I}}$). The square of the total angular momentum of a spin is given by the spin

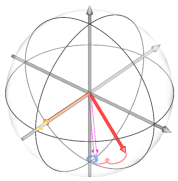

operator $\hat{\mathbf{S}}^2 = (\hat{S_x}^2 + \hat{Sy}^2 + \hat{S_z}^2)$, where $\hat{S}_x, \hat{S}_y$ and $\hat{S}_z$ refer to the projection operators along the x, y and z axis respectively, given by the spin matrices

$$\hat{S}_x = \frac{1}{2}\begin{pmatrix} 0 & 1 \\ 1 & 0 \end{pmatrix}, \tag{2.2}$$

$$\hat{S}_y = \frac{1}{2}\begin{pmatrix} 0 & -i \\ i & 0 \end{pmatrix}, \tag{2.3}$$

$$\hat{S}_z = \frac{1}{2}\begin{pmatrix} 1 & 0 \\ 0 & -1 \end{pmatrix}. \tag{2.4}$$

Note that we ignore the multiplicative factor $\hbar = 1.0546 \times 10^{-34}$ $\mathrm{m^2 kgs^{-1}}$ in our definition of the spin operators, such that any subsequent Hamiltonian terms may be written in units of frequency. Computing the commutator between each of these projection operators gives the following

$$[\hat{S}_x, \hat{S}_y] = i\hat{S}_z, \tag{2.5}$$

$$[\hat{S}_y, \hat{S}_z] = i\hat{S}_x, \tag{2.6}$$

$$[\hat{S}_z, \hat{S}_x] = i\hat{S}_y, \tag{2.7}$$

The fact that the spin projection operators along x, y and z do not commute, tells us that we cannot simultaneously acquire knowledge regarding the projection of the spin along more than one of these three axis, within an uncertainty given by Heisenberg's uncertainty principle, which has important implications for quantum operations.

Both the total spin operator $\hat{\mathbf{S}}$ and the spin projection operator along z, $\hat{S}_z$ share a set of eigenstates $|m_S\rangle$. The projection of the total angular momentum along the z-axis can therefore by written as

$$\hat{S}_z |m_S\rangle = m_S |m_S\rangle, \tag{2.8}$$

where m_S, can only take a set of $2S+1$ discrete values, between $m_S = -S$ and $m_S = S$, where S is the spin quantum number. For example, for the electron spin, with $S = \frac{1}{2}$, the possible projection outcomes along the z-axis are $m_S = \pm\frac{1}{2}$, as depicted schematically in Figure 2.3.

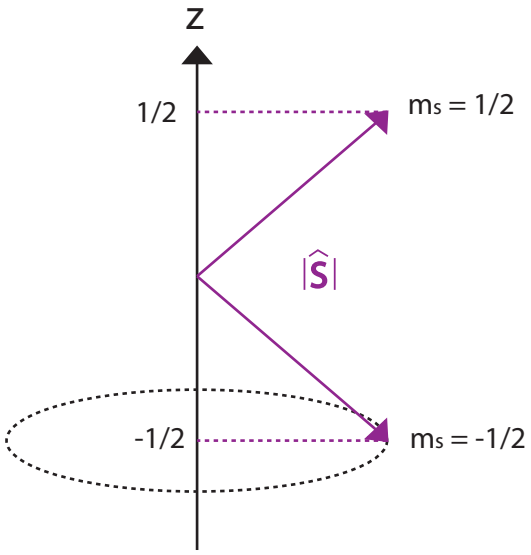

Figure 2.3: **Quantisation of the spin along the z-axis.** The total angular momentum of a spin $S = \frac{1}{2}$ particle is depicted by the purple arrows, with the two possible projections along the z-axis, $\pm\frac{1}{2}$ shown by the dashed purple line. The dashed black circle represents the lack of knowledge regarding the orientation of the spin along the xy plane.

In this thesis, we work with both the spin of an electron and the spin of a ^{31}P nucleus, both of which possess a spin quantum number of $S = \frac{1}{2}$. The possible projection outcomes along the z-axis are therefore

$$\hat{S}_z \left| -\frac{1}{2} \right\rangle = -\frac{1}{2} \left| -\frac{1}{2} \right\rangle , \tag{2.9}$$

$$\hat{S}_z \left| +\frac{1}{2} \right\rangle = +\frac{1}{2} \left| +\frac{1}{2} \right\rangle . \tag{2.10}$$

For the remainder of this thesis, we will refer to the two eigenstates for the projection of

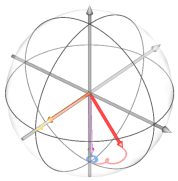

a spin $S = \frac{1}{2}$ along the z-axis, $\left|-\frac{1}{2}\right\rangle$ and $\left|+\frac{1}{2}\right\rangle$, as the spin down, $|\downarrow\rangle$, and spin up, $|\uparrow\rangle$, states respectively.

2.3 Donor spin Hamiltonian

We can determine the energy of a given system by writing down its Hamiltonian. The eigenstates of the Hamiltonian tell us important information regarding the stationary states of a given spin system and thus how the system will evolve as a function of time. For a neutral donor atom in silicon, in the presence of a static magnetic field, there are two primary mechanisms that contribute to the system's overall energy: the Zeeman interaction and the hyperfine interaction.

2.3.1 The Zeeman energy term

For illustrative purposes we can start by considering the case of an isolated ^{31}P nucleus and electron, with no coupling between them. We can denote the spin down (up) states of the isolated electron and nucleus as $|\downarrow\rangle$ ($|\uparrow\rangle$) and $|\Downarrow\rangle$ ($|\Uparrow\rangle$) respectively. In the presence of a magnetic field the electron (nuclear) spin $|\downarrow\rangle$ ($|\Downarrow\rangle$) and spin $|\uparrow\rangle$ ($|\Uparrow\rangle$) states separate in energy as a result of the Zeeman interaction [46]. The magnitude of this energy splitting, known as Zeeman splitting, is given, in units of frequency, by the formula $E_{\text{Zeeman}} = \gamma B_0$, where γ is the gyromagnetic ratio and B_0 is the strength of the magnetic field applied to the spin. The gyromagnetic ratio of an electron spin is given by $\gamma_e = g_e \mu_B / h$, where $h = 6.626 \times 10^{-34} Js$ is Planck's constant, $g_e = 2.002$ is the electron g-factor and $\mu_B = 9.274 \times 10^{-24} J/T$ is the Bohr magneton. In a similar fashion, the gyromagnetic ratio of a ^{31}P nuclear spin is given by the formula $\gamma_n = g_n \mu_n / h$, where $g_n = 2.263$ is the ^{31}P nuclear gyromagnetic ratio and $\mu_n = 5.051 \times 10^{-27} J/T$ the nuclear magneton accordingly [47].

The gyromagnetic ratio of an electron, γ_e = 28.025 GHz/T, is over three orders of magnitude larger then that of the phosphorus nucleus with γ_n = -17.235 MHz/T [48]. Con-

sequently, the energy splitting due to the Zeeman interaction is considerably greater for the electron spin compared to that of the donor nucleus, for a given magnetic field. Note that the difference in sign between the gyromagnetic ratio of the electron and that of the nucleus is indicative of the opposing precession directions of the electron and nuclear spins in the presence of a magnetic field. Figure 2.4 shows the magnitude of Zeeman splitting as a function of increasing magnetic field strength, for both the spin of an isolated electron and the spin of an isolated ^{31}P nucleus.

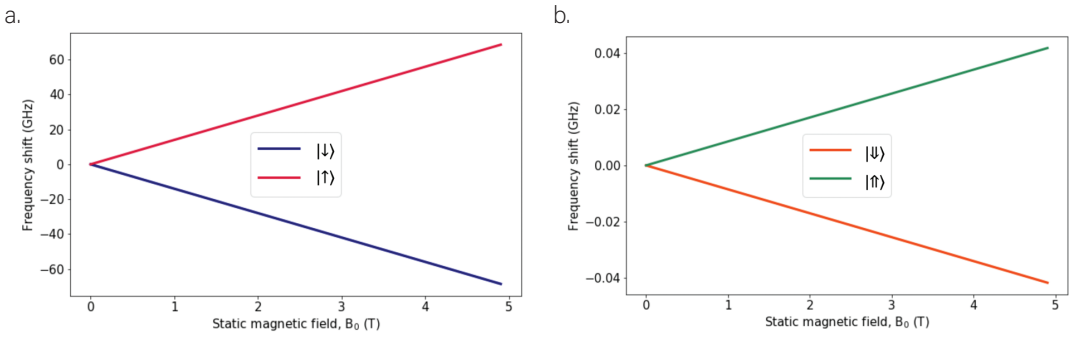

Figure 2.4: **Zeeman splitting with magnetic field.** **a.** Energy eigenvalues of an isolated electron with increasing magnetic field. **b.** Energy eigenvalues of an isolated nucleus with increasing magnetic field. In both **a.** and **b.**, the energy difference between the two eigenvalues for denotes the Zeeman splitting. The vast difference in Zeeman splitting between the electron and the nucleus is due to the fact that the Zeeman spitting is given by $\mathrm{E_z} = \gamma\ \mathrm{B_0}$, where γ is the gyromagnetic ratio of the spin and $\mathrm{B_0}$ is the static magnetic field strength. The electron gyromagnetic ratio is three orders of magnitude larger than that of the nucleus, hence the much larger Zeeman splitting observed.

For the case of an isolated electron and donor nucleus, with no coupling between them, in the presence of a DC magnetic field B_0, the Hamiltonians for the nucleus ($\hat{H}_\mathrm{n}$) and for the electron ($\hat{H}_\mathrm{e}$), are given by the following, in units of frequency:

$$\hat{H}_\mathrm{e} = \gamma_\mathrm{e} B_0 \hat{S}_z\,, \tag{2.11}$$

$$\hat{H}_\mathrm{n} = \gamma_\mathrm{n} B_0 \hat{I}_z\,, \tag{2.12}$$

where $\hat{S}_\mathrm{z}$ and $\hat{I}_\mathrm{z}$ are the spin projection operators along the z-axis for the electron and

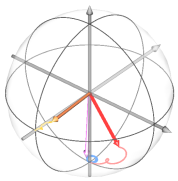

nuclear spin respectively.

Focusing first on the electron spin, the eigenstates of the Hamiltonian $\hat{H}_{\mathrm{e}}$ consist of the $|\downarrow\rangle$ and $|\uparrow\rangle$ spin states, which are orientated along the z-direction of the Bloch sphere, parallel to the static B_0 field. These states thus represent the stationary states of the electron for this Hamiltonian. If however, the electron is initialised into a state that does not constitute an eigenstate of the system, but rather a superposition of these eigenstates, then the spin will precess about the applied B_0 field. The frequency at which the spin precesses about the B_0 field is called the Larmor precession frequency, ω_0 and is given by the energy difference between the eigenvalues of the two eigenstates, $E_\downarrow$ and $E_\uparrow$.

$$\frac{\omega_0}{2\pi} = \frac{E_\uparrow - E_\downarrow}{h} = \gamma B_0, \tag{2.13}$$

where, for the case of an electron, $\gamma = \gamma_{\mathrm{e}}$.

Figure 2.5 shows the precession of the electron spin, after being initialised in the superposition state $\frac{1}{\sqrt{2}}(|\downarrow\rangle + |\uparrow\rangle)$, pointing along the xy plane of the Bloch sphere. As this state is not an eigenstate of the Hamiltonian, the spin is seen to precess about the z-axis at the Larmor precession frequency $\frac{\omega_0}{2\pi}$ = 28.025 GHz, for a B_0 field of 1 T.

The same principles also hold for the nuclear spin in the presence of a static B_0 field, with the eigenstates of the nuclear Hamiltonian, $\hat{H}_{\mathrm{n}}$ consisting of the $|\Downarrow\rangle$ and $|\Uparrow\rangle$ spin states of the nuclei. Similarly to the electron, if the nucleus is initialised into a superposition state that is not an eigenstate of the Hamiltonian, for example, $\frac{1}{\sqrt{2}}(|\Downarrow\rangle + |\Uparrow\rangle)$, then it will precess around the applied B_0 field. For the case of the nucleus however, due to the lower gyromagnetic ratio, its Larmor precession frequency is much slower than that of the electron at $\frac{\omega_{\mathrm{n}}}{2\pi} = \gamma_{\mathrm{n}} B_0$ = -17.235 MHz, for a B_0 of 1 T.

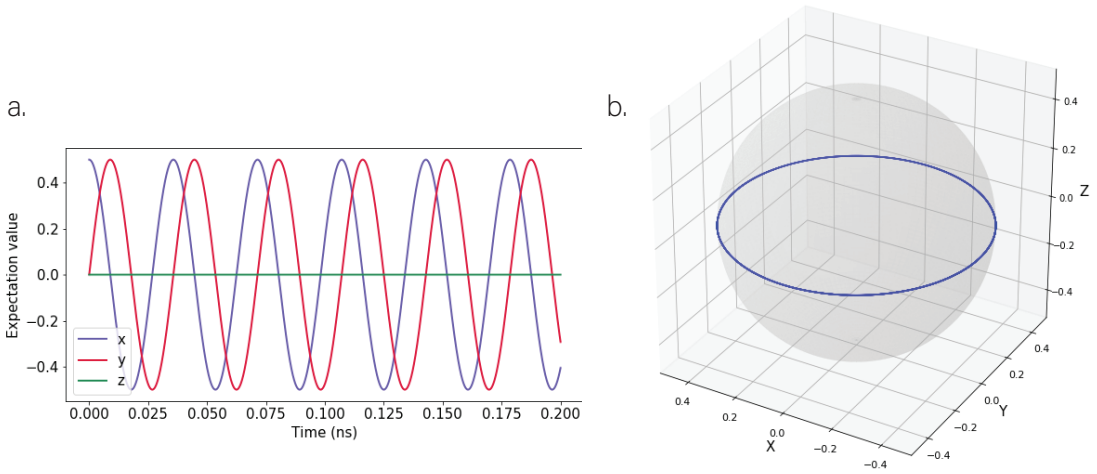

Figure 2.5: **Larmor precession**. Simulation of the Larmor precession of an electron spin, initilised in the state $\frac{1}{\sqrt{2}}(|\downarrow\rangle + |\uparrow\rangle)$, in a DC field pointing along the z-direction of magnitude 1 T. **a.** Simulation of the individual x,y and z expectation values against time. **b.** Expectation values from the simulation in **a**, projected onto a Bloch sphere. The expectation value along z remains constant while the x and y components oscillate at the Larmor precession frequency.

2.3.2 The hyperfine interaction term

In the previous section, we considered an electron and nuclear spin existing in isolation of one another and hence only influenced by the presence of an external, static magnetic field B_0. For neutral donor atoms in silicon however, a more physical situation is described by a donor nucleus coupled to a weakly bound electron. Upon bringing an electron in close proximity to a donor nucleus, ($\lesssim$ 10 nm) a coupling term arises between the nuclear and electron spin, known as the hyperfine interaction.

The hyperfine interaction is comprised of two individual components, which sum together to give the total hyperfine interaction between the electron and nucleus [49]. The first component is known as the Fermi contact hyperfine [50], given by

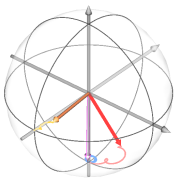

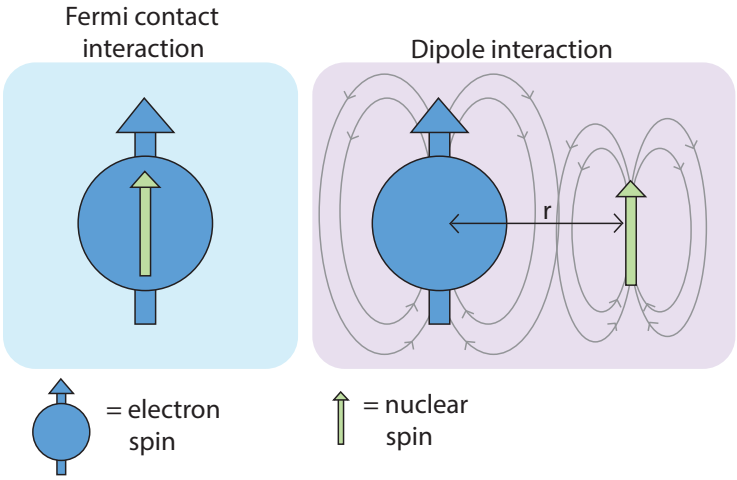

Figure 2.6: **Hyperfine interaction terms.** Schematic depiction of the conceptual differences between the Fermi contact and dipole interaction term that constitute the overall hyperfine interaction.

$$A_{\mathrm{FC}} = -\frac{2}{3}\mu_0 \langle \mu_{\mathrm{n}} \cdot \mu_{\mathrm{B}} \rangle |\psi(0)|^2, \tag{2.14}$$

where $\mu_0 = 4\pi \times 10^{-7}$ H/m is the vacuum magnetic permeability constant and $|\psi(0)|^2$ denotes the probability of finding the electron at the site of the nucleus, in the ground state, ψ_0. As a result of this dependence on the overlap of the wavefunction of the electron at the site of the nucleus, the Fermi contact interaction is only non-zero for the case of an electron occupying an s-like orbital, as all other orbital states possess a node at the nuclear site and hence the probability of finding the electron falls to zero at the site of the nucleus. For donor atoms in silicon, at cryogenic temperatures, the electron resides almost exclusively in an s-orbital and hence the Fermi contact hyperfine is the dominant term in the hyperfine interaction. This interaction is isotropic, meaning that it does not depend on the spins' orientation with respect to the magnetic field.

The second component of the hyperfine interaction is the dipole-dipole interaction [51], given by

$$A_{\mathrm{dd}} = g_{\mathrm{e}} g_{\mathrm{n}} \mu_{\mathrm{B}} \mu_{\mathrm{n}} \left[\frac{3(\hat{\mathbf{S}} \cdot \vec{r})(\hat{\mathbf{I}} \cdot \vec{r})}{r^5} - \frac{\hat{\mathbf{S}} \cdot \hat{\mathbf{I}}}{r^3} \right], \tag{2.15}$$

where $\hat{\mathbf{S}} = (\hat{S}_{\mathrm{x}} + \hat{S}_{\mathrm{y}} + \hat{S}_{\mathrm{z}})$ is the electron spin operator and $\hat{\mathbf{I}} = (\hat{I}_{\mathrm{x}} + \hat{I}_{\mathrm{y}} + \hat{I}_{\mathrm{z}})$ is the nuclear spin operator, r is the distance between the two spins and $\vec{r} = (x\vec{i} + y\vec{j} + z\vec{k})$ is the vector distance between them, where $\vec{i}, \vec{j}, \vec{k}$ are the unit vectors in the three Cartesian directions. This expression reveals that the dipole-dipole hyperfine coupling depends on the distance between the two spins, as well as the orientation of the spins with respect to the external magnetic field, making this an anisotropic interaction.

The overall hyperfine term can therefore be constructed by summing together the contributions from both the Fermi contact and dipole-dipole hyperfine term

$$A = A_{\mathrm{FC}} + A_{\mathrm{dd}}. \tag{2.16}$$

The hyperfine coupling term in the neutral donor Hamiltonian can then be written as:

$$\hat{H}_{\mathrm{hyperfine}} = A\hat{\mathbf{S}} \cdot \hat{\mathbf{I}}. \tag{2.17}$$

The value of the hyperfine interaction strength, A, depends on the donor atomic species. For a ^{31}P nucleus in silicon, the hyperfine strength in the bulk of the sample is A = 117.53 MHz [2]. However, this value is dependent on the strain profile within the device, resulting in the exact hyperfine coupling strength for a given donor deviating according to the exact positioning of the donor within the device. A donor closer to the interface for example, will be in closer proximity to the aluminium gates on the surface of the device. These gates possess a different thermal coefficient of expansion compared to the silicon lattice and hence introduce some strain to the lattice upon cooling to the mK temperatures required to operate the donors as qubits (see section 3.4) [52]. Consequently, donors closer to the interface are known to exhibit greater discrepancies in hyperfine strength from the bulk hyperfine value of A = 117.53 MHz, as a result of the strain deforming the electron wavefunction and therefore influencing the overlap of the electron wavefunction at the site

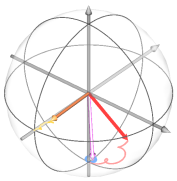

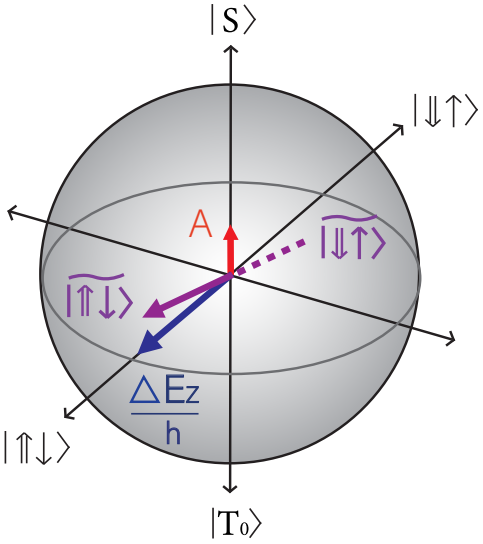

Figure 2.7: **Two qubit electron, nuclear Bloch sphere.** Two-qubit Bloch sphere denoting the electron-nuclear eigenstates in a hyperfine coupled system depending on the ratio between the difference in Zeeman splitting, in units of frequency, $\frac{\Delta E_z}{h}$ and the hyperfine term A. The double arrows denote the nuclear spin state while the single arrows denote the electron spin state. On the poles of the Bloch sphere are the singlet state, $|S\rangle$ and triplet state, $|T_0\rangle$, which represent fully-entangled states between the electron and nucleus. For large values of detuning, the eigenstates become the $|\Downarrow\uparrow\rangle$ and $|\Uparrow\downarrow\rangle$ states. If however, the detuning becomes comparable to the coupling term then the eigenstates of the system become hybridised, resulting in the eigenstates $|\tilde{\Uparrow\downarrow}\rangle$, $|\tilde{\Downarrow\uparrow}\rangle$.

of the nucleus.

For the case of a neutral donor atom in the presence of a static magnetic field, B_0, we can combine the Zeeman interaction term of the electron and nucleus with the hyperfine interaction term to form the following Hamiltonian:

$$\hat{H}_{\text{full}} = \underbrace{\gamma_e B_0 \hat{S}_z}_{\text{Electron Zeeman}} + \underbrace{\gamma_n B_0 \hat{I}_z}_{\text{Nuclear Zeeman}} + \underbrace{A\hat{\mathbf{S}} \cdot \hat{\mathbf{I}}}_{\text{Hyperfine coupling}} \tag{2.18}$$

As this Hamiltonian now includes a coupling term between the two spins, the eigenstates of the system now depend very intimately on the ratio between the coupling and detuning

between the spins, $\frac{A}{\Delta E_z/h}$, where A is the hyperfine coupling and ΔE_z is the difference in Zeeman energy between the nucleus and electron. For the case of a ^{31}P nucleus in a 1 T static magnetic field, $\frac{\Delta E_z}{h} >> A$. Thus, in the high field regime, the eigenstates can be approximated very accurately as the product states between the electron and nuclear spin states. The eigenstates of the Hamiltonian are therefore the following, in order of increasing energy, as depicted in Figure 2.8 [53]:

$$|\phi_1\rangle = |\Uparrow\downarrow\rangle\,, \tag{2.19}$$

$$|\phi_2\rangle = |\Downarrow\downarrow\rangle\,, \tag{2.20}$$

$$|\phi_3\rangle = |\Downarrow\uparrow\rangle\,, \tag{2.21}$$

$$|\phi_4\rangle = |\Uparrow\uparrow\rangle\,. \tag{2.22}$$

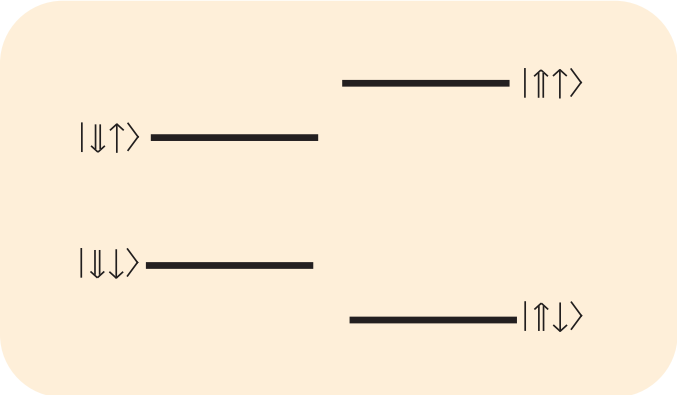

Figure 2.8: **Donor energy levels.** Schematic depiction of the eigenstates of the neutral donor with the lowest energy state at the bottom and the highest energy state at the top.

Figure 2.9 shows the energy levels of these eigenstates with increasing magnetic field. The frequencies required to drive transitions between each of these energy levels, are discussed in greater depth in section 2.4.

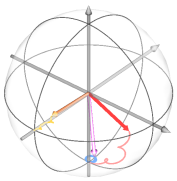

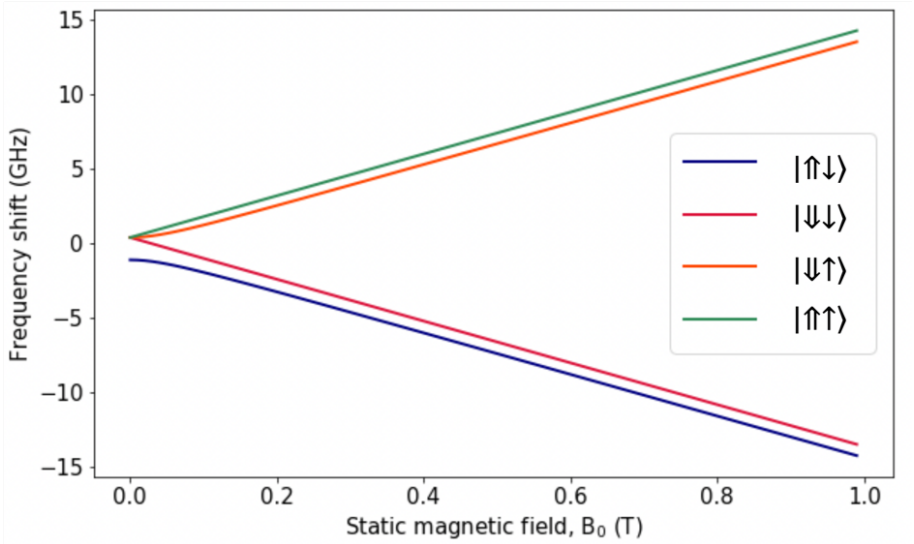

Figure 2.9: **Hyperfine interaction with Zeeman splitting.** Energy levels of the neutral donor with both a Zeeman and hyperfine interaction term. A hyperfine value of 1.5 GHz was used in order to exaggerate the hyperfine splitting of the energy levels for better visual demonstration.

2.4 Coherent control of the spin

2.4.1 Spin resonance

In order to perform useful quantum operations on the donor spin qubits, we require the ability to control the spin, such that we can prepare any arbitrary state on the Bloch sphere. To do this, we make use of a technique known as spin resonance, whereby a rotating B_1 field is applied in a plane orthogonal to the static B_0 field, in order to induce rotations around the Bloch sphere.

This rotating, magnetic field, $\vec{B_1}(t)$, can be written as the following

$$\vec{B_1}(t) = B_1[\cos(\omega t)\vec{i} + \sin(\omega t)\vec{j}], \tag{2.23}$$

where $\vec{i}$ and $\vec{j}$ are the unit vectors in two Cartesian directions, B_1 is the amplitude of the $\vec{B_1}$ field and $\omega = 2\pi\nu$, where ν is the frequency of the rotating field.

For simplicity, we can consider the Hamiltonian of an isolated electron spin in the presence of a static B_0 field along z and a rotating B_1 field in the xy plane, which can be written as

$$\hat{H(t)} = \gamma_e B_0 \hat{S}_z + \gamma_e B_1[\cos(\omega t)\hat{S}_x + \sin(\omega t)\hat{S}_y], \tag{2.24}$$

As the field along z generates a rotation around the xy plane of the Bloch sphere, at the Larmor precession frequency, we can simplify this picture by moving into a rotating frame that rotates around the xy plane with frequency $\frac{\omega}{2\pi}$. To transform the spin states into this rotating frame, we can apply a rotation of angle $\theta(t) = \omega t$ to the states, using the following rotation operator

$$\hat{R(t)} = e^{i\omega t\hat{\sigma_z}/2}, \tag{2.25}$$

where $\hat{\sigma_z} = \begin{pmatrix} 1 & 0 \\ 0 & -1 \end{pmatrix}$ represents the Pauli z operator. The spin states in the rotating frame can therefore be calculated by applying this rotation operator to the states written in the static, also known as laboratory, frame.

$$|\psi_{\mathrm{Rot}}(t)\rangle = \hat{R(t)}\,|\psi_{\mathrm{Lab}}(t)\rangle\,, \tag{2.26}$$

where $|\psi_{\mathrm{Rot}}(t)\rangle$ and $|\psi_{\mathrm{Lab}}(t)\rangle$ are the states in the rotating and laboratory frame respectively. In order to obtain the Hamiltonian of the system in the rotating frame, we can make use of the fact that a transformation of frame should have no influence on the underlying physics of the system and thus the Schrödinger equation must remain valid in the rotating frame

$$i\hbar\frac{d\,|\psi_{\mathrm{Rot}}(t)\rangle}{dt} = \hat{H}_{\mathrm{Rot}}\,|\psi_{\mathrm{Rot}}(t)\rangle\,. \tag{2.27}$$

Substituting the expression for $|\psi_{\mathrm{Rot}}(t)\rangle$ from equation 2.26 into equation 2.27 and rearranging for $\hat{H}_{\mathrm{Rot}}$, we are left with the following expression for the spin Hamiltonian in the

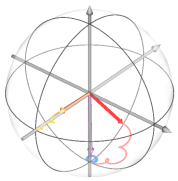

rotating frame, in units of angular frequency [54].

$$\hat{H}_{\text{Rot}} = \underbrace{(\omega_0 - \omega)\hat{S}_z}_{\text{Detuning}} + \underbrace{\omega_1 \hat{S}_x}_{\text{Coupling}}, \tag{2.28}$$

where $\omega_0 = 2\pi\gamma B_0$ is the Larmor precession frequency, $\omega_1 = 2\pi\gamma B_1$ and ω is the angular frequency of the rotating frame. Comparing equation 2.24 and equation 2.28, we can see that transforming from the laboratory to the rotating frame, results in the Hamiltonian losing its time dependency. Consequently, only a time dependency of the spin states remains in the rotating frame.

For the case for which the rotating frame is rotating at the Larmor precession frequency, we can substitute the expression $\omega = \omega_0$ into equation 2.28 and are left with the Hamiltonian

$$\hat{H}_{\text{Rot}} = \omega_1 \hat{S}_x. \tag{2.29}$$

In this reference frame we have therefore effectively 'cancelled out' the precession due to the static B_0 field and are simply left with a field, B_1, pointing along the x direction of the Bloch sphere, which induces a precession of the spin about the B_1 field at an angular frequency of ω_1. We can use this precession to rotate the spin to any arbitrary position on the Bloch sphere, by applying the rotating B_1 field for well calibrated intervals of time, such that the spin is rotated by the desired angle on the sphere.

2.4.2 Rabi frequency

In order to calculate the amount of time for which we need to apply the rotating B_1 field in order to fully invert the spin between the $|\downarrow\rangle$ and $|\uparrow\rangle$ states on the Bloch sphere, we can first calculate the eigenvectors and corresponding eigenvalues of the Hamiltonian derived in the rotating frame in equation 2.28, which can be written in matrix form as

$$\hat{H}_{\text{Rot}} = (\omega_0 - \omega)\hat{S}_z + \omega_1 \hat{S}_x = \begin{pmatrix} (\omega_0 - \omega) & \omega_1 \\ \omega_1 & -(\omega_0 - \omega) \end{pmatrix}. \tag{2.30}$$

The eigenvectors of this Hamiltonian can thus be formulated in the spin $|\downarrow\rangle$ and spin $|\uparrow\rangle$ basis as

$$|\psi_1\rangle = \sin\left(\frac{\theta}{2}\right)|\downarrow\rangle + \cos\left(\frac{\theta}{2}\right)|\uparrow\rangle, \tag{2.31}$$

$$|\psi_2\rangle = \cos\left(\frac{\theta}{2}\right)|\downarrow\rangle - \sin\left(\frac{\theta}{2}\right)|\uparrow\rangle, \tag{2.32}$$

where $\tan\theta = \frac{(\omega_0-\omega)}{\omega_1}$. The corresponding eigenvalues of these eigenvectors are then given, in units of angular frequency, by $E_1 = \sqrt{(\omega_0 - \omega)^2 + \omega_1^2}$ and $E_2 = -\sqrt{(\omega_0 - \omega)^2 + \omega_1^2}$.

Rearranging this expression, the two spin states $|\downarrow\rangle$, $|\uparrow\rangle$ can therefore be re-written in the eigenbasis of $|\psi_1\rangle$, $|\psi_2\rangle$, as the following

$$|\downarrow\rangle = \sin\left(\frac{\theta}{2}\right)|\psi_1\rangle + \cos\left(\frac{\theta}{2}\right)|\psi_2\rangle = \begin{pmatrix} \sin\left(\frac{\theta}{2}\right) \\ \cos\left(\frac{\theta}{2}\right) \end{pmatrix}, \tag{2.33}$$

$$|\uparrow\rangle = \cos\left(\frac{\theta}{2}\right)|\psi_1\rangle - \sin\left(\frac{\theta}{2}\right)|\psi_2\rangle = \begin{pmatrix} \cos\left(\frac{\theta}{2}\right) \\ -\sin\left(\frac{\theta}{2}\right) \end{pmatrix}. \tag{2.34}$$

$$\tag{2.35}$$

In order to understand how a spin initialised along the ±z axis of the Bloch sphere, for example the spin $|\uparrow\rangle$ state, will evolve over time upon the application of a rotating B_1 field, we can apply the time evolution operator to the spin states. For a two-level system, described in the basis of the eigenstates of its Hamiltonian, this operator is given by

$$\hat{U}(t) = \begin{pmatrix} e^{-i\frac{E_1}{\hbar}t} & 0 \\ 0 & e^{-i\frac{E_2}{\hbar}t} \end{pmatrix}, \tag{2.36}$$

where t is the time for which we are evolving the state. Applying this operator to an initial $|\uparrow\rangle$ state gives

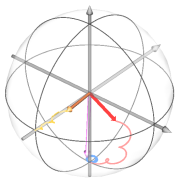

$$|\psi(t)\rangle = \begin{pmatrix} e^{-i\frac{E_1}{\hbar}t}\cos\left(\frac{\theta}{2}\right) \\ -e^{-i\frac{E_2}{\hbar}t}\sin\left(\frac{\theta}{2}\right) \end{pmatrix}. \tag{2.37}$$

To better understand the physical implications of this time evolution, we can look at the projection of this time evolved state onto the $|\downarrow\rangle$ state as a function of time

$$\langle\downarrow|\psi(t)\rangle = \begin{pmatrix} \sin\left(\frac{\theta}{2}\right) & \cos\left(\frac{\theta}{2}\right) \end{pmatrix} \begin{pmatrix} e^{-i\frac{E_1}{\hbar}t}\cos\left(\frac{\theta}{2}\right) \\ -e^{-i\frac{E_2}{\hbar}t}\sin\left(\frac{\theta}{2}\right) \end{pmatrix} \tag{2.38}$$

$$= \sin\left(\frac{\theta}{2}\right)\cos\left(\frac{\theta}{2}\right)e^{-i\frac{E_1}{\hbar}t} - \sin\left(\frac{\theta}{2}\right)\cos\left(\frac{\theta}{2}\right)e^{-i\frac{E_2}{\hbar}t}. \tag{2.39}$$

Substituting in the expression $\sin(\theta) = \frac{(\omega_0-\omega)}{\sqrt{(\omega_0-\omega)^2+\omega_1^2}}$, the expressions for the eigenvalues $E_{1(2)}$ and utilising the trigonometric identity $2\sin(x)\cos(x) = \sin(2x)$ we arrive at the following expression

$$\langle\downarrow|\psi(t)\rangle = i\frac{\omega_1}{\sqrt{(\omega_0-\omega)^2+\omega_1^2}}\sin\left(\frac{\sqrt{(\omega_0-\omega)^2+\omega_1^2}}{\hbar}t\right). \tag{2.40}$$

The probability of the system being found in the $|\downarrow\rangle$ state after being initialised in the state $|\uparrow\rangle$, as function of time, is therefore [45, 55]

$$P_{|\downarrow\rangle\leftrightarrow|\uparrow\rangle} = |\langle\downarrow|\psi(t)\rangle|^2 = \frac{\omega_1^2}{(\omega_0-\omega)^2+\omega_1^2}\sin^2\left(\frac{\sqrt{(\omega_0-\omega)^2+\omega_1^2}}{\hbar}t\right). \tag{2.41}$$

This is known as the Rabi flopping formula and it describes the evolution of a spin upon the application of a rotating B_1 field at a frequency $\frac{\omega}{2\pi}$. We can see that when the driving field is equal to the resonance frequency of the spin, $\omega = \omega_0$, the spin precessess between the spin $|\downarrow\rangle$ and spin $|\uparrow\rangle$ states, at the Rabi frequency, given by $\nu_{\mathrm{R}} = \frac{\omega_1}{2\pi}$. If however, the frequency of the applied field is detuned from resonance, such that $\omega \neq \omega_0$, then the frequency of the resulting Rabi oscillation will increase, while the amplitude will decrease, as explored in greater depth in section 2.7. The Rabi frequency therefore dictates the amount of time for which the B_1 field must be applied in order to fully invert the spin between the $|\downarrow\rangle$ and $|\uparrow\rangle$ states.

2.4.3 Rotating wave approximation

Recall, in section 2.4.1, that in order to control the state of the spin, a rotating B_1 field is applied in a direction perpendicular to the applied B_0 field. In order to efficiently drive the spin, this field is applied at such a frequency that it rotates at the Larmor precession frequency of the spin, $\omega = \omega_0$. In practice however, a rotating magnetic field is difficult to apply. A more easily implementable magnetic field is a linearly oscillating field, which can be driven by an AC current. From the perspective of the spin however, with $B_1 \ll B_0$, only a magnetic field rotating close to the Larmor precession frequency, ω_0, has any influence on its state. We can therefore determine what magnitude of rotating field the spin experiences upon the application of a linearly oscillating field, by decomposing this oscillating field into its constituent rotating fields.

Any linearly oscillating field can be decomposed into two counter-rotating fields, each with half the amplitude [56].

$$\cos(\omega \mathrm{t}) = \frac{1}{2}(\mathrm{e}^{\mathrm{i}\omega \mathrm{t}} + \mathrm{e}^{-\mathrm{i}\omega \mathrm{t}}), \tag{2.42}$$

where ω is the frequency of the driving field. Therefore, from the perspective of the spin, for a resonant driving field, $\omega = \omega_0$, the linearly oscillating field has a component that rotates with the spin at the Larmor precession frequency, ω_0, and a component that rotates in the opposite direction, at $-\omega_0$, and is hence detuned by $2\omega_0$ from the precession frequency of the spin. As this counter rotating component is so far detuned from the spin's precession frequency, we can effectively ignore this counter rotating term, as it has negligible impact on the state of the spin. Therefore, only half the amplitude of the applied oscillating field has any meaningful effect on the spin, and thus, experimentally, the Rabi frequency is given by $\frac{\omega_1}{2}$ instead of ω_1. This neglecting of the far off-resonant term is known as the rotating wave approximation [57].

It should be noted however, that this approximation only holds in the case for which

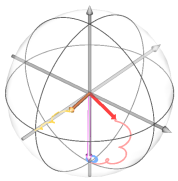

$\omega_0 \gg \omega_1$. Although this is a very good approximation for the situation described in the majority of this thesis, in which $\frac{\omega_0}{2\pi}$ is given by the Zeeman splitting (≈ 30 GHz) and $\frac{\omega_1}{2\pi}$ is given by the Rabi frequency (≈ 1 MHz for the experiments performed in this thesis), there are cases for which this condition does not hold and hence a breakdown in the rotating wave approximation may be observed [58].

2.5 Transition frequencies

The ability to fully invert the spin of the electrons and nuclei is contingent on our knowledge of the resonance frequencies of the system. These resonance frequencies can be determined by first calculating the energy eigenvalues of the donor Hamiltonian. For the case of the donor nucleus, by carefully manipulating the electrostatic environment of the donor using locally applied gate voltages, we are able to selectively remove the electron, such that the nucleus is either in the neutral state, D^0, with the electron bound to the donor, or in the ionised state, D^+, with the electron removed from the donor (see section 3.9.3). For the case of the ionised donor, the only term present in the Hamiltonian is the nuclear Zeeman interaction term. The eigenstates of this Hamiltonian therefore consist of the nuclear spin down $|\Downarrow\rangle$ and spin up $|\Uparrow\rangle$ states. The corresponding eigenvalues for these states, in units of frequency, are the following:

$$E_{|\Downarrow\rangle} = -\gamma_n B_0/2, \tag{2.43}$$

$$E_{|\Uparrow\rangle} = +\gamma_n B_0/2. \tag{2.44}$$

The resonant frequency, ν_{n0}, to excite the transition between the $|\Downarrow\rangle$ and $|\Uparrow\rangle$ states for the ionised donor nucleus is therefore given by:

$$\nu_{n0} = E_{|\Uparrow\rangle} - E_{|\Downarrow\rangle} = \gamma_n B_0. \tag{2.45}$$

For the case of a neutral donor atom in silicon, the Hamiltonian of the system consists of both the Zeeman interaction term for the electron and nucleus, as well as a hyperfine coupling term between the two spins. As discussed in section 2.3.2, the eigenstates of this

system can be well approximated as $|\Uparrow\downarrow\rangle$, $|\Downarrow\downarrow\rangle$, $|\Downarrow\uparrow\rangle$, $|\Uparrow\uparrow\rangle$. The corresponding energy of these eigenstates, in units of frequency, are therefore:

$$E_{|\Uparrow\downarrow\rangle} = \frac{-\sqrt{(\gamma_+ B_0)^2 + A^2} - A/2}{2}, \tag{2.46}$$

$$E_{|\Downarrow\downarrow\rangle} = \frac{-\gamma_- B_0 + A/2}{2}, \tag{2.47}$$

$$E_{|\Downarrow\uparrow\rangle} = \frac{\sqrt{(\gamma_+ B_0)^2 + A^2} - A/2}{2}, \tag{2.48}$$

$$E_{|\Uparrow\uparrow\rangle} = \frac{\gamma_- B_0 + A/2}{2}, \tag{2.49}$$

$$\tag{2.50}$$

where $\gamma_+ = \gamma_\mathrm{e} + \gamma_\mathrm{n}$ and $\gamma_- = \gamma_\mathrm{e} - \gamma_\mathrm{n}$.

The resonance frequencies to transition between the eigenstates of the Hamiltonian are thus given by the following, as depicted schematically in Figure 2.10:

For the electron spin:

$$\nu_{\mathrm{e}1} = E_{|\Downarrow\uparrow\rangle} - E_{|\Downarrow\downarrow\rangle} = \gamma_\mathrm{e} B_0 - A/2, \tag{2.51}$$

$$\nu_{\mathrm{e}2} = E_{|\Uparrow\uparrow\rangle} - E_{|\Uparrow\downarrow\rangle} = \gamma_\mathrm{e} B_0 + A/2. \tag{2.52}$$

For the nuclear spin:

$$\nu_{\mathrm{n}1} = E_{|\Uparrow\downarrow\rangle} - E_{|\Downarrow\downarrow\rangle} = A/2 + \gamma_\mathrm{n} B_0, \tag{2.53}$$

$$\nu_{\mathrm{n}2} = E_{|\Uparrow\uparrow\rangle} - E_{|\Downarrow\uparrow\rangle} = A/2 - \gamma_\mathrm{n} B_0. \tag{2.54}$$

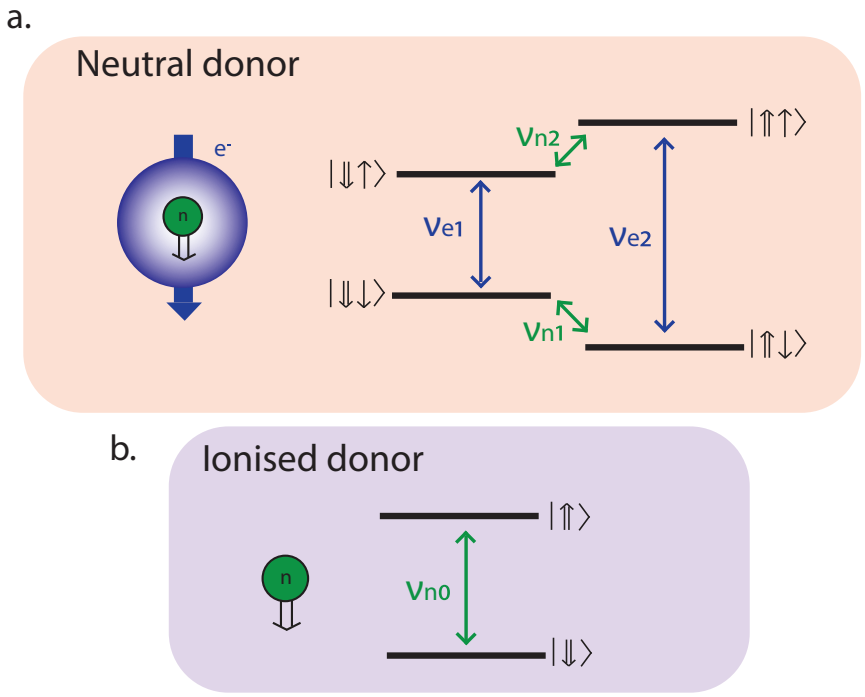

Figure 2.10: **Electron and nuclear transition frequencies.** Energy eigenstates and the corresponding transition frequencies between them for both the neutral (**a.**) and ionised donor atom (**b.**).

2.6 Coherence

The coherence time of a spin is an indication of how long we can faithfully maintain information about where that spin is pointing along the Bloch sphere. Knowledge regarding the exact orientation of the spin at any given time is important as it informs the phase of our applied control pulses, allowing us to manipulate the spin to a desired state.

Loss of knowledge regarding where the spin is pointing along the Bloch sphere can occur as a result of additional terms appearing in the Hamiltonian of the spin that are unknown to us. The most pertinent example of this is noise in the environment, which can add additional terms to the Hamiltonian that are often random in nature and thus difficult for

us to keep track of.

In donor spin qubits more specifically, there are two types of noise in the environment that can introduce random terms to the spin Hamiltonian and thus cause the spin to decohere over time, as highlighted in the following Hamiltonian

$$\hat{H}_{\text{full}} = \gamma_{\text{e}}(B_0 + B_{\text{n}})\hat{S}_{\text{z}} + \gamma_{\text{n}}(B_0 + B_{\text{n}})\hat{I}_{\text{z}} + (A + A_{\text{n}})\hat{\mathbf{S}} \cdot \hat{\mathbf{I}}. \tag{2.55}$$

Magnetic noise

Electric noise

Magnetic noise

The first type of noise is magnetic noise. This magnetic noise can arise primarily due to either noise associated with the source of the static B_0 field, or due to random flipping of coupled ^{29}Si nuclei in the vicinity. Both of these noise sources act to add a random magnetic noise term, B_{n}, to the Zeeman term of the nucleus and electron. As the Larmor precession frequency of the spin is given by γB_0, any change in the B_0 field will thus manifest itself as a change in the Larmor precession frequency of the spin. This unknown change in the precession frequency of the spin on the xy plane of the Bloch sphere results in us no longer possessing knowledge of where the spin is pointing at any given time.

The other prominent noise source in donor atoms is electric noise. This can influence the terms in the donor Hamiltonian in a number of ways but, the most common channel for a ^{31}P donor atom, is via the hyperfine interaction, by adding random noise, A_{n}, to the hyperfine term in the Hamiltonian. Random electric noise caused by lattice phonons or voltage noise on the gates used to control the electrostatic environment of the donors can influence the overlap between the electron and donor nucleus and thus randomly modulate the hyperfine interaction term in the Hamiltonian [28]. This also leads to a loss of knowledge regarding the spin's position on the Bloch sphere.

One experiment that allows us to directly probe the coherence times of our system is a measurement known as a Ramsey experiment [59]. The pulse sequence of a Ramsey

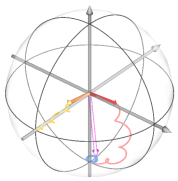

experiment is shown in Figure 2.12. In the Ramsey sequence, the spin is first initialised along the xy plane of the Bloch sphere with a $\frac{\pi}{2}$ pulse, before being allowed to freely precess about the xy plane for some wait time, the duration of which is swept, before a final $\frac{\pi}{2}$ pulse brings the spin to the $\pm$ z axis. In the absence of noise, the spin will precess around the xy plane, during the free precession period, at the Larmor precession frequency, ω_0. In the presence of noise however, this precession frequency becomes $\omega_0 + \omega_n$, where ω_n is the additional frequency induced by the noise, the value of which is unknown to us. The precession of the spin during the wait time of a Ramsey experiment is shown in Figure 2.11. The loss of information regarding the precession frequency of the spin in the presence of noise thus leads us to lose knowledge of the spin orientation along the Bloch sphere and hence results in the loss of spin coherence.

2.6.1 Extending the coherence time

The loss of spin coherence observed in a Ramsey measurement, occurs as a result of the expected value of the spin orientation, becoming misaligned from the actual orientation of the spin. In order to maintain spin coherence therefore, we must utilise schemes that maximise or revive the instances for which the expected and actual spin projections are aligned. One method of doing this, is by applying a refocusing pulse to the spin in a scheme known as a Hahn echo sequence [60], shown in Figure 2.12.

The working principle behind a Hahn echo sequence is shown in Figure 2.13. The Hahn echo is identical to the Ramsey sequence, with the exception of a π pulse applied at the half-way point of the free-precession period, which acts to rotate the spin 180^o on the xy plane. If the noise in the environment was acting to slow down the precession frequency of the spin, such that $\omega_0 + \omega_n < \omega_0$, then, after the refocusing π pulse, the spin is left 'ahead' of the expected spin position on the xy plane. Therefore, during the second half of the precession time, the expected position, precessing at ω_0, catches up to the actual position of the spin and we obtain a revival of coherence. The same is true for the case of $\omega_0 + \omega_n > \omega_0$ however, in this case the refocusing pulse leaves the spin 'behind' the

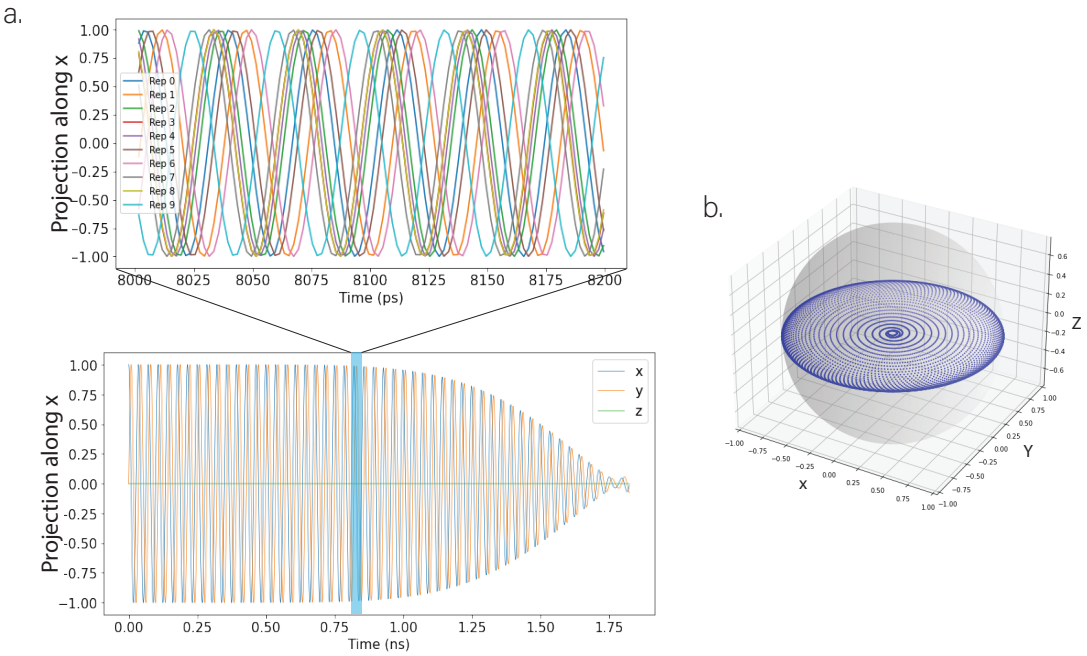

Figure 2.11: **Ramsey measurement simulation. a.** Simulation of the free precession time during a Ramsey measurement on the electron, averaged over 10 repetitions, with a random value of magnetic noise added to each repetition. Upper panel shows a zoomed view of the pale blue highlighted region, where each of the 10 individual Ramsey oscillation repetitions are plotted. The oscillations are given by the Larmor precession frequency of the spin and therefore each of the 10 individual Ramsey oscillation repetitions has a slightly different precession frequency, due to the added noise, and hence when averaged together give an expectation value along z of 0 (i.e. 50% $|\downarrow\rangle$ and 50% $|\uparrow\rangle$) for longer wait times.**b.** Expectation values of these averaged free-precession periods onto the Bloch sphere. We can see that as the wait time increases, the expectation value of the spin spirals towards 0, indicating that we are creating a random state and have thus lost complete knowledge of the state of the spin before the final $\frac{\pi}{2}$ pulse of our Ramsey sequence.

expected spin position on the xy plane, allowing the actual spin position to catch up to the expected position by the end of the wait period; similarly reviving the spin coherence when the expected and actual spin orientations align.

Hahn echo sequences are a useful method of extending the coherence of the spin in the presence of noise that remains constant for the duration of the Hahn experiment and is thus the same before and after the refocusing π pulse. It is easy to see that if the noise changes after the refocusing pulse, then the spin will no longer align on the Bloch sphere

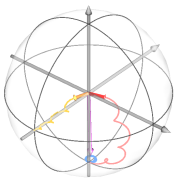

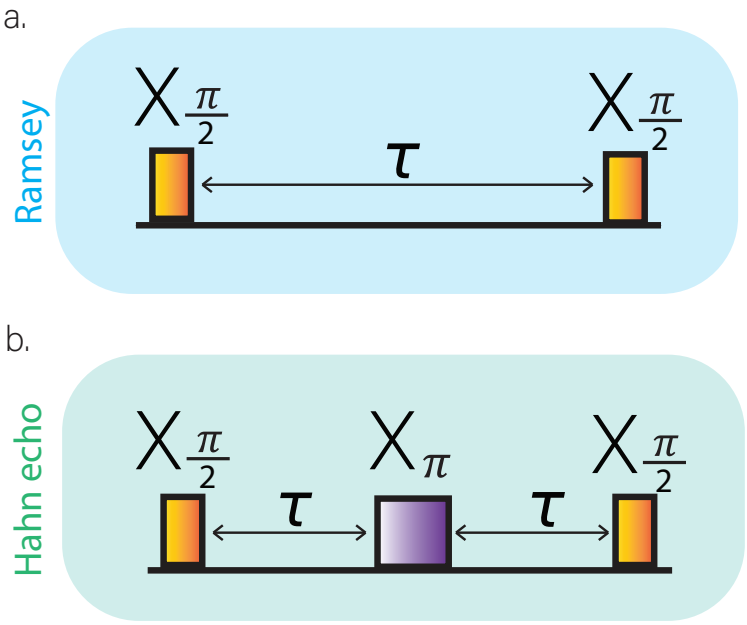

Figure 2.12: **Ramsey and Hahn echo pulse sequences. a.** Schematic of the pulse sequence for a Ramsey experiment. **b.** Schematic of the pulse sequence for a Hahn echo. Note that an X pulse indicates a pulse that is along the x direction of the Bloch sphere. Rotations around a given axis of the Bloch sphere are achieved by altering the phase of the applied pulse.

with its expected direction at the expected time, and hence coherence is not maintained. The Hahn echo sequence is thus sensitive to any noise that changes between the time period before and after the refocusing pulse.

2.6.2 Noise spectroscopy

Although the sensitivity to noise that differs before and after the refocusing pulse limits the applicability of the Hahn echo scheme for coherence extension, the selective noise sensitivity of this sequence can be used as a resource, for probing the noise in the spin's environment. The benefits of probing the noise in the environment of the spin are twofold. Firstly, it allows us to identify the nature of the noise sources and hence attempt to reduce or remove this noise where possible. Secondly, for noise sources that are not able to be removed or reduced, knowledge of the nature of the noise can allow us to design pulse

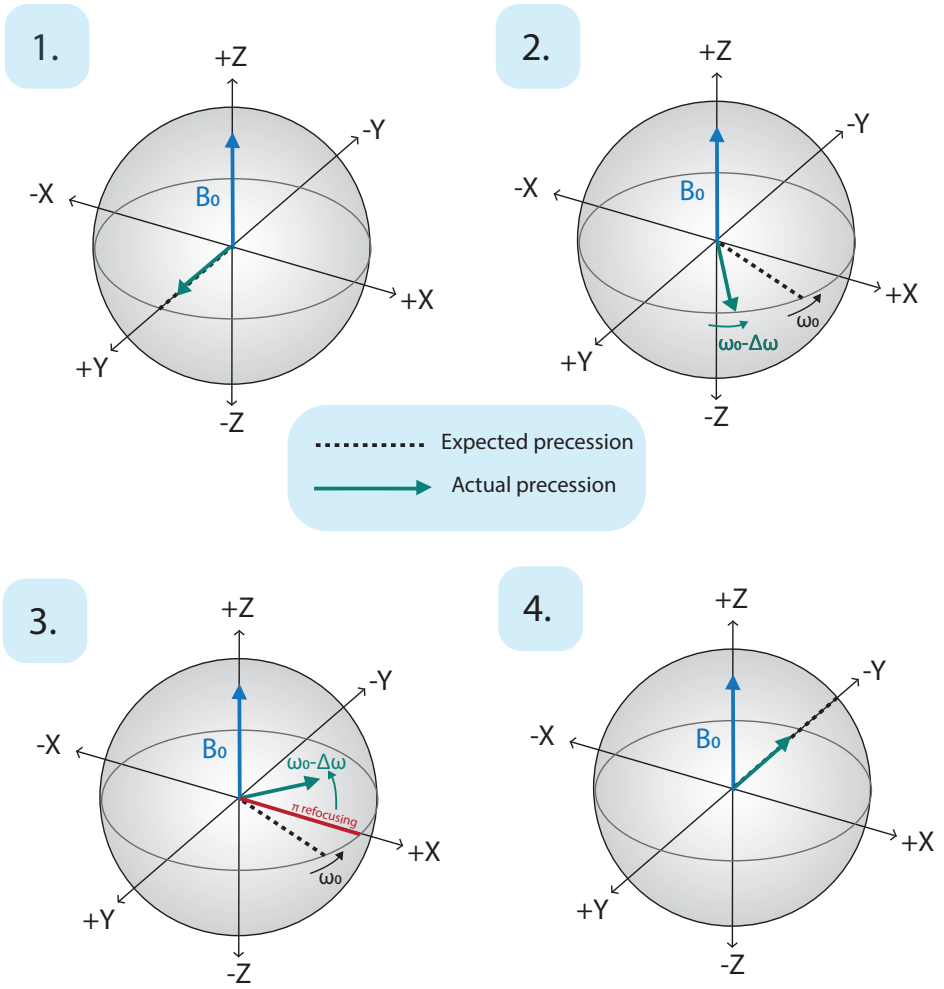

Figure 2.13: **Hahn echo sequence.** Bloch spheres depicting the basic principles behind a Hahn echo sequence. In panel 1, the spin (depicted by the green arrow) is prepared along the xy plane of the Bloch sphere. At this point, the spin direction and the expected direction along the Bloch sphere (depicted by the dashed black line) are aligned. In the second panel, the spin begins to precess about the B_0 field at a frequency $\omega_0 + \omega_\mathrm{n}$, where ω_n is the deviation in the expected Larmor precession frequency as a consequence of the noise. The spin thus starts to precess at a different frequency from the expected precession frequency ω_0. In this example, $\omega_\mathrm{n} < 0$. In panel 3, a refocusing π pulse is applied along the +x axis of the Bloch sphere, which rotates the spin by 180^o around the +x axis. The spin is now ahead of the expected orientation. In panel 4, after another wait time, the expected spin direction now catches up with the spin's actual direction and the coherence of the spin is revived. A final $\frac{\pi}{2}$ pulse is then applied.

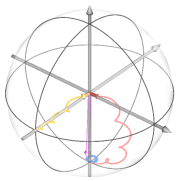

sequences to specifically avoid sensitivity to prevalent noise frequencies in the environment.

The dependence of the measured spin coherence on the applied pulse sequence gives us precious information regarding the nature of the noise affecting the spin. For example, the increased coherence time obtained from a Hahn echo sequence compared to a Ramsey experiment, tells us that the noise affecting the spin systems is dominant at low frequencies, for example a $\frac{1}{f}$ noise distribution. The frequency distribution of the noise from a given noise source, λ, can be expressed through the power spectral density (PSD) of the noise

$$S_\lambda(\omega) = \left(\frac{1}{2\pi}\right) \int_{-\infty}^{\infty} dt \, \langle \lambda(0)\lambda(t) \rangle \, e^{-i\omega t}, \tag{2.56}$$

where ω represents the noise frequency in units of angular frequency [61].

The sequence applied to the spin when it is in a superposition state, acts as a bandpass filter to this noise spectrum, allowing the noise to be sampled over a narrow frequency range. The bandpass frequency filter generated from a given pulse sequence is known as its filter function and is given by

$$F(\omega, t) = \frac{1}{(\omega\tau)^2} |1 + (-1)^{1+N} e^{i\omega\tau} + 2 \sum_{j=1}^{N} (-1)^j e^{i\omega\delta_j\tau} \cos(\frac{\omega\tau_\pi}{2})|^2, \tag{2.57}$$

where τ_π represents the length of a π pulse, τ is the total free precession time of the spin, N is the number of π pulses applied to the spin and δ_j is the normalised position (between 0 and 1) of the j^{th} π pulse between the two $\frac{\pi}{2}$ pulses [61]. We can thus see that the frequency range sampled from a given Hahn-type refocusing sequence depends on both the number of π pulses as well and their distribution within the free precession period. By increasing the number of pulses, N, while keeping the total duration of the free precession, $N\tau$, fixed the filter function shifts towards sampling higher frequencies. Moreover, by keeping the time between neighbouring π pulses fixed and instead increasing N, the frequency range sampled by the filter function becomes more narrow. Figure 2.14 shows the filter functions moving to higher frequency as a function of increased number

of refocusing pulses and a fixed τ.

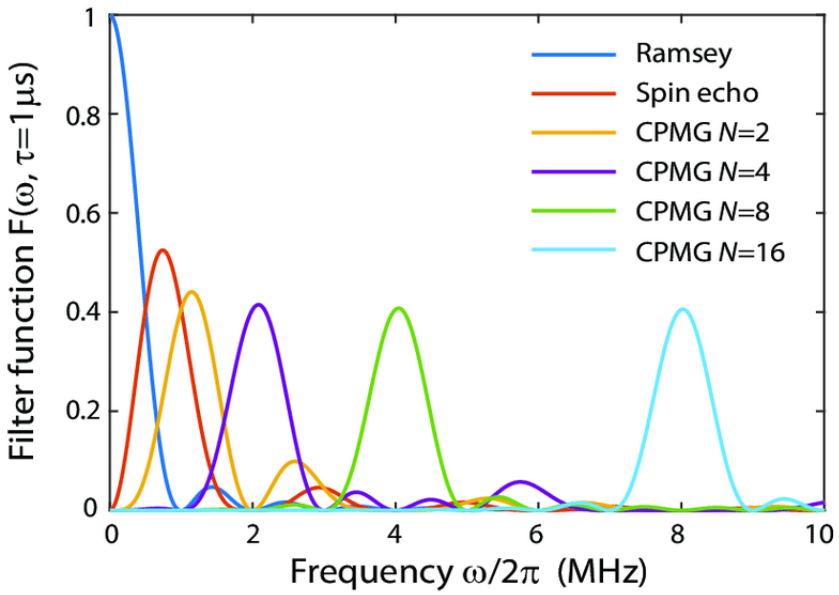

Figure 2.14: **Filter functions with increased number of refocusing pulses.** This plot shows the filter functions, representing the noise frequencies each sequence is sensitive to, for different numbers of refocusing pulses N, ranging from 0 for the Ramsey sequence, to a sequence with N=16 refocusing pulses. Sequences with more than one refocusing pulses are known as Carr-Purcell-Meiboom-Gill (CPMG) sequences. As the number of refocusing pulses increases, we can see that the noise frequencies at which the sequence is sensitive to shifts to higher frequencies. Figure was taken from [62].

These filter functions can be translated into information regarding the noise spectrum of the spin by measuring the coherence of the spin as a function of the frequency range sampled by a given filter function. The coherence, χ of a spin for a given noise spectrum and filter function is given by the overlap between the noise power spectral density and the filter function, as expressed by

$$\chi_{\mathrm{N}}(\tau) = \tau^2 \sum_{\lambda} \left(\frac{\partial \omega_0}{\partial \lambda}\right)^2 \int_0^{\infty} d\omega \; S_{\lambda}(\omega) \; F(\omega, t) \,, \tag{2.58}$$

Noise power spectral density

Filter function

where $\left(\frac{\partial \omega_0}{\partial \lambda}\right)$ is the sensitivity of the Larmor precession frequency of the spin to noise λ. The diffusion of the precession frequency of the spin, over multiple precession periods, is

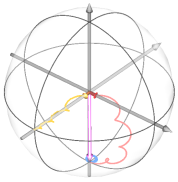

owing the random noise-induced fluctuations in the resonance frequency of the spin, which can be written as

$$\delta_{\psi(t)} = \left(\frac{\partial\omega_0}{\partial\lambda}\right)\int_0^t dt'\delta_{\psi(t')}. \tag{2.59}$$

For a large number of two-level random fluctuators in the environment, weakly coupled to the donor spin, averaging over all resonance frequency fluctuations gives the following dephasing of the spin

$$\langle e^{[i\delta_{\psi(t)}]}\rangle \equiv e^{\chi_{\mathrm{N}}(t)}. \tag{2.60}$$

As the filter function overlaps with a peak in the noise spectral power density, this will result in a decrease in the spin coherence, presenting a convenient method of mapping out the noise in the spin's environment [61, 63].

2.7 Off resonant driving

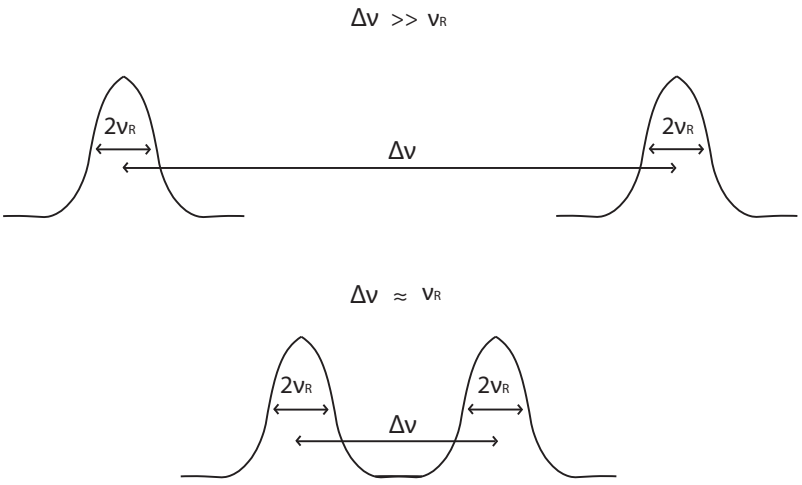

Figure 2.15: **Frequency detuning against Rabi frequency.** Schematic illustration of the peaks observed in a frequency spectrum of a spin for both the case in which the frequency detuning, $\Delta\nu$, between the resonances is much greater than the Rabi frequency, ν_{R} (**a.**) and the case for which $\Delta\nu \approx \nu_{\mathrm{R}}$ (**b.**).

Spins are susceptible to off-resonant effects of the AC driving fields used for spin resonance. When coupling multiple qubits together, for example through a weak exchange interaction, the resonance frequencies become separated by a frequency equal to the coupling strength between them (see section 4.2.2). Therefore, especially in the regime of weak exchange interaction, the detuning between resonance frequencies, $\Delta\nu$, can be comparable to the Rabi frequency, ν_{R}. It thus becomes increasingly important to keep track of and mitigate the off-resonant effects of the AC drive when operating in the regime of weak qubit coupling.

2.7.1 Off-resonant Rabi drive

In order to understand the effect of an off-resonant AC magnetic field on the spin, we need to calculate the effective magnetic field experienced by the spin as we detune the AC field from the resonance frequency. The effect of a detuned AC field is made apparent by examining the Hamiltonian of the spin in the rotating frame, in units of angular frequency, derived in section 2.4

$$\hat{H}_{\mathrm{Rot}} = (\omega_0 - \omega)\hat{S}_{\mathrm{z}} + \omega_1 \hat{S}_x. \tag{2.61}$$

Here we can see that upon application of an AC driving field, we have a term $(\omega_0 - \omega) = \Delta\omega$ along the z-axis of the Bloch sphere, representing the detuning between the frequency of the AC field and the resonance frequency of the spin. Similarly, we have a term $\omega_1 = 2\pi\nu_{\mathrm{R}}$ along the x-axis of the Bloch sphere, representing the Rabi frequency. The frequency with which the spin precesses about the effective magnetic field in the presence of a frequency detuning is thus given by the vector sum of the frequency detuning with ω_1, $\omega_{\mathrm{eff}} = \sqrt{\omega_1^2 + (\omega_0 - \omega)^2}$, as shown in Figure 2.16.

The expression for ω_{eff} also corresponds to the frequency of precession given by the Rabi flopping formula.

$$P_{|\downarrow\rangle \leftrightarrow |\uparrow\rangle} = |\langle\downarrow|\psi(t)\rangle|^2 = \frac{\omega_1^2}{(\omega_0 - \omega)^2 + \omega_1^2} \sin^2\left(\frac{\sqrt{(\omega_0 - \omega)^2 + \omega_1^2}}{\hbar} t\right). \tag{2.62}$$

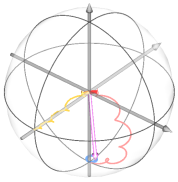

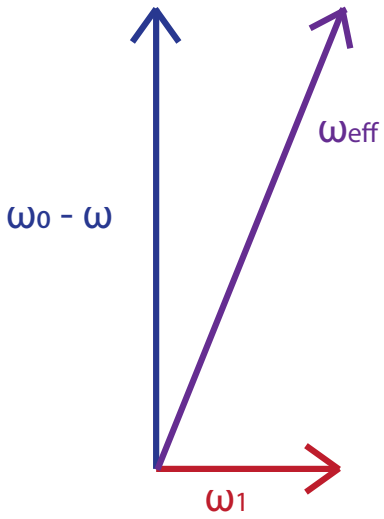

Figure 2.16: **AC field vector sum.** Vector sum between the Rabi frequency in units of angular frequency, ω_1, in red and the frequency detuning between the applied field, ω, and resonance frequency, ω_0 in navy. The result of the vector sum is the effective field experienced by the spin, ω_{eff} shown in purple.

When the field is applied on resonance with the transition frequency, $(\omega_0 - \omega) = 0$, the Rabi flopping formula becomes

$$P_{|\downarrow\rangle \leftrightarrow |\uparrow\rangle} = \sin^2\left(\frac{\omega_1}{\hbar} t\right). \tag{2.63}$$

Comparing this to the original Rabi flopping formula, in equation 2.62, two effects of a detuned AC field, $(\omega_0 - \omega) \neq 0$, become apparent:

1. The Rabi frequency increases as the detuning from the resonance frequency increases.
2. The amplitude of the Rabi oscillations decreases as the detuning from the resonance increases.

These two effects can be conceptually understood as the spin undergoing a precession about a smaller cone on the Bloch sphere when the AC magnetic field is detuned from

resonance, as shown in Figure 2.17.

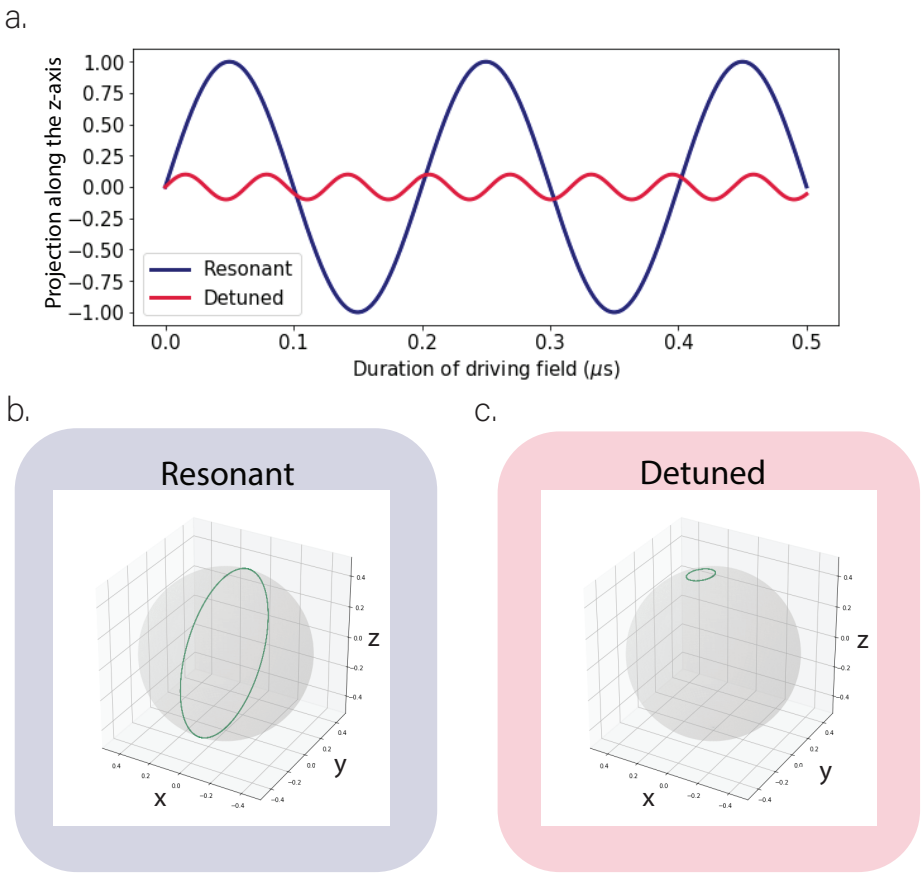

Figure 2.17: **Resonant and detuned Rabi oscillations. a.** Rabi flopping formula plotted for both an on resonant AC driving field and a detuned AC driving field. **b., c.** Plot of the corresponding simulated spin tracjectories on the Bloch sphere for an initial spin state of $|\downarrow\rangle$.

When attempting to drive multiple coupled donors, particularly in systems where the spin resonance transitions are closely spaced, this off-resonant Rabi drive can become non-negligible and result in some unwanted driving between the $|\downarrow\rangle$ and $|\uparrow\rangle$ for the off-resonant state. One method of mitigating the effect of this off-resonant Rabi excitation is to ensure that the off-resonant Rabi drive on the adjacent resonance induces a rotation that is a multiple of 4π, in the time taken to perform a π rotation on the resonance being addressed. The reason a 4π rotation of the spin is desirable, and not simply a 2π rotation, is due to

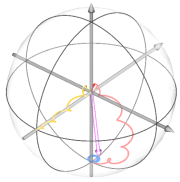

the geometric phase that is incurred by the spin traversing a path across the Bloch sphere, as discussed in section 2.8. Performing a multiple of 4π rotation on an off resonant state, in the time taken to apply a π pulse on resonance, can be achieved by carefully tuning the power of the applied pulse, to increase or decrease the frequency of the off-resonant drive.

2.7.2 AC Zeeman shift

As well as off-resonant Rabi drive, which affects the z-projection of the spin on the Bloch sphere, the effect of off-resonant driving also needs to be considered along the equator of the Bloch sphere. To do this we must re-examine the precession of the spin along the Bloch sphere during off-resonant driving. As stated previously, the vector sum of the detuning and the Rabi frequency gives the precession frequency of the spin about the effective B-field.

$$\omega_{\text{eff}} = \sqrt{\omega_1^2 + (\omega_0 - \omega)^2}, \tag{2.64}$$

where $\omega_1 = 2\pi\nu_{\text{R}}$ is the Rabi frequency in units of angular momentum, ω_0 is the Larmor precession frequency and ω is the frequency of the applied AC field. ω_{eff} is therefore the rotation frequency of the spin when driven by an off-resonant drive. Upon Taylor expanding this formula we are left with the following expression [64, 65] :

$$\omega_{\text{eff}} = \omega_0 - \omega + \frac{\omega_1^2}{2(\omega_0 - \omega)}. \tag{2.65}$$

If we move into the rotating frame of the spin, rotating at a frequency of ω, then this becomes

$$\omega_{\text{eff}} = \omega_0 + \frac{\omega_1^2}{2(\omega_0 - \omega)}. \tag{2.66}$$

This formula thus highlights that, upon introducing a frequency detuning between the resonance frequency and the driving frequency, $\omega_0 - \omega$, there is a correction to its resonance frequency ω_0 of

$$\omega_{\mathrm{AC}} = \frac{\omega_1^2}{2(\omega_0 - \omega)}, \tag{2.67}$$

where ω_{AC} is in units of angular frequency. This correction to the resonance frequency caused by an off resonant magnetic drive is called the AC Zeeman shift. The implications of this effect is hence an instantaneous shift in the resonance frequency of the spin upon the application of an off-resonant AC field, the magnitude of which depends only on the Rabi frequency of the AC pulse, ω_1, and the frequency detuning between the applied pulse and the resonance frequency, $\omega_0 - \omega$.

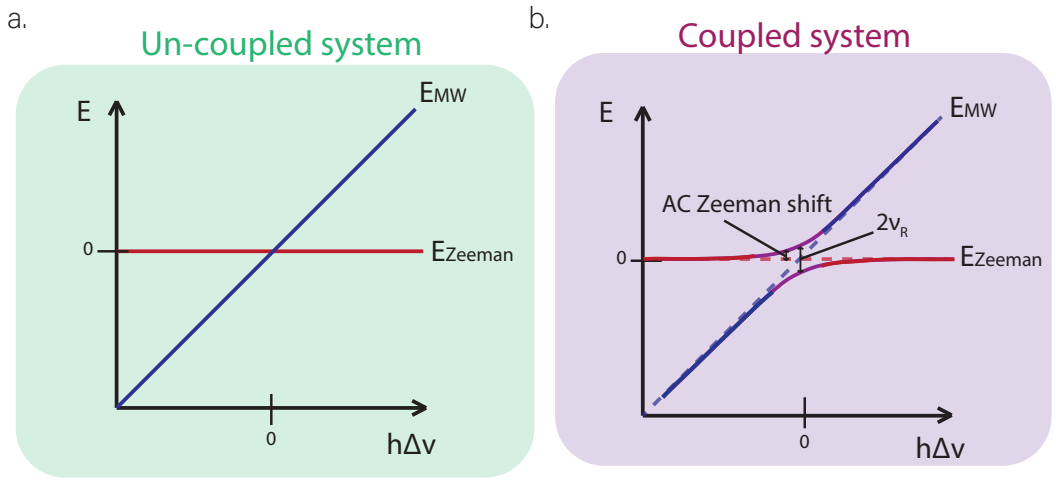

Figure 2.18: **Spin- photon coupling.** Two plots of energy, E, against frequency detuning from the resonance frequency of the spin ($\Delta\nu$). **a.** Zeeman energy splitting of the spin, E_{Zeeman}, (red line) and the energy of the photons in the AC field, E_{MW} (blue line). **b.** Plot of the same energy levels but, with a coupling between the spin and the photons in the AC field, resulting in an avoided crossing between the two. The difference between the two energies on resonance ($\Delta\nu = 0$) is given by twice the Rabi frequency, $2 \times \nu_{\mathrm{R}}$. The deviation of the energy level of the Zeeman splitting from the dashed line close to the resonance frequency is as a result of the AC Zeeman shift.

The physical origin of the AC Zeeman shift can be further understood by considering the coupling between the electron (nuclear) spin and the microwave (radio-frequency) photons of the AC field. To illustrate the implications of this coupling, Figure 2.18 depicts two energies as a function of frequency detuning between the applied AC field and the resonance

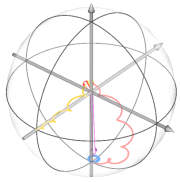

frequency of the spin. These energies are plotted both for the case of no coupling between the photons and the spin (Fig. 2.18, a) and for the presence of a coupling between the photons and the spin (Fig. 2.18, b).

For the uncoupled case, we see that the energy of the spin is given by the Zeeman splitting, E_{Zeeman}, which is independent of the frequency of the applied AC magnetic field and hence is represented by a horizontal line. The energy of the photons however, E_{MW}, is given by the formula $E = h\nu$, where ν is the frequency of the field, and hence the photon energy increases linearly with increasing frequency. When the applied field is on resonance with the transition energy between $|\downarrow\rangle$ and $|\uparrow\rangle$ (i.e, the detuning $\Delta\nu$=0), then the two lines cross and $E_{\text{MW}} = E_{\text{Zeeman}}$.

Upon coupling the photons of the AC field with the spin however, the two energy branches form an avoided crossing at the resonance frequency, $\Delta\nu$=0. Looking along the x-axis, either side of $\Delta\nu$=0, we see that for values of small frequency detuning, the Zeeman splitting deviates from its value in the absence of spin-photon coupling (denoted by the dashed red line). This deviation in Larmor precession frequency, for small values of frequency detuning, is the AC Zeeman shift effect. For large values of detuning, the Zeeman energy converges towards the dashed line, indicating that the AC Zeeman shift becomes negligible.

Interestingly, the energy of the photons also deviates from its original energy (denoted by the blue-dashed line), for small values of frequency detuning from resonance. This effect, symmetric to the AC Zeeman shift, where the photon energy shifts as a result of the coupling between the photons and the spin is called a dispersive shift and is the physical mechanism that underpins an important photon-based spin readout technique called dispersive readout [66].

2.7.2.1 Measuring AC Zeeman shift

As with the case of the off-resonant Rabi drive, in order to perform high-fidelity control of multiple coupled qubits, where the difference between resonance frequencies becomes comparable to the Rabi frequency (as shown in Figure 2.15), we must perform mitigation techniques to account for the unwanted effect of the AC Zeeman shift. For the case of AC Zeeman shift, this mitigation involves accounting for the unwanted phase accumulated during off-resonant driving. Perhaps the most straightforward method of doing this involves keeping track of the AC Zeeman shift induced on each resonance from the applied driving pulses and accounting for the additional induced phase in the subsequent control pulses. For example, if a phase of $\frac{\pi}{4}$ were incurred on a given transition as a result of the AC Zeeman shift, then the subsequent control pulse addressing this transition would be applied with a phase of $\theta = \theta_0 + \frac{\pi}{4}$, where θ_0 is the phase of the pulse that would have been applied in the absence of any phase shift. It should be noted that the additional phase accumulated due to noise in the environment, cannot be accounted for in this way, due to the random nature of the phase accumulations and thus the lack of repeatability.

Although the AC Zeeman shift of a given driving field can be calculated theoretically, using equation 2.67, it is often useful to corroborate this with experimental data. One convenient method of measuring the AC Zeeman shift experimentally is using a Hahn echo pulse sequence, by making use of the fact that this sequence only refocuses noise that is the same before and after the refocusing pulse (discussed in depth in section 2.6). The Hahn echo sequence is generally preferable to a Ramsey sequence for this measurement, due to the fact that the lowest frequency shift detectable with this technique depends on $1/T_2$, where $T_2 = T_2^*(T_2^{\text{Hahn}})$ for the case of a Ramsey (Hahn echo) experiment. As $T_2^{\text{Hahn}} \gg T_2^*$ the Hahn echo experiment therefore increases the sensitivity of the measurement by enabling a lower shift in frequency to be detected.

By applying an off-resonant pulse only in the first half of the Hahn echo sequence, before

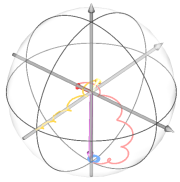

the refocusing pulse, we introduce a phase to the spin through the AC Zeeman shift, that is not refocused by the refocusing pulse. By applying a wait-time dependent phase shift to the final $\frac{\pi}{2}$ pulse, we can induce oscillations in the Hahn echo decay, making the effect of the added phase induced by the AC Zeeman shift easier to distinguish.

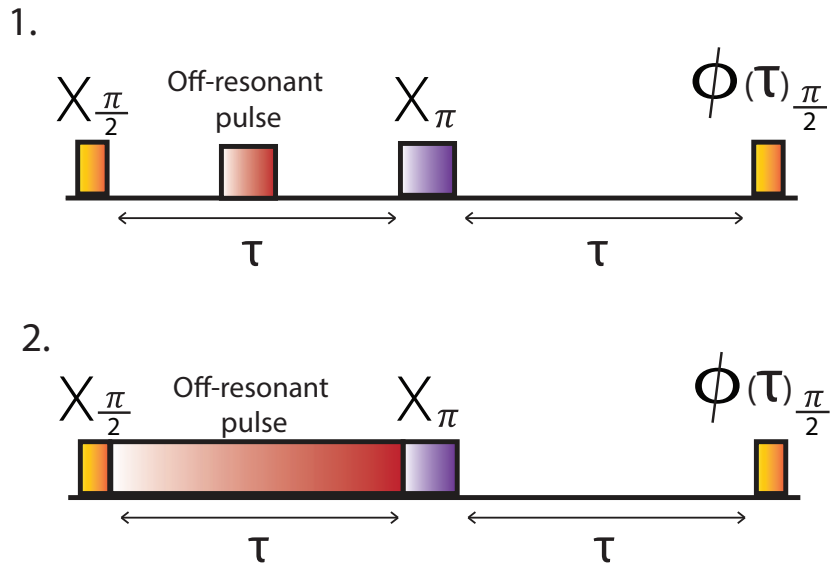

Figure 2.19: **AC Zeeman shift measurement.** Two Hahn echo pulse sequences that can be used to measure AC Zeeman shift. An X pulse represents the application of an AC field along the +x direction of the Bloch sphere (i.e. with a phase of 0), while a ϕ pulse represents a pulse of an arbitrary phase, where the phase of the pulse is swept as a function of the wait time, τ. This thus induces artificial oscillations in the Hahn echo decay. In the pulse sequence in panel 1, an off-resonance pulse is applied for a fixed duration of time. This adds a fixed phase to the Hahn echo oscillation. The second panel shows an off resonance pulse that is applied for the entire duration of the first wait time. As the duration of this pulse is therefore swept, this results in a variable amount of phases added from AC Zeeman shift, which thus manifests itself as a change in the frequency of the resulting Hahn echo oscillations.

If we apply the off-resonant pulse in the first half of the Hahn echo sequence for a fixed duration of time, then a fixed phase will be added to the spin that does not depend on the duration of the Hahn echo wait time, resulting in a change in the phase of the resulting

Hahn echo oscillation. Conversely, if we instead apply the off-resonant pulse for the entire duration of the first wait time of the sequence, i.e. between the first $\frac{\pi}{2}$ pulse and the refocusing pulse, then the phase induced by the AC Zeeman shift on the spin will depend on the duration of this wait time, τ. This will therefore manifest itself as a change in the frequency of the resulting Hahn echo oscillations, equal to the resonance frequency shift caused by the AC Zeeman shift. These two pulse sequences are depicted in Figure 2.19.

2.8 Geometric phase

An important phase to consider, particularly when operating with multiple, coupled spin qubits, where relative phases between the spins become important, is the geometric phase that comes about simply as a result of the topology and geometry of the Bloch sphere across which the spin is traversing [67]. This phase can be calculated by considering an arbitrary state on the Bloch sphere, which can be described with two angles: θ and ϕ. Any given state can therefore be parameterised by the coordinates n_1, n_2, n_3 along, x, y and z respectively

$$n_1 = \sin(\theta)\cos(\phi), \tag{2.68}$$

$$n_2 = \sin(\theta)\sin(\phi), \tag{2.69}$$

$$n_3 = \cos(\theta). \tag{2.70}$$

$$\tag{2.71}$$

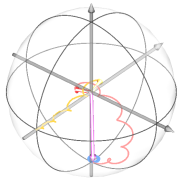

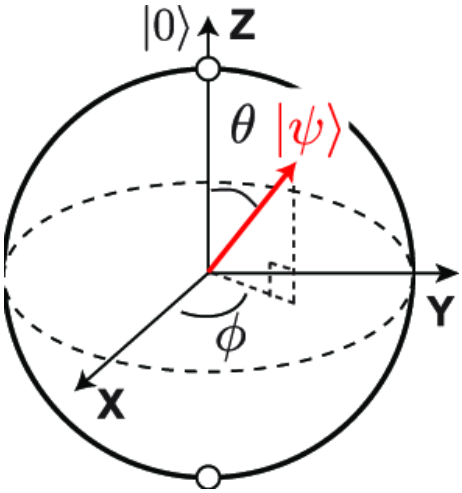

Figure 2.20: **Arbitrary state on the Bloch sphere.** Arbitrary state $|\psi\rangle$ described using the angles θ and ϕ. Image taken from [68].

We can describe the generic path of the evolution of a state on the Bloch sphere using the vector $\vec{n} = (n_1\vec{i}, n_2\vec{j}, n_3\vec{k})$. For illustrative purposes we will consider the case of a state that traverses a closed path on the Bloch sphere however, it is important to note that a geometric phase is acquired by the spin regardless of whether its ultimate trajectory represents a closed path or not. For the case of a closed path traversed on the sphere, the area on the sphere traversed by the path of the state is given by [69]

$$\Delta\Omega = \int_{\text{Surface}} = \vec{n} \cdot dS. \tag{2.72}$$

This represents the solid angle subtended on the sphere by the enclosed path of the state. By utilising Stokes theorem, it can be shown that this expression can be rewritten as a more easily solvable line integral, in terms of the generic path vector $n(\vec{t})$ evolving in time as

$$\Delta\Omega = \int_{\text{Surface}} = \vec{n} \cdot dS = \int_0^\tau \frac{n_1\dot{n_2} - n_2\dot{n_1}}{1 + n_3} dt, \tag{2.73}$$

where $\dot{n_1}$, $\dot{n_2}$ represent the time derivatives of n_1 and n_2 respectively.

In order to determine the phase incurred by a spin traversing an arbitrary path on the Bloch sphere, we can first write down a generic initial state for the spin as

$$|\psi(0)\rangle = \begin{pmatrix} e^{-i\frac{\phi_0}{2}} \cos\left(\frac{\theta_0}{2}\right) \\ e^{i\frac{\phi_0}{2}} \sin\left(\frac{\theta_0}{2}\right) \end{pmatrix}. \tag{2.74}$$

This state can then be time evolved to give

$$|\psi(t)\rangle = \begin{pmatrix} e^{-i\frac{\phi(t)}{2}} \cos\left(\frac{\theta(t)}{2}\right) \\ e^{i\frac{\phi(t)}{2}} \sin\left(\frac{\theta(t)}{2}\right) \end{pmatrix}, \tag{2.75}$$

where $\phi_0 = \phi(0)$ and $\theta_0 = \theta(0)$. As we are considering a state traversing a closed path on the Bloch sphere, we can assume that the state evolution is cyclic, with a period of τ. Thus, with this assumption and by comparing equation 2.75 and 2.74, we can write down the following

$$|\psi(t)\rangle = e^{i\alpha(\tau)} |\psi(0)\rangle, \tag{2.76}$$

$$e^{i\alpha(\tau)} = e^{i\frac{[\phi(\tau)-\phi_0]}{2}}. \tag{2.77}$$

The phase incurred by a spin, ϕ_{G}, between a time 0 and τ is then given by

$$\phi_{\mathrm{G}} = \frac{[\phi(\tau)-\phi_0]}{2} + i\int_0^\tau \langle\psi(t)|\frac{d}{dt}|\psi(t)\rangle \tag{2.78}$$

$$= -\frac{1}{2}\int_0^\tau \dot{\phi}(1-\cos(\theta))dt. \tag{2.79}$$

Using the definitions for n_1, n_2 and n_3 above, along with the fact that $\phi = \tan^{-1}(\frac{n_2}{n_1})$ and, due to us traversing a closed loop with vector $\vec{n}$, $\vec{n}^2 = 1$, we can show that

$$\dot{\phi} = \frac{n_1\dot{n_2} - n_2\dot{n_1}}{1-n_3^2}. \tag{2.80}$$

Finally, by substituting the definitions for n_1, n_2 and n_3 and equation 2.80 into equation 2.79 and comparing this to equation 2.73, we are left with the following expression for the phase incurred by the spin

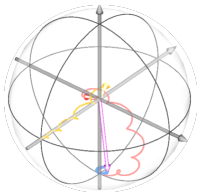

$$\phi_{\mathrm{G}} = -\frac{1}{2}\int_0^{\tau} \frac{n_1\dot{n}_2 - n_2\dot{n}_1}{1+n_3}dt \tag{2.81}$$

$$= -\frac{1}{2}\Delta\Omega. \tag{2.82}$$

This expression thus reveals that whenever the state of the spin traverses a path along the Bloch sphere, it incurs a geometric phase equal to half the solid angle subtended by its path [69]. This geometric phase is known as the Aharonov-Anandan phase [70], which is a generalisation of the Berry phase [71]. The Aharonov-Anandan phase has important implications for spin control and can actually be used as an important resource for quantum computation, as discussed in chapter 6.

3.
Donor spin qubit device

No amount of experimentation can ever prove me right; a single experiment can prove me wrong.

Albert Einstein

This chapter includes results from the following publication:
Section 3.5: C. Adambukulam, V. Sewani, **H. Stemp**, S. Asaad, M. Mądzik, A. Morello, and A. Laucht, "An ultra-stable 1.5 T permanent magnet assembly for qubit experiments at cryogenic temperatures," Review of Scientific Instruments, vol. 92, no. 8, 2021

The author acknowledges Ass Prof Evert van Nieuwenburg from the Univerity of Copenhagen for support in implementing a neural network for single electron transistor (SET) current blip detection.

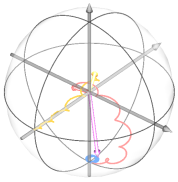

3.1 Device architecture and gate layout

The phosphorus-31 (^{31}P) donor spin qubit devices used in this thesis are fabricated exclusively using silicon-metal oxide semiconductor (Si-MOS) compatible techniques and materials. This allows us to leverage the substantial technological progress of the modern classical electronics industry for qubit fabrication. With this compatibility in mind, the basic structure of our devices consist of a silicon substrate, upon which a series of gates are patterned, allowing us to control, initialise and read out the state of individual donor atoms, introduced into the silicon lattice via ion-implantation.

The substrate used to host our donor qubits is a 500 μm thick wafer of natural silicon. In order to maximise the coherence times of the donor qubits, it is important to minimise the presence of any spin-carrying isotopes within the host material. This is detrimental to the qubit's performance, as any spin-carrying nuclei in the vicinity of the donor, may couple to the donor-bound electron via the hyperfine interaction. This unwanted hyperfine coupling results in the resonance frequency of the electron depending on the state of nearby silicon (Si) nuclei and thus any fluctuations in the state of these nuclei will result in random jumps in the electron's resonance frequency [72], which can in turn negatively affect the performance of the donor qubit. The naturally occurring isotopes present in silicon, in order of abundance, are ^{28}Si (92.2%), ^{29}Si (4.7%) and ^{30}Si (3.1%) [73]. While the isotopes ^{28}Si and ^{30}Si possess no nuclear spin, the nucleus of ^{29}Si possesess a spin of $\frac{1}{2}$. A 900 nm isotopically enriched layer of ^{28}Si is therefore grown on the surface of the silicon wafers via a technique of low pressure chemical vapor deposition (LPCVD) at Keio University in Japan, resulting in a residual ^{29}Si concentration of 0.08%, or 800 ppm [74]. Alternative techniques of isotopic enrichment also exist and have demonstrated residual ^{29}Si concentrations, as low as 0.025%, or 250 ppm [75]. A high-quality layer of SiO_2 is then thermally grown on top of the silicon, in order to provide an insulating barrier between the substrate and the aluminium gates fabricated on the surface of the chip.

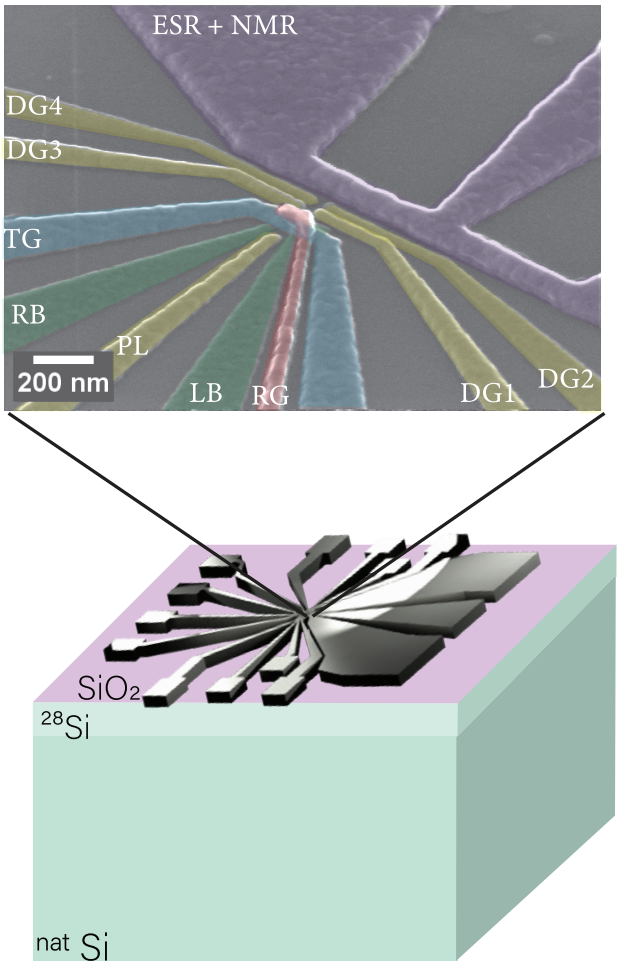

Figure 3.1: **Device gate layout.** False-coloured scanning electron microscope (SEM) image of the aluminium gates used to control and readout the donor. The purple structure is the magnetic antenna used to control the state of the electron and nucleus using ESR and NMR respectively. DG1-4 represent the donor gates, which are used to tune the donor energy levels with respect to the electrochemical potential of the SET, which can be itself tuned with the plunger gate (PL). The rate gate (RG) is used to influence the tunnel coupling between the donors and the single electron transistor (SET). The SET enables us to read out the spin state of the donor and is formed using the top gate (TG) and left and right barrier gates (LB and RB). The gates shown in the SEM image are patterned atop a layer of SiO_2 (dark grey), which is grown on top of a layer of isotopically enriched ^{28}Si (light green). This isotopically enriched layer lies on top of a layer of natural silicon, ^{nat}Si (dark green).

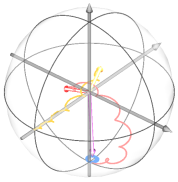

The donor atoms are implanted using a process of timed implantation, into a window of size 90 nm × 90 nm. The energy and fluence of the ion beam are chosen to optimise the following parameters: the average number of addressable donors within the device, the average distance between neighbouring donors and the average donor depth from the interface [37,76]. The optimal values for these parameters will depend on the experimental goals and are discussed in greater depth in section 3.2.

Following the implantation of the donors, aluminium gates are fabricated on top of the SiO_2. These gates can be broadly categorised into: gates for donor readout, gates for control of the electrostatic environment of the donors and gates for magnetic control. Donor readout is done using a single-electron transistor (SET). The SET consists of three aluminium gates: the top gate (TG) and two barrier gates: the left barrier gate (LB) and the right barrier gate (RB). A detailed explanation of the working principles behind the SET is provided in section 3.6. The electrostatic environment of the donor, with respect to the SET, is controlled via a series of gates called donor gates. In Figure 3.1, these donor gates are labelled as DG1, DG2, DG3, DG4 and the plunger gate, PL. Together these gates enable us to identify individual donors within the device as well as carefully tune the energy levels of each donor with respect to the SET, a vital requirement for qubit readout and control. The device used in this thesis also includes a rate gate (RG). The RG lies between the SET and donor gates and was designed with the intention of providing a tuneable barrier between the donor and the SET, in order to control the electron tunnel rates between the two. The small ($\approx$ 30 nm) distance between the donors and the SET however, makes the control of the tunnel barrier difficult to achieve and thus, in the device discussed in this thesis, the RG primarily serves as an additional means of electrostatic tuning of the donor environment.

Finally, a co-planar waveguide antenna, terminated by a short circuit, allows us to control both the states of the donor nucleus and electron via nuclear magnetic resonance (NMR) or electron-spin resonance (ESR) respectively. This is done by applying an oscillating AC

current, at the required frequency, through the shorts at the end of the waveguide, which is translated to an oscillating magnetic field at the site of the donor [77].

3.2 Donor implantation

The donor atoms are introduced into the device via a process of timed implantation with an ion beam at either the University of Melbourne or the Australian National University (ANU). The choice of fluence and implantation energy of the donor atoms in the ion beam are dictated by both the atomic species being implanted and the experimental requirements.

To facilitate the correct parameter choice, simulations of the implantation are performed using the software tool Stopping and Range of Ions in Matter (SRIM) [78]. Figure 3.2 shows an SRIM implantation simulation of both the atomic species ^{31}P and ^{123}Sb for an implantation energy of 14 keV and fluence of 1×10^{12} cm^{-2}. Owing to its higher atomic mass, ^{123}Sb is implanted at a lower mean depth, with a lower spread in the implantation depths, referred to as 'straggle', compared to ^{31}P for the same implantation energy [79]. A higher atomic mass of the species being implanted is therefore beneficial for improving the implantation precision, enabling greater control over the positioning and inter-donor spacing of the atoms [80].

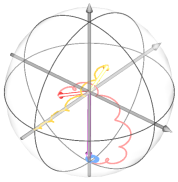

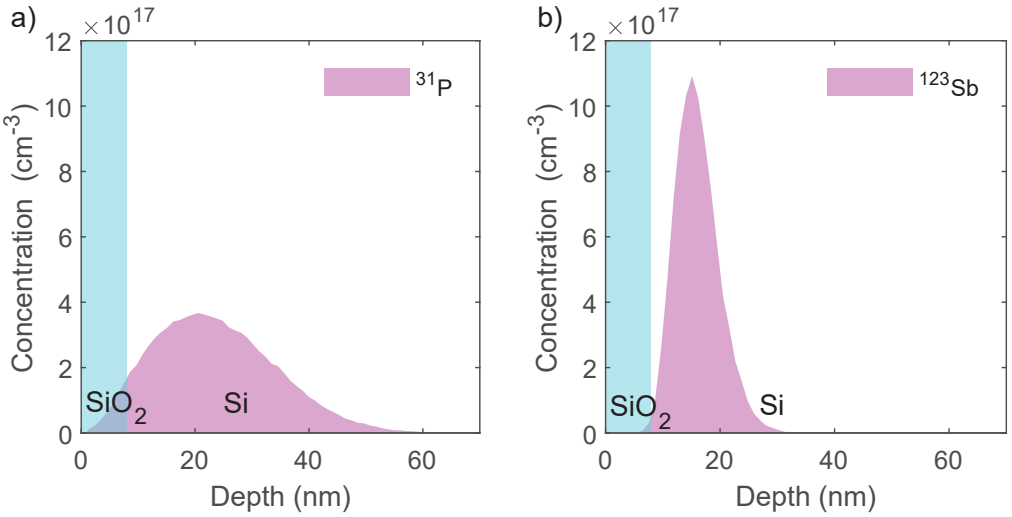

Figure 3.2: **SRIM simulation of ^{31}P (a.) and ^{123}Sb donor (b.) implantation.** Both simulations were carried out with an implantation energy of 14 keV, fluence of 1 $\times$ 10^{12} cm^{-2}, an angle of incidence of 0^o and an 8 nm layer of SiO_2 with a density of 2.2 gcm^{-3}. Simulations were carried out by Dr Danielle Holmes at the University of New South Wales (UNSW).

3.3 Device fabrication

The silicon substrate is a p-type <100> silicon wafer, with a resistivity of 10-20 Ωcm. The device fabrication process can be divided into two steps. The first step is the fabrication of the silicon stock, which is carried out by dedicated fabrication personnel. Once the stock has been fabricated, the implantation window and aluminium gates are then fabricated by members of the research group.

The basic outline of the silicon stock fabrication procedure, omitting details for confidentiality purposes, is as follows:

1. **Defining optical alignment markers.** The alignment markers are defined by first growing a hard SiO_2 mask using a wet oxidation furnace. The marker patterns are

then created using photolithography, followed by a buffered hydrofluoric acid (BHF) and tetramethylammonium hydroxide (TMAH) etching. The hard SiO_2 mask is then removed using buffered HF etching.

2. **Definition of p-doped regions.** P-doped regions are used to reduce unwanted leakage currents flowing at the ^{28}Si - SiO_2 interface, between the n-doped regions of the device. The regions are first defined by growing a hard SiO_2 mask, followed by optical lithography. The regions are then doped using thermal diffusion of boron (B). The SiO_2 hard mask is once again removed using buffered HF etching.

3. **Definition of n-doped regions.** N-doped regions are created in the same process as the p-type regions however, this time phosphorus (P) is used instead of B.

4. **Repairing damage caused by the creation of the doped regions.** A two-step thermal oxidation process repairs the defects caused by the thermal diffusion process and ensures the P and B is well integrated into the silicon.

5. **Growth of a field oxide layer.** A layer of field oxide, 200 nm in thickness, is grown in a wet oxidation furnace.

6. **Growth of high quality gate oxide.** A 26 μm $\times$ 60 μm opening in the field oxide is etched in the centre of each device using BHF, followed by the growth of an 8 nm thick layer of high quality, dry thermal oxide. The high quality oxide is important as the donors and SET will be situated in close proximity ($\approx$ 10 nm) to the interface between silicon and this thermally-grown oxide.

7. **Definition of large alignment markers.** Large alignment markers are patterned using optical lithography followed by electron-beam evaporation of 15 nm of platinum and 65 nm of titanium. Unwanted regions of metal are lifted off with warm N-Methyl-2-pyrrolidone (NMP).

Following the stock fabrication, the silicon wafer is then diced and device fabrication can begin. The donor devices are fabricated on silicon stock using the following fabrication steps:

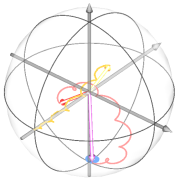

1. **Patterning of small alignment markers.** These markers are patterned using electron bean lithography (EBL), followed by electron-beam evaporation of 15 nm of titanium and 65 nm of platinum and liftoff in NMP.

2. **Definition of the implantation window.** A 90 nm × 90 nm implantation window is patterned into a layer of poly-methyl-methacrylate (PMMA) electron-beam resist. The sample is then subsequently sent to the University of Melbourne or the Australian National University, where the phosphorus donors are implanted into this window.

3. **Repair of the damage caused by ion implantation.** A rapid thermal anneal is performed for 5 seconds at 1000 ^{o}C. This both reduces the damage of the silicon lattice caused by the donor implantation, while also acting to activate the donors.

4. **Definition of ohmic contacts to the n-doped regions.** Ohmic contacts are created by etching through the field oxide using buffered HF etching, followed by electron-beam evaporation of 200 nm of aluminium, liftoff and a 15 minute anneal in forming gas (consisting of 5% hydrogen and 95% nitrogen) at 400 ^{o}C.

5. **Patterning of the gates.** Patterning of the gates is done in a three-step EBL process. Before every step a PMMA mask is spun onto the chip. The gates are then patterned into the PMMA using EBL, followed by evaporation of aluminium (Al) and liftoff in either acetone or warm NMP. In the first EBL layer, the SET barrier gates and two-donor gates are patterned and evaporated with 30 nm of Al. For the second EBL step, the SET top gate and the remaining donor gates are patterned and evaporated with 50 nm of Al. For the third EBL step, the antenna is patterned and evaporated with 80 nm of Al. Each deposition of metal is insulated from the subsequent layers with a layer of native Al_xO_y oxide, that naturally coats the Al upon exposure to air.

6. **Dicing.** The chips are diced into 2.8 mm × 1.4 mm pieces, with each sample containing two devices.

7. **Passivating the oxide traps.** A final anneal with forming gas, consisting of 95%

N_2 and 5% H_2, is performed for 15 minutes at 400 ^oC to passivate the charge traps in the gate oxide caused by damage from EBL.

Once these fabrication steps have been successfully concluded, the devices are ready to be bonded into an enclosure and mounted into a dilution refrigerator, ready for measurements to commence.

3.4 Device instrumentation

Readout and control of the donors requires the use of DC, radio-frequency (RF) and microwave-frequency control lines. For this reason, we make use of a custom printed circuit board (PCB), that contains both microwave and low frequency lines. These lines are centered around a rectangular cut-out in the centre of the PCB, where the donor device is situated. The PCB is mounted to a copper enclosure, which possesses SK 2.92 mm standard connectors, suitable for high frequency operation up to 40 GHz, as well as MMCX connectors suitable for frequencies less than 6 GHz. The device sample is glued to the copper enclosure, through the cut-out in the PCB, using a thermally conductive adhesive that ensures that the device is well thermalised with the enclosure. The device is then aluminium wire bonded to the PCB and bolted to a permanent magnet assembly, which provides a strong, static magnetic field, B_0, to Zeeman split the spin states of the donor electrons and nuclei. The details of this permanent magnetic assembly are discussed in greater depth in section 3.5.

The permanent magnet assembly is then mounted onto the mixing chamber plate of a Bluefors BF-LD400 cryogen free dilution refrigerator, enabling us to cool the device to a base temperature of approximately 20 mK. These temperatures are essential for the spin-dependent electron tunnelling readout scheme used to measure the state of the donor-bound electrons, discussed in section 3.6.

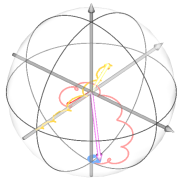

3.4.1 Control lines

Connecting the device to the instruments required to control and readout the donor qubits is a delicate matter and careful consideration must be put into ensuring that the lines are well filtered and correctly thermalised at each stage of the dilution fridge, such that the thermal noise reaching the device is minimised. Additionally, vibrations, originating from the pulse tube of the dilution fridge, can manifest as triboelectric noise seen by the device, unless careful consideration is placed into the materials used for the device control lines [81]. With these considerations in mind, the instrumentation layout for the readout and control of the donor device is displayed in Figure 3.3. As stated previously, this control scheme can be separated according to three regimes of operation: DC, RF and microwave frequencies.

DC lines are required in order to apply static DC voltages to the donor gates, as well as to bias the source and drain, such that a current may flow between the two leads when the device has reached turn-on (see section 3.7.2). These DC lines consist of a constantan loom, which is low pass filtered with a 20 Hz cutoff at the mixing chamber stage.

RF lines are used in order to dynamically control a selection of donor gates for fast pulsing between the donor operation and readout positions in gate space. An RF line is also required for controlling the donor nucleus through nuclear magnetic resonance (NMR) and for the return signal coming from the single-electron transistor (SET). Furthermore, RF lines are used to transmit the input signals for the in-phase (I) and quadrature (Q) inputs used for single-sideband modulation of a microwave signal, in order to perform electron spin resonance (ESR). The RF lines are made from a flexible copper-nickel (Cu-Ni) coaxial line. These lines are graphite coated to reduce triboelectric noise [81] and filtered to a cutoff frequency of 145 MHz at the mixing chamber plate.

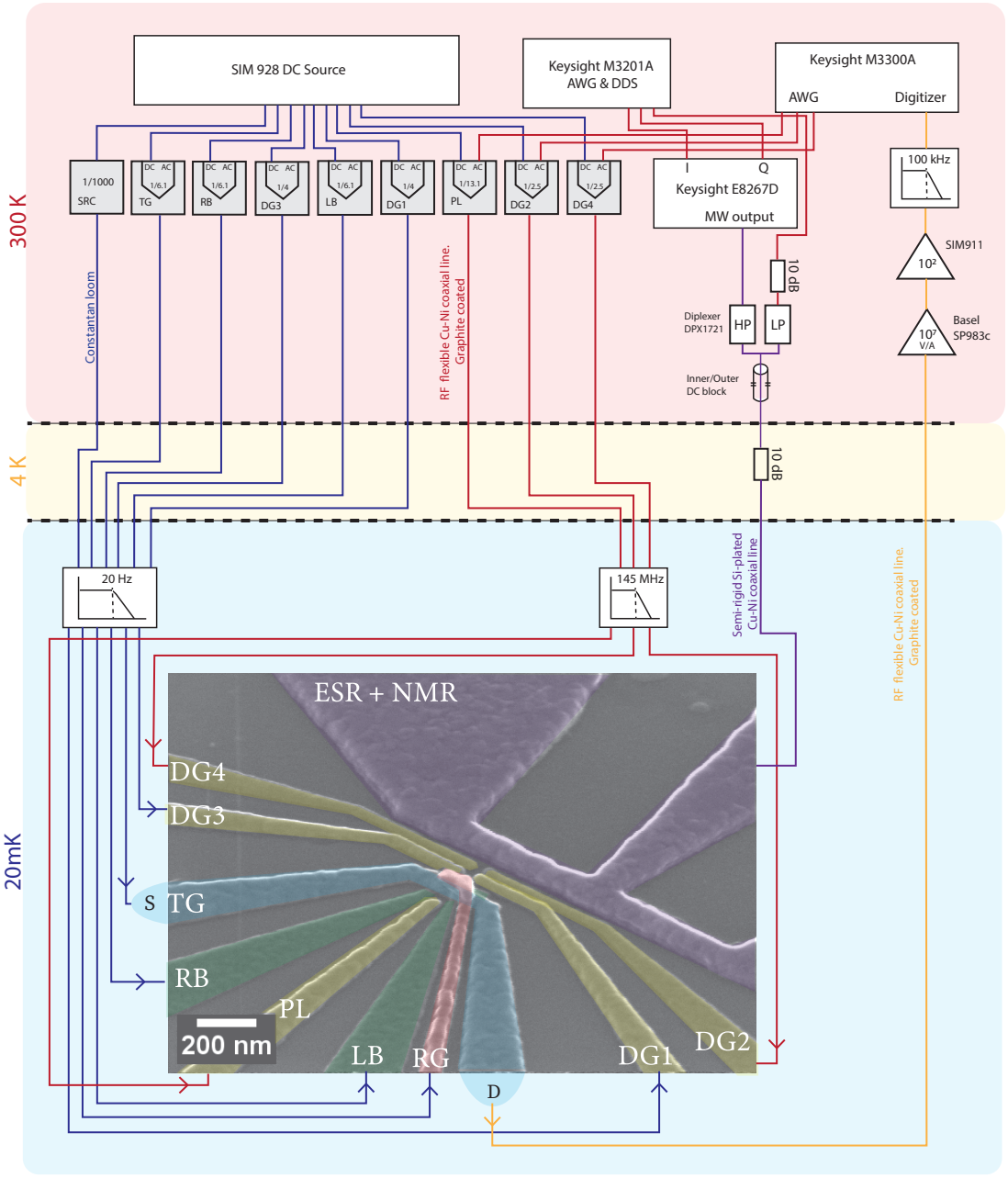

Figure 3.3: **Device instrumentation layout.** Diagram depicting the control lines and electronic equipment used to operate the donor spin qubits. Blue lines are used to indicate DC lines, while red and gold lines indicate radio-frequency (RF lines) and the purple line represents the microwave line. The different temperature stages at which the instrumentation is placed are indicated by the 300 K, 4 K and 20 mK boxes, which represent the room temperature setup, setup at the 4 K plate of the dilution fridge and setup at the mixing chamber of the dilution fridge respectively.

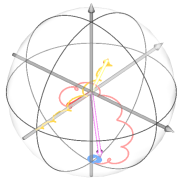

A single microwave line is used to carry both the NMR and ESR control pulses. This microwave line consists of a semi-rigid, silver-plated Cu-Ni coaxial line. The line passes through an inner/outer DC block at room temperature, to prevent possible voltage offsets from creating a DC current through the thin short circuit termination of the microwave antenna. Additionally, this line is attenuated by 10 dB, with an attenuator positioned at the 4K stage of the dilution refrigerator.

3.4.2 Electronic equipment

The DC voltages applied to the donor gates in order to provide static tuning of the donor's electrostatic environment are provided by 9 Stanford Research systems (SRS) SIM 928 DC sources, hosted in two SIM 900 mainframes. The voltages each pass through an AC/DC combiner, which divides the incoming voltage, the division values of which are depicted in Figure 3.3. Three of the donor gates, namely the PL, DG2 and DG4 gates also have an AC input to allow for fast dynamic tuning of these gate voltages for fast control of the readout position of the donor. These RF signals are provided by a Keysight M3300A arbitrary waveform generator (AWG), which is bandwidth limited to 200 MHz, and passed into the AC inputs of the AC/DC combiners for these gates. This thus allows for an RF modulation to be added on top of a static DC voltage applied to these donor gates.

A Keysight M3201A module hosts a field-programmable gate array (FPGA), on which we have built an in-house direct digital synthesis (DDS) system (described in more detail in section 3.4.4). The DDS provides RF input signals to the I and Q inputs of a Keysight E8267D PSG vector microwave source, to allow for single and dual-sideband modulation of a microwave tone produced by the vector source, for control of the electron spin. Details regarding the single and dual-sideband modulation techniques utilised for ESR are provided in section 3.4.3. Additionally, the DDS provides the RF signal for control of the nuclear spin through NMR. The NMR signal is attenuated by 10 dB at room temperature, to protect the antenna from any unexpected spikes in NMR amplitude, before being com-

bined with the microwave output of the vector source using a DPX1721 diplexer, allowing both NMR and ESR signals to travel down the same line to the device's antenna.

The SET current returning from the drain is passed through a Basel SP983c transimpedence amplifier, which converts the current into a voltage with a gain of 10^7 V/A and frequency bandwidth of 100 kHz. The voltage signal is then passed into a SIM911 bipolar junction transistor (BJT) amplifier, which is housed in the same SIM900 mainframe as the DC sources and provides an additional gain of 10^2. This amplifier also has the important function of breaking the ground between the fridge and the measurement setup, to avoid the formation of ground-loops that can introduce additional noise to the system. As the BJT amplifier can add additional noise to the current signal, the signal is passed through a further passive low pass filter, with a cutoff at 100 kHz. The signal then enters the digitiser channel of the Keysight M3300A, with a sample rate of 100 megasamples-per-second, before the SET current trace is recorded and analysed.

3.4.3 Phase modulation

For a range of operation sequences on the donor spin qubits, we are required to rapidly switch between frequencies, such that we can sweep over a range of frequencies, or apply multiple frequencies within the same pulse sequence. When applying a microwave pulse to drive ESR on the donor electrons, one option would be to simply output a microwave signal at a given frequency from the vector microwave source. This method however, does not allow for the fast switching of frequencies required in the majority of pulse sequences. We can thus make use of single and dual-sideband modulation techniques in order to switch frequencies at the rate required to operate our donor spin qubits.

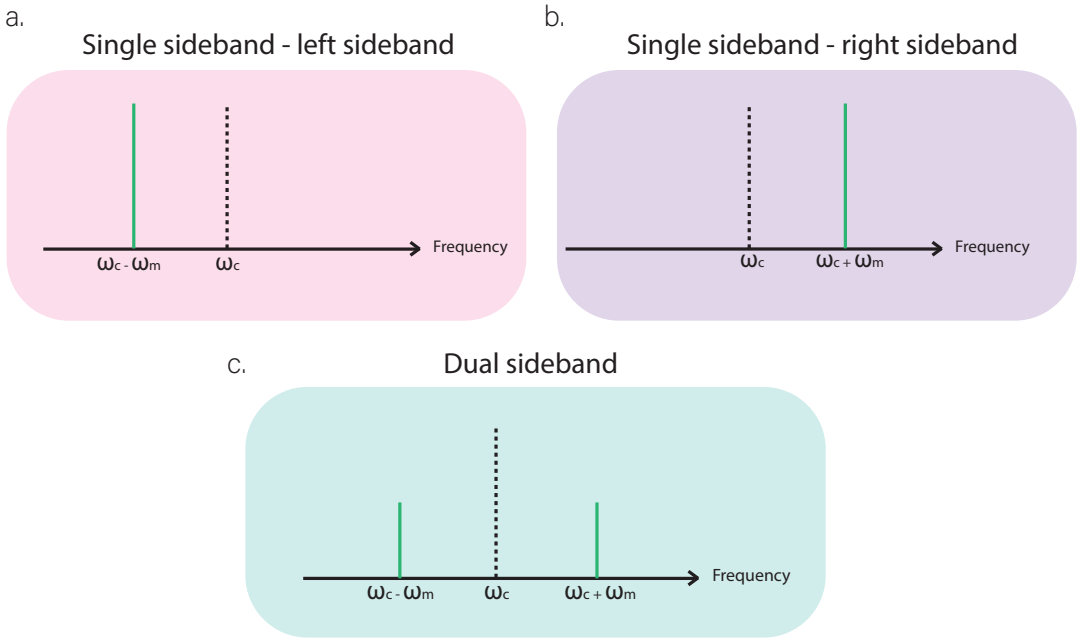

Figure 3.4: **Single and dual sideband modulation.** Single sideband modulation with either the left sideband active, **a.**, or the right sideband active, **b.**. $\omega_{\mathrm{c.}}$ represents the carrier frequency, while ω_{m} represents the modulation frequency. **c.** Dual sideband operation, with both sidebands active, each possessing half the amplitude of the input signal.

3.4.3.1 Single-sideband modulation

Single-sideband modulation involves inputting two signals, I and Q, that are phase shifted by 90^o with respect to each other, into a vector microwave source. These input signals are generated using the DDS of the Keysight M3201A module. Let us therefore define the input signals for I and Q as follows [82]:

$$I(t) = \cos(\omega_{\mathrm{m}} t), \tag{3.1}$$

$$Q(t) = \cos(\omega_{\mathrm{m}} t - \frac{\pi}{2}) = \sin(\omega_{\mathrm{m}} t), \tag{3.2}$$

where $I(t)$ is the input signal for the I port, $Q(t)$ is the input signal for the Q port and ω_{m} is the modulation frequency. The microwave source generates a signal, which we refer to as the carrier signal. The carrier signal is of microwave frequency and forms the central

frequency about which we form our sidebands. The carrier signal can be defined as:

$$C(t) = \cos(\omega_{\mathrm{c}} t), \tag{3.3}$$

where ω_{c} is the carrier frequency. Inside the vector source, the I signal is multiplied with the carrier signal, while the Q signal is multiplied with a carrier signal that has been shifted by 90^o. In order to calculate the output of these multiplications we can make use of the following trigonometric identities:

$$\sin\mu \sin\nu = \frac{1}{2}[\cos(\mu - \nu) - \cos(\mu + \nu)], \tag{3.4}$$

$$\cos\mu \cos\nu = \frac{1}{2}[\cos(\mu - \nu) + \cos(\mu + \nu)]. \tag{3.5}$$

Using these identities we can calculate the resultant signals, $a(t)$ and $b(t)$:

$$a(t) = \cos(\omega_{\mathrm{c}} t)\cos(\omega_{\mathrm{m}} t) \tag{3.6}$$

$$= \frac{1}{2}[(\cos(\omega_{\mathrm{c}} - \omega_{\mathrm{m}})t) + \cos(\omega_{\mathrm{c}} + \omega_{\mathrm{m}})t)], \tag{3.7}$$

$$b(t) = \sin(\omega_{\mathrm{c}} t)\sin(\omega_{\mathrm{m}} t) \tag{3.8}$$

$$= \frac{1}{2}[(\cos(\omega_{\mathrm{c}} - \omega_{\mathrm{m}})t) - \cos(\omega_{\mathrm{c}} + \omega_{\mathrm{m}})t)]. \tag{3.9}$$

For single-sideband modulation, we can choose which of the sidebands is present, either to the left of the carrier frequency or the right of the carrier frequency, by either performing the operation $a + b$ or $a - b$ respectively in the vector microwave source.

$$a(t) + b(t) = \cos(\omega_{\mathrm{c}} - \omega_{\mathrm{m}})t, \tag{3.10}$$

$$a(t) - b(t) = \cos(\omega_{\mathrm{c}} + \omega_{\mathrm{m}})t. \tag{3.11}$$

We are hence left with a single-sideband signal, of full amplitude, that is either at a frequency $\omega_{\mathrm{c}} - \omega_{\mathrm{m}}$ or $\omega_{\mathrm{c}} + \omega_{\mathrm{m}}$, as shown in panel **a.** and panel **b.** in Figure 3.4 [82]. As the modulation frequency ω_{m} can be switched very rapidly, this therefore allows for fast switching of the output frequency.

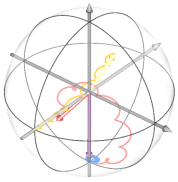

3.4.3.2 Dual-sideband modulation

For dual-sideband modulation, the exact same principle as that used for single-sideband modulation is utilised, with the only difference being that in this case, a signal is applied only to either the I or the Q input of the vector microwave source, while the input of the other channel is 0. Therefore in this case:

$$I(t) = \cos(\omega_{\mathrm{m}} t), \tag{3.12}$$

$$Q(t) = 0. \tag{3.13}$$

Using the same method of multiplying the carrier signal with the I and Q inputs as used for single-sideband modulation, we are therefore left with the following signals:

$$a(t) = \cos(\omega_{\mathrm{c}} t)\cos(\omega_{\mathrm{m}} t) \tag{3.14}$$

$$= \frac{1}{2}[(\cos(\omega_{\mathrm{c}} - \omega_{\mathrm{m}})t) + \cos(\omega_{\mathrm{c}} + \omega_{\mathrm{m}})t)], \tag{3.15}$$

$$b(t) = \sin(\omega_{\mathrm{c}} t) \times 0 = 0. \tag{3.16}$$

Thus, in this case, whether we perform the operation $a + b$ or $a - b$, we are left with the same result

$$a + b = a - b = \frac{1}{2}[(\cos(\omega_{\mathrm{c}} - \omega_{\mathrm{m}})t) + \cos(\omega_{\mathrm{c}} + \omega_{\mathrm{m}})t)]. \tag{3.17}$$

We therefore observe two sideband frequencies present simultaneously, each with half the amplitude of the input signal, one at a frequency of $\omega_{\mathrm{c}} - \omega_{\mathrm{m}}$ and the other at a frequency of $\omega_{\mathrm{c}} + \omega_{\mathrm{m}}$, as shown in panel **c.** of Figure 3.4 [82]. This mode of operation is useful when two frequencies need to be applied simultaneously. However, this does come at the cost of each frequency possessing half the amplitude of the original signal, resulting in a slower driving of the spin states.

3.4.4 Phase coherent DDS

As stated in section 3.4, the RF pulses required for the I and Q inputs of the vector microwave source (used for sideband modulation for ESR) as well as for the NMR pulses used to control the nuclei, are generated using an in-house direct digital synthesis (DDS). This DDS was designed to maintain phase coherence of the generated signals.

Phase coherence is vital for the coherent control of the donor spins. As stated previously, in a typical pulse sequence, applied to either the donor nucleus or electron, we are frequently required to switch between multiple frequencies within the same pulse sequence. It is imperative for coherent control therefore, that when switching between multiple frequencies within the same control sequence, the DDS possesses an internal clock for each of the applied frequencies. These individual clocks, held for each outputted frequency means that when the DDS switches back to a previously applied frequency within the pulse sequence, the instrument can apply the correct phase to the outputted pulse, such that the pulse is still able to coherently manipulate the spin. Figure 3.5 shows an example of this phase coherence in action. In this figure, we are applying three instances of a pulse of the same frequency, and between each pulse we are adding some wait time, during which we output a pulse of a different frequency, not shown in the figure. The coloured lines show the output pulses taken from an oscilloscope, while the dashed black lines show an extrapolated fit to the original pulse. We can see that with the application of the second and third pulse, these pulses do not start with a phase of 0, as with the original pulse, but instead begin with such a phase that they perfectly line up with the extrapolated fit of the first pulse. This allows us to keep track of the state of the spin, such that we maintain coherent control, even with the spin undergoing Larmor precession between intermittent control pulses.

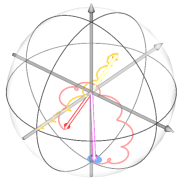

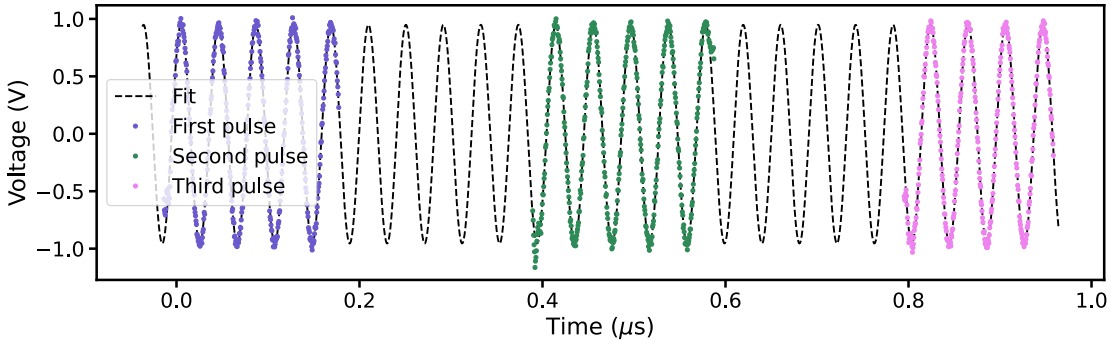

Figure 3.5: **Phase coherence of the DDS output.** Three outputted pulses of the same frequency, with a wait time between, during which we apply a pulse of a different frequency, not shown in the figure. The black dashed line shows an extrapolated fit of the first pulse. The second and third pulse line up with the extrapolated fit, indicating that the pulses are phase coherent.

3.5 Static DC magnetic field

In order to induce the Zeeman splitting required to lift the degeneracy of the $|\downarrow\rangle$ and $|\uparrow\rangle$ spin states, we must apply a static magnetic field, of typically around 1 T, along the z-axis of the spin. Experimentally, this field is typically provided by a superconducting solenoid. However, superconducting solenoids are very large and expensive and can result in slow drifts in the magnetic field over time, as a result of the slow loss in the superconducting current used to generate the magnetic field. One benefit of using a superconducting solenoid to provide the static B_0 field is that this field can be swept in order to vary the magnitude of the field. However, in the majority of experiments, the B_0 field is simply 'set and forget' and hence this tuneability of the field becomes redundant. A simpler solution that we have explored is to place the spin qubit device into an assembly of strong, permanent magnets which, although lacking in tuneability, offers a much cheaper and more compact alternative to a superconducting solenoid. Figure 3.6 shows the layout of the magnet assembly and the positioning of the donor device within it.

An additional benefit of replacing the superconducting solenoid with permanent magnets,

is the elimination of any risk of quenching. In the event of any technical faults associated with the dilution refrigerator, that cause the solenoid's temperature to rise above its critical temperature, the superconducting wire inside the magnet will turn normal, causing the magnet to 'quench' and resulting in a rapid increase in the temperature of the fridge used to cool the qubit devices. As the permanent magnet assembly does not contain any superconducting elements, quenching is not an issue for these magnets, allowing the user more time to deal with dilution fridge faults before the qubit device is warmed significantly.

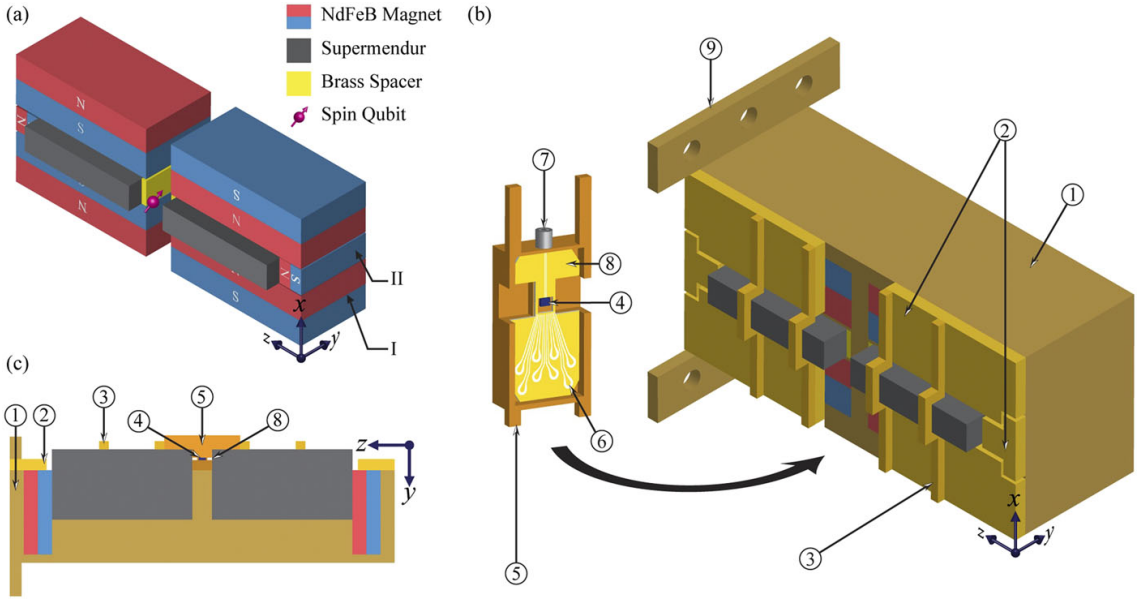

Figure 3.6: **Permanent magnet assembly.** **a.** Diagram of the permanent magnet assembly, with N and S, and I and II denoting north and south, and the two permanent magnet shapes, respectively. **b.** Diagram of the magnet assembly inside the copper enclosure used to keep the magnets in place. This copper enclosure is bolted to the mixing chamber of the dilution refrigerator. **c.** Diagram of a cross-section of the magnet assembly in the yz-plane. Figure taken from [83].

Although permanent magnets offer a number of attractive benefits over superconducting solenoids, before adopting them into the qubit setup it was important to assess the level of magnetic drift present in these magnets, compared to the approximately 40 parts per billion per hour drift in magnetic field experienced by the superconducting solenoids, while in persistent current mode. In order to assess this magnetic drift, we repeatedly measured the resonance frequency of the ionised nucleus of a ^{31}P donor atom implanted into a device

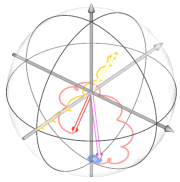

that was subsequently bolted to a permanent magnet assembly. The Hamiltonian of the ionised phosphorus nucleus, as defined in section 2.3.1, is given by

$$\hat{H} = \gamma_{\mathrm{n}} B_0 \hat{I}_z. \tag{3.18}$$

As this Hamiltonian possesses only a magnetic term, any changes in the resonance frequency of the ionised nucleus are caused by changes in the magnetic field at the site of the nucleus. Tracking changes in the resonance frequency of the ionised nucleus hence offers a convenient and highly precise means of tracking any magnetic field drift experienced by the donor.

We utilised two techniques in order to obtain the resonance frequency of a single spin with high accuracy. The first, was to perform a low-power frequency spectrum of the spin, such that the linewidth of the resonance peak approached the intrinsic linewidth of the system. The other, was to perform a Ramsey experiment on the spin, with the oscillation frequency of the measured Ramsey fringes directly corresponding to the frequency detuning between the AC drive and the resonance frequency of the system.

Figure 3.7 shows a repeated Ramsey measurement performed on the ionised donor nucleus in the permanent magnet assembly. Approximately 70 repetitions of the Ramsey measurement were performed, which took a total of around 25 hours to measure, allowing us to track the frequency drift over a time period of 25 hours. By repeating this long Ramsey experiment over a number of repeated occasions, we were able to track the magnetic field drift over a significant length of time, as shown in Figure 3.8. The decay in the field observed from hours 0 to 400 we believe to be attributed to the temperature dependence of the magnets, as these measurements were taken immediately following the cooldown of the magnet assembly from room temperature to 20 mK in a dilution fridge. Once the temperature effects of the magnets had fully stabilised however (after approximately 3 weeks of continuous operation at 20 mK), we extracted a magnetic field drift rate of $<$ 2.8 parts per billion per hour, more than a factor of 10 lower than the magnetic field drift

rate observed in the superconducting solenoid.

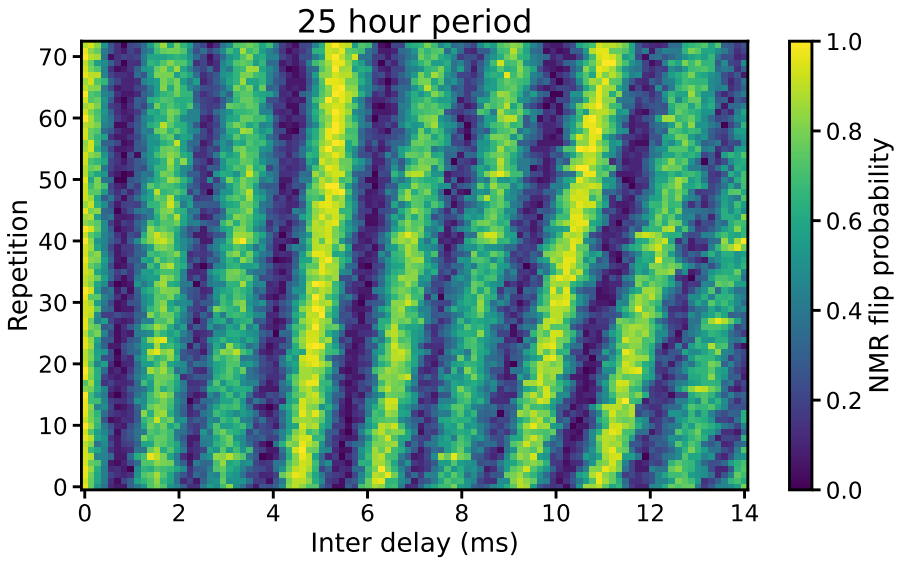

Figure 3.7: **Magnetic field drift measured by Ramsey fringes.** Repeated Ramsey measurement performed on the ionised nucleus over a 25 hour time period, in a permenant magnet setup, with the repetitions of the Ramsey fringes along the y axis. The shift in the frequency of the Ramsey oscillations is as a result of the shift in the magnetic field experienced by the spin.

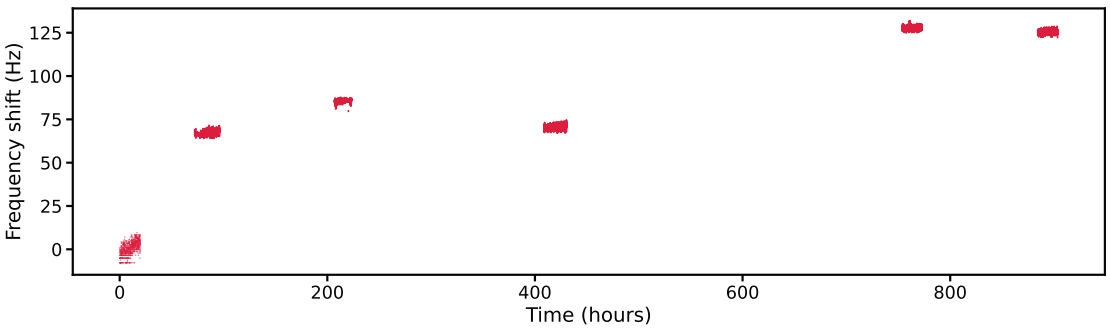

Figure 3.8: **Long-term frequency tracking of the ionised nucleus.** Repeated overnight Ramsey measurements of the ionised nucleus taken over an $\approx$ 900 hour time period. The increased shift in NMR frequency for the measurement duration between 0-400 hours is as a result of the magnetic field stabilising after cooling down the permanent magnet assembly to the mK base temperature of the dilution fridge. After the magnets had stabilised in temperature, the magnetic field drift rate, extracted from the drift in ionised NMR frequency, was found to be < 2.8 parts per billion, per hour.

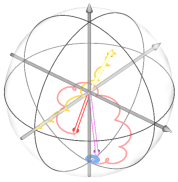

In order to more thoroughly investigate the effect of temperature change on the magnetic field of the permanent magnet assembly, after cooling the magnets to 20 mK in a dilution fridge for a sufficient length of time for the temperature induced magnetic field drift to stabilise, we applied a small amount of heat to the mixing chamber plate, leading to a small increase in the temperature of the permanent magnets. By performing a repeated Ramsey measurement on the ionised ^{31}P nucleus, we were able to monitor the shift in magnetic field as a function of temperature. Figure 3.9 shows the resulting drift in the frequency of the Ramsey oscillations, and thus the magnetic field, upon switching the mixing chamber heater on and off. We observed a shift of approximately 40 parts per million in the frequency of the ionised nucleus, for a temperature change of 60 mK.

These measurements all corroborate that, in the normal operating regime of a qubit device in a dilution refrigerator, the permanent magnet assembly provides a more stable source of static magnetic field than a superconducting solenoid in persistent current mode.

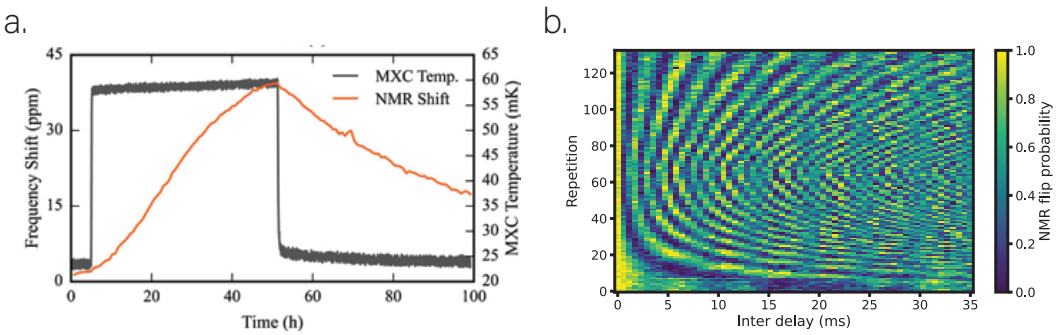

Figure 3.9: **Effect of temperature on the magnetic field.** We measured the effect of temperature on the magnetic field of the permanent magnet assembly, by cooling the magnets down to the base temperature of the dilution fridge ($\approx$ 20 mK) before applying a small amount of heat to the mixing chamber plate. **a.** Mixing chamber temperature as a function of time, with the sudden increase and decrease in temperature indicating the times when the heater was switched on and off and the corresponding shift in ionised nuclear magnetic resonance (NMR) frequency. **b.** Repeated Ramsey measurements used to extract this frequency shift. From this measurement we extracted a change in the NMR frequency of $\approx$ 40 parts per million with a temperature shift of 60 mK. The plot in **a.** was taken from [83].

3.6 The single-electron transistor (SET)

For the readout and initialisation of the donor bound electron we employ an SET, which acts as a highly sensitive detector of charge movement in its vicinity. Principally, the SET is comprised of a large quantum dot, referred to as the SET island, which consists of ≈ 100 electrons. At this electron occupation, the spacing between energy levels is reduced to such an extent that the levels form a near-continuum of states. The energy levels of the island can thus be described by a Fermi distribution, with occupied electron energy levels lying below the electrochemical potential of the SET (μ_{SET}) and un-occupied electron states above μ_{SET} [84]. At finite temperature (T), where T$>$ 0, this Fermi distribution deviates from a step function and is instead smeared according to $k_B T$, where k_B is the Boltzmann constant. This smearing results in some residual occupation of states existing above μ_{SET}, the implications of which are discussed in section 3.10. The method of experimentally realising the SET is discussed in section 3.7.2.

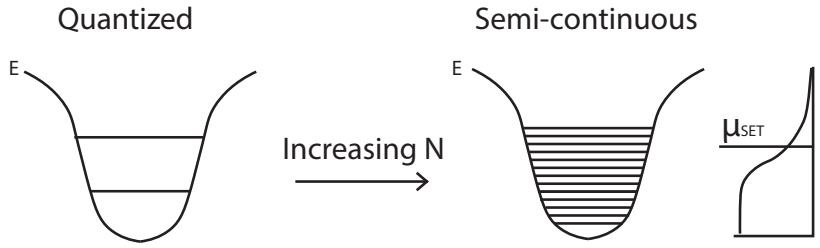

Figure 3.10: **Potential well of the SET island.** Depiction of the potential well of a quantum dot with increasing numbers of electrons, N. The left well depicts the potential well of the dot with only a few electrons, resulting in well quantised energy levels. The right well on the other hand, depicts the energy levels of the dot with increasing electron occupation, N. As the number of electrons in the dot is increased, the energy levels of the well become more closely spaced, until they become a semi-continuum of states. This semi-continuum of states can be described by a Fermi distribution, depicted schematically on the far right; with un-occupied states above the electrochemical potential energy and occupied states below.

Although the purpose of the SET, namely to measure the spin state of a single electron

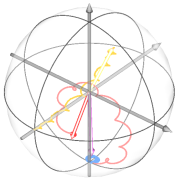

along the Z-axis of the Bloch sphere, is decidedly quantum in nature, the working principle behind its operation can be explained chiefly through classical capacitive couplings, plus the ability of electrons to tunnel on and off the island. The SET can thus be represented as a circuit diagram, shown in Figure 3.11.

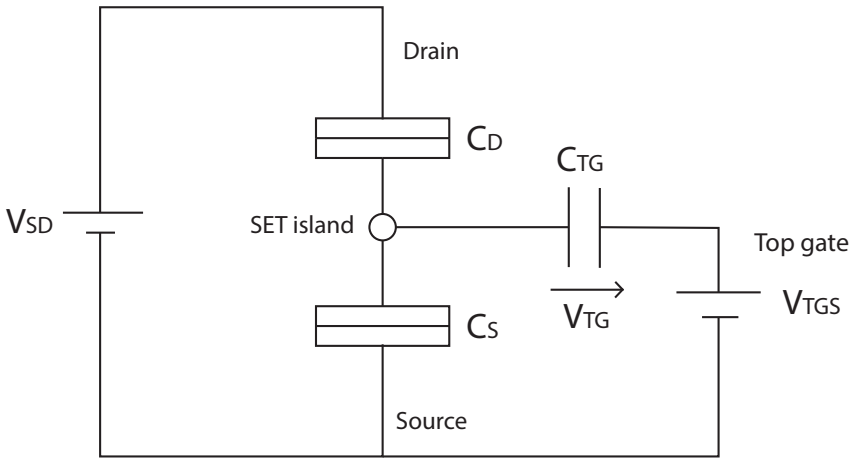

Figure 3.11: **SET circuit diagram.** Circuit diagram depicting the capacitive couplings to the SET. V_{SD} represents the voltage bias applied between the source and drain leads, C_{D} (C_{S}) represents the capacitive coupling between the SET island and the drain (source) lead. V_{TGS} represents the voltage applied to the top gate, while V_{TG} represents the voltage from the top gate experienced by the SET, which may differ from V_{TGS} due to losses at the source contact. C_{TG} represents the capacitive coupling between the SET island and the top gate, which is used to control the electron occupation of the island.

The SET island possesses three capacitive couplings: one to the source lead, C_{S}, one to the drain lead, C_{D}, and one to the top gate C_{TG}. Together, these make up the total capacitive coupling experienced by the SET island, C_{Σ}

$$C_{\Sigma} = C_{\mathrm{S}} + C_{\mathrm{D}} + C_{\mathrm{TG}}. \tag{3.19}$$

The occupation of the SET island is controlled using the voltage applied to the gate TG. The total energy of the SET island when a voltage of V_{TG} is applied to the TG is given by the following formula (which has been simplified for clarity):

$$E(N) = \frac{[-eN + C_{\mathrm{TG}}V_{\mathrm{VG}}]^2}{2C_\Sigma}, \tag{3.20}$$

where N is the number of electrons on the island and e is the charge of each electron. The energy required to add the N^{th} electron to the SET island, with an occupation of $N-1$ electrons, is referred to as the electrochemical potential of the SET island and is given by

$$\mu(N) = E(N) - E(N-1), \tag{3.21}$$

$$= \frac{[-eN + C_{\mathrm{TG}}V_{\mathrm{VG}}]^2}{2C_\Sigma} - \frac{[-e(N-1) + C_{\mathrm{TG}}V_{\mathrm{VG}}]^2}{2C_\Sigma}, \tag{3.22}$$

$$= \frac{e^2}{C_\Sigma}\left(N - \frac{1}{2} - \frac{C_{\mathrm{TG}}V_{\mathrm{VG}}}{e}\right). \tag{3.23}$$

As the applied voltage V_{TG} is increased, electrons are sequentially added to the SET island, resulting in the formation of a ladder of electrochemical potential levels. The spacing between these levels is given by

$$E_C = \mu(N) - \mu(N-1), \tag{3.24}$$

$$= \frac{e^2}{2C_\Sigma}. \tag{3.25}$$

The spacing between adjacent electrochemical potential levels in the ladder represents the energetic cost of adding an additional electron to the SET island, referred to as the addition or charging energy, and depends exclusively on the total capacitive coupling experienced by the island.

Figure 3.12 depicts the equidistant ladder of electrochemical potential levels present in the SET island. By applying a voltage difference (bias) between the source and drain, V_{SD}, we can detune the electrochemical potentials of the source and drain (μ_{S} and μ_{D} respectively) from one another. Whether or not a current can flow through the SET island, now depends very sensitively on whether an electrochemical energy level lies in the energy region between μ_{D} and μ_{S}, highlighted in green in Figure 3.12.

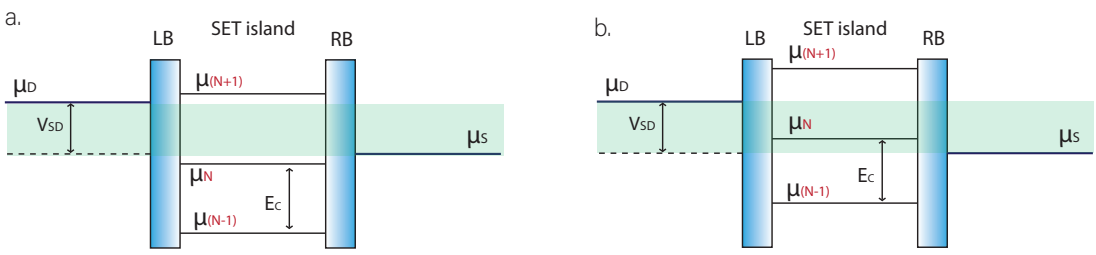

Figure 3.12: **Operation of the SET. a** and **b** both illustrate the electrochemical potential levels in the SET island, with μ_{N+1} representing the energy to add an additional electron to the island. The island is enclosed by two barrier gates, the left barrier gate (LB) and right barrier gate (RB). μ_{D} and μ_{S} represent the drain and source potentials respectively, with the green box highlighting the region between the drain and source level. **a.** The case for which the electrochemical potentials of the island lie outside of the region between the drain and source. This results in tunneling from the drain to the island being prohibited and thus blocking any current from flowing between the source and drain, through the island. **b.** The case for which the electrochemical potential of the island lies in the region between the drain and source and thus an electron can tunnel onto the island from the drain, allowing a current to flow between the source and drain. E_{C} represents the charging energy.

The tunnel coupling between the SET island and the source and drain leads means that if the electrochemical potential of the SET lies within the region, between μ_{D} and μ_{S}, then an electron can tunnel from the drain, onto the island and to the source. If however, the electrochemical potential of the SET lies outside of this region, then tunneling of the electron is prohibited and hence no current will flow between the source and drain. We call this regime of prohibited tunneling through the SET, Coulomb blockade. The capacitive coupling between the island and the TG means that by changing the voltage applied to the TG, we can shift the ladder of electrochemical potentials in the SET island higher or lower in energy. Therefore, by sweeping the voltage applied to the TG, the ladder of electrochemical potentials in the SET will move sequentially through the green highlighted region between the source and drain and thus the SET will move in and out of Coulomb blockade, resulting in peaks in the current running through the SET, as a function of V_{TG}. We call these oscillations in current with sweeping gate voltage, Coulomb oscillations [85].

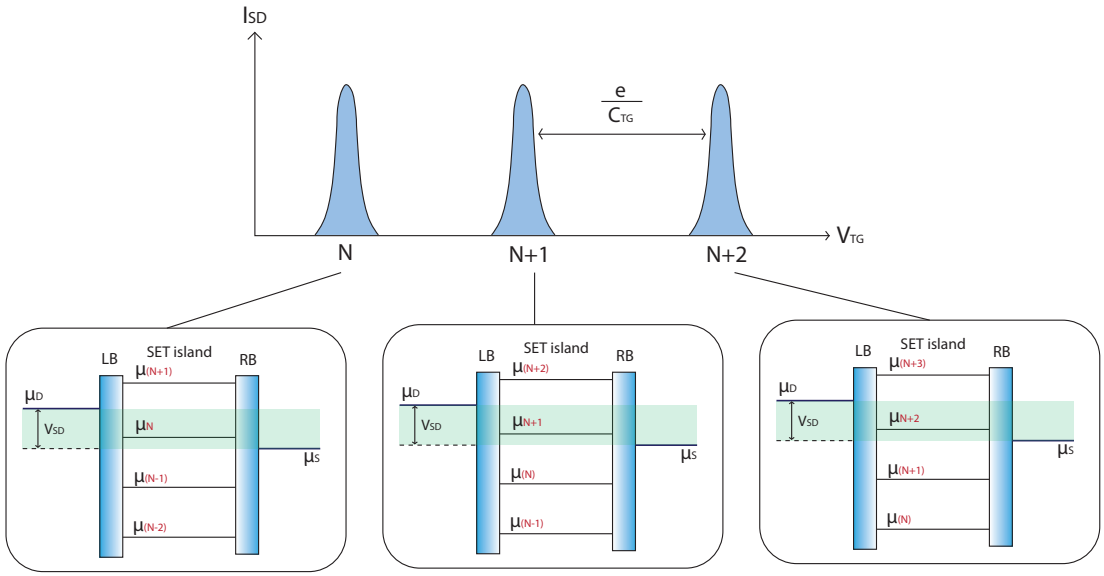

Figure 3.13: **One-dimensional Coulomb oscillations.** Diagram illustrating the current through the SET (I_{SET}) against the voltage applied to the top gate (V_{TG}). As V_{TG} is increased, the electrochemical potential ladder of the SET island is shifted sequentially through the region between the drain and source potentials, as highlighted in the green box. Every time an electrochemical potential level of the island enters this region, current can flow through the SET. When the levels are shifted outside of this region however, the current through the SET is blocked and the SET is in Coulomb blockade. The oscillation of the current in and out of Coulomb blockade with the application of a gate voltage is referred to as Coulomb oscillations.

The concept behind the detection of charge movement in the vicinity of the SET is illustrated in Figure 3.14. The movement of a charge in the vicinity of the SET, results in a shift of $\frac{\Delta q}{e}$ to the levels in the electrochemical potential ladder, where Δq is the charge induced on the SET island. This shift in the electrochemical potential of the SET is known as the charge-transfer signal and its strength depends on a number of factors. If the charge transfer signal is sufficiently large then, upon the movement of charge, the electrochemical potential of the SET can shift from outside the region between the source and drain potentials, to inside this region, resulting in a binary shift between no current flowing through the SET and current flowing through the SET. This binary shift in current through the SET therefore represents a clear indication of the movement of charge in the SET's vicinity.

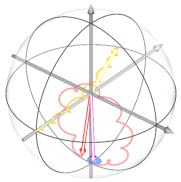

For readout of the donor-bound electron, we selectively remove the electron from the donor, dependent on its spin state, such that we can detect this movement of the electron with the SET [86, 87]. In order to maximise the readout signal of this ionisation event, we fabricate the SET island close enough to the donor, such that the donor electron is tunnel-coupled to the SET island. This results in the donor electron tunneling onto the SET island itself, thereby maximising the resulting shift in the electrochemical potential and thus the change in current through the SET as a result of the ionisation [88]. Figure 3.14 shows the resultant shift in the SET Coulomb peaks as a result of the donor electron tunneling onto the SET island.

In order to convert this charge detection from the ionisation of the donor into information regarding the electron's spin state, we can manipulate the relative positioning between the energy levels of the donor and the electrochemical potential of the SET, such that the tunneling of the donor electron onto the SET island is dependent on its spin state. To do this we can make use of the Zeeman interaction, which splits the energy level of the spin $|\downarrow\rangle$ and spin $|\uparrow\rangle$ states in the presence of a magnetic field. It is important to note that this method of spin readout relies on the fact that the Fermi distribution of the SET is sharp in the energy scale defined by the Zeeman splitting [88], which is discussed in greater depth in section 3.10. For this reason, we operate the donor spin qubit devices at ≈ 20 mK in a dilution refrigerator.

Using local gates that are capacitively coupled to the donor, along with gates capacitively coupled to the SET island, we can manipulate the energy levels of the donor, such that the spin $|\uparrow\rangle$ and spin $|\downarrow\rangle$ energy levels straddle the electrochemical potential of the SET. Consequently, only a spin $|\uparrow\rangle$ electron is able to tunnel onto the SET island, while tunneling of the spin $|\downarrow\rangle$ electron is prohibited. We refer to this point of operation of the gates as the 'read' level. The tunneling of the electron onto the SET island results in the ionised donor nucleus being left with a positive charge, causing a shift in the electrochemical potential, as described above, resulting in the SET being shifted out of Coulomb blockade and hence

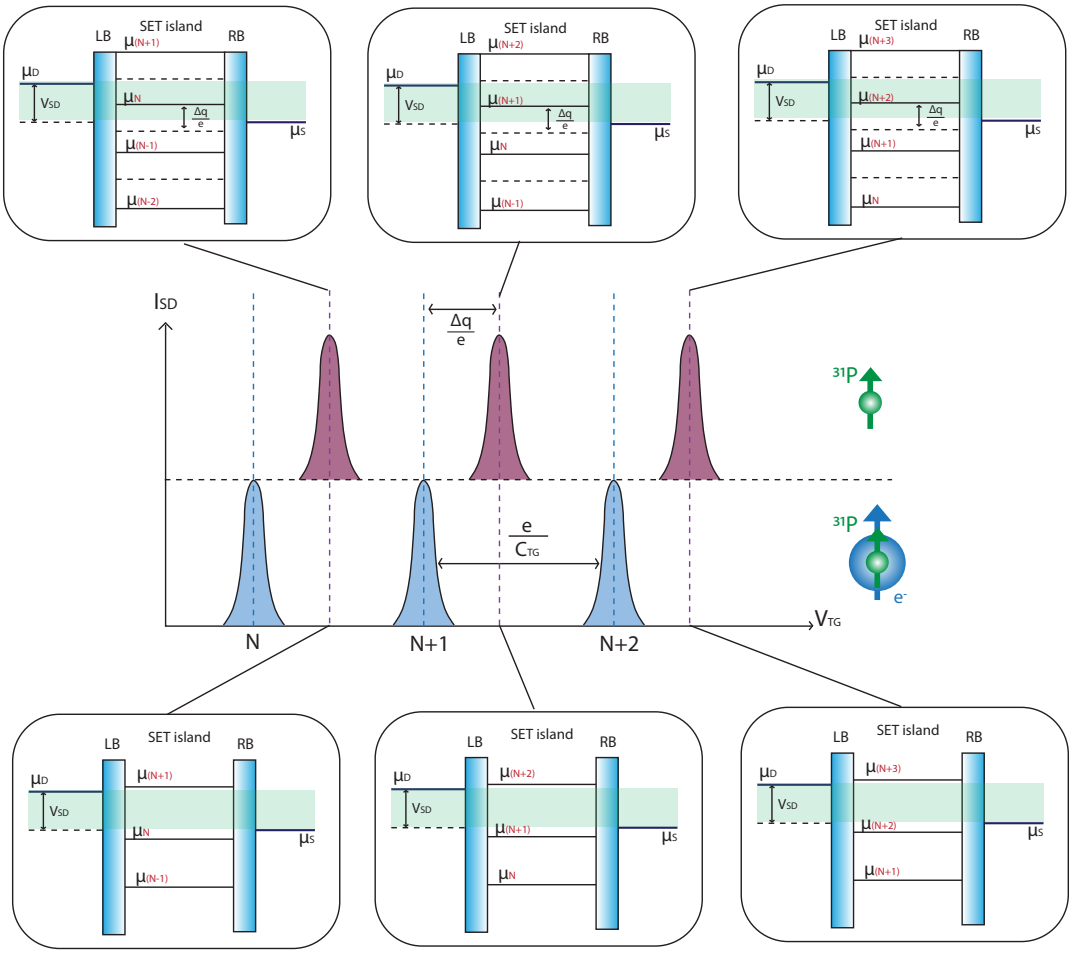

Figure 3.14: **Shift in Coulomb oscillations.** Two plots of Coulomb oscillations for the case of both a neutral and ionised donor atom in the vicinity of the SET. The purple current peaks are artificially offset along the y axis from the blue current peaks, for clarity. The purple and blue peaks are shifted from one another by the charge transfer signal, $\frac{\Delta q}{e}$, where Δq represents the change in charge on the island. The panels surrounding the figure indicate the positioning of the electrochemical potentials of the SET island with respect to the source and drain potentials, μ_S and μ_D.

a current flowing between the source and drain. Conversely, in this configuration, a spin $|\downarrow\rangle$ electron is able to tunnel from the SET island, back onto the donor, while the tunneling of a spin $|\uparrow\rangle$ electron is prohibited. Thus, after some time, a spin $|\downarrow\rangle$ electron will tunnel from the island, back onto the donor, causing the electrochemical potentials of the SET

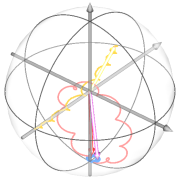

to move back to their original position with respect to the source-drain window, resulting in the SET returning to Coulomb blockade and the current being blocked. The tunneling of a spin $|\uparrow\rangle$ electron can therefore be detected by looking for instances where the current through the SET is high for the duration it takes for a spin $|\downarrow\rangle$ electron to tunnel back onto the donor from the island. We call this a 'blip' of current and it allows us to convert the charge movement of the electron, into the detection of a spin $|\uparrow\rangle$ state. Similarly, the observation of no current blip for the duration of the read period is indicative of the presence of a spin $|\downarrow\rangle$ electron.

Using the same principles as those underpinning the read out of the donor electron, we ionise the donor by manipulating both energy levels of the donor electron above the electrochemical potential of the SET, such that the electron can tunnel onto the island, regardless of its spin state. We refer to the gate voltage at which we enter this regime as the 'empty' level. Moreover, when actively performing operations on the electron, it is important that the electron remain continuously bound to the donor. During operation on the electron, we can therefore manipulate the electron energy levels, such that they both lie below the electrochemical potential of the SET island, prohibiting the electron from tunneling to the island, regardless of its charge state, which we refer to as the 'load' or 'plunge' regime.

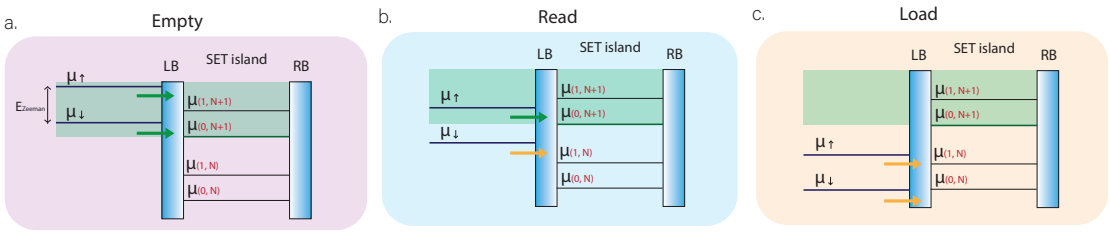

Figure 3.15: **Spin readout with an SET.** Diagram of the spin $|\downarrow\rangle$ and spin $|\uparrow\rangle$ donor electron energy levels, with respect to the electrochemical potential of the SET for the case of the device being at the empty, **a.**, read, **b.**, and load, **c.** position. The green arrows represent the energy levels for which tunneling is allowed, while the orange arrows represent the energy levels for which tunneling is prohibited. For the empty case, the donor electron can tunnel onto the SET island regardless of its spin state. For the read level however, only a spin $|\uparrow\rangle$ electron can tunnel onto the island, while a spin $|\downarrow\rangle$ state is prohibited from tunneling. Conversely, for the load case, both the $|\downarrow\rangle$ and $|\uparrow\rangle$ electron states are prohibited from tunneling onto the island.

The shifts in the electrochemical potential of the SET caused by the tunneling of a donor bound electron to the SET island is most clearly observed by sweeping the voltages applied to two gates in the device and measuring the resulting Coulomb oscillations, as shown in Figure 3.16. By sweeping two gates, we are able to observe the Coulomb oscillations in two-dimensions, with the gradient of the oscillations depending on the relative strength of the capacitive couplings between each gate and the SET island, as discussed in greater depth in section 3.10.3. As with the one-dimensional case, we can observe clear discontinuities in the Coulomb peaks, indicative of the movement of charge in the vicinity of the SET, which results in a shift in the electrochemical potential of the island. Each break in the Coulomb peaks is referred to as a charge transition, with each transition representing a unique movement of charge in the vicinity of the SET.

Further investigation is required in order to identify which of these transitions may be associated with the tunneling of a donor bound electron onto the SET island and which are simply caused by the displacement of charge traps in the vicinity of the SET. The process of distinguishing between these two cases is detailed in section 3.8.

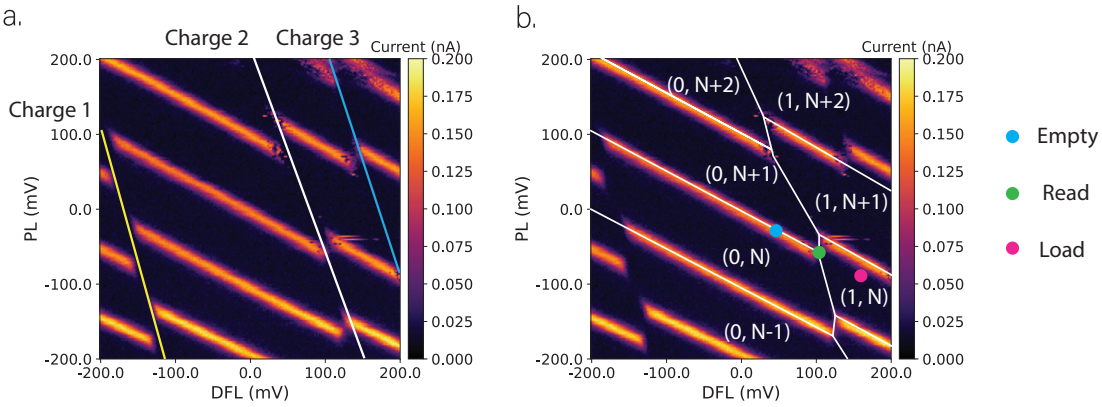

Figure 3.16: **Two-dimensional charge stability diagram.** Plot of Coulomb oscillations through the SET as a function of two gate voltages. The breaks in the Coulomb oscillations represent the movement of charge in the vicinity of the SET island, which shift the electrochemical potential levels of the SET island. **a.** Charge stability map highlighting the different transitions caused by the displacement of charge in the SET vicinity. **b.** Charge stability map highlighting the donor and SET occupation at various locations on the charge stability map, where the labelling (x, y) corresponds to x = donor electron occupancy and y = SET island electron occupancy. The donor electron occupancy of 0(1) represents the ionised (neutral) state of the donor, while the SET island occupancy of N represents the number of additional electrons added to the SET island.

3.7 Device characterisation

After fabricating the qubit devices, there are a number of steps that must be carried out before donor qubit experiments can commence. This process involves first testing that all gates on the device are working correctly, before cooling the device down to milli-kelvin (mK) temperatures in a dilution refrigerator, forming a working SET and ensuring that Coulomb oscillations can be performed with every gate.

3.7.1 Testing at 4K

The fabrication yield of donor qubit devices is not 100% and therefore it is important to carefully screen for working devices upon completion of device fabrication, in order to identify promising candidates for donor spin experiments. Cooling down a device in a

dilution fridge is a time intensive process and thus it is far more time efficient to carry out the preliminary testing of the device functionality at 4.2 K, in a liquid helium dewar. The first test that should be carried out is to assess the functionality of the gates, by determining if there are any current leakage channels within the device. There are a number of different mechanisms through which current leakage can occur in a device however, the primary mechanisms observed are the following:

1. Metallic shorting of the gates. This can occur for example through issues with the device fabrication or the wires used for bonding making contact with one another.
2. Gate to ohmic contact leakage. This is often due to a poor quality oxide layer between the silicon and the aluminium gates.
3. Leakage between the source and drain of the SET. This leakage mechanism is often caused by positive charges trapped in the oxide, which result in a conductive channel of electrons being drawn towards the SiO_2/Si interface, allowing current to flow between the source and drain even with no voltage applied to the top gate.

In order to test for current leakage within the device at 4.2 K, we carry out the following process:

1. Ground all the gates in the device.
2. Connect the gate that we wish to test for leakage to a source measure unit (SMU), which is capable of both sourcing a voltage and measuring a current simultaneously. Unground this gate.
3. Using the SMU, slowly increase the voltage applied to the ungrounded gate, up to the voltage that would typically be applied in experiments. As the voltage applied to this gate is increased, a potential difference is introduced between this gate and the remaining gates at ground.

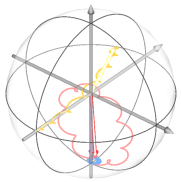

4. Monitor the SMU for any resultant current detected. If the leakage current is low (typically ≈ 20 pA) when the maximum voltage applied to the gate is reached, then this gate is deemed to be free of leakage channels. If however, the current increases above a chosen threshold upon increasing in the gate voltage then this is indicative of leakage from the gate.

5. If the gate is determined to be leaking, then we can attempt to identify which gate it might be leaking to, for diagnostic purposes, by sequentially ungrounding each of the other gates in the device, while continuing to monitor the current with the SMU. If we unground the gate to which our gate of interest is leaking, then we allow the two gates to equalise, removing the voltage differential between them. This results in the elimination of the current flowing from the gate to ground and hence the observation of the current measured by the SMU dropping to 0.

6. These steps are repeated for every gate, until all the gates are either verified to be free of current leakage or the device is deemed unsuitable for donor experiments.

3.7.2 Forming an SET

Once all the gates in a device have been assessed for gate leakage, the next step is to determine if we are able to form a working SET. The first step towards forming an SET is ascertaining if we are able to induce a conductive channel of electrons underneath the top gate, known as a two-dimensional electron gas (2DEG). To do this, all the gates associated with the SET are first ungrounded, namely the top gate, left and right barrier gate and source. A small voltage is applied to the source to produce a source-drain bias potential. An increasing voltage is then simultaneously applied to the top gate and both barrier gates, while the current between the source and drain is monitored. This increasing positive voltage draws electrons towards the SiO_2/Si interface, resulting in a conductive channel of electrons forming at the silicon-oxide interface. When the voltage reaches the value at which this 2DEG continuously connects the source and drain, known as the 'turn-on voltage', a current can flow between the two. This measurement is hence known as a

'turn-on' measurement.

Once a conductive channel has been formed and a current is flowing between the source and drain, we can test if the barrier gates are capable of successfully blocking this conductive channel. For this measurement we typically test each of the barrier gates individually. With voltages applied to the top gate, barrier gates and source-drain bias such that a 2DEG is present between the source and drain, we then ramp the voltage applied to one of the barriers to more negative voltages while monitoring the current between the source and drain. As the barrier gate becomes more negative in voltage, it begins to repel electrons from the 2DEG beneath it and thus breaks the conductive channel between the source and drain, resulting in the observation of the current dropping to zero below a certain barrier voltage. We call this measurement 'pinch-off' as we are pinching off the current between the source and drain contacts. We can then ramp this barrier back to the turn on voltage regime and repeat this process with the other barrier.

After a successful turn on and pinch-off measurement, we can once again return the voltages to the turn-on regime, before ramping both barriers together to more negative voltages, thus repelling the 2DEG from underneath both the barriers simultanelously. Once the current between the source and drain has been pinched off by both barriers, we are left with a small reservoir of electrons underneath the TG, between the two barrier gates, thus forming our SET island.

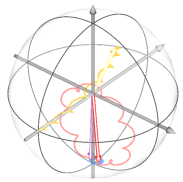

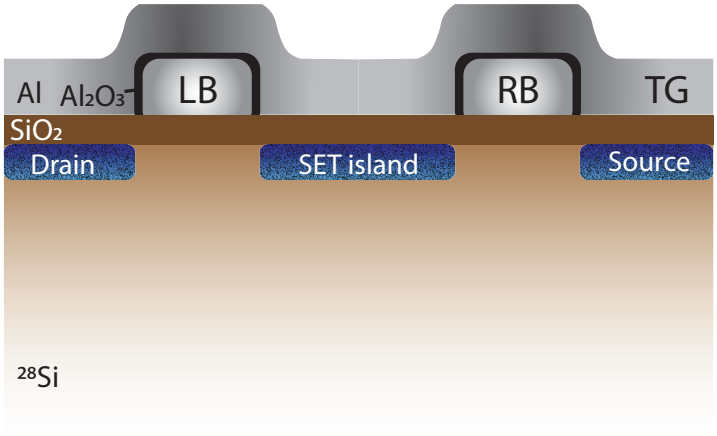

Figure 3.17: **Working SET.** Depiction of the 2DEG after the formation of a working SET, with the 2DEG repelled from underneath the barrier gates, in order to form a reservoir of electrons between the two, which we use as our SET island.

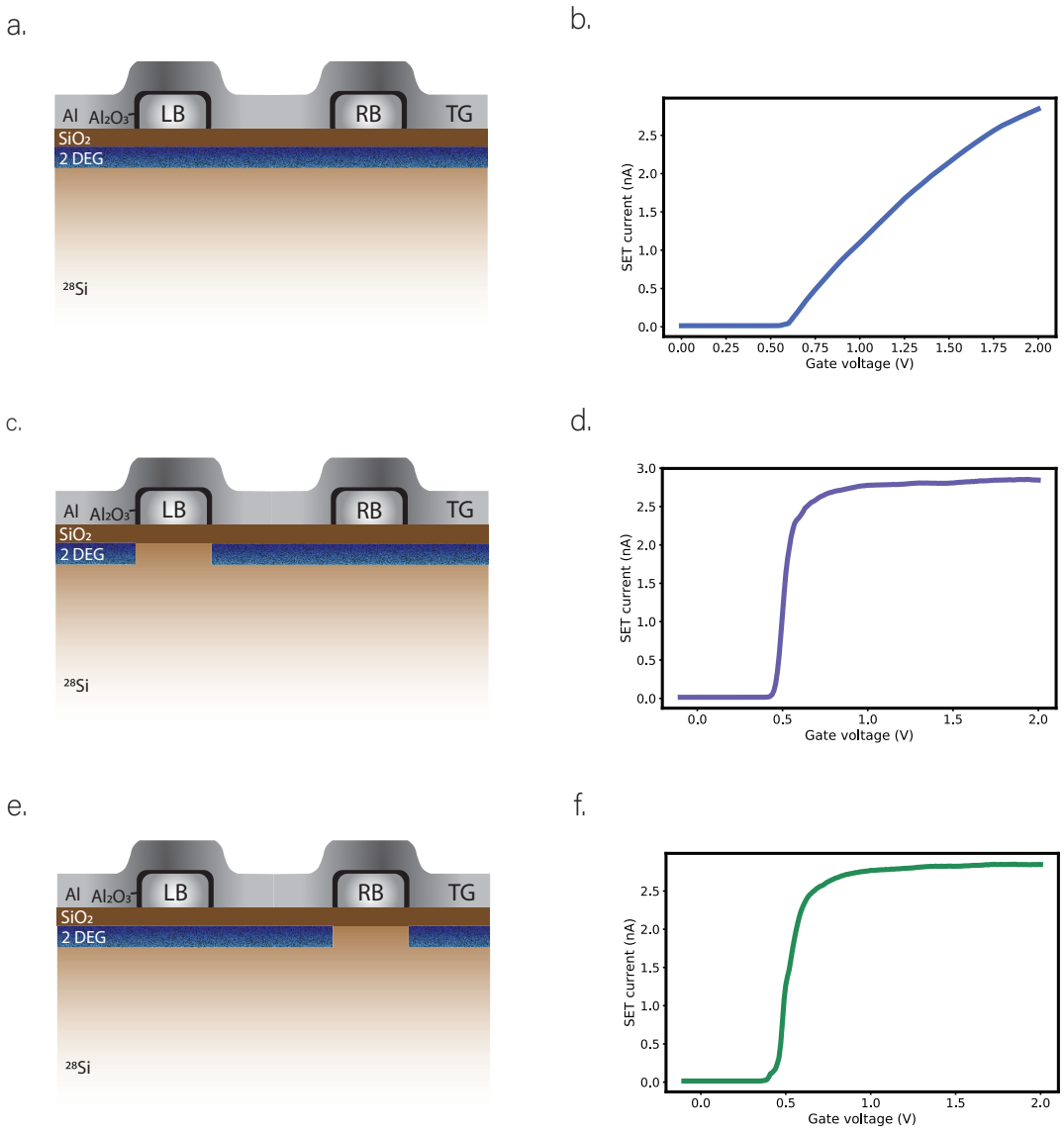

Figure 3.18: **Device turn on and pinch off. a.** Device schematic during a turn on measurement. In this measurement the voltages of the top gate (TG), LB and RB are swept simultaneously, until turn on voltage is reached, at which point a 2DEG is formed, forming a conductive channel between the source and drain. **b.** Turn on measurement, showing a current flowing through the SET once the turn on voltage is reached. **c.** Device schematic during a pinch-off measurement of the left barrier (LB). In this measurement the two-dimensional electron gas (2DEG) is depleted from underneath the LB.**d.** Pinch-off measurement of the left barrier, showing the SET current being cut off below the pinch-off voltage applied to LB. **e.** Device schematic during a pinch-off measurement of the right barrier (RB). In this measurement the 2DEG is depleted from underneath the RB. **f.** Pinch-off measurement of the right barrier, showing the SET current being cut off below the pinch-off voltage applied to RB. The measurements in **b,d,f** were performed by Dr Danielle Holmes at the University of New South Wales, with a source-drain bias of 1 mV.

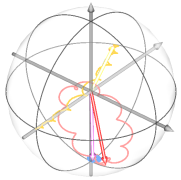

3.8 Donor search

Once the functionality of the device gates have been verified at 4K, the device can be cooled to $\approx$ 20 mK in a dilution fridge and the search for a donor atom can commence.

After forming an SET, we can sweep the voltages on pairs of gates to obtain Coulomb oscillations in the SET current. As stated previously, any breaks in these oscillations represent the movement of charge in the vicinity and can be investigated as a potential donor transition. The number of donor transitions present in the device will depend on the donor implantation parameters chosen and thus the number of addressable donors in the vicinity of the SET island. Although the exact pattern of Coulomb peaks can vary between instances of warming to room temperature and cooling it back down to mK temperature (referred to as a thermal cycle), the slope of the charge transitions through the Coulomb peaks forms a unique fingerprint for each device, as this gradient is dictated by the capacitive coupling between the SET and the charge responsible for the transition. The slope of a transition can therefore be used as a method of identifying key transitions in a device through multiple cooldowns. Figure 3.19 shows a series of Coulomb oscillations taken before and after a thermal cycle of the device in a dilution fridge. Although the maps show significant changes between thermal cycles, the gradient of the charge transitions (i.e. the breaks in the Coulomb peaks) remain constant between each cooldown.

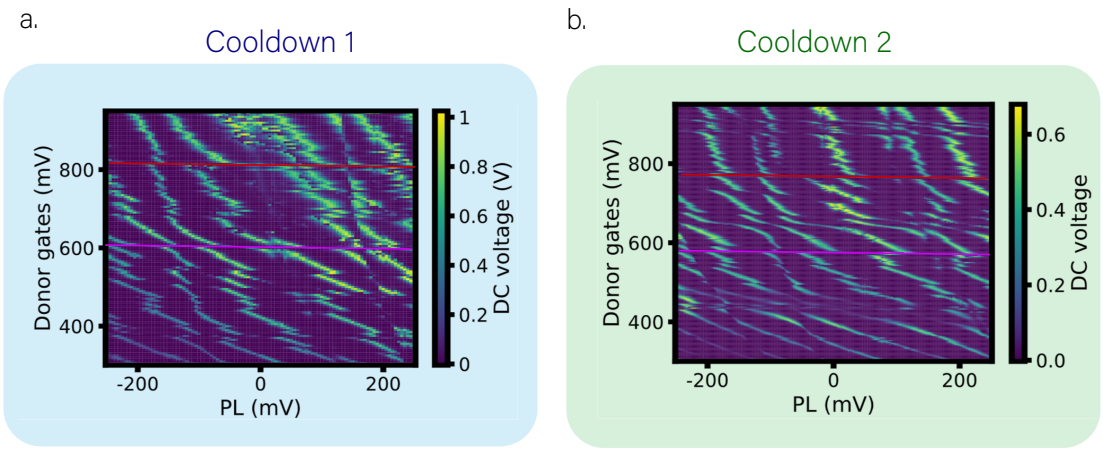

Figure 3.19: **Charge stability map across cooldowns.** Coulomb oscillations on the same device carried out before, **a.**, and after, **b.**, a thermal cycle of the device from mK temperaures to room temperature and back to mK. The two red lines in both **a.** and **b.** are of the same slope, which is an indication that the transitions covered by the red line belong to the same charge transition. Similarly the purple lines in both **a.** and **b.** are of the same slope, indicating that this transition belongs to the same charge transition.

3.8.0.1 Distinguishing a donor from a charge trap

Before discussing the methods by which we can distinguish a donor transition from that of a charge trap, it is pertinent to briefly comment on the physical mechanism behind the origin of charge traps in these devices. One of the most common source of defects in these devices are dangling-bond (DB) defects that occur at the Si/SiO_2 interface, usually as a result of an oxygen deficiency at the interface [89]. These DBs typically occupy a range of energy levels that span the entire semiconductor band gap. When the DB energy level falls within an energy range k_BT of the interface Fermi level, then it can act as a trapping centre for interface electrons. Additionally, DBs can couple to structural defects in the silicon, associated with a local reordering of the atomic positions of a non-crystalline material. These structural defects act as tunneling two-level systems. The random switching of these two-level fluctuators introduces a source of charge noise, in the environment of the donor spin. When averaging over many two-level fluctuators, each switching randomly, the resultant charge noise has a characteristic $\frac{1}{f}$ behaviour. This tunneling of electrons

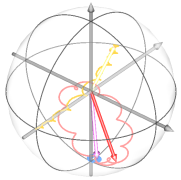

as a function of gate voltage, either between neighbouring defects or between defects and the SET island also results in charge transitions observed in the Coulomb oscillations of the SET [89, 90].

In order to investigate an individual transition, the gate voltages, identified from the 2D gate sweep, are focused to a particular transition and Coulomb peak in gate space. Figure 3.20 shows a focused gate sweep around a given charge transition, representing the ionisation of a donor atom, with the the gate regions corresponding to the neutral and ionised donor state highlighted in blue and green respectively. Although any region above or below the transition could be chosen as our load/empty region of gate space, voltages are typically chosen that lie on the slope of the Coulomb peak as shown in Figure 3.20. We refer to this mode of operation as 'compensated' loading or emptying of the donor, because we typically use one gate to move above or below the transition in gate space and another gate to compensate for this movement, such that we always stay on the slope of the Coulomb peak. Although not strictly necessary, this compensation ensures that the SET electrochemical potential is kept constant, while the donor potential is being moved up or down. In the quantum dot community, this mode of operation is often referred to as a 'virtual gate' [91].

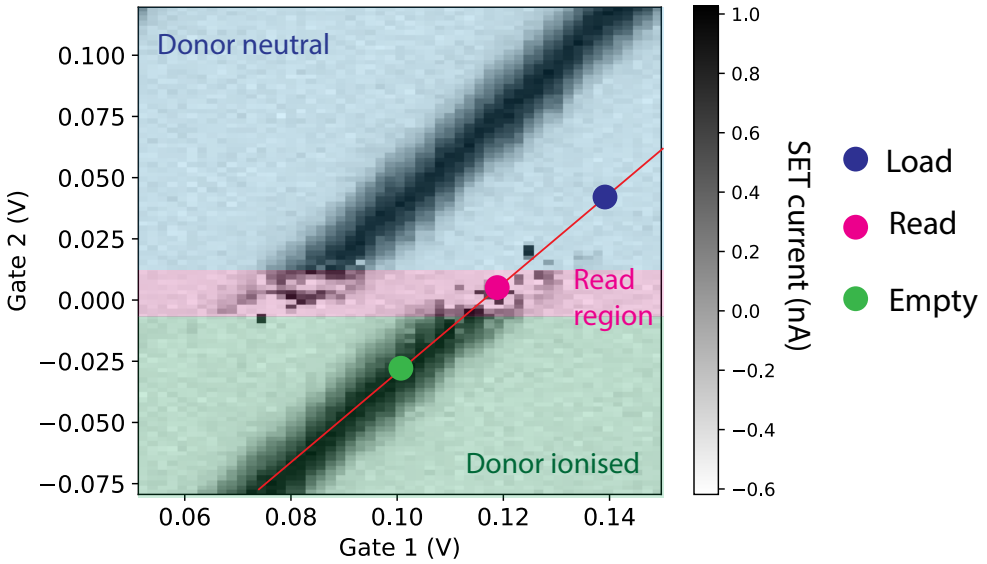

Figure 3.20: **Donor charge transition.** Region of donor operation in gate space, showing the empty, load and read points for the donor. The dark grey stripes represent the Coulomb peaks, with the break in this peak originating from the donor charge transition. The blue region represents the gate space for which the donor is neutral, while the green region represents the gate voltages for which the donor is ionised. Red line indicates the direction along which the voltages are swept between the load, read and empty position when sweeping in a compensated mode. The slope of this red line matches the slope of the Coulomb peak.

In order to distinguish whether a transition such as the one shown in Figure 3.20 belongs to a donor atom or to the discharging of charge from a defect in the lattice, we can perform a T_1 measurement to measure the relaxation time of the spin associated with the charge transition. The typical relaxation time of a donor electron is of order 1 s, compared to of order a few μs for a charge trap [89,92]. The relaxation time is therefore a clear indication of the nature of the transition. If the transition belongs to a charge trap, then we can continue exploring gate space for a more favourable transition.

In a typical donor experiment, the relaxation time is measured by initialising the electron spin into a spin $|\downarrow\rangle$ state, applying an oscillating B_1 field for the duration required to flip

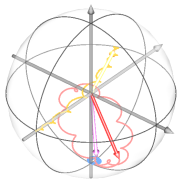

the spin into the $|\uparrow\rangle$ state and then sweeping the wait duration before reading out the state of the spin. This process however, relies on the ability to invert the spin from the $|\downarrow\rangle$ to the $|\uparrow\rangle$ state and thus the knowledge of the resonance frequencies of the system. If however, we are still in the process of identifying if this transition belongs to a donor, than these frequencies are unknown to us. In this case, we can measure the relaxation time, by setting the voltages to the load point in order to randomly load a spin $|\downarrow\rangle$ or $|\uparrow\rangle$ electron onto the donor, and then sweeping the wait time before reading the electron. As a result of the multiple repetitions of this sequence necessary to gain statistics, this method thus results in a spin up proportion of ≈ 0.5 being observed at the beginning of the wait time, with the spin up proportion decaying to 0 as the spin relaxes.

3.9 Control and readout of the electron spin

3.9.1 Adiabatic electron spin resonance (ESR)

Immediately upon the discovery of a donor transition, a number of key donor parameters, namely the resonance frequencies and π pulse durations of the electron and nuclear spin, are unknown to us. This makes the search for the resonance frequencies somewhat difficult when first calibrating the donor. To make this process easier, we use a method of spin inversion that is agnostic to the exact duration or resonance frequency of the applied pulse. This technique is known as adiabatic electron spin resonance (adiabatic ESR) [93].

The process of adiabatic ESR involves applying an oscillating B_1 pulse to the spin, which is swept in frequency from a frequency that is negatively detuned from the resonance frequency, to a frequency that is positively detuned from the resonance frequency. The exact duration of the pulse, and hence the rate at which this frequency is swept is not important, as long as the sweeping rate of the pulse frequency meets the following requirement

$$\frac{\partial}{\partial t}\Delta\nu \ll \nu_R^2, \tag{3.26}$$

where $\frac{\partial}{\partial t}\Delta\nu$ is the frequency sweep rate in units of s^{-2} and ν_R is the Rabi frequency of

the spin [93]. Similarly, the exact frequency range of the frequency sweep is not important, provided that the range is large enough, such that the frequency sweep starts and ends highly detuned (i.e. the detuning is much larger than the Rabi frequency) from the resonance frequency of the spin, as shown in Figure 3.21.

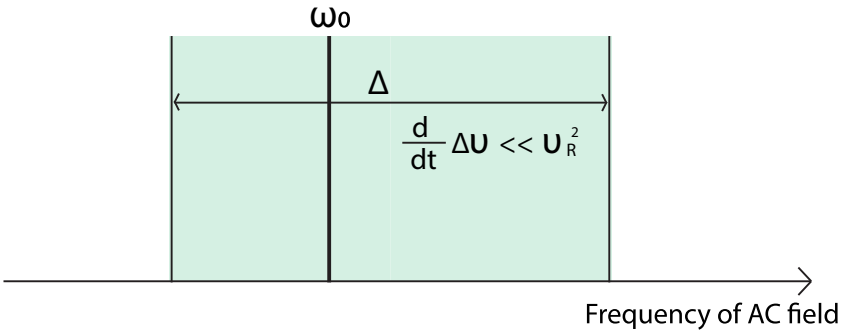

Figure 3.21: **Adiabatic frequency sweeping.** Diagram showing the sweeping of the AC magnetic field used to adiabatically invert the spin. The frequency of the AC field sweeps a range of Δ about the resonance frequency, ω_0. The asymmetry of the sweep about the resonance frequency is representative of the fact that the resonance frequency does not have to lie in the centre of the adiabatic frequency sweep in order to be successfully inverted by the adiabatic pulse, provided that the adiabatic frequency sweep begins and ends at sufficient frequency detuning from ω_0. This makes adiabatic frequency sweeps a useful tool for inverting the spin without requiring knowledge of the exact resonance frequency of the system, for example when finding the resonance frequencies for the first time or when noise in the environment causes the resonance frequency of the spin to change frequently. In order to adiabatically invert the spin the sweep rate $\frac{d}{dt}\Delta$ must be much smaller than ν_{R}^2.

If the spin is initialised in the $|\downarrow\rangle$ state then, when the field is highly detuned from the resonance frequency, this state represents an eigenstate of the system and thus the spin remains stationary. As we slowly sweep the frequency of the B_1 field however, towards the resonance frequency of the spin, then the detuning along the z-axis of the Bloch sphere becomes gradually smaller, while the B_1 along the xy plane remains the same magnitude. Thus the vector sum between the two fields results in the effective field experienced by the spin pointing further away from the -z-axis and hence this field gradually moves around the Bloch sphere, as the frequency detuning decreases. If this change in the direction of

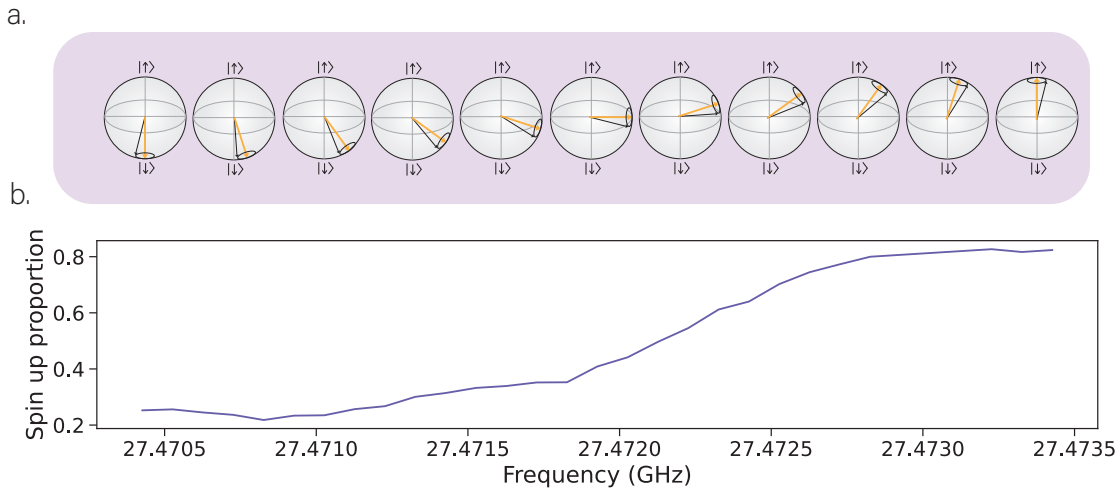

Figure 3.22: **Adiabatic inversion. a.** Bloch sphere of the spin, with the yellow line representing the effective field experienced by the field (calculated with the vector sum between the Rabi frequency of the spin and the frequency detuning of the B_1 field) and the black line representing the spin state. As the detuning of the applied B_1 field is swept, the effective field slowly moves around the Bloch sphere. As the change in the instantaneous eigenstate of the Hamiltonian is gradual, the spin follows the instantaneous eigenstate around the Bloch sphere. **b.** The resultant spin up proportion of the spin.

the field is gradual enough, then the effective field will only be displaced very subtly from its previous position and hence the instantaneous eigenstate of the Hamiltonian will only change very subtly. If this change is slow enough compared to the precession frequency of the spin, caused by the small deviation of the instantaneous eigenstate of the system from the spin's state, then the spin will undergo a small precession about the new eigenstate and thus follow the field around the Bloch sphere. This movement of the spin around the Bloch sphere, following the instantaneous eigenstate of the system, is shown in Figure 3.22. Adiabatic ESR is thus a very helpful tool for donor calibration, as it allows us to invert the spin without knowledge of its exact resonance frequency or π pulse duration.

Although adiabatic ESR can be performed without knowledge of the exact resonance frequency or Rabi frequency of the spin, it is important to select the frequency range and duration of the adiabatic pulse such that it remains adiabatic in nature. Figure 3.23 shows

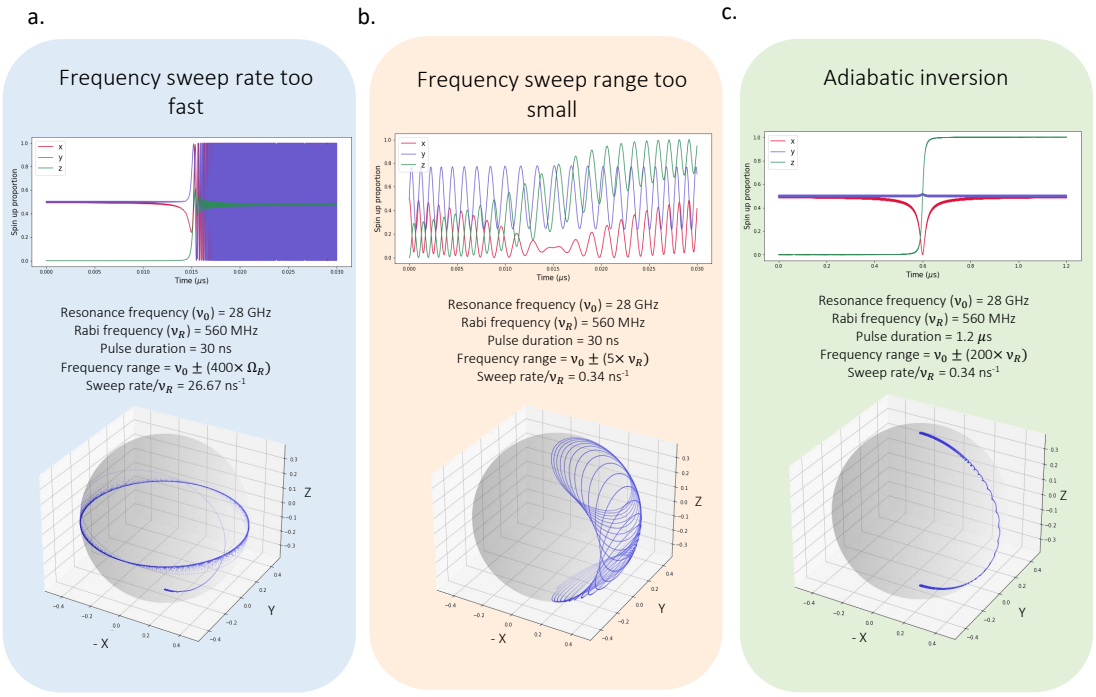

Figure 3.23: **Adiabatic inversion simulation.** Three separate simulations of driving the state of an electron spin initialised in the $|\downarrow\rangle$ state. In order to adiabatically invert the spin, the sweep rate must be sufficiently slower than the Rabi frequency of the spin. We therefore simulate the adiabatic inversion with: a too fast sweep rate, **a.**, a too small sweep range, **b.**, and with the correct parameters, **c.**. Note that the Rabi frequency used in these simulations is much faster than the Rabi frequencies achieved experimentally for the electron spin ($\approx$ 1 MHz) in order to reduce the time required for the simulations.

a simulation of the adiabatic inversion of the spin for three distinct cases: the case in which the frequency ramp rate of the adiabatic pulse is too fast, the case in which the frequency sweep range is too small and the case for which the frequency ramp rate and range are sufficient to adiabatically invert the spin.

If the frequency sweep rate is too fast, then the physical implication of this is that the instantaneous eigenstate of the spin moves too quickly across the Bloch sphere. This means that the spin is not able to follow the direction of the effective field, as it is traversing

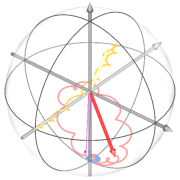

the Bloch sphere much faster than the spin is able to precess about it. Thus, the field direction becomes far displaced from the spin direction on the Bloch sphere, mimicking the conditions of coherent ESR and thus the inversion is no longer adiabatic in nature.

Moreover, if the frequency range of the adiabatic sweep is not sufficiently large, then the field does not start highly detuned from the resonance frequency. The physical implication of this is that the eigenstate of the system does not begin the adiabatic inversion aligned with the state of the spin. This results in the spin traversing larger precession cones around the Bloch sphere as it follows the instantaneous eigenstate of the system. If these become too large, then the drive once again loses its adiabatic nature and mimics coherent drive instead.

If however, the frequency range and sweep rate are sufficient for adiabatic inversion, then the spin will be dragged around the Bloch sphere with the applied field. In order to find the resonance frequencies of the donor electron we therefore apply adiabatic pulses (where the frequency of the pulse is swept over an intelligently chosen range and duration), while also sweeping the centre frequency of the adiabatic pulse about the frequencies we expect the resonances to occur, given the strength of the static B_0 field. This should result in peaks observed in the spin up proportion of the electron, indicating that the adiabatic pulse has inverted the electron spin.

3.9.2 Coherent ESR

After the approximate electron spin resonance (ESR) resonance frequencies have been found adiabatically, we can proceed with performing coherent ESR. Coherent ESR is important to demonstrate, as it facilitates the preparation of any arbitrary state of the electron spin on the Bloch sphere. In order to obtain coherent ESR we must calibrate the frequency and duration of our applied B_1 field, such that upon the application of a π pulse, the spin performs a 180^o rotation on the Bloch sphere.

3.9.2.1 Calibrating resonance frequencies

After obtaining the approximate resonance frequencies of the electron spin adiabatically, we can obtain the resonance frequencies of the spin more accurately using coherent ESR, by first initialising the electron into the $|\downarrow\rangle$ state, before sweeping the frequency of an applied B_1 pulse about the resonances found with adiabatic ESR. As the correct π pulse duration is initially unknown to us, we can begin by applying the pulse for some reasonably chosen duration, the value of which will depend on the pulse power. When the frequency of the B_1 field reaches the active resonance frequency of the spin, a peak in the spin up proportion will be observed, the fitting of which will return the centre frequency of this resonance.

The linewidth of a power broadened resonance peak can be understood by studying the component of the Rabi flopping formula that governs the amplitude of the Rabi oscillations

$$A = \frac{\nu_R^2}{(\nu_R^2 + \Delta^2)}, \tag{3.27}$$

where ν_R is the Rabi frequency and Δ is the frequency detuning between the resonance frequency of the spin and the frequency of the B_1 field. Plotting the amplitude, A, as a function of the frequency detuning, Δ, results in a Lorenzian lineshape with a full-width at half-maximum of $2\nu_R$ [94]. Consequently, by applying a lower power B_1 field, the amplitude of the Rabi oscillations is decreased, along with the linewidth of the resonance peaks. In order to more accurately determine the ESR resonance frequencies, we can therefore lower the power of the driving field B_1, such that the centre frequency of the resonance peak can be more accurately determined. Experimental data showing the linewidth of an ESR resonance peak as a function of B_1 power is shown in Figure 3.24. The minimum linewidth of a resonance peak, is given by the intrinsic linewidth, which depends on the coherence time T_2^* of the spin.

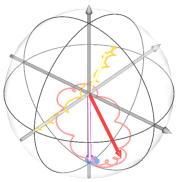

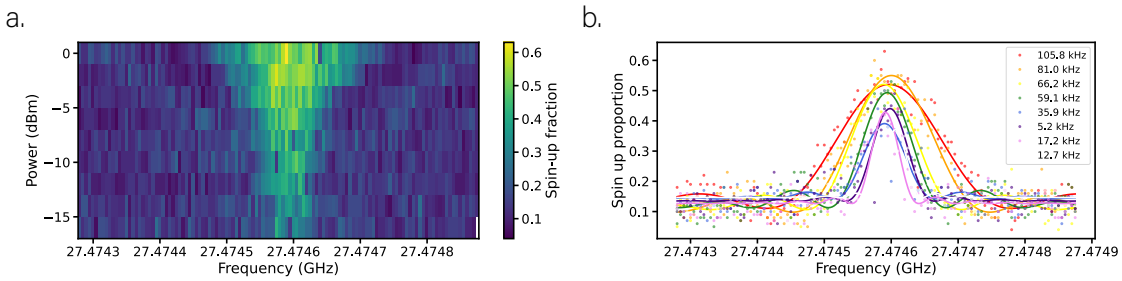

Figure 3.24: **Power broadening. a.** ESR frequency spectra as a function of B_1 power along the y-axis. Each spectrum is performed by sweeping the frequency of an oscillating B_1 field and measuring the resulting spin-up proportion. A peak in spin up proportion is observed when the B_1 field frequency is equal to the resonance frequency of the spin, as explained in section 2.4. **b.** Each individual ESR frequency spectra from **a.** plotted on top of one another. The frequency spectrum for each value of B_1 power is fit with a Lorentzian, with the resulting linewidth extracted from each fit stated in the legend.

3.9.2.2 Calibrating pulse duration

In order to calibrate the duration of the π pulse used to coherently invert the spin between the $|\downarrow\rangle$ and $|\uparrow\rangle$ states, a Rabi measurement is performed. This measurement involves first initialising the spin in the $|\downarrow\rangle$ state, before applying an oscillating B_1 field at the resonance frequency, while sweeping the duration for which this pulse is applied. In the absence of state preparation and measurement (SPAM) error, as a function of pulse duration, we should observe the up proportion of the spin to oscillate between 0 and 1 as the spin rotates between the $\pm$ z poles of the Bloch sphere. In practice however, SPAM error will reduce the amplitude of our Rabi oscillations. An example Rabi oscillation is shown in Figure 3.26. As discussed in section 2.7, the frequency of the Rabi oscillation is given by

$$\nu_R^{\text{eff}} = \sqrt{\nu_R^2 + \Delta^2}. \tag{3.28}$$

The frequency of the measured Rabi oscillation, ν_R^{eff} thus depends on the frequency detuning of the B_1 field from the resonance frequency of the spin. For $\Delta = 0$, $\nu_R^{\text{eff}} = \nu_R$ and therefore, it is important to ensure that the frequency of the applied B_1 field is exactly on resonance when performing a Rabi measurement in order to attain an accurate calibration

of the π pulse time required to fully rotate the spin between the $|\downarrow\rangle$ and $|\uparrow\rangle$ state, for a given B_1 power.

3.9.3 Electron readout

As discussed in depth in section 3.6, the state of the donor electron is read out via spin dependent tunnelling to the SET island. Upon the tunnelling of a spin $|\uparrow\rangle$ electron from the donor onto the SET island, the SET is shifted out of Coulomb blockade, and thus current flows through the SET. Conversely, when a $|\downarrow\rangle$ electron tunnels back onto the donor from the SET island, the SET is shifted back into Coulomb blockade and thus the current through the SET is blocked. This thus results in a 'blip' of current appearing through the SET as the SET is shifted out and in of Coulomb blockade through the ionisation event. In order to detect this blip of current, we can set a value of 'threshold current'. If the SET current rises above this value during the read period, we determine the electron to be in the spin $|\uparrow\rangle$ state, whereas if the SET current remains below this threshold for the read duration, we determine the electron to be in the spin $|\downarrow\rangle$ state. Figure 3.25 shows an example readout current trace following the preparation of a spin $|\uparrow\rangle$ electron by initialising the electron in the $|\downarrow\rangle$ state and then inverting the spin with an adiabatic pulse (Fig.3.25, **a**) or the preparation of a spin $|\downarrow\rangle$ electron,(Fig.3.25, **b**) via spin-dependant tunneling from the SET to the donor. For the case of the spin $|\downarrow\rangle$ electron, the SET current remains below the threshold current for the duration of the read period. For the case of the spin $|\uparrow\rangle$ electron on the other hand, the current rises above the threshold current indicating that the electron has tunnelled onto the SET island, leaving behind an ionised donor nucleus. The SET current then falls below the threshold current after the time taken for another electron to tunnel back onto the donor from the SET.

The threshold current can either be determined statically, by manually selecting a value of threshold current in advance based on observation of the SET current trace, or dynamically, where a threshold current is determined for each readout automatically. This is done by plotting a histogram of the SET current for each readout trace. In the presence of current blips this should result in two histograms, with one histogram centered about the

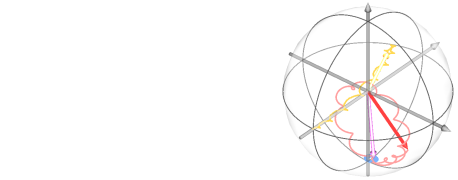

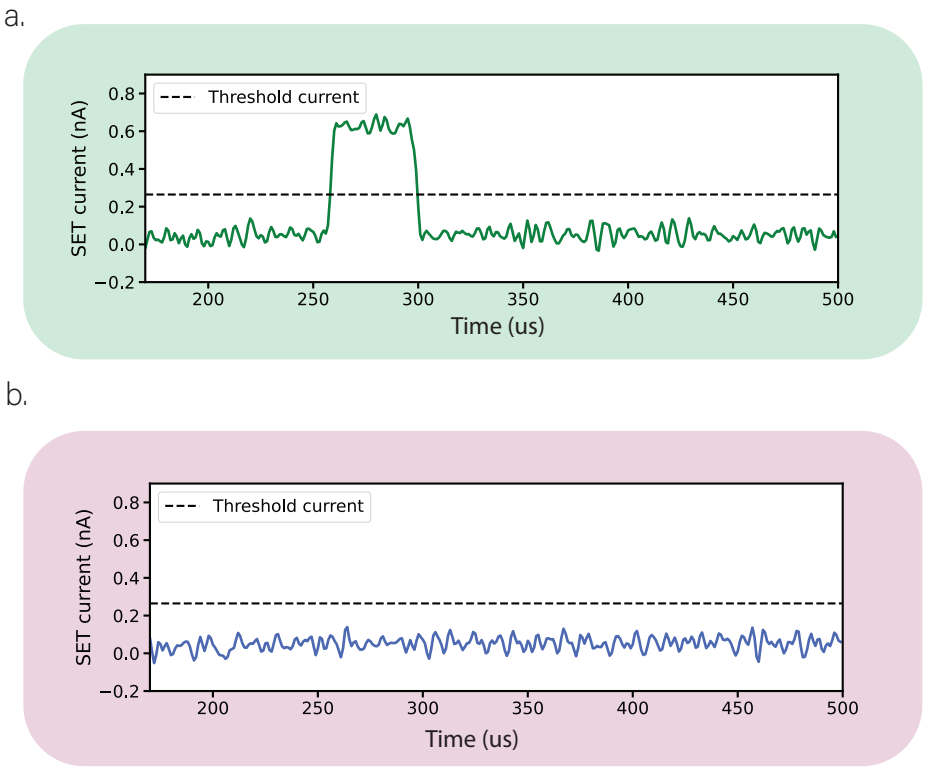

Figure 3.25: **SET current traces. a.** Example readout current trace following the preparation of a spin $|\uparrow\rangle$ state electron. The $|\uparrow\rangle$ electron tunnels from the donor onto the SET, before a spin $|\downarrow\rangle$ electron tunnels from the SET to the donor to take its place. This is indicated by the blip of current in the readout trace, whereby the current rises above the threshold current for the duration of time it takes for a spin $|\downarrow\rangle$ electron to tunnel from the SET to the donor. **b.** Example readout current trace following the preparation of a spin $|\downarrow\rangle$ state electron. As the electron is in the $|\downarrow\rangle$ state it is prohibited from tunnelling from the donor to the SET island, resulting in no blip of current being observed, as indicated by the current remaining below the threshold current for the duration of the readout period. Note that these current traces show a zoomed in region of the total read duration in order to better observe the current blip. The nominal duration of the readout period is ≈ 1 ms (depending on tunnel times of the donor).

mean background current of the SET, $\bar{I}_{\text{low}}$ and the other centred around the mean high current caused by the current blips, $\bar{I}_{\text{high}}$. Fitting the histograms to determine $\bar{I}_{\text{low}}$ and $\bar{I}_{\text{high}}$, the current threshold is then determined with either of the two following formula

$$I_{\text{threshold}} = \bar{I}_{\text{low}} + 5\sigma_I, \tag{3.29}$$

$$I_{\text{threshold}} = \bar{I}_{\text{high}} - 5\sigma_I, \tag{3.30}$$

where σ_I represents the standard deviation of the current trace. Dynamically choosing the threshold current has the advantage of being robust against changes in the background current of the SET, which is in turn dictated by the noise in the device. Dynamical threshold current selection, using equation 3.29, is therefore the method used for readout in the entirety of experiments discussed in this thesis.

As each readout trace only gives a single bit of information, namely a 0 if the electron is found to be in the $|\downarrow\rangle$ state and a 1 if the electron is found to be in the $|\uparrow\rangle$ state, we must repeat each pulse sequence and readout many times, in order to gain information regarding the nature of an electron superposition state. This allows us to obtain the spin up proportion, given by the formula

$$P_{\text{up prop}} = \frac{N_{\uparrow}}{N_{\text{total}}}, \tag{3.31}$$

where $N_{\uparrow}$ are the number of readout traces for which a blip of current indicating a spin $|\uparrow\rangle$ electron was detected and N_{total} is the total number of readout traces.

Figure 3.26 shows the readout window for 30 repetitions of a pulse sequence, taken at different points on a Rabi oscillation. When the spin is at the minima of the Rabi oscillation, i.e. in the $|\downarrow\rangle$ state then very few readout repetitions show a blip of current. The number of blips at the minima of the Rabi oscillation is not zero due to the thermal broadening of the SET Fermi distribution, which can lead to errors in electron initialisation and readout, as discussed in greater depth in section 3.10. The number of blips observed in the readout repetitions increases as the spin rotates around the Bloch sphere to the $|\uparrow\rangle$ state, corresponding to an increase in the spin up proportion measured.

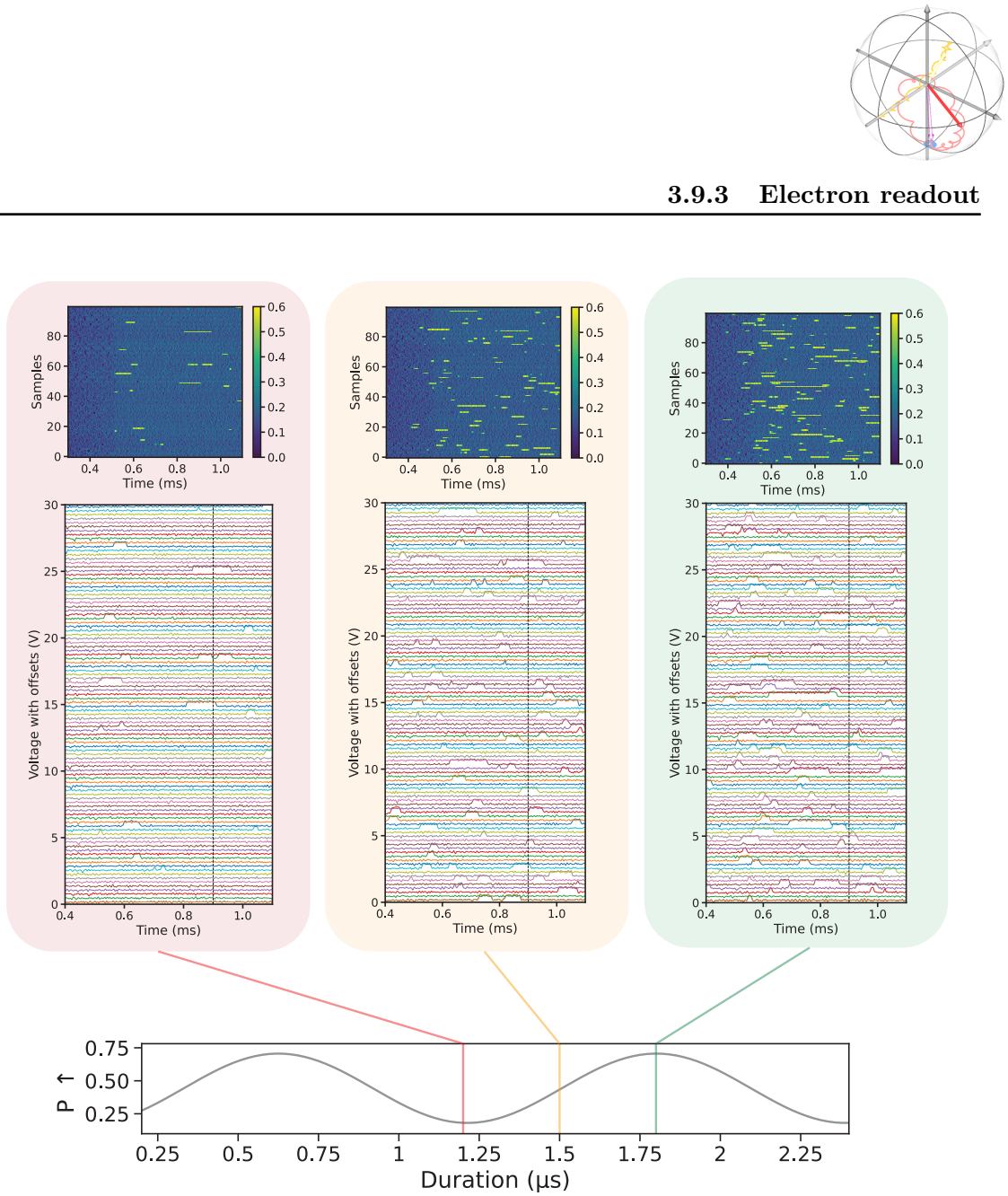

Figure 3.26: **Rabi oscillations with SET traces.** The bottom plot shows a fit to a measured Rabi oscillation on an electron. Each point on the Rabi oscillation was measured 100 times, with the readout period from 30 of these repetitions shown in the top plots. These readout traces were taken at the minima (red), maxima (green) and half way in between the two (yellow) points on the Rabi oscillation. The black dashed, vertical line in the readout traces shows the read time, before which the detection of a current blip is counted as a spin $|\uparrow\rangle$ electron. After this time, the wait time becomes comparable to the tunnel time of a spin $|\downarrow\rangle$ electron, and thus the detection of a current blip may also indicate the presence of a spin $|\downarrow\rangle$ electron. Current blips are therefore not counted after this time.

3.10 Electron readout contrast optimisation

For the construction of a scalable quantum processor, error correction schemes demand not only that the quantum operations are performed reliably with high fidelity (greater than the error correcting threshold) but, also that the infidelity associated with initialisation and readout of the qubits remains sufficiently low ($< 1\%$) [95]. It is therefore of great importance that the qubit readout and initialisation fidelity is maximised. For the case of the electron, the readout fidelity can be maximised by carefully tuning the electrostatic environment of the donor with respect to the SET, such that the electron readout contrast is optimised.

3.10.1 Readout contrast

The readout contrast of the electron spans between 0 and 1, and refers to the ability to correctly distinguish the presence of a spin $|\downarrow\rangle$ electron from the presence of a spin $|\uparrow\rangle$ electron during readout. Denoting the probability of a spin $|\uparrow\rangle$ or spin $|\downarrow\rangle$ electron tunnelling off of the donor, onto the SET island within the read duration, t_{read}, as $P_{|\uparrow\rangle}(t_{\text{read}})$ and $P_{|\downarrow\rangle}(t_{\text{read}})$ respectively, the readout contrast can be defined as

$$C(t_{\text{read}}) = P_{|\uparrow\rangle}(t_{\text{read}}) - P_{|\downarrow\rangle}(t_{\text{read}}), \tag{3.32}$$

$$= -\exp\left(-\frac{t_{\text{read}}}{\tau_{|\uparrow\rangle\rightarrow\text{SET}}}\right) + \exp\left(-\frac{t_{\text{read}}}{\tau_{|\downarrow\rangle\rightarrow\text{SET}}}\right), \tag{3.33}$$

where $\tau_{|\downarrow\rangle\rightarrow\text{SET}}$ and $\tau_{|\uparrow\rangle\rightarrow\text{SET}}$ are the tunnel times of a spin $|\downarrow\rangle$ and spin $|\uparrow\rangle$ electron from the donor, onto the SET island. The tunnel time $\tau_{|\downarrow\rangle\rightarrow\text{SET}}$ depends on the density of unoccupied $|\downarrow\rangle$ states in the SET island at the electrochemical potential of the $|\downarrow\rangle$ donor-bound electron state, $\mu_{\downarrow}$. Similarly, the tunnel time $\tau_{|\uparrow\rangle\rightarrow\text{SET}}$ depends on the density of unoccupied $|\uparrow\rangle$ states in the SET island that face the electrochemical potential of the $|\uparrow\rangle$ electron state, $\mu_{\uparrow}$.

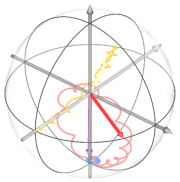

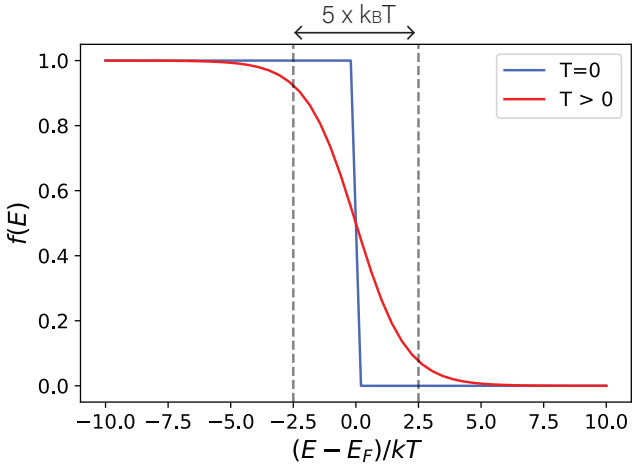

Figure 3.27: **Fermi-Dirac distribution of the SET island.** $E - E_F$ represents the electron energy with respect to the Fermi energy, E_F, while $f(E)$ represents the Fermi-Dirac distribution. At a temperature $T = 0$ (blue line) the Fermi-Dirac distribution is given by a step function. As T increases (red line) the function broadens by an amount proportional to $\approx 5 \times k_B T$.

At a temperature T=0, the Fermi distribution of the SET island is represented by a step function, as shown in Figure 3.27. In this case, the density of unoccupied $|\downarrow\rangle$ states in the SET island at $\mu_\downarrow$ is 0. Thus, at T=0, $P_{|\downarrow\rangle}(t_{\text{read}}) = 0$ and $P_{|\uparrow\rangle}(t_{\text{read}}) = 1$ resulting in a readout contrast of $C(t_{\text{read}}) = 1$. At $T > 0$ however, the Fermi distribution of the SET island becomes thermally broadened, resulting in a finite density of unoccupied $|\downarrow\rangle$ states at $\mu_\downarrow$. In this case, although $P_{|\downarrow\rangle}(t_{\text{read}}) \ll P_{|\uparrow\rangle}(t_{\text{read}})$, $P_{|\downarrow\rangle}(t_{\text{read}})$ is now finite, resulting in a reduction in readout contrast.

Experimentally, we minimise the reduction in readout contrast brought about by thermal broadening of the Fermi distribution of the SET, by cooling the spin qubit devices to $T \approx$ 20 mK in a dilution refrigerator. However, despite the silicon lattice of the device being at a temperature of $T \approx 20$ mK, the temperature of relevance to the thermal broadening of the Fermi distribution of the SET is the electron temperature of the SET, T_e. T_e is determined experimentally by measuring the broadening of the Coulomb peaks through the SET as a function of the mixing chamber temperature of the dilution fridge [96, 97],

with temperatures of $T_e \approx 260$ mK being reported using this technique [98]. There are a number of factors that result in the large deviation between the temperature of the device and the electron temperature of the SET, such as the thermal load induced by the radiation travelling through the high-frequency cables, used for spin control. Additionally, the sporadic current flowing through the SET during spin readout, can also lead to heating of the SET [98]. The electron temperature can thus be minimised through careful attenuation of the signals travelling down the lines, along with potentially increasing the tunnel barrier between the source and drain leads and the SET, such that the peak current through the SET, when the device is outside of Coloumb blockade, is reduced.

Furthermore, the reduction in readout contrast caused by thermal broadening of the SET Fermi distribution can also be reduced by increasing the Zeeman splitting between the electron $|\downarrow\rangle$ and $|\uparrow\rangle$ states, through increasing the magnetic field, B_0 [85]. For this reason, we typically perform the spin qubit experiments in a strong $B_0 \approx$ 1-1.4 T. The reason for staying below $B_0 \approx 1.4$ T is due to both the shortening relaxation time of the spin as a function of increasing B_0 [99] and also due to the reduced cost effectiveness and experimental practicality of applying frequencies $\gamma_e B_0 > 44$ GHz for spin control.

One of the simplest methods of measuring the readout contrast of a spin system experimentally is to perform a Rabi measurement. In a Rabi measurement, an AC B_1 pulse of sweeping duration is applied at the resonance frequency of the spin, resulting in the spin oscillating between the spin $|\downarrow\rangle$ and spin $|\uparrow\rangle$ states. With a well calibrated B_1 frequency (see section 3.9.2), and a readout contrast, $C(t_{\text{read}}) = 1$, the Rabi oscillation will span between a spin up proportion of 0 and 1, indicating that we can perfectly distinguish the presence of a spin $|\downarrow\rangle$ electron from a spin $|\uparrow\rangle$. In the presence of thermal broadening of the Fermi distribution of the SET however, $C(t_{\text{read}}) \leq 1$, which can result in a reduction in the amplitude of the Rabi oscillation. The readout error mechanisms that cause the trough of the Rabi oscillation to increase from a spin up proportion of 0 include: a spin $|\downarrow\rangle$ electron erroneously tunnelling from the donor to the SET during the readout period

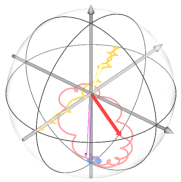

or a spin $|\uparrow\rangle$ electron erroneously tunneling onto the donor from the SET during the read period and tunnelling back off of the donor onto the SET during the same read period, before any pulse has been applied to this electron. Moreover, the readout error mechanisms that cause the peak of the Rabi oscillations to decrease from an up proportion of 1 include: a spin $|\uparrow\rangle$ electron erroneously tunneling onto the donor from the SET during the read period, before being inverted to the spin $|\downarrow\rangle$ state during a π rotation in the Rabi oscillation, and hence not tunnelling during the subsequent read period.

Additionally, the peak in the Rabi oscillation can decrease due to missed current blips in the readout period. Upon the ionisation of the donor, the duration of time for which the current through the SET remains above the threshold current is dictated by the time taken for a spin $|\downarrow\rangle$ electron to tunnel back onto the donor, $\tau_{\mathrm{SET}\rightarrow|\downarrow\rangle}$. If $\tau_{\mathrm{SET}\rightarrow|\downarrow\rangle}$ is sufficiently fast, such that it is faster than the bandwidth of the instruments, then the SET current may not have sufficient time to rise above the threshold current before the electron tunnels back onto the donor. A fast tunnel rate can therefore lead to the misattributing of a spin $|\uparrow\rangle$ electron as a spin $|\downarrow\rangle$ electron, through missed current blips. The device measured in this thesis possessed a fast tunnel time of $\tau_{\mathrm{SET}\rightarrow|\downarrow\rangle} \approx 20$ μs, at the limit of the readout bandwidth, resulting in missing blips constituting a large proportion of the electron readout error in this device.

3.10.2 Readout optimisation with manual tuning

There are a number of parameters that can be systematically swept in order to find the optimal value for electron readout contrast in a given device. Perhaps the most straightforward of these is the read duration, t_{read}. The optimal t_{read} is determined by the electron tunnel rates and is chosen such that $P_{|\uparrow\rangle}(t_{\mathrm{read}})$ is maximised and $P_{|\downarrow\rangle}(t_{\mathrm{read}})$ is minimised. The read duration that gives maximum readout contrast is therefore given by the formula [100]

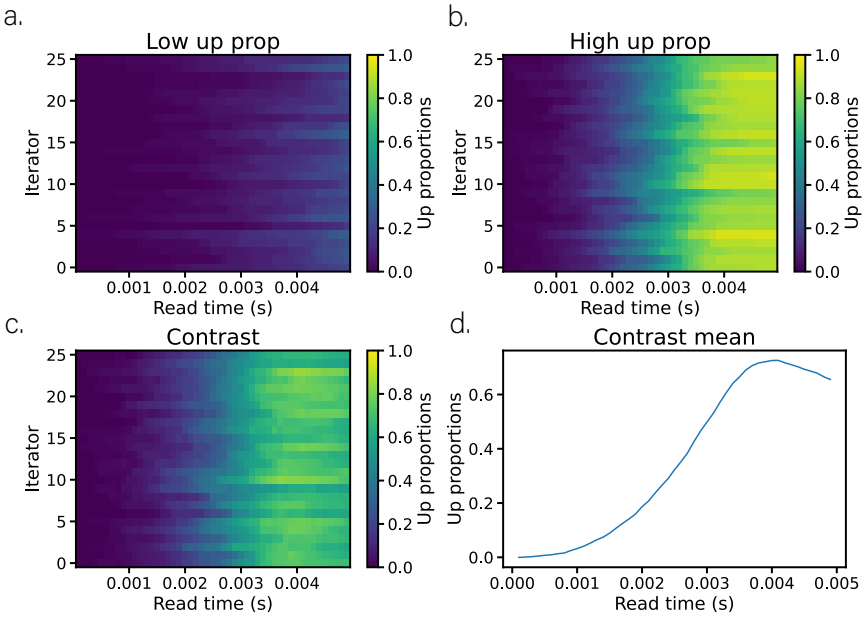

Figure 3.28: **Optimal read duration.** **a.** the spin up proportion calculated for 25 iterations, as a function of read duration, for the case in which we attempt to prepare and then read a spin $|\downarrow\rangle$ electron, via spin dependent tunnelling from the SET. **b.** the spin up proportion calculated for 25 iterations, as a function of read duration, for the case in which we attempt to prepare and then read a spin $|\uparrow\rangle$ electron. This is done by first preparing a spin $|\downarrow\rangle$ state via spin dependent tunnelling from the SET, followed by an adiabatic pulse to invert the spin to the $|\uparrow\rangle$ state. **c.** Readout contrast calculated by subtracting the spin up proportion from **a.** from the spin up proportion from **b.**. **d.** Average over the 25 repetitions of calculated readout contrast. The peak in the contrast identifies the optimal read duration.

$$t_{\text{read, max}} = \frac{\tau_{|\uparrow\rangle\rightarrow\text{SET}} \times \tau_{|\downarrow\rangle\rightarrow\text{SET}}}{\tau_{|\uparrow\rangle\rightarrow\text{SET}} - \tau_{|\downarrow\rangle\rightarrow\text{SET}}} \log\left(\frac{\tau_{|\uparrow\rangle\rightarrow\text{SET}}}{\tau_{|\downarrow\rangle\rightarrow\text{SET}}}\right). \tag{3.34}$$

Figure 3.28 shows an experiment whereby the spin is initialised in the $|\downarrow\rangle$ state via spin dependent tunnelling from the SET to the donor and either directly read out (Fig. 3.28,**a**) or, inverted to the $|\uparrow\rangle$ state with an adiabatic pulse and then read out (Fig. 3.28,**b**). The read duration is swept and the readout contrast is determined. Repeating this measurement over multiple iterations and taking the mean of the contrast reveals a peak in contrast at the optimal t_{read} value.

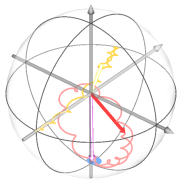

3.10.3 Readout optimisation with machine learning (ML)

The readout contrast of the electron is maximised by carefully tuning the gate voltages such that the the electrochemical potential of the SET island lies at such a position with respect to the donor energy levels that the ratio between the $|\downarrow\rangle$ and $|\uparrow\rangle$ tunnel times is maximised, as discussed in section 3.10. When tuning the readout position for a donor-bound electron this process is often done manually, with the user sequentially manipulating the gate voltages and measuring the resulting readout contrast. This process is not scalable however, and does not allow us to fully explore the multi-dimensional gate space available for tuning, as a result of the difficulty and time cost associated with humans navigating such a high-dimensional landscape. We can therefore make use of machine learning algorithms to help improve the scalability of this process. Additionally, machine learning allows us to more easily compare the tuneup process of donor readout over multiple devices, potentially enabling some insight to be made into the physics that underpins the optimisation of electron readout contrast.

3.10.3.1 ML for fast readout tuning

There are two areas of readout optimisation for which we have implemented machine learning (ML) to automate the optimisation process. The first is for the fast, automated retuning of the readout contrast during long measurement routines. For this we make use of the Nelder-Mead algorithm; a numerical method used to find the maxima or minima of a function in a multi-dimensional space [101–103]. The input parameters for this method are the gate voltages to be manipulated for the readout optimisation. We typically use two gates in the retuning sequence, in order to speed up the time taken for the optimisation process, such that the algorithm is efficient to run during a measurement. The cost function being optimised is the readout contrast of the electron. Although this readout contrast could be measured by determining the amplitude of a Rabi oscillation performed on resonance with the spin, this measurement is time consuming to perform and therefore not ideal as a method of determining the readout contrast for fast readout optimisation.

Consequently, we can determine the readout contrast of the electron much more efficiently, by first initialising the electron into the $|\downarrow\rangle$ state and then simply performing two adiabatic ESR pulses, one on the ESR resonance conditional on the nucleus being in the spin $|\Downarrow\rangle$ state and one on the ESR resonance conditional on the nucleus being in the spin $|\Uparrow\rangle$ state. The difference in up proportion obtained between the two readout traces gives the readout contrast.

Figure 3.29 shows a plot of the readout contrast against repetition number of the retuning sequence. Between each repetition, the retuning sequence evaluates the readout contrast at the current gate position, before feeding this value into the Nelder-Mead algorithm, which subsequently provides a new position in gate space to test. The retuning sequence then ramps the gate voltages to this new position. This process is repeated until either a readout contrast of 1 is achieved, or the maximum number of iterations of the retuning sequence has been reached. The maximum retuning iterations is typically chosen to be $10 + 10n$, where n is the number of device gates included in the retuning process. For $n = 2$, the retuning sequence takes approximately 30 seconds to run and is thus a fast and efficient method to determine the optimal electron readout spot in a very localised region about the donor transition, helping us account for both slow drifts and sudden jumps in the readout position over the period of time it takes to run a given measurement on the system. It should be noted however, that the efficiency of the Nelder-Mead algorithm deteriorates rapidly as the dimensionality of the optimisation problem is increased [103, 104]. Thus, when attempting to include $n > 2$ gates into the automated retuning sequence, the time taken to run the sequence quickly becomes impractical on the timescale required for fast, automated retuning of the readout position.

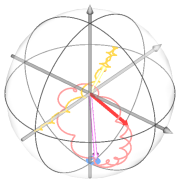

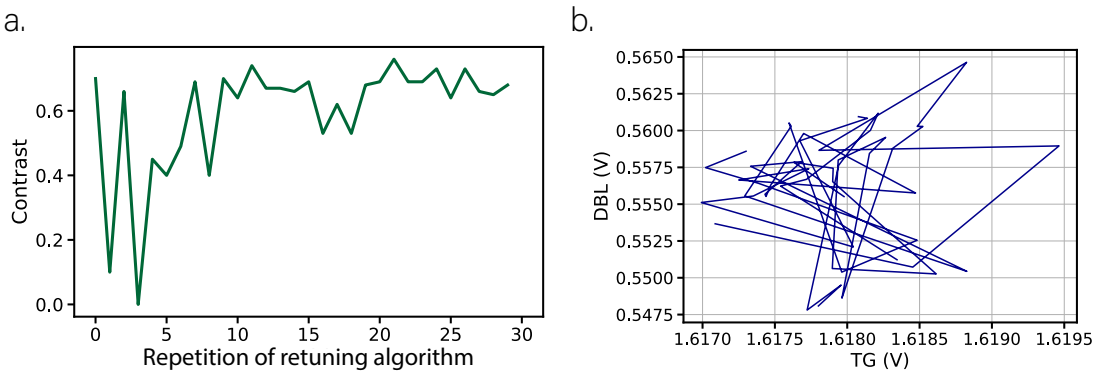

Figure 3.29: **Nelder-Mead retuning algorithm. a.** Single run of the automated retuning sequence. Each repetition of the retuning sequence, along the x-axis, involves evaluating the readout contrast at the current gate position, before inputting this value into a Nelder-Mead algorithm, which subsequently outputs the next set of gate voltages to ramp the device to. The readout contrast can be seen to converge towards the optimal value over 30 repetitions of the retuning algorithm. **b.** The gate voltage applied to one of the gates used in the optimisation algorithm (DBL) against the voltage applied to the gate used for compensation (TG) in order to remain on the Coulomb peak and donor transition throughout the retuning sequence.

In order to optimise the efficiency of the Nelder-Mead retuning algorithm we can employ virtual 'compensation gates' to remain on a given Coulomb peak and charge transition throughout the tuning process. To do this we first select a gate in the device to act as the 'compensation gate', for example the top gate (TG). We can then measure a two-dimensional gate map for each of the gates, by sweeping the compensation gate along the x-axis and the gate of interest along the y axis. The gradient of the donor transition, α_{T}, is dictated by the relative capacitive coupling of the gate being tested and the compensation gate and is given by

$$\alpha_{\mathrm{T}} = \frac{\Delta V_{\mathrm{G}}}{\Delta V_{\mathrm{C}}}, \tag{3.35}$$

where ΔV_{G} is the change in voltage of the gate being tested and ΔV_{C} is the change in voltage of the compensation gate required to remain on the donor transition. Similarly, by extracting the slope of the Coulomb peak, α_{C}, for every gate we can determine the relative capacitive coupling of each gate to the SET island. This allows us to determine the voltage

that must be applied to the compensation gate, in order to compensate for any change in voltage applied to each of the device gates, such that we remain on the correct Coulomb peak and donor transition during the automated retuning algorithm. The measurement of the relative capacitive couplings to the donor and SET island, for an example gate, are shown in Figure 3.30.

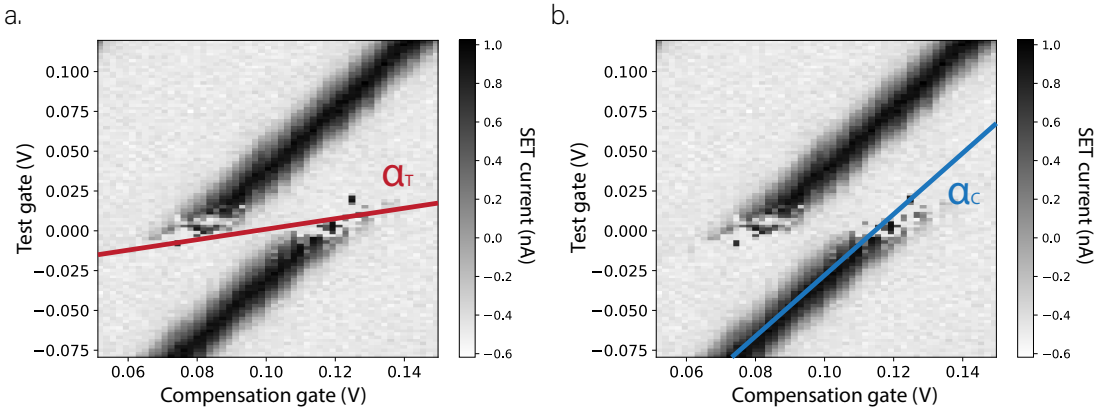

Figure 3.30: **Capacitive couplings to the donor and SET.** Current through the SET in a two dimensional gate voltage sweep across a donor transition. **a.** The red line highlights the slope of the donor transition, α_{T}. The value of α_{T} tells us the relative capacitive couplings between the compensation and test gate to the donor. **b.** The blue line highlights the slope of the Coloumb peak, α_{C}. The value of α_{C} tells us the relative capacitive couplings between the compensation gate and the test gate to the SET. Measuring these slopes for each of the device gates tells us how much voltage to apply to the compensation gate, in order to remain on the donor transition and Coulomb peak while changing the voltage of the test gate. This process is repeated in order to test the relative capacitive coupling of every gate in the device with respect to the compensation gate.

3.10.3.2 ML for invesigating fundamental spin dependent tunnelling principles

Additionally, along with fast, automated retuning of the readout position involving only two gates for optimisation, we can utilise more advanced optimisation protocols, involving a greater number of gates, in an attempt to investigate the underlying physical principles behind optimal readout contrast in these devices. For this purpose we made use of the

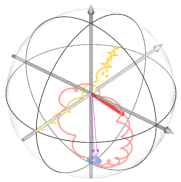

3.10.3 Readout optimisation with machine learning (ML)

Boulder Opal optimisation tools provided over the cloud by the company Q-CTRL [105]. The purpose of utilising these tools to optimise the readout contrast in the device were twofold:

1. To incorporate more gates into the optimisation algorithm in order to explore and find a position of maximum readout contrast in a larger dimensional gate landscape.
2. To invesigate some of the underlying physical principles that dictate the maximum readout contrast in these devices.

The optimisation procedure involved evaluating the readout contrast, C, at a given position in gate space, using the same measurement discussed in section 3.10.3.1. The readout contrast was then converted into a cost score (given by 1-C) and sent over the cloud to the Boulder Opal optimisation software, which used a Gaussian process based optimizer [106, 107] to calculate the next set of gate voltages to be tested, which were subsequently sent back to us via the cloud. The new gate voltages were then automatically read in by our measurement software, which then ramped the gate voltages to the next position in gate space and repeated the procedure. A 'cost-array' was thus calculated by determining the cost score at each location in gate space tested during the optimisation procedure. Figure 3.31 shows a three-dimensional map of this cost array for two example runs of the optimisation algorithm, each using $n = 3$ gates in the optimisation procedure.

We found that when incorporating $n > 2$ gates into the optimisation algorithm, we were unable to converge to a position of maximum readout contrast in any reasonable time. This may however, have been due to the lack of compensation gate used to stay on the donor transition and Coulomb peak at the time these experiments were performed. Additionally, although no clear trends emerged from the gate exploration that provided definitive insight into the physical mechanisms governing the improvement of readout contrast, we did find that the amount of current flowing through the SET appeared to have an influence on the readout contrast. Some evidence was found that suggested more opaque SET barrier

gates, combined with a lower source drain bias, and thus less current through the SET, led to a trend towards higher readout contrast. Figure 3.31 shows a three-dimensional map of the cost array of the optimisation function as a function of the gate voltages applied to the three gates.

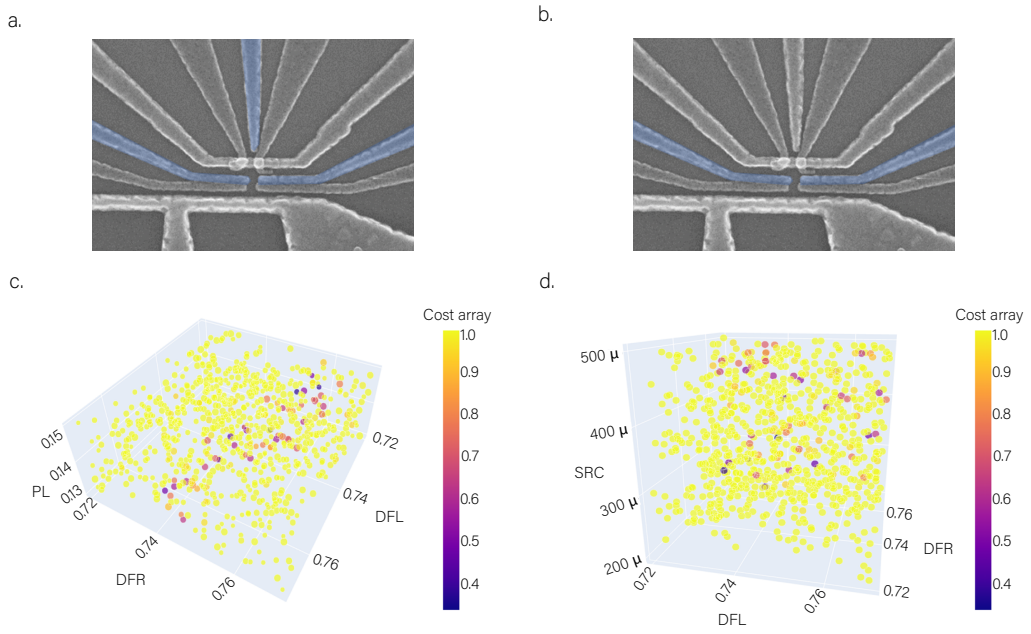

Figure 3.31: **Boulder Opal readout optimisation.** Optimisation of readout contrast using Q-CTRL's neural network optimisation software. **a.(b.)** Gates highlighted in blue are the gates used in the readout contrast optimisation algorithm, the results of which are shown in **c(d)**. **c.** Cost array for an example optimisation run using the Boulder Opal Gaussian process optimiser. Each point of the cost array plotted represents 1-C, where C is the electron readout contrast, for each set of voltages tested. The gates used were PL, DFR and DFL. **d.** Cost array for an example optimisation run using the Boulder Opal Gaussian process optimiser using the SRC (source-drain bias), gates DFL and DFR.

3.10.3.3 ML for detecting SET current blips

Another area of readout optimisation for which we can utilise machine learning is in the detection of current blips through the SET. Normally, the binary response of the SET current to the ionisation event of the donor, along with the high signal to noise ratio, means that the threshold current method, discussed in section 3.9.3, is entirely sufficient

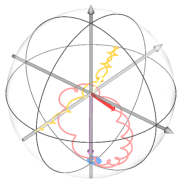

to determine the tunnelling event of an electron onto the SET island. However, if the tunnel rate of a spin $|\downarrow\rangle$ electron from the SET island to the donor is sufficiently fast, such that it is faster than the bandwidth of the instruments, then the current may not have sufficient time to rise above the threshold and therefore the current blip will go un-detected. This thus leads to the missing of spin $|\uparrow\rangle$ electron tunnelling events and hence a reduction in readout contrast.

Although generally effective, the threshold current technique is somewhat rudimentary in nature and hence an obvious question is whether a more advanced technique such as machine learning can help alleviate this issue of missing blips. We therefore trained a neural network from the open source library Keras to detect the tunnelling event of a spin $|\uparrow\rangle$ electron onto the SET island [108]. The steps involved in using this neural network for SET blip detection were as follows:

1. Initialise the nucleus into the $|\Uparrow\rangle$ state.

2. Perform a measurement involving two adiabatic ESR pulses, each followed by a read period, with one adiabatic pulse applied at the ESR frequency conditional on the donor nucleus being in the $|\Downarrow\rangle$ state and one pulse applied at the ESR frequency conditional on the donor nucleus being in the $|\Uparrow\rangle$ state. Repeat this measurement 5000 times. As the nucleus is initialised in the $|\Uparrow\rangle$ state, the adiabatic ESR pulse conditional on the nucleus being in the $|\Downarrow\rangle$ should not be on resonance and thus the electron should remain in the $|\downarrow\rangle$ state. Consequently, the readout period following this pulse should give a low spin up proportion. We assign the readout traces following this adiabatic pulse the label 'low'. On the other hand, the adiabatic pulse conditional on the nucleus being in the $|\Uparrow\rangle$ state, should be on resonance and hence invert the electron to the $|\uparrow\rangle$ state. The readout period following this pulse should therefore give a high spin up proportion. We thus label the readout traces following this adiabatic pulse as 'high'.

3. Divide the 5000 repetitions of the measurement into a training dataset and a testing

dataset (e.g. 4000 repetitions for training and 1000 repetitions for testing).

4. Input the training dataset, with the associated labels, into the model, such that the model can learn to identify which features of the current traces correspond to the presence of a spin $|\uparrow\rangle$ electron (defined as the traces belonging to the 'high' dataset) and which belong to a spin $|\downarrow\rangle$ (defined as belonging to the 'low' dataset).

5. Test the model on the testing dataset, by using the neural network to determine if each current trace possesses a 'high' or a 'low' label and scoring the output based on the success rate of the model's classification. Success is defined as the model assigning the 'low' label to a readout period that was following an adiabatic ESR pulse dependent on the nuclear state $|\Downarrow\rangle$ or a 'high' label to a readout period that was following an adiabatic ESR pulse dependent on the $|\Uparrow\rangle$ nuclear state.

6. The model is now trained and can be used to determine the presence of a spin $|\uparrow\rangle$ tunnelling event in the SET current. For every measurement, the current traces are then fed into the model, which assigns a 'high' or a 'low' label to each trace depending on if it identifies the presence of a spin $|\uparrow\rangle$ tunnelling event in the current trace. The spin up proportion is then calculated by $P_{\text{up prop}} = \frac{N_{\text{high}}}{(N_{\text{high}}+N_{\text{low}})}$, where N_{high} is the number of traces determined to belong to the 'high' label and N_{low} is the number of traces determined to belong to the 'low' label.

In order to test how well the neural network detects the presence of a spin $|\uparrow\rangle$ tunnelling event, we can repeat the measurement used to determine the readout contrast of the electron using both the trained neural network and the nominal threshold current technique. We therefore measured 1000 repetitions of this pulse sequence, where we prepare the nucleus in the $|\Uparrow\rangle$ state, before performing one adiabatic ESR pulse at the ESR resonance conditional on the nucleus $|\Downarrow\rangle$ state and one adiabatic ESR pulse at the ESR resonance conditional on the nucleus being in the $|\Uparrow\rangle$ state. We then used both the neural network and the current thresholding method to determine the spin up proportion for each readout trace. Figure 3.32 shows the results of this measurement, repeated 20 times.

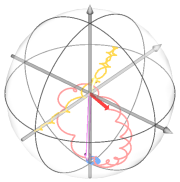

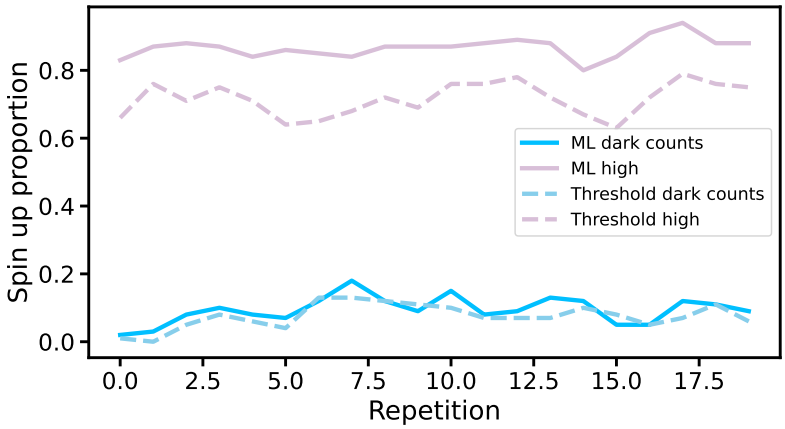

Figure 3.32: **Determination of spin up proportion with ML.** Up proportion of a current trace measuring a spin $|\downarrow\rangle$ electron (blue lines) and up proportion of a current trace measuring a spin $|\uparrow\rangle$ electron (purple lines). The up proportion was determined using either the threshold current technique (solid line) or machine learning (ML), (dashed line).

Both the neural network and the threshold method determined very similar up proportions for the traces following an adiabatic pulse conditional on the nucleus being in the $|\Downarrow\rangle$ state, which we assume belongs to a spin $|\downarrow\rangle$ electron. However, the neutral network consistently finds a higher spin up proportion for the current traces that follow an adiabatic pulse conditional on the nucleus being in the $|\Uparrow\rangle$ state, which we assume belongs to a spin $|\uparrow\rangle$ electron. This suggests, that the neural network is more proficient at identifying a spin $|\uparrow\rangle$ tunnelling event than the threshold technique and is therefore less susceptible to missing blips. This measurement was performed on a donor with very fast tunnel times, such that there is a high probability of missing blips using the threshold current method. Further study must therefore be performed, to determine if this gain in readout contrast is unique to donors for which the electron tunnel time from the SET island to the donor is very fast (i.e. blip detection is limited by the bandwidth of the instruments).

3.11 Control and readout of the ^{31}P nuclear spin

3.11.1 Coherent nuclear magnetic resonance (NMR)

The process behind the coherent manipulation of the nuclear spin is very similar to that of the electron, with the noticeable exception of the initialisation and readout scheme. As with the spin of the electron, the resonance frequency is found by making an initial guess of the π pulse duration, before sweeping the frequency of the B_1 field about the expected resonance frequencies. A Rabi experiment is then performed at that resonance frequency and used to inform the pulse duration used in a subsequent frequency spectrum. Due to the significantly ($\approx$ 1000 times) lower gyromagnetic ratio of the nuclear spin compared to the electron spin, the resonance frequency of the nuclear spin is in the radio frequency regime for a DC magnetic field of 1 T, compared to the microwave regime of the electron resonance frequency. Similarly, the π time (defined as time taken to full invert the spin between the $|\downarrow\rangle$ and $|\uparrow\rangle$ state) of the nucleus is typically of order 100 μs, compared to the $\approx$ 1 μs π time of the electron.

3.11.2 Nuclear readout

As the donor nuclei cannot be read out directly via spin-dependent tunnelling to the SET, we instead read out the nuclei indirectly, via the donor-bound electrons. We do this by rotating the electron conditionally on the state of the nucleus, before reading out the electron via spin dependent tunneling to the SET [19]. We can thus infer, from whether the electron is successfully rotated to the spin $|\uparrow\rangle$ state or not, the state of the donor nucleus.

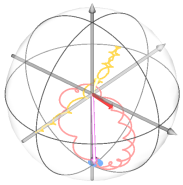

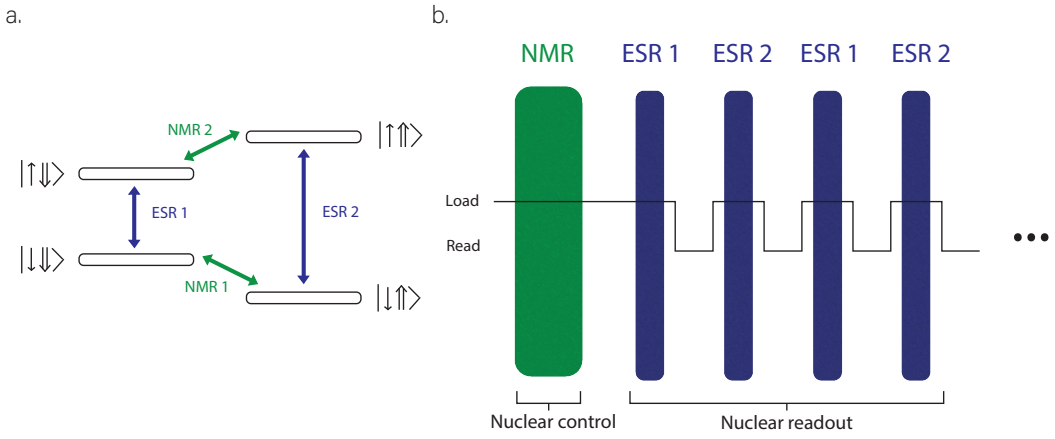

Figure 3.33: **Nuclear readout sequence. a.** Schematic depicting the eigenstates of the donor and the corresponding ESR and NMR transitions between them. **b.** A schematic illustration of the nuclear readout process. This process first begins by performing the desired control sequence on the nucleus as depicted with the green box. For nuclear readout we then sequentially apply ESR 1 and ESR 2, which rotates the electron conditional on the nucleus being in the $|\Downarrow\rangle$ state or $|\Uparrow\rangle$ state respectively. After each conditional rotation the electron is read out. The conditional rotations are repeated multiple times after the same pulse sequence in order to perform quantum non-demolition (QND) readout. The entire pulse sequence including nuclear control is then repeated many times in order to obtain a nuclear flip probability.

The postulates of quantum mechanics state that, when performing a measurement of a quantum state, that state will be projected into one of its eigenstates. Thus when we measure the state of the spin of the donor nucleus or electron we will only ever receive an outcome of 0 or 1. We must therefore repeat the measurement many times, by re-preparing the state and measuring it, in order to build the statistics necessary to determine the nature of any superposition state. For the case of the electron, the spin is initialised into the spin $|\downarrow\rangle$ state automatically after every iteration of the pulse sequence, as the readout process automatically results in the initialisation of a spin $|\downarrow\rangle$ electron onto the donor. For the case of the nuclei on the other hand, the nucleus is not automatically initialised into the $|\Downarrow\rangle$ state automatically at the end of each pulse sequence. We therefore have two options:

1. Manually initialise the nuclei at the beginning of every pulse sequence into the $|\Downarrow\rangle$

state.

2. Do not initialise the nuclei and instead measure the flip probability between the nuclear $|\Downarrow\rangle$ and $|\Uparrow\rangle$ state between each repetition of the pulse sequence.

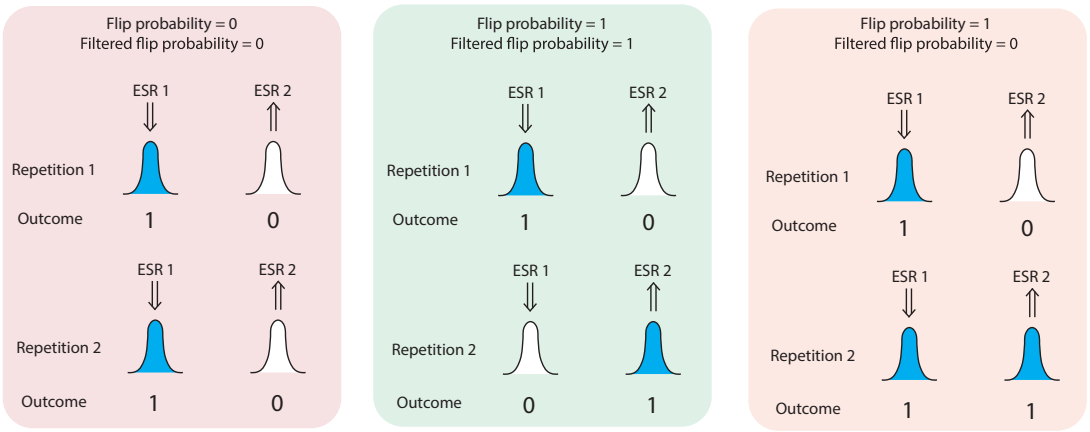

Figure 3.34: **Flip and filtered flip probability.** Demonstration of the principles behind measuring both the flip and filtered flip probability of the nucleus. ESR 1 and ESR 2 represent the rotation of the electron, conditional on the nucleus being either in the $|\Downarrow\rangle$ state or $|\Uparrow\rangle$ state respectively. The repetition number indicates if the outcome belongs to the first or second repetition of the nuclear control sequence. The flip probability represents the probability of the nucleus flipping state between repetition 1 and repetition 2 of the pulse sequence. This is indicated by the active ESR resonance (indicated in blue) flipping between ESR 1 and ESR 2 between a repetition of the pulse sequence. Filtered flip probability is used to distinguish if this flipping of active resonances between ESR 1 and ESR 2 is likely attributed to readout error.

Measuring the flip probability is a convenient method to avoid initialising the nuclei for every repetition of the pulse sequence, as this is a time costly process. There are two methods by which we can determine if the nucleus has flipped between sequential repetitions of the nuclear pulse sequence:

1. Measure only one of the conditional rotations of the electron e.g. either ESR 1 or ESR 2. We refer to this as the flip probability.

2. Measure both of the conditional rotations on the electron, i.e. both ESR 1 and ESR

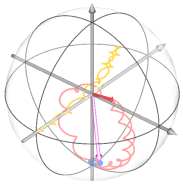

2 and verify that they display the opposite behaviours (i.e. when ESR 1 gives a high up proportion then ESR2 should give a low up proportion.) This method provides a convenient method of ascertaining if the electron readout position is in tune during an experiment on the nuclei and is referred to as the filtered flip probability as, if the outcomes of ESR 1 and ESR 2 do not corroborate each other then this datapoint is filtered from the dataset as a readout error.

3.11.2.1 Quantum non-demolition (QND) readout of the donor nucleus

An added benefit of reading out the nucleus indirectly via the electron, is that the nucleus can be readout in a process known as quantum non-demolition (QND) measurement. The principal concept behind QND readout is that, upon measuring some physical quantity of a system, described by a Hermitian operator $\hat{A}$, with an outcome a_n, the system will be projected into the corresponding eigenstate $|\phi_n\rangle$ and remain in this post-measurement state. Consequently, every subsequent measurement of $\hat{A}$, should result in the same outcome, a_n [109]. In practice, errors in the readout process can mean that, after the system has been projected into $|\phi_n\rangle$, repeated measurements of the system will not necessarily return the same outcome, a_n. However, the ability to perform repeated QND measurements and average over the results, allows us to greatly increase our confidence of the measurement outcome in the presence of readout errors, thus increasing the readout fidelity.

Experimentally, the QND readout procedure generally consists of the system of interest, denoted $\hat{H}_Q$ (this system represents a qubit in the context of quantum information), the ancillary system, $\hat{H}_A$, which can be read out either destructively or non-destructively, and a coupling term between these systems, $\hat{H}_C$. In order to constitute a true QND readout, the condition that must be fulfilled is that $\hat{H}_Q$ must commute with $\hat{H}_C$ [19, 109, 110]

$$[\hat{H}_C, \hat{H}_Q] = 0. \tag{3.36}$$

For the case of nuclear readout, $\hat{H}_Q$ describes the nucleus, $\hat{H}_A$ describes the electron and $\hat{H}_C$ represents the hyperfine coupling between them. In this case $[\hat{H}_C, \hat{H}_Q] \neq 0$ and thus

the readout of the nucleus via the electron is not perfectly QND in nature. The effect of this is that, with every repetition of the QND readout process, the nucleus and the electron become weakly entangled with one another. This results in a small but finite probability of flipping the nucleus every time the electron is measured projectively; thus constituting an error channel for the QND readout. The magnitude of this QND error depends on the degree to which the eigenstates of the qubit-ancilla system become hybridised through the weak entanglement, as a consequence of $[\hat{H}_C, \hat{H}_Q] \neq 0$. The hybridised eigenstates of the qubit-ancilla system can be written, in the basis $\{\uparrow_{A/Q}, \downarrow_{A/Q}\}$, as [109]

$$\widetilde{|\uparrow_A\downarrow_Q\rangle} = c\,|\uparrow_A\downarrow_Q\rangle + s\,|\downarrow_A\uparrow_Q\rangle\,, \tag{3.37}$$

$$\widetilde{|\downarrow_A\uparrow_Q\rangle} = c\,|\downarrow_A\uparrow_Q\rangle + s\,|\uparrow_A\downarrow_Q\rangle\,, \tag{3.38}$$

where $s = \cos(\theta)$ and $c = \sin(\theta)$, where $\tan(2\theta) = \frac{\nu_C}{\Delta\epsilon}$. ν_C represents the coupling between the qubit and the ancilla, in units of frequency, and $\Delta\epsilon = \epsilon_A - \epsilon_Q$ represents the difference in the frequency splitting of the spin states of the ancilla, ϵ_A, and of the qubit, ϵ_Q.

Given the eigenstates stated in equations 3.37 and 3.38, the probability of flipping the qubit spin when a projective measurement is made on the ancilla is given by [109]

$$P_{\text{flip}} = \frac{s^2}{(1+s^2)}. \tag{3.39}$$

For the case of a donor nucleus, ν_C represents the hyperfine coupling strength, $A \approx 117$ MHz, while ϵ_Q and ϵ_A are given by the Zeeman splitting of the donor nucleus and electron respectively. As a result of the vastly different gyromagnetic ratios of the nucleus and electron, $|\gamma_e/\gamma_n| \approx 10^3$, for a B_0 field of 1.4 T, $\Delta\epsilon \approx 40$ GHz.

The experimental QND readout procedure for the donor nucleus, involves repeating the process of loading an electron onto the donor, rotating the electron conditional on the

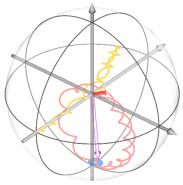

state of the nucleus and then projectively measuring the state of the electron. Given the parameters for ν_C and $\Delta\epsilon$ stated above, the probability of flipping the nucleus every time the electron is projectively measured in this QND procedure, is $P_{\text{flip}} \approx 10^{-6}$. The readout of the nucleus is thus, to a very good approximation, QND in nature, despite the fact that there are noncommuting terms in its Hamiltonian. This allows for very high readout fidelities, $> 99\%$ [19], to be achieved when reading out the nucleus with QND readout. It should be noted however, that this discussion only considered the case for which the hyperfine interaction is isotropic in nature. For the case of an anisotropic hyperfine interaction, additional error channels are introduced into the QND measurement, which can increase the erroneous flipping rate of the nucleus during repeated QND readout [109].

3.11.3 Nuclear initialisation

As stated in the previous section, the donor nuclei, unlike the electrons, cannot be initialised via spin dependent tunnelling to and from the SET reservoir and must therefore be initialised using specially designed pulse sequences. For nuclear initialisation, we therefore make use of a technique known as electron-nuclear double resonance spectroscopy (ENDOR) [2,111–113]; a widely used technique that is characterised by the hybrid addressing of both the electron and the nuclei within the same pulse sequence.

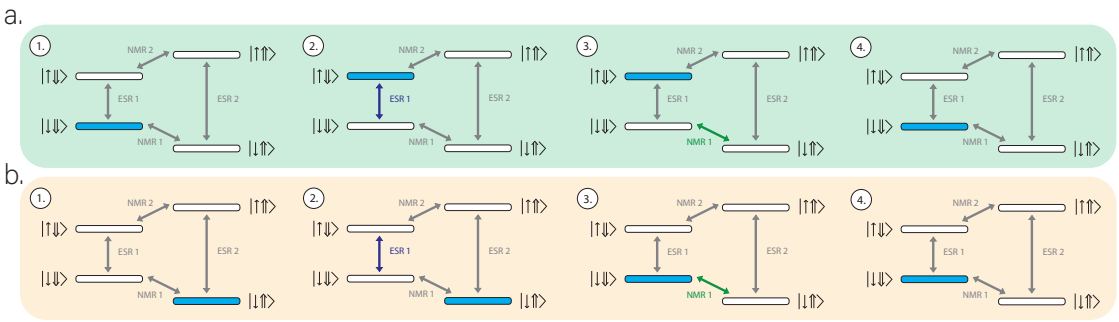

Figure 3.35: **Electron-nuclear double resonance spectroscopy (ENDOR) nuclear initialisation sequence.** Depiction of the process behind nuclear initialisation, with the coloured eigenstate levels representing the occupied levels and the coloured transition frequencies indicating the applied pulse frequencies. **a.** The sequence for the case of the nucleus being in the spin $|\Downarrow\rangle$ state at the start of the experiment. **b.** The sequence for the case of the nucleus being in the spin $|\Uparrow\rangle$ state at the start of the experiment. Both of these sequences result in the nucleus being initialised in the spin $|\Downarrow\rangle$ state at the end of the sequence.

Crucially, for the initialisation of the donor nuclei, the ENDOR sequence acts to initialise the donor nucleus regardless of its initial state. Figure 3.35 shows the steps comprising the scheme to initialise the nucleus into the $|\Downarrow\rangle$ state, for both the case of the nucleus being initially in the $|\Downarrow\rangle$ state or in the $|\Uparrow\rangle$ state. It is important at this point to reiterate the nomenclature that a small arrow ($\downarrow$ or $\uparrow$) represents the state of the donor bound electron, while a large arrow ($\Downarrow$ or $\Uparrow$) represents the state of the donor nucleus. With this nomenclature in mind, the nuclear initialisation steps depicted schematically in Figure 3.35 are as follows:

1. Initialise the electron into the $|\downarrow\rangle$ state via spin dependent tunnelling from the SET island, such that either the $|\downarrow\Downarrow\rangle$ or $|\downarrow\Uparrow\rangle$ state is occupied.

2. Apply an ESR pulse at the resonance for ESR 1, which flips the electron conditional on the nucleus being in the $|\Downarrow\rangle$ state. If the nucleus is in the $|\Downarrow\rangle$ state then this pulse is on resonance and hence the electron is flipped into the $|\uparrow\rangle$ state. If however, the nucleus is in the $|\Uparrow\rangle$ state, then this pulse on the electron will not be on resonance and hence the electron will remain in the $|\downarrow\rangle$ state.

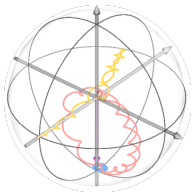

3. Apply an NMR pulse at the resonance for NMR 1, which flips the nucleus conditional on the electron being in the $|\downarrow\rangle$ state. If the electron is in the $|\downarrow\rangle$ state, then the system occupies the state $|\downarrow\Uparrow\rangle$ and thus the NMR pulse flips the nucleus such that the state $|\downarrow\Downarrow\rangle$ is now occupied. Conversely, if the electron is in the $|\uparrow\rangle$ state, then the $|\uparrow\Downarrow\rangle$ state is occupied. The NMR pulse is therefore off resonance as the electron is in the $|\uparrow\rangle$ state and therefore the system remains in the $|\uparrow\Downarrow\rangle$ state.

4. Finally, the electron is re-initialised into the $|\downarrow\rangle$ state via spin dependent tunnelling from the SET island, leaving us in the $|\downarrow\Downarrow\rangle$ state in both cases.

3.12 Donor characterisation

Piecing together the techniques discussed in sections 3.9,-3.11, following the identification of a donor transition, the full process for characterising the donor is summarised in Figure 3.36. The goal of this workflow is to go from identifying a charge transition in gate space to having comprehensive control over the donor electron and nuclear state, along with high fidelity readout, such that more complex measurements can then be carried out on the donor.

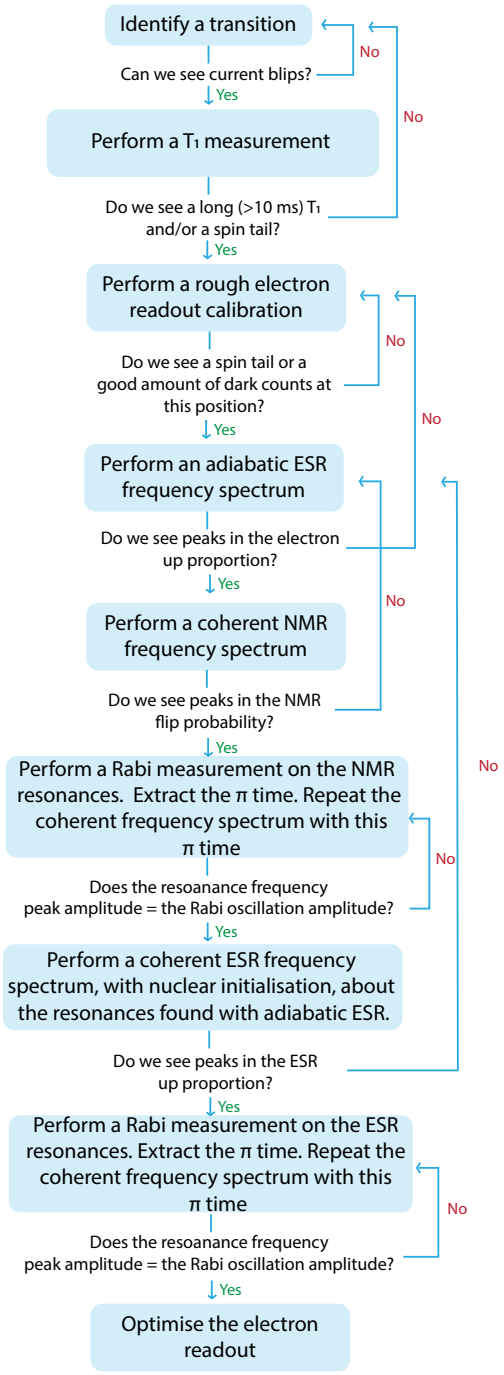

Figure 3.36: **Donor calibration workflow.**

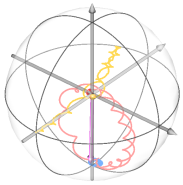

4.
Theory of exchange-coupled ^{31}P donors

The best that most of us can hope to achieve in physics is simply to misunderstand at a deeper level.

Wolfgang Pauli

In the previous chapters, we have predominantly focused on the case of a single donor atom, consisting of a ^{31}P nucleus and a single, bound electron. However, in order to construct a scalable quantum processor using donor atoms in silicon, it is vital that we are able to couple multiple donor atoms together, such that we can perform multi-qubit operations. As mentioned in section 1.1, a range of different coupling mechanisms between donors in silicon exist, spanning a large range of distances [29–33]. In this thesis we will focus primarily on the exchange coupling interaction, which can be utilised over a relatively robust range of intermediate inter-donor distances ($\approx$ 10-30 nm) [114].

4.1 The exchange interaction

The exchange interaction is a vital resource for quantum computation in semiconductor spin qubits and has been exploited in almost the entirity of semiconductor spin qubit platforms [115] for either the implementation of single-qubit [116–118] or two-qubit [119–122] operations. Although a rich and complex topic, the fundamental principles behind the origin of the exchange interaction can be introduced by considering the simple case of two electrons, with spatial coordinates $\mathbf{r_1}$ and $\mathbf{r_2}$ respectively. The spatial component of the wave functions of these two electrons can be expressed as $\psi_a(\mathbf{r_1})$ and $\psi_b(\mathbf{r_2})$. In order to find the joint state for the spatial component of the wave function of the two electrons we can take the product of the two electron states to give $\psi_a(\mathbf{r_1})\psi_b(\mathbf{r_2})$. However, empirical evidence tells us that indistinguishable particles must obey an exchange symmetry, meaning that if we exchange the two electrons we are left with a multiple of the original state [123]. For the example two-electron wave function given above, this symmetry condition is not satisfied, since $\psi_a(\mathbf{r_1})\psi_b(\mathbf{r_2}) \neq c(\psi_a(\mathbf{r_2})\psi_b(\mathbf{r_1}))$ where c represents a constant. Consequently, the only allowed states for the spatial component of the wave function for a joint system are either symmetrised or antisymmetrised product states, which obey the principle of exchange symmetry. These allowed states can be written as the following [123]

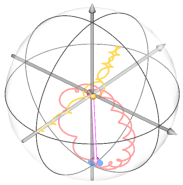

$$\psi_S = \frac{1}{\sqrt{2}}[\psi_a(\mathbf{r_1})\psi_b(\mathbf{r_2}) + \psi_a(\mathbf{r_2})\psi_b(\mathbf{r_1})], \tag{4.1}$$

$$\psi_A = \frac{1}{\sqrt{2}}[\psi_a(\mathbf{r_1})\psi_b(\mathbf{r_2}) - \psi_a(\mathbf{r_2})\psi_b(\mathbf{r_1})], \tag{4.2}$$

where ψ_S and ψ_A represent the symmetric and antisymmetric spatial wave functions respectively.

The overall wave function of a particle, Ψ, is comprised not only of a spatial component, ψ, but also of a spin component, χ, such that

$$\Psi = \psi\chi. \tag{4.3}$$

The Pauli exclusion principle demands that the overall wave function of any Fermion is antisymmetric [124]. As the electron is a Fermion this therefore offers two possibilities for the two-electron wave function. The first possibility, is that the spatial component of the wave function is symmetric, ψ_S. In this case, in order to preserve an antisymmetric overall electron wave function it is necessary for the electron to possess an antisymmetric spin state, χ_A. The second possibility, is that the spatial component of the wavefunction is antisymmetric, ψ_A. In this case, an overall antisymmetric wavefunction is only maintained if the spin component of the wavefunction is symmetric, χ_S. The two possible wave functions can thus be written as [123]

$$\Psi_I = \frac{1}{\sqrt{2}}[\psi_a(\mathbf{r_1})\psi_b(\mathbf{r_2}) + \psi_a(\mathbf{r_2})\psi_b(\mathbf{r_1})]\chi_A,$$
$$\Psi_{II} = \frac{1}{\sqrt{2}}[\psi_a(\mathbf{r_1})\psi_b(\mathbf{r_2}) - \psi_a(\mathbf{r_2})\psi_b(\mathbf{r_1})]\chi_S,$$

with corresponding energies

$$E_I = \int \Psi_I^* \hat{H} \Psi_I d\mathbf{r_1} d\mathbf{r_2},$$
$$E_{II} = \int \Psi_{II}^* \hat{H} \Psi_{II} d\mathbf{r_1} d\mathbf{r_2},$$

where $\hat{H}$ represents the Hamiltonian of the system. The difference in the energy of the two possible wave functions is therefore given by

$$E_I - E_{II} = 2 \int \psi_a^*(\mathbf{r_1})\psi_b^*(\mathbf{r_2})\hat{H}\psi_a(\mathbf{r_2})\psi_b(\mathbf{r_1})d\mathbf{r_1}d\mathbf{r_2}. \tag{4.4}$$

The exchange constant, J, is defined as [123]

$$J = \frac{E_I - E_{II}}{2} = \int \psi_a^*(\mathbf{r_1})\psi_b^*(\mathbf{r_2})\hat{H}\psi_a(\mathbf{r_2})\psi_b(\mathbf{r_1})d\mathbf{r_1}d\mathbf{r_2}. \tag{4.5}$$

Focusing on the implications of this on the spin component of the wavefunction, for the case of $J < 0$, $E_{II} > E_I$ and thus the most energetically favourable state is Ψ_I. The most energetically favourable spin wave function for the case of $J < 0$ is therefore the anti-symmetric wavefunction, χ_A. There is a single state that corresponds to an antisymmetric spin wavefunction, which is known as the singlet state $|S\rangle$ where

$$|S\rangle = \frac{1}{\sqrt{2}}(|\uparrow\downarrow\rangle - |\downarrow\uparrow\rangle). \tag{4.6}$$

Geometrically, the singlet state represents a state of two spins that point anti-parallel to one another in an undefined direction in space, as illustrated in Fig.4.1, a.

Conversely, for the case of $J > 0$, $E_I > E_{II}$ and thus the most energetically favourable state is Ψ_{II}, with an associated symmetric spin wavefunction, χ_S. There are three states that correspond to a symmetric spin wavefunction, known as the triplet states, $|T_-\rangle, |T_0\rangle$ and $|T_+\rangle$

$$|T_-\rangle = |\downarrow\downarrow\rangle, \tag{4.7}$$

$$|T_0\rangle = \frac{1}{\sqrt{2}}(|\uparrow\downarrow\rangle + |\downarrow\uparrow\rangle), \tag{4.8}$$

$$|T_+\rangle = |\uparrow\uparrow\rangle. \tag{4.9}$$

Geometrically, the $|T_-\rangle$ and $|T_+\rangle$ states represents a state of two spins pointing towards the -z or +z direction of the Bloch sphere respectively. The $|T_0\rangle$ state represents a state of two spins pointing parallel to one another, along some undefined direction in the xy plane of the Bloch sphere. These geometric interpretations are represented schematically in Fig.4.1, b.

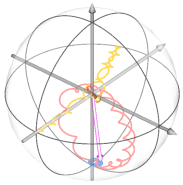

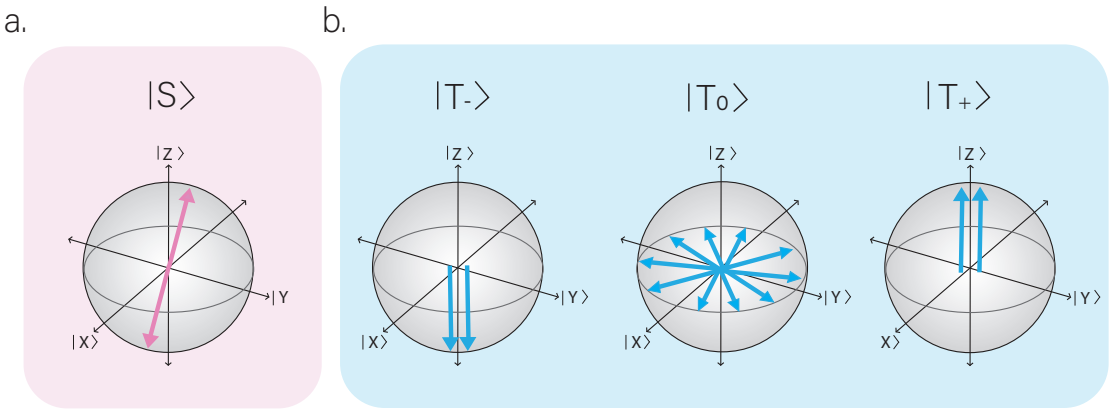

Figure 4.1: **Geometric interpretation of singlet and triplet states. a.** Schematic of the geometric interpretation of the singlet state $|S\rangle = \frac{1}{\sqrt{2}}(|\uparrow\downarrow\rangle - |\downarrow\uparrow\rangle)$ on the Bloch sphere. The singlet state represent a state of anti-parallel spins that point in an undefined direction in space. **b.** Schematic of the geometric interpretation of the triplet states on a Bloch sphere. The $|T_-\rangle = |\downarrow\downarrow\rangle$ state represents a state of two spins pointing along the -z direction of the Bloch sphere. The $|T_0\rangle = \frac{1}{\sqrt{2}}(|\uparrow\downarrow\rangle + |\downarrow\uparrow\rangle)$ state represents the state of two parallel spins pointing in an undefined direction in the xy-plane of the Bloch sphere. The $|T_+\rangle = |\uparrow\uparrow\rangle$ state represents a state of two spins pointing along the +z direction of the Bloch sphere.

4.2 The exchange interaction in a two ^{31}P system

4.2.1 Hamiltonian of an exchange coupled two-donor system

The Hamiltonian of a system of two ^{31}P donors, coupled via an exchange interaction between the the two donor-bound electrons is given by

$$H_{\text{full}} = \underbrace{\gamma_e B_0(\hat{S}_{z1} + \hat{S}_{z2})}_{\text{Electron Zeeman}} + \underbrace{\gamma_n B_0(\hat{I}_{z1} + \hat{I}_{z2})}_{\text{Nuclear Zeeman}} + \underbrace{A_1(\hat{\mathbf{S_1}} \cdot \hat{\mathbf{I_1}}) + A_2(\hat{\mathbf{S_2}} \cdot \hat{\mathbf{I_2}})}_{\text{Hyperfine coupling}} + \underbrace{J(\hat{\mathbf{S_1}} \cdot \hat{\mathbf{S_2}})}_{\text{Exchange interaction}},$$

where the subscripts 1 and 2 denote donor 1 and donor 2 and hence A_1 and A_2 denote the hyperfine coupling strengths for donor 1 and donor 2 respectively. As discussed in section 2.3.2, the hyperfine coupling strength of the donor will depend on factors such as the exact positioning of the donor within the device and the local electric fields in the donor's environment. For this reason A_1 and A_2 are not necessarily equivalent. We therefore define two quantities: $\Delta A = |A_1 - A_2|$ which represents the difference in hyperfine coupling between the two donors and $\bar{A} = \frac{A_1+A_2}{2}$, which represents the average hyperfine coupling of the two donors.

The eigenstates of the electrons in a two-qubit exchange-coupled system depend very intimately on the ratio between the coupling, J, and the detuning between the electron spins, Δ. In the quantum dots community, a detuning between the two electrons of an exchange-coupled system is often achieved by introducing a magnetic field gradient to the system, such that the magnetic field experienced by the two electrons differs by an amount ΔB_z [125]. In the case of donors, this detuning can instead be introduced in a binary fashion by initialising the donor nuclei in either a parallel or an anti-parallel spin orientation.

For the case of a parallel nuclear orientation, the detuning between the two electrons, in

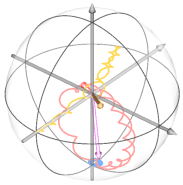

units of frequency, is given by $\Delta = \Delta A$. ΔA arises from spatial inhomogeneity of electric fields and strain in the device. For donors spaced by ≈ 20 nm, as required for the values of J we are interested in, one typically finds $\Delta A \approx$ a few MHz. For the case of the nuclei being in an anti-parallel orientation on the other hand, the detuning between the electrons is given by $\Delta = \bar{A}$, where $\bar{A} \approx 117$ MHz (the bulk value for the hyperfine interaction in silicon). For the case in which $\Delta A < J < \bar{A}$, there is therefore the opportunity to transition between the regimes of $J < \Delta$ to $J > \Delta$, simply by choosing to initialise the nuclei in either a parallel or anti-parallel orientation. It is therefore insightful to evaluate the eigenstates of the exchange-coupled donor Hamiltonian for each of the orientations of the two donor nuclei individually.

4.2.2 Eigenstates of an exchange coupled system

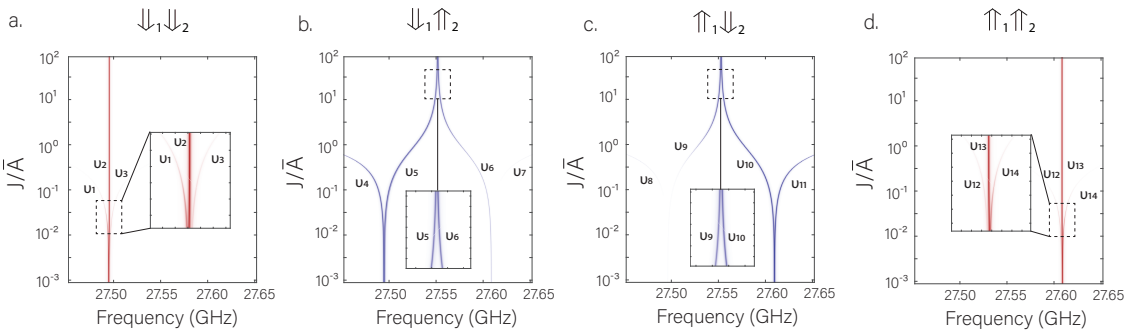

Figure 4.2: Simulated ESR frequency spectrum for electron 1 for the case of the nuclei in the state $|\Downarrow_1\Downarrow_2\rangle$ **(a.)**, $|\Downarrow_1\Uparrow_2\rangle$ **(b.)**, $|\Uparrow_1\Downarrow_2\rangle$ **(c.)**, $|\Uparrow_1\Uparrow_2\rangle$ **(d.)** plotted on a log scale of $J/\bar{A}$. Each inset shows a zoomed region of the plot for clarity. The colors of the transitions are scaled according to the probility of the transition, given by $P_{\text{ESR}}\Delta S_{1z}$ where $P_{\text{ESR}} = |\langle\psi_i|(S_{1x} + S_{2x})|\psi_f\rangle|^2$ and $\Delta S_{1z} = \langle\psi_f|S_{1z}|\psi_f\rangle - \langle\psi_i|S_{1z}|\psi_i\rangle$ where $|\psi_i\rangle$ and $|\psi_f\rangle$ represent the initial and final state of electron 1 respectively. The term ΔS_{1z} is present in the scaling factor to mimic the readout of the electron experimentally, which occurs along the z-axis of the Bloch sphere (see section 3.9.3). The simulation code used for these simulations was written by Dr Rachpon Kalra during his time at the University of New South Wales [114].

Figure 4.2 shows the simulated ESR spectrum for the electron bound to donor 1, referred to as electron 1, in an exchange-coupled donor system. The system has been simulated

for each of the four possible two-nuclear states: $|\Downarrow_1\Downarrow_2\rangle, |\Downarrow_1\Uparrow_2\rangle, |\Uparrow_1\Downarrow_2\rangle$ and $|\Uparrow_1\Uparrow_2\rangle$ over a range of J values spanning from $J \ll \bar{A}$ to $J \gg \bar{A}$.

For the case of the nuclei in the $|\Downarrow_1\Downarrow_2\rangle$ configuration (Fig.4.2, a) the following transition frequencies are present:

$$\nu_1 = T_- \longleftrightarrow \widetilde{S}, \tag{4.10}$$

$$\nu_2 = T_- \longleftrightarrow T_0, T_0 \longleftrightarrow T_+, \tag{4.11}$$

$$\nu_3 = \widetilde{S} \longleftrightarrow T_+, \tag{4.12}$$

where $\widetilde{S}$ represents a singlet-like state. In the limits of high J this singlet-like state becomes a pure singlet, with a total spin of zero and thus can no longer be driven with ESR. For the case of $J \gg \bar{A}$, ν_2 represents the combined transition between $T_- \longleftrightarrow T_0$ and $T_0 \longleftrightarrow T_+$. In the limit of small J however, these transitions become split in frequency by $\Delta A = |A_1 - A_2|$ and hence can be individually addressed.

For the case of the nuclei in the $|\Downarrow_1\Uparrow_2\rangle$ configuration (Fig.4.2, b) the transition frequencies present are the following. Electron 1 has been highlighted in blue to indicate that we are considering the frequency spectrum of this electron only, in the following discussion:

$$\nu_4 = |\downarrow_1 \downarrow_2\rangle \longleftrightarrow |\widetilde{\uparrow_1 \downarrow_2}\rangle, \tag{4.13}$$

$$\nu_5 = |\widetilde{\downarrow_1 \uparrow_2}\rangle \longleftrightarrow |\uparrow_1 \uparrow_2\rangle, \tag{4.14}$$

$$\nu_6 = |\downarrow_1 \downarrow_2\rangle \longleftrightarrow |\widetilde{\downarrow_1 \uparrow_2}\rangle, \tag{4.15}$$

$$\nu_7 = |\widetilde{\uparrow_1 \downarrow_2}\rangle \longleftrightarrow |\uparrow_1 \uparrow_2\rangle, \tag{4.16}$$

where $|\widetilde{\downarrow_1 \uparrow_2}\rangle = \cos(\theta)\,|\downarrow_1 \uparrow_2\rangle + \sin(\theta)\,|\uparrow_1 \downarrow_2\rangle$, $|\widetilde{\uparrow_1 \downarrow_2}\rangle = \cos(\theta)\,|\uparrow_1 \downarrow_2\rangle + \sin(\theta)\,|\downarrow_1 \uparrow_2\rangle$ and $\tan(2\theta) = \frac{J}{\bar{A}}$. ν_6 and ν_7 represents transitions to flip electron 2 for the $|\Downarrow_1\Uparrow_2\rangle$ nuclear state. The reason that these transitions are seen in the ESR spectrum for electron 1 is due to the fact that for $J > 0$, the eigenstates of the two-electron system are no longer the product

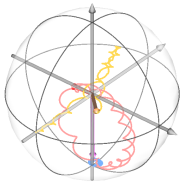

states $|\downarrow_1\downarrow_2\rangle$, $|\downarrow_1\uparrow_2\rangle$, $|\uparrow_1\downarrow_2\rangle$ and $|\uparrow_1\uparrow_2\rangle$ but rather the hybridised states $|\downarrow_1\downarrow_2\rangle$, $\widetilde{|\downarrow_1\uparrow_2\rangle}$, $\widetilde{|\uparrow_1\downarrow_2\rangle}$ and $|\uparrow_1\uparrow_2\rangle$. This hybridisation of states introduces an additional excitation of electron 1 upon driving electron 2 (and vice versa for driving electron 1). The magnitude of this excitation depends on the value of $\theta = \frac{1}{2}\arctan(\frac{J}{A})$. For $J \to \infty, \theta \to \frac{\pi}{4}$ and hence $\widetilde{|\downarrow_1\uparrow_2\rangle} = \widetilde{|\uparrow_1\downarrow_2\rangle} = \frac{1}{\sqrt{2}}(|\downarrow_1\uparrow_2\rangle + |\uparrow_1\downarrow_2\rangle)$. For $J \to 0$ however $\theta \to 0$ and hence $\widetilde{|\uparrow_1\downarrow_2\rangle} = |\uparrow_1\downarrow_2\rangle$ and $\widetilde{|\downarrow_1\uparrow_2\rangle} = |\downarrow_1\uparrow_2\rangle$ resulting in an increasingly smaller excitation of electron 1 upon driving electron 2.

As J increases, ν_5 and ν_6 tend towards the transitions $T_0 \longleftrightarrow T_+$ and $T_- \longleftrightarrow T_0$ respectively. In the limits of low J these transitions are split by ΔA however, the two transitions become degenerate as $J \to \infty$.

For the case of the nuclei in the $|\Uparrow_1\Downarrow_2\rangle$ configuration (Fig.4.2, c) the transition frequencies present are the following:

$$\nu_8 = |\downarrow_1 \downarrow_2\rangle \longleftrightarrow \widetilde{|\downarrow_1 \uparrow_2\rangle}, \tag{4.17}$$

$$\nu_9 = \widetilde{|\uparrow_1 \downarrow_2\rangle} \longleftrightarrow |\uparrow_1 \uparrow_2\rangle\,, \tag{4.18}$$

$$\nu_{10} = |\downarrow_1 \downarrow_2\rangle \longleftrightarrow \widetilde{|\uparrow_1 \downarrow_2\rangle}, \tag{4.19}$$

$$\nu_{11} = \widetilde{|\downarrow_1 \uparrow_2\rangle} \longleftrightarrow |\uparrow_1 \uparrow_2\rangle\,. \tag{4.20}$$

$\nu 8$ and ν_9 represent transitions to flip electron 2 conditional on the nuclear state $|\Uparrow_1\Downarrow_2\rangle$. These transitions are observed in the ESR spectrum of electron 1 as a result of the hybridisation of the electron states for $J > 0$ as explained above. As for the case of the $|\Downarrow_1\Uparrow_2\rangle$ nuclear state, ν_9 and ν_{10} become degenerate as $J \to \infty$.

For the case of the nuclei in the $|\Uparrow_1\Uparrow_2\rangle$ configuration (Fig.4.2, d) the transition frequencies present are:

$$\nu_{12} = T_- \longleftrightarrow \widetilde{S}, \tag{4.21}$$

$$\nu_{13} = T_- \longleftrightarrow T_0, T_0 \longleftrightarrow T_+, \tag{4.22}$$

$$\nu_{14} = \widetilde{S} \longleftrightarrow T_+. \tag{4.23}$$

These transitions are identical in nature to the transitions present for the $|\Downarrow_1\Downarrow_2\rangle$ nuclear state.

4.2.3 Two-qubit gates in an exchange-coupled system

There exists two distinct two-qubit gate implementations that are native to the electrons of an exchange-coupled system: the SWAP$^\alpha$ gate and the controlled-rotation (CROT) gate [114].

4.2.3.1 The SWAP$^\alpha$ gate

The SWAP$^\alpha$ gate represents one of the simplest two-qubit entangling operations which, when combined with single qubit rotations, makes up a universal gate set for quantum computation [126]. The implementation of the SWAP$^\alpha$ gate can be understood by studying the $|S\rangle - |T_0\rangle$ Bloch sphere of a two-spin system, as shown in Figure 4.3.

A SWAP$^\alpha$ operation represents a rotation by an angle $\alpha\pi$ about the J-axis of the $|S\rangle - |T_0\rangle$ Bloch sphere shown in Figure 4.3. In the limit of $J \gg \Delta$, the eigenstates of the system are approximately the $|S\rangle$ and $|T_0\rangle$ states. Therefore, upon initialising the two electrons in either the $|\downarrow\uparrow\rangle$ or $|\uparrow\downarrow\rangle$ state, the electrons will precess about the J axis of the $|S\rangle - |T_0\rangle$ Bloch sphere, between the states $|\downarrow\uparrow\rangle$ and $|\uparrow\downarrow\rangle$.

The implementation of a high-fidelity SWAP$^\alpha$ gate in an exchange-coupled system requires the ability to tune J to the regime for which $J \gg \Delta$ for the amount of time required for the spins to rotate an angle α around the J axis, given by $t = \frac{\alpha}{2\sqrt{J^2+\Delta^2}}$, before tuning J to the regime for which $J \ll \Delta$, such that no residual, unwanted rotation between the $|\downarrow\uparrow\rangle$ and $|\uparrow\downarrow\rangle$ states occurs once the SWAP$^\alpha$ gate has been implemented. In the donor system,

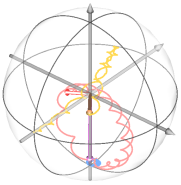

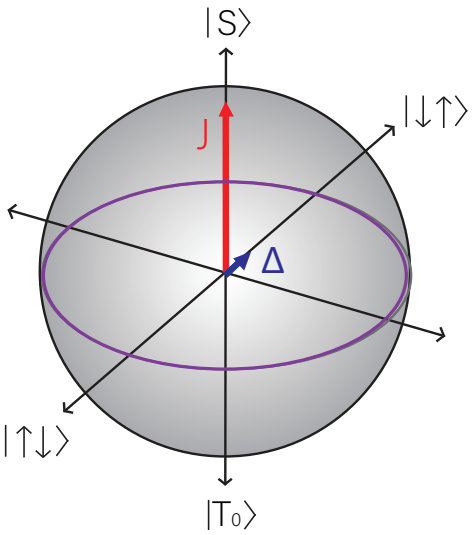

Figure 4.3: $S - T_0$ **Bloch sphere.** J is pointing along the $|S\rangle - |T_0\rangle$ axis, while the detuning between the qubits, Δ is along the $|{\downarrow\uparrow}\rangle$, $|{\uparrow\downarrow}\rangle$ axis. The purple line depicts the path around the Bloch sphere of a spin initialised in the $|{\downarrow\uparrow}\rangle$ or $|{\uparrow\downarrow}\rangle$ for the case of $J \gg \Delta$.

as mentioned in section 4.2.2, the J value can be switched in a binary fashion between the regimes of $J \gg \Delta = \Delta A$ and $J \ll \Delta = \bar{A}$ simply by flipping the donor nuclei from a parallel to an anti-parallel spin orientation. A SWAP$^\alpha$ gate can therefore be implemented in this system by initialising the electrons into an anti-parallel spin orientation of either $|{\downarrow\uparrow}\rangle$ or $|{\uparrow\downarrow}\rangle$ and digitally switching between the 'on' and 'off' regime (defined as the regimes of $J \ll \Delta$ and $J \gg \Delta$ respectively) by flipping the nuclei between a parallel and anti-parallel spin orientation. The fidelity of the SWAP$^\alpha$ gate implemented using this technique however, becomes compromised as the value of J approaches $\frac{1}{t_{\pi,n}}$ where $t_{\pi,n}$ is the π time of the nucleus. As $t_{\pi,n} \approx 100\mu$s in a typical donor system, this places severe restraints on the maximum value of J that still allows a high fidelity SWAP$^\alpha$ to be implemented with this technique.

4.2.3.2 The CROT gate

Another native two-qubit gate present in the exchange-coupled system is the controlled rotation (CROT) gate or zero-controlled rotation (zCROT). In this thesis we define the

CROT gate as a rotation of the target electron, conditional on the control electron being in the spin $|\downarrow\rangle = |1\rangle$ state and the zCROT gate as a rotation of the target electron, conditional on the control electron being in the spin $|\uparrow\rangle = |0\rangle$ state.

For a rotation around the x-axis of the Bloch sphere the unitary operations that define the CROT and zCROT gates for electrons 1 and 2 are therefore the following:

$$\mathrm{CROT}_{\updownarrow_1\downarrow_2} = \begin{pmatrix} 0 & 0 & -i & 0 \\ 0 & 1 & 0 & 0 \\ -i & 0 & 0 & 0 \\ 0 & 0 & 0 & 1 \end{pmatrix}, \mathrm{CROT}_{\downarrow_1\updownarrow_2} = \begin{pmatrix} 0 & -i & 0 & 0 \\ -i & 0 & 0 & 0 \\ 0 & 0 & 1 & 0 \\ 0 & 0 & 0 & 1 \end{pmatrix} \tag{4.24}$$

$$\mathrm{zCROT}_{\updownarrow_1\uparrow_2} = \begin{pmatrix} 1 & 0 & 0 & 0 \\ 0 & 0 & 0 & -i \\ 0 & 0 & 1 & 0 \\ 0 & -i & 0 & 0 \end{pmatrix}, \mathrm{zCROT}_{\uparrow_1\updownarrow_2} = \begin{pmatrix} 1 & 0 & 0 & 0 \\ 0 & 1 & 0 & 0 \\ 0 & 0 & 0 & -i \\ 0 & 0 & -i & 0 \end{pmatrix}, \tag{4.25}$$

where $\updownarrow$ represents the electron being driven during the gate implementation. The CROT gate is equivalent to a CNOT gate but, with the addition of a phase imparted on the control qubit. This phase comes about as a result of the geometric phase imparted by the target electron on the control and is equal to half the rotation angle of the target electron.

As introduced in section 4.2.2, in the regime for which $J \gg \Delta$, created by initialising the nuclei in an anti-parallel spin orientation, whereby $\Delta = \bar{A}$, each resonance on the electrons represents a rotation of one electron, conditional on the state of the other electron. In this regime, a π rotation of either electron thus constitutes the implementation of a native CROT or zCROT gate.

In the perfect implementation of a CROT or zCROT gate, the electrons would undergo

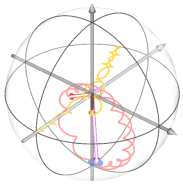

rotations between the exact computational states, $|{\downarrow_1}{\downarrow_2}\rangle, |{\downarrow_1}{\uparrow_2}\rangle, |{\uparrow_1}{\downarrow_2}\rangle, |{\uparrow_1}{\uparrow_2}\rangle$. For example, for the case of the ideal CROT gate performed on electron 1, the electrons would undergo a transition between the states $|{\downarrow_1}{\downarrow_2}\rangle \longleftrightarrow |{\uparrow_1}{\downarrow_2}\rangle$. As discussed in section 4.2.2, in the regime for which $\Delta A < J < \bar{A}$ however, the eigenstates of the electrons are instead the hybridised states $|{\downarrow_1}{\downarrow_2}\rangle, \widetilde{|{\downarrow_1}{\uparrow_2}\rangle}, \widetilde{|{\uparrow_1}{\downarrow_2}\rangle}, |{\uparrow_1}{\uparrow_2}\rangle$ and hence a CROT gate on electron 1 represents a transition between the states $|{\downarrow_1}{\downarrow_2}\rangle \longleftrightarrow \widetilde{|{\uparrow_1}{\downarrow_2}\rangle}$. The hybridisation of states thus introduces an inherent error associated with the implementation of the CROT or zCROT gate, the magnitude of which is given by $\sin^2(\theta)$, where $\tan(2\theta) = \frac{J}{\Delta}$.

4.3 Entanglement

4.3.1 Generating entanglement in an exchange-coupled system

A universal gate set for quantum computation cannot consist solely of single-qubit gates alone but, must also consist of a two-qubit gate that is capable of generating entanglement. As discussed in section 4.2.3, in the presence of the exchange interaction, two native two-qubit gates exist in the system: the SWAP$^\alpha$ gate and the CROT gate. Although the SWAP$^\alpha$ gate also represents an entangling operation between qubits (for the case of $\alpha = \frac{\pi}{2}$), we will focus primarily on the utilisation of the native CROT gate to generate entanglement, as the CROT and zCROT gates form the basis of the majority of the work carried out in this thesis.

In the exchange-coupled donor system, we use the two-qubit CROT gate to generate entanglement between the electrons by first preparing one of the electrons in the spin down state, $|\downarrow\rangle$, and the other electron in a superposition state, $\frac{1}{\sqrt{2}}(|\downarrow + \uparrow\rangle)$, with a $\frac{\pi}{2}$ pulse. The state of the two electrons is therefore given by the following

$$|\downarrow\rangle \otimes \frac{1}{\sqrt{2}}(|\downarrow\rangle + |\uparrow\rangle) = \frac{1}{\sqrt{2}}(|\downarrow\downarrow\rangle + |\downarrow\uparrow\rangle). \tag{4.26}$$

A CROT or zCROT pulse is then applied to the electron in the $|\downarrow\rangle$ state, to flip this electron conditional on the electron in a superposition state being in the spin $|\downarrow\rangle$ state or

$|\uparrow\rangle$ state respectively. For the example of a CROT gate this thus results in the following

$$\frac{1}{\sqrt{2}}(|\downarrow\downarrow\rangle + |\downarrow\uparrow\rangle) \rightarrow^{\text{CROT}} \frac{1}{\sqrt{2}}(|\uparrow\downarrow\rangle + |\downarrow\uparrow\rangle), \tag{4.27}$$

where $\frac{1}{\sqrt{2}}(|\uparrow\downarrow\rangle + |\downarrow\uparrow\rangle)$ represents a fully entangled state (see section 4.3.3). And similarly for the application of a zCROT gate

$$\frac{1}{\sqrt{2}}(|\downarrow\downarrow\rangle + |\downarrow\uparrow\rangle) \rightarrow^{\text{zCROT}} \frac{1}{\sqrt{2}}(|\downarrow\downarrow\rangle + |\uparrow\uparrow\rangle), \tag{4.28}$$

where $\frac{1}{\sqrt{2}}(|\downarrow\downarrow\rangle + |\uparrow\uparrow\rangle)$ also represents a fully entangled state (see section 4.3.3).

Figure 4.4 introduces the circuit representation of the procedure outlined above, the notation of which will be used throughout the remainder of this thesis.

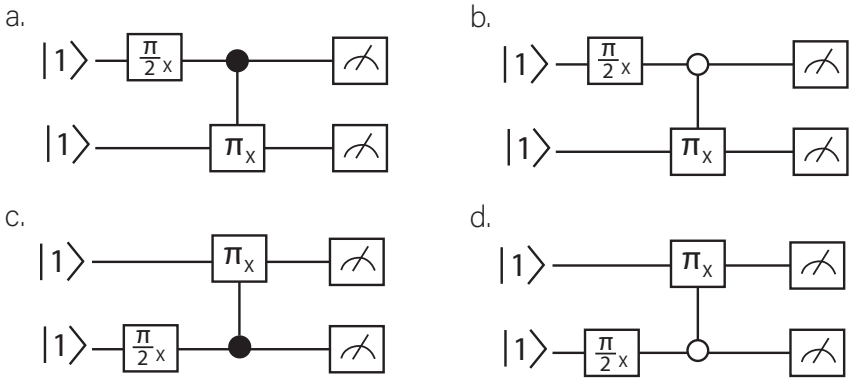

Figure 4.4: **Circuit diagram representation of generating entanglement with the CROT gate.** The top(bottom) horizontal line of each circuit diagram depicts the operations performed on electron 1(2). The electrons are initially prepared in the $|\downarrow\rangle = |1\rangle$ state. The $\frac{\pi}{2}_X$ represents a $\frac{\pi}{2}$ pulse applied along the x-direction of the Bloch sphere. The CROT or zCROT gate (which are also applied along the x-direction of the Bloch sphere in this example) are represented by the conditional π_X gate, with the state on which the gate is conditioned indicated by either a full circle ($|\downarrow\rangle = |1\rangle$ state) or an empty circle ($|\uparrow\rangle = ||0\rangle\rangle$ state). Consequently, **a,c** represents circuits containing CROT operations, while **b,d** represent circuits containing the zCROT operation. At the end of each circuit both electrons are measured as indicated by the circuit symbol for a measurement on both the upper and lower circuit line.

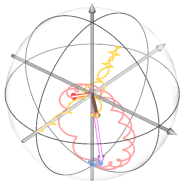

4.3.2 Quantifying entanglement

Entanglement is a precious resource for quantum computing and thus it is important, when assessing the fidelity of a quantum processor, to ascertain the degree of entanglement that we are able to generate. There are three well-established metrics used to ascertain the degree of entanglement of a state: entanglement entropy, concurrence and state fidelity.

4.3.2.1 Entanglement entropy

One of the defining features of an entangled state between two subsystems, which we can refer to as subsystem A and B, is that upon entangling A and B together, both subsystems no longer possess their own definite quantum state. Entanglement entropy is a metric that uses the classical analogy of entropy from thermodynamics, to quantify the degree of uncertainty that arises from the lack of definite quantum state associated with a particle that forms a subsystem of an entangled state [127].

The entanglement entropy of the subsystem A of a joint state of A and B can be calculated with the expression

$$S_A = -\mathrm{Tr}_A\{\hat{\rho_A}\ln(\hat{\rho_A})\}, \tag{4.29}$$

where Tr_A represents the partial trace used to extract the component space of the density matrix, A, and $\hat{\rho_A}$ is the density matrix associated with subsystem A [127].

The quantity of entanglement entropy has the following bounds

$$0 \leq S_A \leq \ln(d), \tag{4.30}$$

where d represents the dimensions of the individual constituents of the entangled system. The origin of the upper bound for the entanglement entropy can be understood by

considering the example of the fully-entangled singlet state, $|S\rangle$, which consists of two subsystems, each with a dimension of $d = 2$. The density operator for the singlet state, $\hat{\rho}(S)$ is given by

$$\hat{\rho}(S) = |S\rangle \langle S| = \frac{1}{2}(|\uparrow\downarrow\rangle - |\downarrow\uparrow\rangle)(\langle\uparrow\downarrow| - \langle\downarrow\uparrow|). \tag{4.31}$$

Tracing out the subsystem B, which describes the second spin, we are left with the following reduced density matrix

$$\hat{\rho_A} = \frac{1}{2}(|\uparrow\uparrow + \downarrow\downarrow\rangle). \tag{4.32}$$

Written in the basis $\{|\downarrow\rangle, |\uparrow\rangle\}$, $\hat{\rho_A}$ can be written in matrix form as

$$\hat{\rho_A} = \begin{pmatrix} \frac{1}{2} & 0 \\ 0 & \frac{1}{2} \end{pmatrix}. \tag{4.33}$$

The entanglement entropy is therefore calculated as [127]

$$S_A = -\mathrm{Tr}_A\{\hat{\rho_A}\ln(\hat{\rho_A})\} = -\mathrm{Tr}\begin{pmatrix} \frac{1}{2}\ln(\frac{1}{2}) & 0 \\ 0 & \frac{1}{2}\ln(\frac{1}{2}) \end{pmatrix} = \ln(2). \tag{4.34}$$

The entanglement entropy of a fully entangled state, where the dimension of the subsystems that make up the entangled state are each $d = 2$, is thus $\ln(2)$.

4.3.2.2 Concurrence

Another metric used to determine the degree of entanglement is a quantity known as concurrence, C. The definition of concurrence, which currently only exists for pairs of qubits, is given by [128]

$$C = |\langle\Phi|\tilde{\Phi}\rangle|, \tag{4.35}$$

where $|\Phi\rangle$ is the state of a pair of qubits, written in the basis $\{|00\rangle, |01\rangle, |10\rangle, |11\rangle\}$. $|\tilde{\Phi}\rangle = (\hat{\sigma_y} \otimes \hat{\sigma_y})|\Phi^*\rangle$ is the 'spin-flip' operation where $|\Phi^*\rangle$ is the complex conjugate of $|\Phi\rangle$

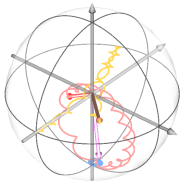

and σ_y is the Pauli-y matrix. When applied to a state, the spin-flip operator will take each qubit to the orthogonal state on the Bloch sphere. Physically the concurrence therefore represents the overlap between a state $|\Phi\rangle$ and a state that is diametrically opposite to $|\Phi\rangle$ on the Bloch sphere.

For the case in which $|\Phi\rangle$ represents a pure state, the overlap between $|\Phi\rangle$ and a state that is orthogonal to $|\Phi\rangle$ on the Bloch sphere, $|\tilde{\Phi}\rangle$, is 0 and thus for the case of a pure state, the concurrence, $C = 0$. In order to understand the implications of applying the spin flip operation to an entangled state, we can use the example of the singlet state, $|S\rangle$, and the triplet state, $|T_0\rangle$; referring back to the geometric interpretations of these states discussed in section 4.1. For the case of the singlet state, which geometrically represents a state of anti-parallel spins pointing along some undefined direction on the Bloch sphere, this state is left invariant, up to a phase factor, to a spin flip. In this case the overlap $|\langle\Phi|\tilde{\Phi}\rangle| = 1$ and thus $C = 1$. Similarly, for the case of the $|T_0\rangle$ state, which geometrically represents, a state of parallel spins pointing along some undefined direction in the xy plane of the Bloch sphere, this state is also invariant to the spin flip operation and therefore the concurrence $C = 1$ also for this state. A concurrence value of 1 therefore represents a fully entangled state, while a concurrence value of 0 represents a completely pure state [129,130].

Experimentally, the most straightforward method of calculating the concurrence is by reconstructing the density matrix of the physical system (as discussed in sections 4.3.3 and 4.3.4) and calculating the quantity [128]

$$\hat{R} = \sqrt{\sqrt{\hat{\rho}}\tilde{\rho}\sqrt{\hat{\rho}}}. \tag{4.36}$$

where $\hat{\rho}$ is the measured density matrix and $\tilde{\rho}$ is the result of applying the spin flip operation to $\hat{\rho}$, given by

$$\tilde{\rho} = (\hat{\sigma}_y \otimes \hat{\sigma}_y)\hat{\rho}^*(\hat{\sigma}_y \otimes \hat{\sigma}_y), \tag{4.37}$$

where $\hat{\rho}^*$ is the complex conjugate transpose of the measured density matrix. The value of concurrence is then given by

$$C = max\{0, \lambda_1 - \lambda_2 - \lambda_3 - \lambda_4\}, \tag{4.38}$$

where λ_i are the square roots of the eigenvalues of $\hat{R}$ in decreasing order.

4.3.2.3 State fidelity

The final commonly utilised method of quantifying the degree of entanglement in a system is to prepare a known entangled state and then calculate the fidelity with which the measured state that has been experimentally prepared, corresponds to the expected entangled state. This fidelity is obtained by calculating the overlap between the measured density matrix, $\hat{\rho}$ (discussed in sections 4.3.3 and 4.3.4) and the entangled state that we wished to prepare, $\hat{\rho}_{\text{entangled}}$, which is given by

$$F = \langle \psi_{\text{entangled}} | \hat{\rho} | \psi_{\text{entangled}} \rangle \, . \tag{4.39}$$

where $\hat{\rho}_{\text{entangled}} = |\psi_{\text{entangled}}\rangle \langle \psi_{\text{entangled}}|$. A fidelity of 1 indicates that the prepared state, $\hat{\rho}$ fully overlaps with the entangled state $\hat{\rho}_{\text{entangled}}$. A fidelity of 0 on the other hand, indicates that there is no overlap between the prepared state $\hat{\rho}$ and the entangled state $\hat{\rho}_{\text{entangled}}$. Although this does not necessarily mean that $\hat{\rho}$ does not represent an entangled state (as it could represent a different entangled state that is orthogonal to $\hat{\rho}_{\text{entangled}}$) a fidelity of < 1 is an indication that there has been some error in preparing the intended entangled state $\hat{\rho}_{\text{entangled}}$.

All of these techniques of quantifying the degree of entanglement of a density matrix, $\hat{\rho}$, require us to have access to the density matrix of a given prepared state. The two most commonly used methods of experimentally extracting the density matrix of a prepared entangled state are: Bell state tomography [131] and phase reversal tomography [132].

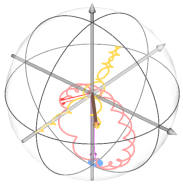

4.3.3 Bell state tomography

Bell states are four specific, maximally entangled states of a two-qubit system and are given by

$$|\Phi^+\rangle = \frac{1}{\sqrt{2}}(|00\rangle + |11\rangle), \tag{4.40}$$

$$|\Phi^-\rangle = \frac{1}{\sqrt{2}}(|00\rangle - |11\rangle), \tag{4.41}$$

$$|\Psi^+\rangle = \frac{1}{\sqrt{2}}(|01\rangle + |10\rangle), \tag{4.42}$$

$$|\Psi^-\rangle = \frac{1}{\sqrt{2}}(|01\rangle - |10\rangle). \tag{4.43}$$

Bell state tomography involves preparing a given Bell state, before reconstructing the density matrix of the prepared state, using state tomography, and comparing the resulting matrix to the expected density matrix.

Any qubit density matrix can be written as a superposition of the Pauli matrices, $\hat{\sigma}_{\mathbb{I}} = \begin{pmatrix} 1 & 0 \\ 0 & 1 \end{pmatrix}, \hat{\sigma}_x = \begin{pmatrix} 0 & 1 \\ 1 & 0 \end{pmatrix}, \hat{\sigma}_y = \begin{pmatrix} 0 & -j \\ j & 0 \end{pmatrix}, \hat{\sigma}_z = \begin{pmatrix} 1 & 0 \\ 0 & -1 \end{pmatrix}$ using the following:

$$\hat{\rho} = \frac{1}{2}\mathbb{I} + \frac{1}{2}\sum_{i=1}^{i=4^n-1} S_i\hat{\sigma}_i, \tag{4.44}$$

where n represents the number of qubits in the system, $\sigma_i = \{\hat{\sigma}_{\mathbb{I}}, \hat{\sigma}_x, \hat{\sigma}_y, \hat{\sigma}_z\}$ and S_i are the Stokes parameters, which together form the Stokes vector, $\vec{S} = (S_1, S_2, S_3, ...S_{4^n-1})$ [133, 134]. For the case of a pure state, the magnitude of the Stokes vector is $|\vec{S}| = 1$. For a mixed state however, the state no longer lies on the surface of the Bloch sphere and instead shrinks towards the centre of the Bloch sphere, resulting in $|\vec{S}| < 1$.

The Stokes parameters can be calculated from the the density matrix $\hat{\rho}$ with the following formula

$$S_i = \mathrm{Tr}[\hat{\sigma}_i \hat{\rho}]. \tag{4.45}$$

In order to experimentally determine the Stokes parameters for a given system and hence reconstruct the density matrix we must therefore perform a set of measurements on the qubits in the three bases: x, y and z. We can define $P_{|\downarrow_i\rangle}(P_{|\uparrow_i\rangle})$ as the probability of obtaining the result $|\downarrow_i\rangle\,(|\uparrow_i\rangle)$ upon measuring the qubit in the basis $\{|\downarrow_i\rangle, |\uparrow_i\rangle\}$. Using this notation, the Stokes parameters for the example of a single qubit can be calculated as the following [131, 133, 134]

$$S_0 = S_i = P_{|\downarrow_x\rangle} + P_{|\uparrow_x\rangle} = P_{|\downarrow_y\rangle} + P_{|\uparrow_y\rangle} = P_{|\downarrow_z\rangle} + P_{|\uparrow_z\rangle} = 1, \tag{4.46}$$

$$S_1 = S_x = P_{|\downarrow_x\rangle} - P_{|\uparrow_x\rangle}, \tag{4.47}$$

$$S_2 = S_y = P_{|\downarrow_y\rangle} - P_{|\uparrow_y\rangle}, \tag{4.48}$$

$$S_3 = S_z = P_{|\downarrow_z\rangle} - P_{|\uparrow_z\rangle}. \tag{4.49}$$

Similarly, for the case of a two-qubit system the Stokes parameters are calculated as:

$$\begin{aligned}
S_0 = S_{ii} &= (P_{|\downarrow_z\rangle} + P_{|\uparrow_z\rangle}) \otimes (P_{|\downarrow_z\rangle} + P_{|\uparrow_z\rangle}) = P_{|\downarrow_z\downarrow_z\rangle} + P_{|\downarrow_z\uparrow_z\rangle} + P_{|\uparrow_z\downarrow_z\rangle} + P_{|\uparrow_z\uparrow_z\rangle},\\
S_1 = S_{iz} &= (P_{|\downarrow_z\rangle} + P_{|\uparrow_z\rangle}) \otimes (P_{|\downarrow_z\rangle} - P_{|\uparrow_z\rangle}) = P_{|\downarrow_z\downarrow_z\rangle} - P_{|\downarrow_z\uparrow_z\rangle} + P_{|\uparrow_z\downarrow_z\rangle} - P_{|\uparrow_z\uparrow_z\rangle},\\
S_2 = S_{ix} &= (P_{|\downarrow_z\rangle} + P_{|\uparrow_z\rangle}) \otimes (P_{|\downarrow_x\rangle} - P_{|\uparrow_x\rangle}) = P_{|\downarrow_z\downarrow_x\rangle} - P_{|\downarrow_z\uparrow_x\rangle} + P_{|\uparrow_z\downarrow_x\rangle} - P_{|\uparrow_z\uparrow_x\rangle},\\
S_3 = S_{iy} &= (P_{|\downarrow_z\rangle} + P_{|\uparrow_z\rangle}) \otimes (P_{|\downarrow_y\rangle} - P_{|\uparrow_y\rangle}) = P_{|\downarrow_z\downarrow_y\rangle} - P_{|\downarrow_z\uparrow_y\rangle} + P_{|\uparrow_z\downarrow_y\rangle} - P_{|\uparrow_z\uparrow_y\rangle},
\end{aligned}$$

$$\begin{aligned}
S_4 = S_{xi} &= (P_{|\downarrow_x\rangle} - P_{|\uparrow_x\rangle}) \otimes (P_{|\downarrow_z\rangle} + P_{|\uparrow_z\rangle}) = P_{|\downarrow_x\downarrow_z\rangle} + P_{|\downarrow_x\uparrow_z\rangle} - P_{|\uparrow_x\downarrow_z\rangle} - P_{|\uparrow_x\uparrow_z\rangle},\\
S_5 = S_{xz} &= (P_{|\downarrow_x\rangle} - P_{|\uparrow_x\rangle}) \otimes (P_{|\downarrow_z\rangle} - P_{|\uparrow_z\rangle}) = P_{|\downarrow_x\downarrow_z\rangle} - P_{|\downarrow_x\uparrow_z\rangle} - P_{|\uparrow_x\downarrow_z\rangle} + P_{|\uparrow_x\uparrow_z\rangle},\\
S_6 = S_{xx} &= (P_{|\downarrow_x\rangle} - P_{|\uparrow_x\rangle}) \otimes (P_{|\downarrow_x\rangle} - P_{|\uparrow_x\rangle}) = P_{|\downarrow_x\downarrow_x\rangle} - P_{|\downarrow_x\uparrow_x\rangle} - P_{|\uparrow_x\downarrow_x\rangle} + P_{|\uparrow_x\uparrow_x\rangle},\\
S_7 = S_{xy} &= (P_{|\downarrow_x\rangle} - P_{|\uparrow_x\rangle}) \otimes (P_{|\downarrow_y\rangle} - P_{|\uparrow_y\rangle}) = P_{|\downarrow_x\downarrow_y\rangle} - P_{|\downarrow_x\uparrow_y\rangle} - P_{|\uparrow_x\downarrow_y\rangle} + P_{|\uparrow_x\uparrow_y\rangle},
\end{aligned}$$

$$\begin{aligned}
S_8 = S_{yi} &= (P_{|\downarrow_y\rangle} - P_{|\uparrow_y\rangle}) \otimes (P_{|\downarrow_z\rangle} + P_{|\uparrow_z\rangle}) = P_{|\downarrow_y\downarrow_z\rangle} + P_{|\downarrow_y\uparrow_z\rangle} - P_{|\uparrow_y\downarrow_z\rangle} - P_{|\uparrow_y\uparrow_z\rangle},\\
S_9 = S_{yz} &= (P_{|\downarrow_y\rangle} - P_{|\uparrow_y\rangle}) \otimes (P_{|\downarrow_z\rangle} - P_{|\uparrow_z\rangle}) = P_{|\downarrow_y\downarrow_z\rangle} - P_{|\downarrow_y\uparrow_z\rangle} - P_{|\uparrow_y\downarrow_z\rangle} + P_{|\uparrow_y\uparrow_z\rangle},\\
S_{10} = S_{yx} &= (P_{|\downarrow_y\rangle} - P_{|\uparrow_y\rangle}) \otimes (P_{|\downarrow_x\rangle} - P_{|\uparrow_x\rangle}) = P_{|\downarrow_y\downarrow_x\rangle} - P_{|\downarrow_y\uparrow_x\rangle} - P_{|\uparrow_y\downarrow_x\rangle} + P_{|\uparrow_y\uparrow_x\rangle},\\
S_{11} = S_{yy} &= (P_{|\downarrow_y\rangle} - P_{|\uparrow_y\rangle}) \otimes (P_{|\downarrow_y\rangle} - P_{|\uparrow_y\rangle}) = P_{|\downarrow_y\downarrow_y\rangle} - P_{|\downarrow_y\uparrow_y\rangle} - P_{|\uparrow_y\downarrow_y\rangle} + P_{|\uparrow_y\uparrow_y\rangle},
\end{aligned}$$

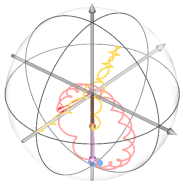

$$S_{12} = S_{zi} = (P_{|\downarrow_z\rangle} - P_{|\uparrow_z\rangle}) \otimes (P_{|\downarrow_z\rangle} + P_{|\uparrow_z\rangle}) = P_{|\downarrow_z\downarrow_z\rangle} + P_{|\downarrow_z\uparrow_z\rangle} - P_{|\uparrow_z\downarrow_z\rangle} - P_{|\uparrow_z\uparrow_z\rangle},$$
$$S_{13} = S_{zz} = (P_{|\downarrow_z\rangle} - P_{|\uparrow_z\rangle}) \otimes (P_{|\downarrow_z\rangle} - P_{|\uparrow_z\rangle}) = P_{|\downarrow_z\downarrow_z\rangle} - P_{|\downarrow_z\uparrow_z\rangle} - P_{|\uparrow_z\downarrow_z\rangle} + P_{|\uparrow_z\uparrow_z\rangle},$$
$$S_{14} = S_{zx} = (P_{|\downarrow_z\rangle} - P_{|\uparrow_z\rangle}) \otimes (P_{|\downarrow_x\rangle} - P_{|\uparrow_x\rangle}) = P_{|\downarrow_z\downarrow_x\rangle} - P_{|\downarrow_z\uparrow_x\rangle} - P_{|\uparrow_z\downarrow_x\rangle} + P_{|\uparrow_z\uparrow_x\rangle},$$
$$S_{15} = S_{zy} = (P_{|\downarrow_z\rangle} - P_{|\uparrow_z\rangle}) \otimes (P_{|\downarrow_y\rangle} - P_{|\uparrow_y\rangle}) = P_{|\downarrow_z\downarrow_y\rangle} - P_{|\downarrow_z\uparrow_y\rangle} - P_{|\uparrow_z\downarrow_y\rangle} + P_{|\uparrow_z\uparrow_y\rangle}.$$

Experimentally, in order to measure the Bell states along the different projection axis, we must re-prepare the Bell state for each projection axis measured. In the donor spin system, we are only able to directly measure along the z-axis of the spin using spin dependent tunneling (see section 3.9.3). In order to measure the projection along the x or y axis we must therefore append a projection pulse to the end of the Bell state preparation pulse, to map the information along the x or y axis onto the z-axis of the Bloch sphere. For example, to measure the projection along the +x axis, we can apply a $\frac{\pi}{2}$ projection pulse about the -y axis (i.e. with a phase of -90^0) in order to rotate the information along the +x axis, to the +z axis of the Bloch sphere, where it can then be read out via spin-dependent tunnelling.

Upon measuring the required Stokes parameters, the density matrix, $\hat{\rho}$, of the state can be reconstructed using equation 4.44. For the example of a two-qubit system the density matrix is calculated from the measured Stokes parameters with the following

$$\mathbb{II} = \frac{S_{ii}}{4S_{ii}}\hat{\sigma_{\mathbb{I}}} \otimes \hat{\sigma_{\mathbb{I}}}, \mathbb{IZ} = \frac{S_{iz}}{4S_{ii}}\hat{\sigma_{\mathbb{I}}} \otimes \hat{\sigma_z}, \mathbb{IX} = \frac{S_{ix}}{4S_{ii}}\hat{\sigma_{\mathbb{I}}} \otimes \hat{\sigma_x}, \mathbb{IY} = \frac{S_{iy}}{4S_{ii}}\hat{\sigma_{\mathbb{I}}} \otimes \hat{\sigma_y}$$
$$\mathbb{XI} = \frac{S_{xi}}{4S_{ii}}\hat{\sigma_x} \otimes \hat{\sigma_{\mathbb{I}}}, \mathbb{XZ} = \frac{S_{xz}}{4S_{ii}}\hat{\sigma_x} \otimes \hat{\sigma_z}, \mathbb{XX} = \frac{S_{xx}}{4S_{ii}}\hat{\sigma_x} \otimes \hat{\sigma_x}, \mathbb{XY} = \frac{S_{xy}}{4S_{ii}}\hat{\sigma_x} \otimes \hat{\sigma_y}$$
$$\mathbb{YI} = \frac{S_{yi}}{4S_{ii}}\hat{\sigma_y} \otimes \hat{\sigma_{\mathbb{I}}}, \mathbb{YZ} = \frac{S_{yz}}{4S_{ii}}\hat{\sigma_y} \otimes \hat{\sigma_z}, \mathbb{YX} = \frac{S_{yx}}{4S_{ii}}\hat{\sigma_y} \otimes \hat{\sigma_x}, \mathbb{YY} = \frac{S_{yy}}{4S_{ii}}\hat{\sigma_y} \otimes \hat{\sigma_y}$$
$$\mathbb{ZI} = \frac{S_{zi}}{4S_{ii}}\hat{\sigma_z} \otimes \hat{\sigma_{\mathbb{I}}}, \mathbb{ZX} = \frac{S_{zx}}{4S_{ii}}\hat{\sigma_z} \otimes \hat{\sigma_x}, \mathbb{ZZ} = \frac{S_{zz}}{4S_{ii}}\hat{\sigma_z} \otimes \hat{\sigma_z}, \mathbb{ZY} = \frac{S_{zy}}{4S_{ii}}\hat{\sigma_z} \otimes \hat{\sigma_y}.$$

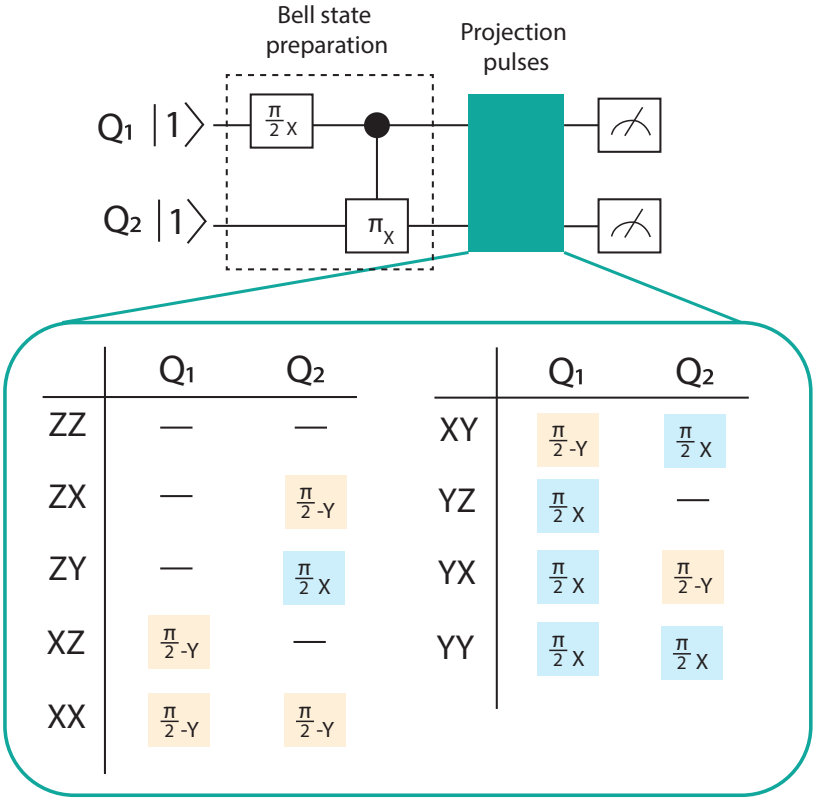

Figure 4.5: **Bell state tomography pulses.** Pulse sequence for carrying out Bell state tomography on two qubits, Q_1 and Q_2. In order to carry out full tomography of a state, this state must be measured along the x, y and z axis of the Bloch sphere. As we are only able to directly measure the qubits along the z-axis of the Bloch sphere, this means that we require projection pulses appended to the end of the Bell state preparation, in order to rotate the information along the x and y axis to the z-axis of the Bloch sphere, such that it can be read out. The table thus indicates which projection must be applied to Q_1 and Q_2 for each of the two-qubit projection axes.

$$\hat{\rho} = \mathbb{II} + \mathbb{IZ} + \mathbb{IX} + \mathbb{IY} \tag{4.50}$$

$$+ \mathbb{XI} + \mathbb{XZ} + \mathbb{XX} + \mathbb{XY} \tag{4.51}$$

$$+ \mathbb{YI} + \mathbb{YZ} + \mathbb{YX} + \mathbb{YY} \tag{4.52}$$

$$+ \mathbb{ZI} + \mathbb{ZX} + \mathbb{ZZ} + \mathbb{ZY} \tag{4.53}$$

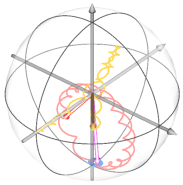

4.3.4 Phase reversal tomography

Another method of reconstructing the density matrix of an entangled state, is phase reversal tomography, which is related to the parity scan commonly used in trapped ions [29, 132, 135]. This method can be beneficial over Bell state tomography for cases where there exists a large difference in the coherence times of the two qubits constituting the entangled pair, such that the coherence time of one of the spins becomes comparable to the operation time of the other. This situation is the case for the entanglement between the donor nucleus and electron. The difference in coherence times leads to the electron spin dephasing in the time taken to perform the projection pulse on the nucleus required for Bell state tomography. Phase reversal tomography on the other hand, is generally agnostic to the ratio of coherence times between the two spins of the entangled pair, as the spin with the shortest coherence time can be entangled last and immediately projected into an eigenstate with the reversal pulses.

In its most basic form, phase reversal tomography allows for the extraction of the corner elements of the density matrix, $\rho_{11}, \rho_{14}, \rho_{41}$ and ρ_{44} where

$$\hat{\rho} = \begin{pmatrix} \rho_{11} & \rho_{12} & \rho_{13} & \rho_{14} \\ \rho_{21} & \rho_{22} & \rho_{23} & \rho_{24} \\ \rho_{31} & \rho_{32} & \rho_{33} & \rho_{34} \\ \rho_{41} & \rho_{42} & \rho_{43} & \rho_{44} \end{pmatrix}. \tag{4.54}$$

This is sufficient to extract the fidelity for any state that has non-zero elements only in the corners of the density matrix. Examples of such states include the $|\Phi^+\rangle = \frac{1}{\sqrt{2}}(|00\rangle + |11\rangle)$ Bell state and Greenberger–Horne–Zeilinger (GHZ) states [136], which are both vital resources for quantum computation. The reason that only calculating the elements $\rho_{11}, \rho_{14}, \rho_{41}$ and ρ_{44} is sufficient in these cases, can be understood by examining the method of calculating state fidelity. As discussed in section 4.3.2.3, the formula for calculating the state fidelity is given by

$$F = \langle\psi|\hat{\rho}|\psi\rangle\,. \tag{4.55}$$

where $|\psi\rangle$ represents the state that we are attempting to create. For the example of $|\psi\rangle = \frac{1}{\sqrt{2}}(|00\rangle + |11\rangle)$, which can be represented in vector form, written in the basis $\{|00\rangle, |01\rangle, |10\rangle, |11\rangle\}$, as

$$|\psi\rangle = \frac{1}{\sqrt{2}}\begin{pmatrix}1\\0\\0\\1\end{pmatrix}, \tag{4.56}$$

the fidelity of $\hat{\rho}$ in this case is calculated as the following

$$F = \frac{1}{2}\begin{pmatrix}1 & 0 & 0 & 1\end{pmatrix}\begin{pmatrix}\rho_{11} & \rho_{12} & \rho_{13} & \rho_{14}\\ \rho_{21} & \rho_{22} & \rho_{23} & \rho_{24}\\ \rho_{31} & \rho_{32} & \rho_{33} & \rho_{34}\\ \rho_{41} & \rho_{42} & \rho_{43} & \rho_{44}\end{pmatrix}\begin{pmatrix}1\\0\\0\\1\end{pmatrix} \tag{4.57}$$

$$= \frac{1}{2}\begin{pmatrix}1 & 0 & 0 & 1\end{pmatrix}\begin{pmatrix}1\times\rho_{11} & 0\times & \rho_{12} & 0\times\rho_{13} & 1\times\rho_{14}\\ 1\times\rho_{21} & 0\times & \rho_{22} & 0\times\rho_{23} & 1\times\rho_{24}\\ 1\times\rho_{31} & 0\times & \rho_{32} & 0\times\rho_{33} & 1\times\rho_{34}\\ 1\times\rho_{41} & 0\times & \rho_{42} & 0\times\rho_{43} & 1\times\rho_{44}\end{pmatrix} \tag{4.58}$$

$$= \frac{1}{2}\begin{pmatrix}1 & 0 & 0 & 1\end{pmatrix}\begin{pmatrix}\rho_{11}+\rho_{14}\\ \rho_{21}+\rho_{24}\\ \rho_{31}+\rho_{34}\\ \rho_{41}+\rho_{44}\end{pmatrix} \tag{4.59}$$

$$= \frac{1}{2}(\rho_{11}+\rho_{14}+\rho_{41}+\rho_{44}). \tag{4.60}$$

Thus, only the corner elements of the measured density matrix contribute to the fidelity and hence only these matrix elements must be extracted experimentally in order to assess the fidelity of $\hat{\rho}$.

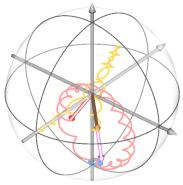

The process of phase reversal tomography can be broken down into two distinct steps, with the first step allowing for the extraction of the diagonal elements of $\hat{\rho}$, ρ_{11} and ρ_{44}, and the second step allowing for the extraction of the off-diagonal elements of $\hat{\rho}$, ρ_{14} and ρ_{41}.

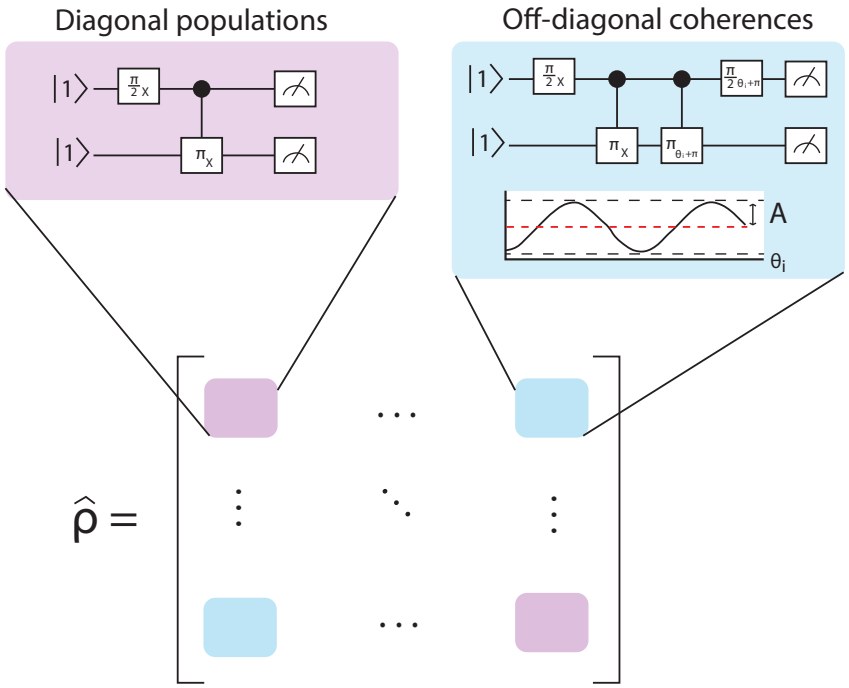

Figure 4.6: **Phase reversal tomography density matrix elements.** Depiction of the processes required to extract the corner elements of the density matrix. The diagonal, population elements depicted in purple, are obtained simply by preparing the state and measuring it along the z-axis. The off-diagonal, coherence elements on the other hand, depicted in blue, are obtained by preparing the state and then reversing the state, while sweeping the phase of the reversal pulses. The resulting oscillation is then fit, with the amplitude and phase extracted from this fit, giving the corner off-diagonal matrix elements.

4.3.4.1 Extracting the diagonal elements of $\hat{\rho}$

In order to extract the matrix elements ρ_{11} and ρ_{44}, we first initialise the electrons in the $|\downarrow\downarrow\rangle = |11\rangle$ state, and then prepare the $|\Phi^+\rangle = \frac{1}{\sqrt{2}}(|00\rangle + |11\rangle)$ Bell state using the process described in section 4.2.3, namely by performing a $\frac{\pi}{2}$ pulse on one electron and a zCROT

gate on the other electron, to rotate the second electron conditional on the electron in the superposition being in the $|\uparrow\rangle$ state. We then measure the state of the electron along the Z-direction of the Bloch sphere using two qubit readout to obtain

$$|\psi\rangle = \alpha\,|\downarrow\downarrow\rangle + \beta\,|\downarrow\uparrow\rangle + \gamma\,|\uparrow\downarrow\rangle + \delta\,|\uparrow\uparrow\rangle\,, \tag{4.61}$$

where $|\psi\rangle$ is the measured qubit state and α, β, γ and δ are the measured populations for each of the four two-qubit states. The diagonal elements of $\hat{\rho}$ are then given by the measured populations for the $|\downarrow\downarrow\rangle$ and $|\uparrow\uparrow\rangle$ states, such that $\rho_{11} = \alpha$ and $\rho_{44} = \delta$.

4.3.4.2 Extracting the off-diagonal elements of $\hat{\rho}$

In order to extract the off-diagonal elements of the density matrix $\hat{\rho}$, ρ_{14} and ρ_{41}, we perform the following steps:

1. Initialise the electrons in the $|\downarrow\downarrow\rangle$ state.
2. Perform a $\frac{\pi}{2}$ pulse on electron 1 with a phase of $\theta = 0$.
3. Perform a zCROT gate on electron 2 with a phase of $\theta = 0$.
4. Perform a zCROT gate on electron 2 with a phase of $\theta = \theta_k + \pi$ where θ_k is swept from a value of 0 to 2π.
5. Perform a $\frac{\pi}{2}$ gate on electron 1 with a phase of $\theta = \theta_k + \pi$ where θ_k is swept from a value of 0 to 2π.
6. Measure the state of the electrons.

Steps 1-3 above prepare the Bell state $|\Phi^+\rangle = \frac{1}{\sqrt{2}}(|00\rangle + |11\rangle)$. For a value of $\theta_k = 0$, steps 4-5 will exactly reverse the preparation of this Bell state, such that the electrons return to the $|\downarrow\downarrow\rangle$ state at the end of the sequence. However, as θ_k is swept from a value of 0 to 2π the ability for the pulses applied in steps 4 and 5 to return the electrons to their initial state will oscillate as a function of θ_k. For the pulses outlined in steps 2-5 this therefore

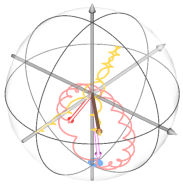

results in an oscillation observed in the populations of the measured two-qubit states $|\downarrow\downarrow\rangle$ and $|\uparrow\downarrow\rangle$ (the states between which an oscillation occurs will depend on which electron of the pair we apply the zCROT gate to). This oscillation is then fit with the following curve

$$P = A\sin(2\pi\nu\theta_k + B) + C, \tag{4.62}$$

where A represents the amplitude of the oscillations from the centre of the oscillation to the peak or trough, ν is the frequency of the oscillation as a function of θ_k, B is the phase of the oscillation and C is the offset of the oscillation from 0. The phase and amplitude of this oscillation can then be used to calculate the off-diagonal elements of the density matrix using the following expressions

$$\rho_{14} = A\cos(B) + iA\sin(B), \tag{4.63}$$

$$\rho_{41} = A\cos(B) - iA\sin(B). \tag{4.64}$$

The difference in sign between equations 4.63 and 4.64 ensures that the resulting density matrix is Hermitian.

Figure 4.6 depicts the process of extracting both the diagonal and off diagonal corner elements of $\hat{\rho}$ using phase reversal tomography.

4.3.5 Finding a physical density matrix

The density matrix, $\hat{\rho}$, calculated using the two methods above, does not necessarily represent a physical density matrix, as a result of imperfections in the measurement process. For example, these measurement imperfections may result in the measured density matrix possessing negative eigenvalues. To best represent the true density matrix of the state, we must therefore find the closest physical density matrix that represents the measured density matrix. The method by which the closest physical density matrix is found will depend on which density matrix elements have been obtained experimentally and thus, the

procedure will differ depending on if Bell state tomography or phase reversal tomography is used to obtain $\hat{\rho}$.

4.3.5.1 $\hat{\rho}$ with Bell state tomography

After performing Bell state tomography, to obtain the Bell state density matrix, $\hat{\rho}$, all elements of the density matrix have been measured experimentally. The following method of maximum likelihood estimation can therefore be utilised in order to estimate the closest possible physical density matrix to the calculated $\hat{\rho}$ [131]:

1. Construct an initial guess from the measured density matrix. This is done by first generating the following lower-triangular matrix.

$$T = \begin{pmatrix} t_1 & 0 & 0 & 0 \\ t_5 + it_6 & t_2 & 0 & 0 \\ t_{11} + it_{12} & t_7 + it_8 & t_3 & 0 \\ t_{15} + it_{16} & t_{13} + it_{14} & t_9 + it_{10} & t_4 \end{pmatrix}, \tag{4.65}$$

   where t_n represent the initial guess for the respective matrix elements.

2. Calculate the following cost function

$$\mathcal{L} = \sum_{\nu=1}^{16} \frac{[\langle\psi_i| T(t_1, t_2, ..., t_{16}) |\psi_i\rangle - P_{|\psi_i\rangle}]^2}{2 \langle\psi_i| T(t_1, t_2, ..., t_{16}) |\psi_i\rangle}. \tag{4.66}$$

   where $|\psi_i\rangle$ is the basis state of the projection i (see section 4.3.3) and $P_{|\psi_i\rangle}$ is the measured probability of the basis state $|\psi_i\rangle$.

3. Vary the parameters t_n and recalculate the cost function $\mathcal{L}$. In this way we can use numerical methods to iteratively minimise this cost function. Once this cost function has been minimised we have found the closest possible physical density matrix to the measured estimate.

4. Once the values of t_n that result in the minimisation of $\mathcal{L}$ have been found, the physical density matrix can then be expressed in terms of T using the following formula

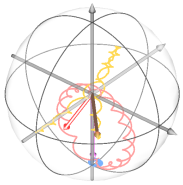

$$\hat{\rho}(t) = \frac{T^{\dagger}(t)T(t)}{Tr(T^{\dagger}(t)T(t))}. \tag{4.67}$$

This density matrix represents a physical density matrix with a trace of 1 and non-negative eigenvalues.

4.3.5.2 $\hat{\rho}$ with phase reversal tomography

The method of extracting the closest physical density matrix to the density matrix obtained experimentally is very similar for the case of $\hat{\rho}$ being obtained through phase reversal tomography, with a few alterations depending on the exact density matrix elements measured. For the case described in section 4.3.4, in which only the corner elements of the $\frac{1}{\sqrt{2}}(|\downarrow\downarrow\rangle + |\uparrow\uparrow\rangle)$ density matrix are extracted with phase reversal tomography, the following procedure can be followed:

1. Construct an initial guess from the real part of the measured density matrix. This is done by generating the following lower-triangular matrix.

$$T = \begin{pmatrix} t_1 & 0 & 0 & 0 \\ 0 & t_2 & 0 & 0 \\ 0 & 0 & t_3 & 0 \\ t_4 + it_5 & 0 & 0 & t_6 \end{pmatrix}, \tag{4.68}$$

It is important to note that, although calculating the Bell state fidelity of the $\frac{1}{\sqrt{2}}(|\downarrow\downarrow\rangle + |\uparrow\uparrow\rangle)$ state only requires knowledge of the four corner elements of the density matrix, when using an optimisation process to find the nearest physical density matrix, the remaining elements along the diagonal of the matrix $(\rho_{22}, \rho_{33}, \rho_{44})$ must also be included in the optimisation procedure. This is due to the fact that, during the procedure, the trace of the density matrix, $\mathrm{Tr}(\hat{\rho})$ is forced to a value of 1. Therefore, if the entire diagonal of the matrix is not measured, the corner elements may be artificially increased in amplitude during the optimisation process, resulting in an artificially high Bell state fidelity obtained from the resulting density matrix. The entire diagonal of the matrix is obtained by preparing the Bell state and mea-

suring it along the z-axis to obtain each of the 4 state probabilities: $|\downarrow\downarrow\rangle$, $|\downarrow\uparrow\rangle$, $|\uparrow\downarrow\rangle$ and $|\uparrow\uparrow\rangle$ (see section 4.3.4.1).

2. Calculate an estimated density matrix from T using

$$\hat{\sigma}(t) = \frac{T^{\dagger}(t)T(t)}{Tr(T^{\dagger}(t)T(t))}. \tag{4.69}$$

This density matrix represents a physical density matrix with a trace of 1 and non-negative eigenvalues.

3. Calculate the overlap between this density matrix and the measured density matrix, using the formula

$$\mathcal{L} = (\mathrm{Tr}\sqrt{\sqrt{\hat{\rho}}\hat{\sigma}(t)\sqrt{\hat{\rho}}})^2 \tag{4.70}$$

4. Vary the parameters t_n and recalculate the cost function $\mathcal{L}$. In this way we can use numerical methods to iteratively minimise this cost function. Once this cost function has been minimised we have found the closest possible physical density matrix to the measured estimate. The final density matrix is then given by $\hat{\sigma}(t)$.

4.4 Implantation parameters and donor distance

As discussed in section 4.2.3, in the presence of an exchange coupling between the electrons of neighbouring donor atoms, depending on the orientation of the donor nuclei, the native two-qubit gate between the electrons is either the SWAP$^{\alpha}$ or CROT gate. In the case of the CROT operation, present for the case of the nuclei in an antiparallel configuration, the requirement for this gate to be implemented with high fidelity, is that the resonance frequencies to flip the target electron, conditional on the control electron being in the spin $|\downarrow\rangle$ or $|\uparrow\rangle$ state (Figure 4.2) are well separated, such that they can be individually addressed. This condition is met, for a power-broadened pulse, provided that $J > 2\nu_R$, where ν_R is the Rabi frequency of the electron. The ability to meet this condition therefore depends on the two donors being in close enough proximity, as a result of the value of J depending very sensitively on the inter-donor distance [137,138]. Although an inherently probabilistic process, we can maximise the probability of finding a pair of exchange-coupled donors at

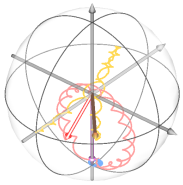

a favourable inter-donor distance, by optimising the parameters of the ion implantation process (see section 3.2 for details on the ion implantation parameters).

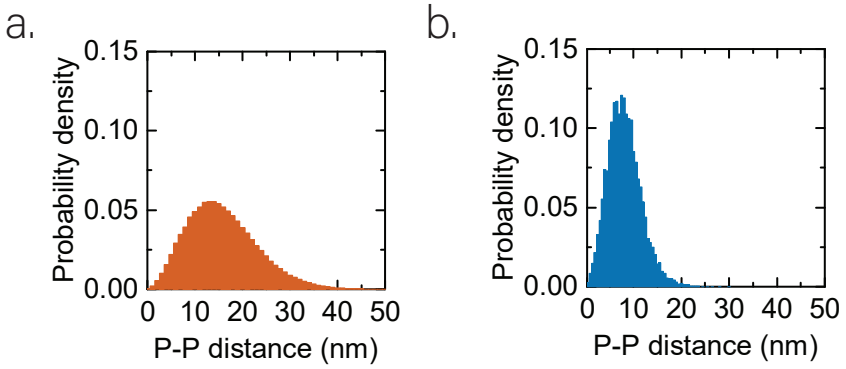

Figure 4.7: **Implantation SRIM simulations for P_2^+ and P^+ ions. a.** Stopping and Range of Ions in Matter (SRIM) simulation performed for a 10 kV ion beam of P_2^+ ions at a fluence of $5 \times 10^{10}\text{cm}^{-2}$. **b.** SRIM simulation performed for a 10 kV ion beam of P^+ ions at a fluence of $1.25 \times 10^{12}\text{cm}^{-2}$. A higher density of small inter-donor distances is observed for the case of the higher fluence P^+ beam. Figures taken from [30].

There are two methods by which we can optimise the average inter-donor distance between ion implanted ^{31}P donors. The first method is to implant P_2^+ molecular ions rather than P^+ ions. When the P_2^+ molecule hits the surface of the chip, the two P atoms break apart and come to rest at an inter-donor distance that depends on the implantation energy. The implantation energy can thus be chosen such that the probability of a favourable inter-donor distance between the two P atoms is maximised. The other method of optimising the inter-donor distance is to simply increase the fluence of P^+ ions in the ion beam, such that the probability of two donors being implanted in close proximity to one another is similarly maximised. Figure 4.7 shows a Stopping and Range of Ions in Matter (SRIM) simulation performed for a 10 kV ion beam for the case of either a beam of P_2^+ molecular ions at a fluence of $5 \times 10^{10}\text{cm}^{-2}$ (Fig 4.7 ,a) or a beam of P^+ ions at a fluence of $1.25 \times 10^{12}\text{cm}^{-2}$ (Fig 4.7 ,b). For the case of the higher fluence beam of P^+ ions, a much higher density of smaller inter-donor distances is observed. A high fluence P^+ beam thus allows us to best optimise the probability of finding two P donor atoms at a close enough

inter-donor distance such that the condition $J > 2\nu_R$ is met.

The implantation parameters for the donor device used in this thesis consisted of a beam of P^+ ions with an implantation fluence of $1.4 \times 10^{12}\text{cm}^{-2}$ and an implantation energy of 10 kV. These parameters were chosen following SRIM simulations, which estimated an average inter-donor distance of 8 nm for these implantation parameters and an 8 nm thick oxide layer [78].

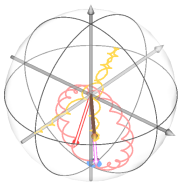

5.
Two-qubit electron conditional rotation gates in a J-coupled system

Sometimes it's the detours which turn out to be the fruitful ideas.

Roger Penrose

This chapter includes results from the following publications:

H. G. Stemp, S. Asaad, M. van Blankenstein, A. Vaartjes, M. A. I. Johnson, M. T. Mądzik, A. J. A. Heskes, H.R. Firgau, Y.Su, C.H. Yang, A. Laucht, K. M. Rudinger, R. Blume-Kohout, F. E. Hudson, A. S. Dzurak, K. M. Itoh, A. M. Jakob, B.C. Johnson, D. N. Jamieson, and A. Morello, **"Tomography of universal two-qubit logic operations in exchange-coupled donor electron spin qubits"** arXiv preprint arXiv:2309.15463, 2023

Section 5.9: B. Joecker, **H. G. Stemp**, I. Fernandez De Fuentes, M. A. I. Johnson, and A. Morello, "Error channels in quantum nondemolition measurements on spin systems" arXiv preprint arXiv:2307.14103, 2023

5.1 Introduction

The exchange interaction, J, is a fundamental form of coupling between electron spins. It stems from the Pauli exclusion principle, and arises in the presence of an overlap between the wave functions of the electrons [115]. In the context of spin-based quantum information processing, the exchange interaction features prominently as a natural method to enable entangling operations between electron spins [16]. In early experiments on electron spin qubits in quantum dots, J was controlled by detuning the two electrons' potentials with respect to each other [117, 120, 139]. More recently, J was varied over many orders of magnitude by controlling the height of the tunnel barrier between the dots [140,141]. This method also reduces the sensitivity to charge noise [142, 143].

The situation is more complicated in donor-based spin qubits. Encoding quantum information in the nuclear spin of donor atoms in silicon was one of the earliest proposals for solid-state quantum computers [25]. This vision has been corroborated by the experimental demonstration of exceptionally long spin coherence times, exceeding 30 seconds [34], and 1- and 2-qubit gate fidelities above 99% [29, 35]. The Coulomb potential of a donor also naturally binds an electron, which is itself an excellent qubit, with demonstrated single-qubit gate fidelity up to 99.98% [144]. However, electron two-qubit logic gates based on exchange face the challenge that J is both oscillating and exponentially dependent on inter-donor distance [137, 138, 145]. The useful range of the exchange is only $\sim 10-20$ nm, making it extremely difficult to fabricate and align metallic gates to control the tunnel barrier between the donors. Therefore, the only example of exchange control in donor systems to date was achieved by detuning the electrochemical potentials of a pair of multi-donor quantum dots, resulting in gate-controlled SWAP oscillations [126]. Since the donor-bound electrons were not operated as qubits, it was not possible to benchmark the fidelity of such operations, nor to demonstrate spin entanglement.

Here we present the first experimental demonstration of exchange-based, entangling two-qubit logic gates between electrons bound to individual ^{31}P donors in silicon. This is obtained by implementing a scheme exploiting a fixed J, weaker than the electron-nuclear

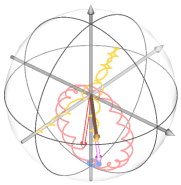

hyperfine interaction, A [114]. In this regime, preparing the two ^{31}P nuclei in an opposite state detunes the two electrons by $A \gg J$ and renders each electron's resonance frequency dependent on the state of the other. The native two-qubit operation is a CROT gate (similar to a CNOT, plus a phase), implemented by electron spin resonance [30]. Since the precise value of J is irrelevant, provided it is $\ll A$ and larger than the resonance linewdith, this scheme is relatively insensitive to uncertainties in the precise location of the donors. It is thus well suited to ion-implanted donor spins [37, 146], which retain compatibility with standard metal-oxide-semiconductor manufacturing processes [147], at the cost of some uncertainty ($\sim 5-10$ nm, depending on implantation energy and donor species) in the final location of the implanted donor [80]. Both electron spins are operated coherently as individual qubits [26] and read out in single-shot, either directly [88] or via quantum logic [148, 149]. This allows us to perform accurate tomography of the one- and two-qubit gate operations, and show that the weak-J regime does not affect the coherence of the individual spins.

5.2 Operation of the two-electron processor

The two-qubit processor consists of electron spins, Q1 and Q2, each with spin S=1/2 and basis states $|\downarrow\rangle$, $|\uparrow\rangle$, bound to ^{31}P donor nuclei with spin I=1/2 and basis states $|\Downarrow\rangle$, $|\Uparrow\rangle$ (Fig. 5.1b). Denoting with $\mathbf{S_{1,2}}, \mathbf{I_{1,2}}$ the vector spin operators for each electron and nucleus, and $A_{1,2}$ the electron-nuclear hyperfine couplings on each atom, the Hamiltonian of the system (in frequency units) is:

$$\begin{aligned} H =& (\mu_B/h) B_0 (g_1 S_{z1} + g_2 S_{z2}) + \\ & \gamma_n B_0 (I_{z1} + I_{z2}) + \\ & A_1 \mathbf{S_1} \cdot \mathbf{I_1} + A_2 \mathbf{S_2} \cdot \mathbf{I_2} + \\ & J(\mathbf{S_1} \cdot \mathbf{S_2}), \end{aligned} \tag{5.1}$$

where μ_B is the Bohr magneton, h is Planck's constant, $g_{1,2} \approx 1.9985$ the Landé g-factors of each electron spin, $g\mu_B/h \approx 27.97$ GHz/T and $\gamma_n \approx 17.23$ MHz/T is the ^{31}P nuclear gyromagnetic ratio.

We use aluminium gate electrodes, patterned on the surface of the silicon chip via electron beam lithography, to control the electrostatic environment of the donors for donor initialisation and readout [19, 26]. A broadband antenna delivers oscillating microwave or radio frequency (RF) magnetic fields to control the spin of the electrons and nuclei using electron spin resonance (ESR) or nuclear magnetic resonance (NMR), respectively (Fig. 5.1a).

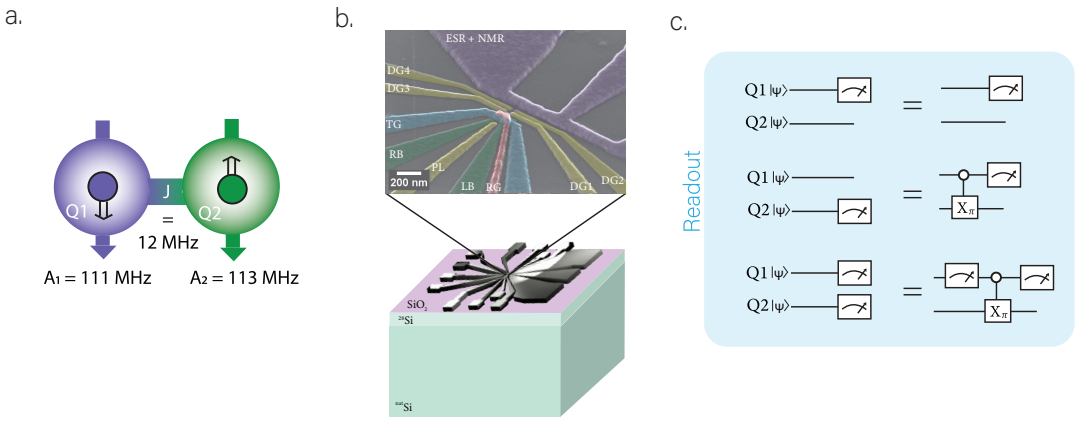

Figure 5.1: **Two-qubit phosphorus device operation. a.** Schematic of the system consisting of two phosphorus donors, each with their own single, bound electron. Setting the nuclei in an anti-parallel configuration results in an effective ΔB_z between the two electrons, which is given by the average hyperfine, $\bar{A}$, between the two donors. **b.** Device layout showing the silicon substrate upon which Al gates are fabricated for device control and readout. The top of the figure shows an enlarged, false-coloured SEM image of the Al gate layout. **c.** Quantum circuits denoting the readout process for Q1 and Q2. Q1 is readout via spin dependent-tunneling to an SET reservoir, while Q2 is instead readout indirectly via Q1 using quantum logic.

The Q1 electron is read out and initialised directly via the standard method of energy-dependent tunnelling to a nearby single-electron transistor (SET) island [86, 88]. This readout also automatically initialises Q1 in the $|\downarrow\rangle$ ground state. The Q2 electron is read out indirectly via quantum logic with Q1, by first initialising Q1 into the $|\downarrow\rangle$ state, then rotating Q1 conditional on the state of Q2, then reading out Q1. To initialise Q2, we first prepare Q1 in the $|\downarrow\rangle$ state, before transferring the spin state from Q1 to Q2 using a process similar in nature to the well established electron-nuclear double resonance (ENDOR)

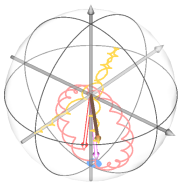

technique [150].

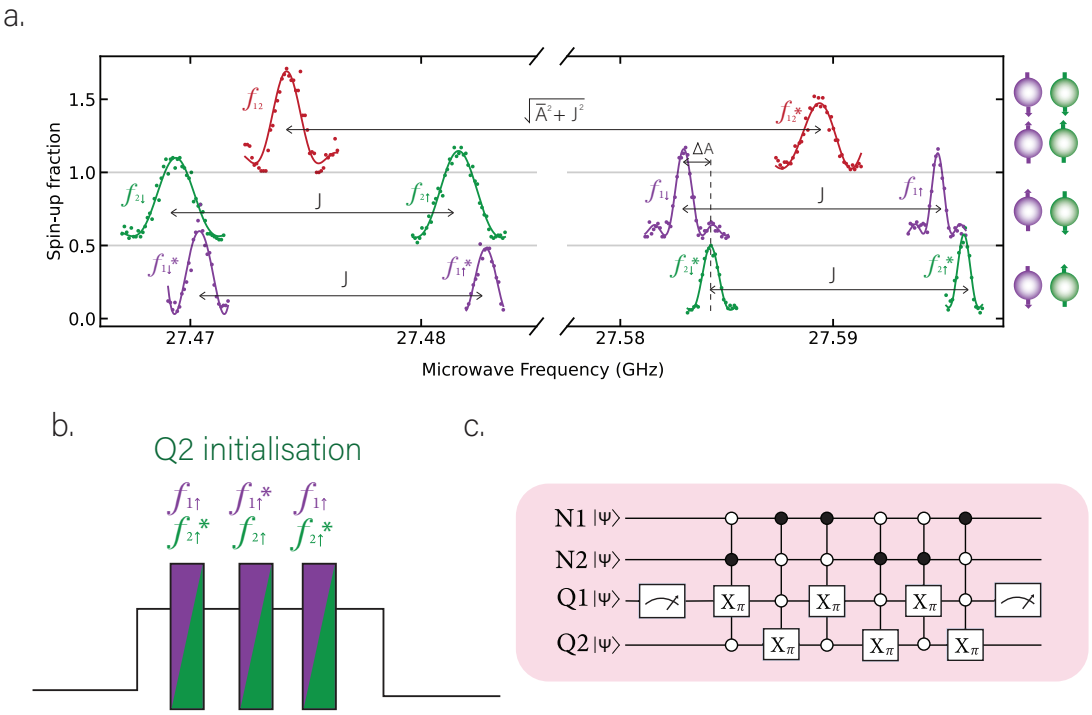

Figure 5.2: **Electron Q2 initialisation scheme. a.** Full ESR frequency spectrum showing the ESR resonances for both electron 1 and electron 2 for each nuclear configuration. The number in the frequency subscripts represents which electron is being addressed by each resonance, while the arrow denotes the spin state of the idle electron. **b.** Pulse sequence for the initialisation of Q2 into the spin $|\downarrow\rangle$ state. Each box represents an adiabatic pulse, with a frequency range chosen such that it addresses both resonances listed above each pulse simultaneously, as indicated by the striped purple and green colour. **c.** Circuit diagram depicting the Q2 initialisation scheme, where N1 and N2 represent the donor nucleus 1 and 2 respectively.

The electron Q2 initialisation scheme is designed in such a way that Q2 is initialised in the $|\downarrow\rangle$ state regardless of if the nuclei are in the $|\Downarrow\Uparrow\rangle$ or $|\Uparrow\Downarrow\rangle$ state (if the nuclei are in a parallel spin configuration then the electrons can no longer be individually addressed, as discussed in section 5.10). Figure 5.2,b shows the pulse sequence for the initialisation of Q2, consisting of three adiabatic pulses. Although only three pulses are applied, each of these pulses addresses two resonance frequencies simultaneously, as a result of $\Delta\nu_A > \Delta\nu_f$ where $\Delta\nu_A = 3$ MHz is the frequency range of the adiabatic pulses and $\Delta\nu_f = \Delta A = 2$

MHz is the difference in frequency between the frequencies listed above each pulse in Fig.5.2, b. To understand this pulse sequence we can first consider the case for which the nuclei are in the $\Downarrow\Uparrow$ configuration. We assume that the electron Q1 has been initialised in the $|\downarrow_1\rangle$ state at the beginning of the Q2 initialisation sequence using the initialisation process described above. Electron Q1 is also read out at the end of this pulse sequence such that it is always re-initialised into the $|\downarrow_1\rangle$ state. With the assumption that Q1 is in the $|\downarrow\rangle$ state, there are two possible states for the two electrons before the start of the Q2 initialisation scheme: $|\downarrow_1\downarrow_2\rangle$ or $|\downarrow_1\uparrow_2\rangle$.

If the electrons start in the $|\downarrow_1\downarrow_2\rangle$ state then the Q2 initialisation scheme will do the following:

1. Apply an adiabatic pulse to address resonances $f_{1\uparrow}$ and $f^*_{2\uparrow}$ simultaneously (see Fig.5.2,a). As we are assuming that the nuclei are in the $\Downarrow\Uparrow$ for this example, the resonance that is active for this nuclear configuration is $f^*_{2\uparrow}$, which flips Q2 conditional on Q1 being in the $|\uparrow_1\rangle$ state. As Q1 is in the $|\downarrow_1\rangle$ state in this example, this pulse therefore does nothing and we remain in the $|\downarrow_1\downarrow_2\rangle$ electron state.

2. Apply an adiabatic pulse to address resonances $f^*_{1\uparrow}$ and $f_{2\uparrow}$ simultaneously. As we are assuming that the nuclei are in the $\Downarrow\Uparrow$ for this example, the resonance that is active for this nuclear configuration is $f^*_{1\uparrow}$, which flips Q1 conditional on Q2 being in the $|\uparrow_2\rangle$ state. As Q2 is in the $|\downarrow_2\rangle$ state in this example, this pulse therefore does nothing and we remain in the $|\downarrow_1\downarrow_2\rangle$ electron state.

3. Apply an adiabatic pulse to address resonances $f_{1\uparrow}$ and $f^*_{2\uparrow}$ simultaneously. As we are assuming that the nuclei are in the $\Downarrow\Uparrow$ for this example, the resonance that is active for this nuclear configuration is $f^*_{2\uparrow}$, which flips Q2 conditional on Q1 being in the $|\uparrow_1\rangle$ state. As Q1 is in the $|\downarrow_1\rangle$ state in this example, this pulse therefore does nothing and we remain in the $|\downarrow_1\downarrow_2\rangle$ electron state.

By the end of this sequence Q2 is therefore left in the $|\downarrow_2\rangle$ state.

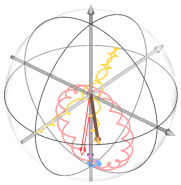

If the electrons instead start in the $|\downarrow_1\uparrow_2\rangle$ state (still considering the case for which the nuclei are in the $\Downarrow\Uparrow$ configuration) then the Q2 initialisation scheme will do the following:

1. Apply an adiabatic pulse to address resonances $f_{1\uparrow}$ and $f^*_{2\uparrow}$ simultaneously. As we are assuming that the nuclei are in the $\Downarrow\Uparrow$ state for this example, the resonance that is active for this nuclear configuration is $f^*_{2\uparrow}$, which flips Q2 conditional on Q1 being in the $|\uparrow_1\rangle$ state. As Q1 is in the $|\downarrow_1\rangle$ state in this example, this pulse therefore does nothing and we remain in the $|\downarrow_1\downarrow_2\rangle$ electron state.

2. Apply an adiabatic pulse to address resonances $f^*_{1\uparrow}$ and $f_{2\uparrow}$ simultaneously. As we are assuming that the nuclei are in the $\Downarrow\Uparrow$ state for this example, the resonance that is active for this nuclear configuration is $f^*_{1\uparrow}$, which flips Q1 conditional on Q2 being in the $|\uparrow_2\rangle$ state. As Q2 is in the $|\uparrow_2\rangle$ state in this example, this pulse therefore flips Q1 and hence we are left in the $|\uparrow_1\uparrow_2\rangle$ electron state.

3. Apply an adiabatic pulse to address resonances $f_{1\uparrow}$ and $f^*_{2\uparrow}$ simultaneously. As we are assuming that the nuclei are in the $\Downarrow\Uparrow$ state for this example, the resonance that is active for this nuclear configuration is $f^*_{2\uparrow}$, which flips Q2 conditional on Q1 being in the $|\uparrow_1\rangle$ state. As Q1 is in the $|\uparrow_1\rangle$ state now, this pulse therefore flips Q2 and we are left in the state $|\uparrow_1\downarrow_2\rangle$.

By the end of this sequence Q2 is therefore left in the $|\downarrow_2\rangle$ state.

This process can be sequentially worked through also for the example of the nuclei being initialised in the $\Uparrow\Downarrow$ configuration, revealing that Q2 is initialised in the $|\downarrow_2\rangle$ at the end of the pulse sequence regardless of which anti-parallel spin state the nuclei occupy.

Reading out the Q2 electron indirectly via Q1 presents several advantages, compared to reading both electrons individually via spin-dependent tunnelling. Firstly, the Q2 electron can be read out via repetitive quantum nondemolition (QND) measurements [148, 149],

thanks to its long spin relaxation time ($T_1 \approx 1.4$ s) and the fact that $J \ll A$ renders the exchange interaction approximately of Ising type, fulfilling the QND condition [109]. The QND readout is performed by loading a $|\downarrow\rangle$ Q1 electron from the reservoir, rotating Q1 conditional on the state of Q2, reading out Q1, and repeating the cycle 11 times. The resulting readout contrast is greatly enhanced, from a bare 0.48 to 0.76. Fig.5.3 shows the effect of QND readout on the readout contrast of the electron, as ascertained by a Rabi oscillation performed on Q2 both with no QND readout and with 11 shots of QND readout. Fig.5.3,**b** shows the readout contrast of Q2 as a function of the number of QND readout repetitions performed. A peak in the readout contrast is observed for a QND readout repetition number of approximately 11. The decline in readout contrast beyond a certain number of QND readout shots, we believe to be attributed to the QND error associated with the hybridisation of electron states, as discussed in section 5.9 [109].

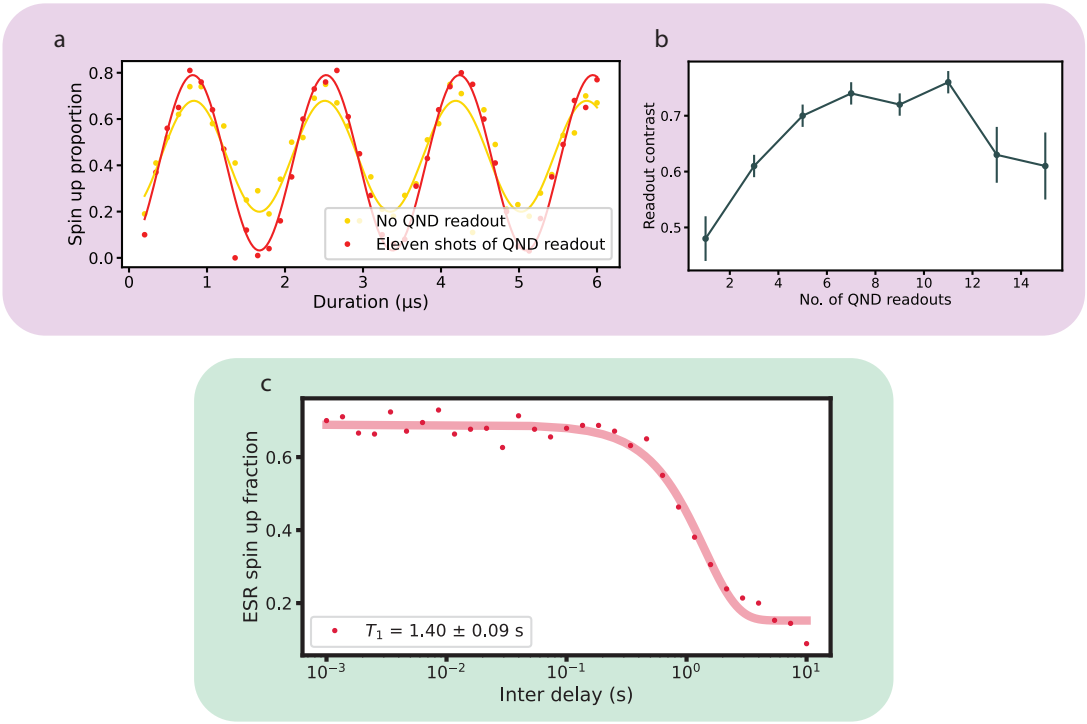

Figure 5.3: **QND readout of the electron. a** Rabi measurement performed on electron Q2, with and without 11 shots of QND readout. The readout contrast increased from 0.48 without QND readout to 0.76 with 11 repetitions of QND readout. **b** Readout contrast of the electron as a function of number of QND readout repetitions, showing an optimum at approximately 11 QND shots. **c** T_1 measurement of the electron, showing a T_1 relaxation time of 1.4 ± 0.09 seconds. This time far exceeds the time taken to perform 11 QND readout shots, indicating that relaxation of the electron is not the limiting factor for QND readout.

The second benefit of this indirect readout scheme, is that the electron Q2 never leaves the donor. When the electron is present on the donor, there exists a hyperfine coupling between the donor-bound electron and the spin carrying Si isotopes, ^{29}Si, in the vicinity of the donor. The strength of this hyperfine coupling depends on the distance between the electron and the surrounding ^{29}Si and hence each individual ^{29}Si in the donor vicinity possess a unique hyperfine coupling to the donor-bound electron. This difference in hyperfine interaction strength between different ^{29}Si nuclei thus detunes the neighbouring ^{29}Si from one another in energy. If this detuning is sufficiently large, such that it is greater than

the coupling strength between the ^{29}Si nuclei, then any flip-flopping between the nuclei is suppressed; an effect known as nuclear freezing [151]. This nuclear freezing removes any magnetic fluctuations caused by flip-flopping of the spin bath surrounding donor 2 and hence results in a considerably more stable resonance frequency for electron Q2. Conversely, donor 1 is ionised during the readout of electron Q1 and hence the flip-flopping of the spin bath surrounding donor 1 is 'unfrozen' every time the electron is removed for readout. These ^{29}Si nuclear spin flips in the surrounding spin bath result in jumps observed in the resonance frequency of Q1, as shown in Figure 5.4.

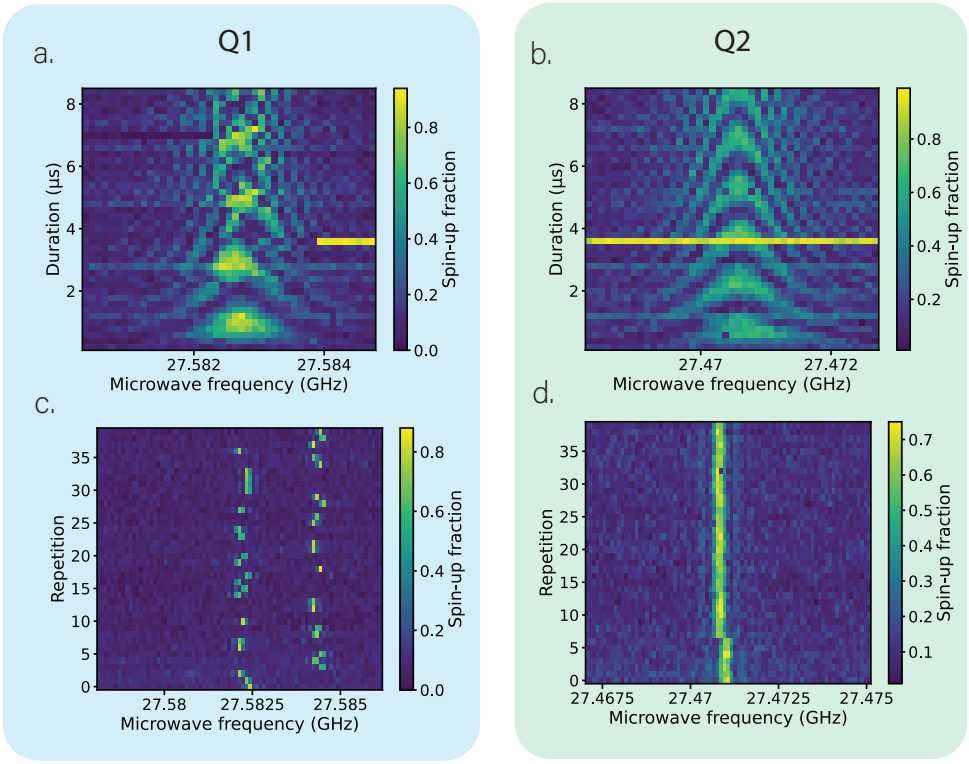

Figure 5.4: **Electron frequency stability. a.**(**b.**) Rabi chevrons performed on electron Q1(Q2) showing the greater stability of Q2. An automated retuning algorithm was run after the completion of every frequency sweep, in order to stay at the correct gate tuning position for gate readout. The yellow horizontal lines present in the Rabi chevrons are due to the device readout position drifting out of tune during the measurement, resulting in a spin up proportion of 1 being erraneously measured. As the retuning algorithm is only repeated once every frequency sweep, the device hence remains out of tune until the end of the frequency sweep. **c.** Repeated ESR frequency spectrum of Q1 taken over a time period of a few hours. The jumps observed in the resonance frequency of Q1 are as a result of two ^{29}Si nuclei that are hyperfine coupled to Q1 with a hyperfine coupling of 200 kHz and 2 MHz respectively. **d.** Repeated ESR frequency spectrum of Q2 taken over a time period of a few hours, exhibiting a much more stable ESR frequency as a result of nuclear freezing.

In a similar fashion to the readout of electron Q2, the donor nuclei are read out indirectly via the electron Q1. In order to read out the state of the nucleus of either donor 1 or 2, Q1 is initialised in the $|\downarrow\rangle$ state and then rotated conditional on the state of the nucleus, before being read out. As with electron Q2, the nuclei can hence be read out using QND

readout, resulting in high nuclear readout fidelities, exceeding 99% [19]. The nuclei are initialised using an ENDOR technique [150].

5.3 Effect of weak exchange on qubit coherence

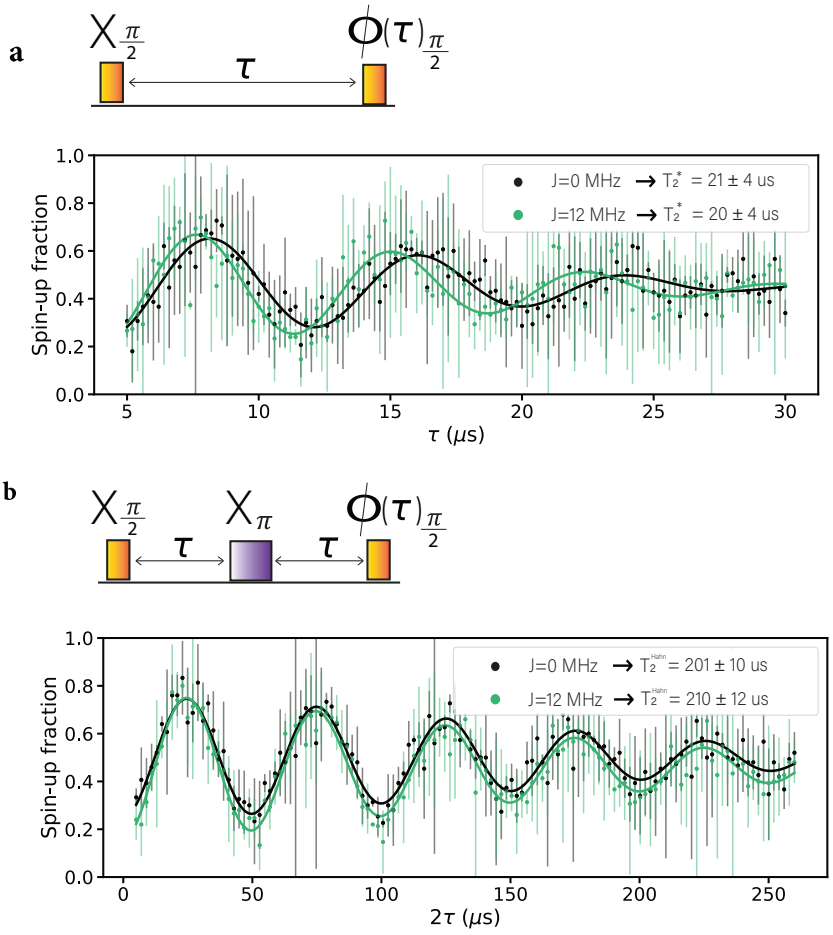

Figure 5.5: **Effect of weak exchange on electron coherence time. a.** Electron spin dephasing measurements by Ramsey experiment performed on Q2 with (green) and without (black) the presence of an exchange interaction J with Q1. The regime without J was created by ionising nucleus 1. **b.** Hahn echo experiment performed on Q2 with and without the presence of the exchange coupling. The oscillations are artificially introduced by a wait time dependent phase shift added to the final $\frac{\pi}{2}$ pulse.

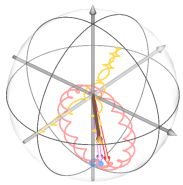

One significant advantage of operating in the always-on, weak exchange regime is that the exchange interaction is not detrimental to the qubit coherence. We investigated the effect of the exchange interaction on the coherence of the electrons by performing Ramsey and Hahn echo experiments on electron Q2 both with donor 1 in the neutral and ionised state. Donor 1 was ionised by tuning the device gate voltages such that electron Q1 is able to tunnel from the donor to the SET island. With the removal of Q1, the exchange coupling is no longer present in the system. The T_2^* and T_2^{Hahn} times of Q2 did not change within the error bars for the fits (shown in Figure 5.5) with the removal of the exchange coupling, indicating that the noise in the exchange interaction is not a dominant source of decoherence of the qubits.

5.4 Exchange-based two-qubit gates

Two-qubit controlled rotation (CROT) gates are naturally obtained by preparing the two donor nuclear spins in an anti-parallel configuration, i.e. either $|\Downarrow\Uparrow\rangle$ or $|\Uparrow\Downarrow\rangle$. In doing so, the two electron spins are frequency-detuned by the average hyperfine coupling $\overline{A} = \frac{(A_1+A_2)}{2}$. This can be thought of as the switchable, digital version of the detuning caused by a gradient in Overhauser field ΔB_z in double quantum dots [117], i.e. $\Delta B_z = \pm\overline{A}$ (Fig. 5.6).

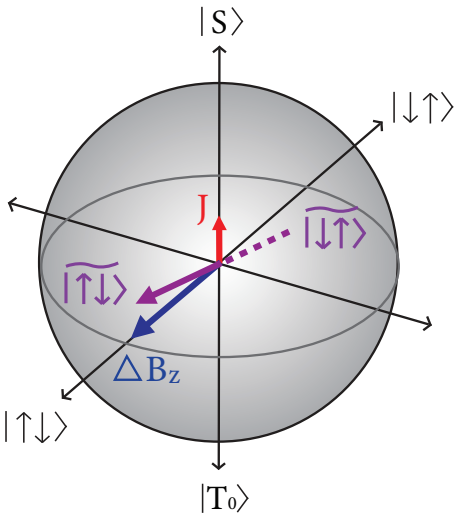

Figure 5.6: **Exchange vs detuning hybridisation of states.** Bloch sphere denoting the hybridised states brought about by the ratio of the energy detuning ΔB_z with the exchange coupling J, which constitute the eigenstates of the system in the weak J regime.

The two-electron spin eigenstates of the system are as shown in Table 5.1, where $\tan(2\theta) = J/\overline{A}$. In the present device, $J \approx 12$ MHz $\ll \overline{A} \approx 112$ MHz results in $\cos(\theta) = 0.9986$, so that the eigenstates are almost (but not exactly) the tensor products of the individual spins' basis states $\{|\downarrow\rangle, |\uparrow\rangle\}$.

$\lvert$Q1Q2$\rangle$	Eigenbasis	S_z basis
$\lvert 11\rangle$	$\lvert\downarrow\downarrow\rangle$	$\lvert\downarrow\downarrow\rangle$
$\lvert 10\rangle$	$\widetilde{\lvert\downarrow\uparrow\rangle}$	$\cos(\theta)\lvert\downarrow\uparrow\rangle + \sin(\theta)\lvert\uparrow\downarrow\rangle$
$\lvert 01\rangle$	$\widetilde{\lvert\uparrow\downarrow\rangle}$	$\cos(\theta)\lvert\uparrow\downarrow\rangle + \sin(\theta)\lvert\downarrow\uparrow\rangle$
$\lvert 00\rangle$	$\lvert\uparrow\uparrow\rangle$	$\lvert\uparrow\uparrow\rangle$

Table 5.1: Two-qubit electron spin states.

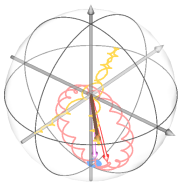

An electron spin resonance (ESR) transition between any of these states, that exist when the nuclei are in an anti-parallel spin orientation, (Fig. 5.7) results in a rotation of one electron conditional on the state of the other, constituting a native CROT or zCROT gate. For the entirety of this work we therefore set the nuclei into an anti-parallel spin configuration, of $|\Uparrow_1\Downarrow_2\rangle$, such that the ESR transitions constitute native two-qubit conditional rotations, similar to experiments in double quantum dots with fixed exchange [122, 152].

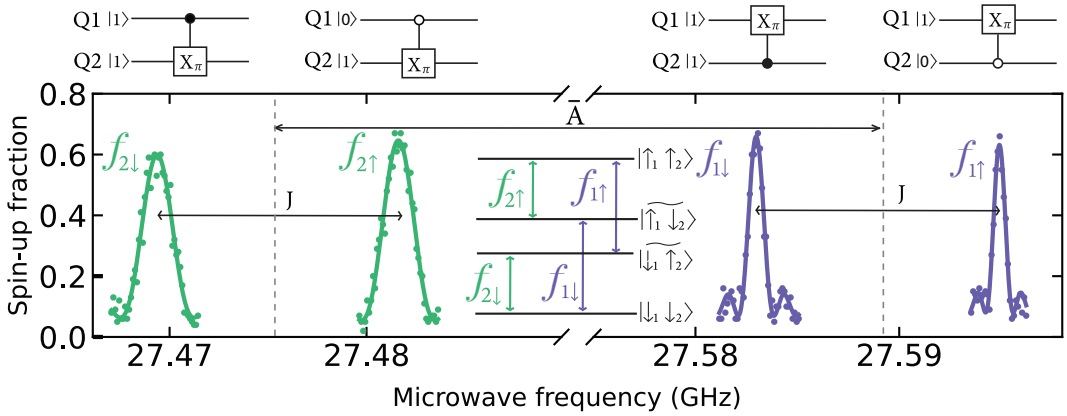

Figure 5.7: **Antiparallel nuclei ESR spectrum.** ESR spectrum showing the resonant frequencies used to control electron 1 (purple) and electron 2 (green). These resonant frequencies appear when the nuclei are in an antiparallel configuration, with nucleus 1 in the down state and nucleus 2 in the up state. A resonant π pulse on any of these resonant frequencies represents a two-qubit CROT or zCROT gate, as shown in the circuit diagrams above each resonance.

5.5 Fidelity benchmarking

5.5.1 Single-qubit GST

Since the native gates in this J-coupled system are two-qubit CROT operations, a one-qubit electron gate is performed by two sequential CROT gates, in order to rotate one electron unconditional on the state of the other electron [152]. We then use gate set tomography (GST) [29, 144, 153] to quantify the fidelity of the operations. We perform three distinct runs of one-qubit GST on each of the qubits, where the idle qubit is kept either in the $|\downarrow\rangle$, or $\frac{1}{\sqrt{2}}(|\downarrow\rangle+|\uparrow\rangle)$, or $|\uparrow\rangle$ state for the duration of the experiment. Figure 5.8

shows the estimated $X_{\frac{\pi}{2}}$ (rotation of the target qubit by an angle $\pi/2$ around the X-axis) error rates for each of the unconditional single-qubit operations. Notwithstanding the longer gate times compared to the native conditional operations, all $X_{\frac{\pi}{2}}$ and $Y_{\frac{\pi}{2}}$ fidelities exceed 99.00±0.29%

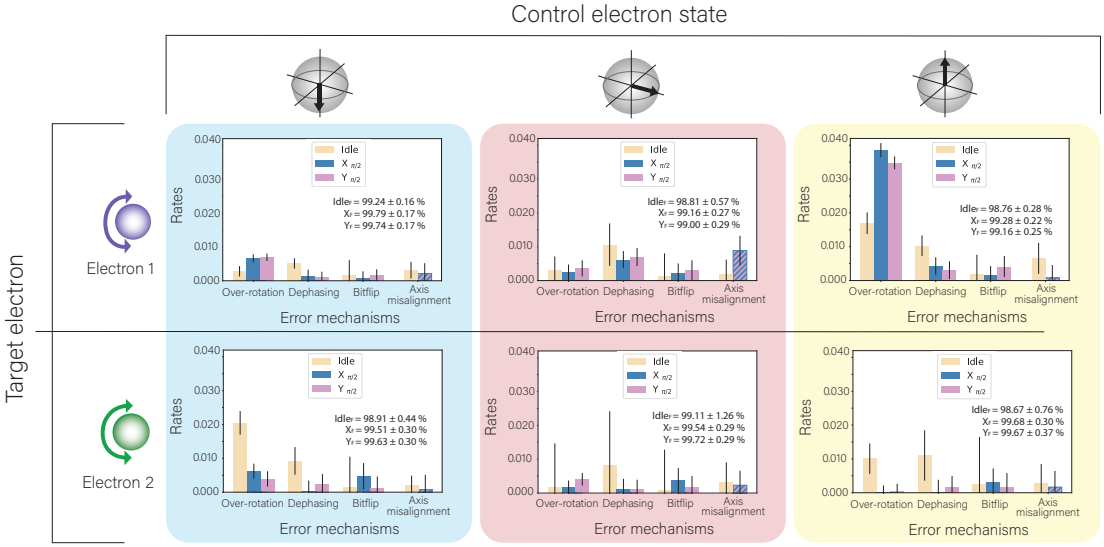

Figure 5.8: **Unconditional single-qubit GST.** Error rates for the unconditional, single-qubit gates, estimated with single-qubit GST. The unconditional gates were implemented by applying two sequential $\frac{\pi}{2}$ rotations to Q1(Q2), one conditional on Q2(Q1) being in the spin $|\downarrow\rangle$ state and one conditional on Q2(Q1) being in the $|\uparrow\rangle$ state, in order to rotate one electron unconditional on the state of the other electron. To test the effectiveness of this unconditional gate, we performed three separate GST experiments on each electron, with the other electron intialised in either the $|\downarrow\rangle$ state, a superposition state of $\frac{1}{\sqrt{2}}(|\downarrow\rangle + |\uparrow\rangle)$ or the $|\uparrow\rangle$ state. The diagrams to the left of the rows indicate which electron is acting as the target electron in each GST experiment, while the Bloch sphere schematics above each of the columns denotes the state of the corresponding control electron throughout each GST experiment. The fidelities estimated for each gate are quoted in the inset of each plot. The error rates for each error mechanism were calculated through simple combinations of stochastic and coherent Pauli projections, extracted from the GST results. The 'Axis misalignment' of the idle gate quantifies the component of the idle gate's rotation perpendicular to the Z-axis of the Bloch sphere. The 'Axis misalignment' of the $X_{\frac{\pi}{2}}$ and $Y_{\frac{\pi}{2}}$ gates on the other hand, represents the error associated with the relative angle between the X and Y rotation axis of the qubit and hence is represented by a single striped column, to indicate that this error is associated with both the $X_{\frac{\pi}{2}}$ and $Y_{\frac{\pi}{2}}$ gates.

We additionally performed one-qubit GST on each of the four native conditional rotation

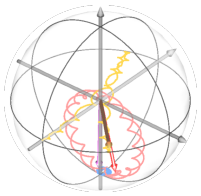

operations, by keeping the idle electron in one of its eigenstates, either $|\downarrow\rangle$ or $|\uparrow\rangle$, for the duration of the experiment, effectively truncating the Hilbert space of the two-electron system into a one-qubit subspace. Figure 5.9 shows the one-qubit error rates obtained for each of the $X_{\frac{\pi}{2}}$ gates generated using either the native CROT and zCROT gates, with the other electron initialised in an eigenstate. The $X_{\frac{\pi}{2}}$ and $Y_{\frac{\pi}{2}}$ gate fidelity of both electrons extracted from the GST results for the native conditional rotations exceeded 99.63±0.07%.

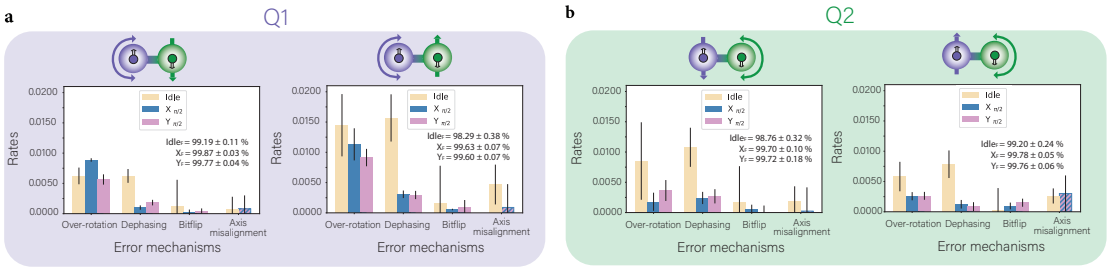

Figure 5.9: **Conditional single-qubit GST on both electrons. a.** Error rates for the native, conditional gates performed on electron Q1, estimated using single-qubit GST. The schematics above each plot depict the state in which electron Q2 was initialised and upon which each gate on Q1 was conditioned, for the two separate GST experiments. **b.** Error rates for the native, conditional gates performed on electron Q2, estimated using single-qubit GST. For both **a.,b.** the error rates for each error mechanism were calculated using combinations of Pauli projections extracted from the single-qubit GST results. The fidelities estimated for each gate are quoted in the inset of each plot.

5.5.2 Two-qubit GST

Next, we performed full two-qubit GST on a gate set consisting of the eight native CROT and zCROT gates (Fig. 5.10) together with a global idle. The analysis of the two-qubit GST results tells a more complicated story, revealing error mechanisms that were otherwise invisible when operating the device as an effectively one-qubit system as above. The error budget in the two qubit case is dominated by three main sources. For the CROT and zCROT gates there are systematic coherent errors that correspond to relational axis misalignment errors between pairs of CROT and zCROT gates acting on different control and target qubits. Additionally, the CROT and zCROT gates induce a significant amount of dephasing on the control qubit. For the idle gate, on the other hand, the error is

predominantly depolarization.

From the perspective of understanding the underlying device characteristics it is useful to separate out coherent errors, which are primarily attributable to the control system and can largely be corrected through calibration, from stochastic errors which typically arise from the device physics. Using the generator fidelity introduced in [29] we can perform such a partition, dividing the infidelity into its coherent and incoherent contributions. Doing so we find that the CROT and zCROT gates have incoherent contributions to their infidelities ranging from 6.91% to 21.88%, with an average of 12.54±6.40%.

While significantly lower than the fidelity obtained when restricting our attention to a one-qubit subspace, these results have elucidated the existence of error mechanisms coming from the device physics that, while previously known about, have greater than expected impacts on device performance. We conjecture, for example, that a significant amount of the observed uptick in dephasing on the control qubit, can be attributed to jumps in the resonance frequency of the target qubit, induced by changes in the orientation of weakly coupled, residual ^{29}Si nuclei in the vicinity of the donor, as discussed in section 5.2. The impact of these small jumps in frequency could potentially play a significant role in the dephasing observed on the control qubit, as a result of the geometric phase induced on the control qubit upon performing a rotation of the target qubit. The magnitude of the geometric phase imparted on the control qubit is equal to half the solid angle traversed by the target qubit on the Bloch sphere. As a consequence of this, the exact phase imparted on the control will depend very sensitively on any frequency detuning between the resonance frequency and the frequency of the microwave driving field. Thus, even a small shift in the resonance frequency ($\Delta\nu \ll 2\nu_{\text{Rabi}}$, where $\Delta\nu$ is the shift in the resonance frequency and ν_{Rabi} is the Rabi frequency of the target electron) of the target qubit, can alter the path traversed by the target qubit on the Bloch sphere and thus manifest itself as a noticeable stochastic error induced on the phase of the control qubit. Although this effect can often be mitigated through careful frequency re-calibration of the microwave driving field, for example using a Ramsey experiment, this strategy becomes increasingly difficult as the coupling strength of the fluctuating ^{29}Si nuclei approaches the intrinsic

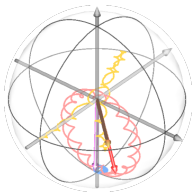

linewidth of the target qubit, proportional to $\frac{1}{T_2^*}$. In these cases, pulse engineering could be utilised to design a drive that is more robust against these small shifts in the resonance frequency. Additional work is currently underway validating this conjecture and exploring other possible decoherence mechanisms which could be partially responsible for the observed dephasing rates.

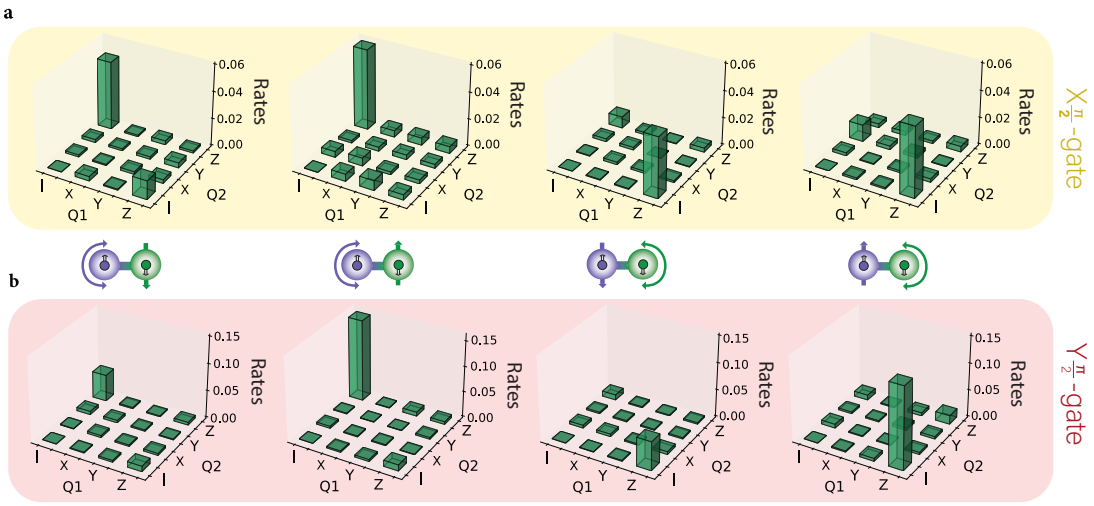

Figure 5.10: **Two-qubit GST on the electrons.** Stochastic error rates estimated using two-qubit GST for both the $X_{\frac{\pi}{2}}$ (**a.**) and $Y_{\frac{\pi}{2}}$ (**b.**) gates. From left to right in **a.**(**b.**) these $X_{\frac{\pi}{2}}(Y_{\frac{\pi}{2}})$ rotations were performed on: Q1, conditional on Q2 being in the $|\downarrow\rangle$ state, Q1 conditional on Q2 being in the $|\uparrow\rangle$ state, Q2 conditional on Q1 being in the $|\downarrow\rangle$ state and Q2 conditional on Q1 being in the $|\uparrow\rangle$ state. These eight gates were all tested in the same two-qubit GST experiment.

5.6 Electron spin Bell state tomography

We demonstrated the entangling nature of the two-qubit CROT operations by creating and tomographing electron Bell states. We created a two-electron Bell state by initialising the spins in the state $|\text{Q1Q2}\rangle = |\downarrow\downarrow\rangle$, performing an $\text{X}\frac{\pi}{2}$ gate on Q1, and then an entangling CROT operation on Q2. The fidelity of the resulting state was benchmarked using phase reversal tomography [36,132,135,136], whereby the pulses used to create the Bell state are applied in reverse, but with a progressively increasing phase (Fig. 5.11a). Accordingly, the

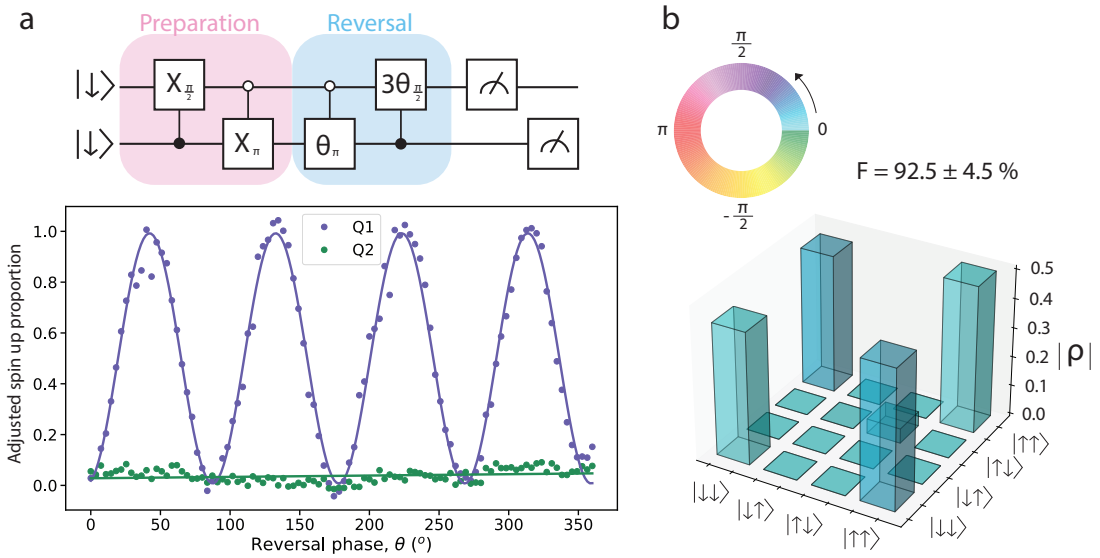

Figure 5.11: **Electron phase reversal tomography. a.** Top shows the circuit diagram associated with the preparation of the $\Phi^+ = \frac{1}{\sqrt{2}}(|\downarrow\downarrow\rangle + |\uparrow\uparrow\rangle)$ Bell state. Bottom plot shows the oscillation in the spin up proportion of electron Q1 and Q2 as a function of the phase of the reversal pulses, with amplitude of the oscillations corrected for SPAM error. **b.** Reconstructed density matrix of the Φ^+ state using phase reversal tomography. The magnitude of the density matrix elements are represented by the height of the respective bars, while the phase of each element is denoted by the associated color on the color wheel. From this density matrix a Bell state fidelity of 92.5 ± 4.5% was extracted.

ability to reverse the electrons back to their initial state oscillates according to the phase of the reversal pulses. This results in the spin up proportion of the electron oscillating as a function of reversal phase, with a spin up proportion of 0 at a reversal phase of 0 indicating that the electrons have been successfully reversed to their initial state. The amplitude and phase of these oscillations allows for the reconstruction of the off-diagonal corner elements of the two-qubit density matrix, ρ_{14}, ρ_{41}. In order to obtain the diagonal corner elements, ρ_{11}, ρ_{44}, we directly measured the Bell state populations in the Z-basis immediately following the state's preparation. By choosing to prepare the $\Phi^+ = \frac{1}{\sqrt{2}}(|\downarrow\downarrow\rangle + |\uparrow\uparrow\rangle)$ Bell state, which only has non-zero elements in each of the four corners of the density matrix, the fidelity of this Bell state can be ascertained using these four matrix elements. Using this method we obtained a Bell state fidelity of 93 ± 9%, with state preparation and measurement (SPAM) error removed and 73 ± 6% without SPAM removal. The full

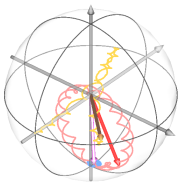

measured density matrices with and without SPAM are the following:

$$\hat{\rho}_{\text{SPAM}} = \tag{5.2}$$

$$\begin{pmatrix} 0.460 \pm 0.032 & 0 & 0 & 0.332 \pm 0.062 + 0.109 \pm 0.096j \\ 0 & 0.116 \pm 0.012 & 0 & 0 \\ 0 & 0 & 0.097 \pm 0.016 & 0 \\ 0.332 \pm 0.062 - 0.109 \pm 0.096j & 0 & 0 & 0.327 \pm 0.032 \end{pmatrix} \tag{5.3}$$

$$\hat{\rho}_{\text{no SPAM}} = \tag{5.4}$$

$$\begin{pmatrix} 0.431 \pm 0.058 & 0 & 0 & 0.464 \pm 0.084 + 0.154 \pm 0.136j \\ 0 & -0.023 \pm 0.058 & 0 & 0 \\ 0 & 0 & 0.050 \pm 0.064 & 0 \\ 0.464 \pm 0.084 - 0.154 \pm 0.136j & 0 & 0 & 0.485 \pm 0.038 \end{pmatrix} \tag{5.5}$$

The error bars were obtained through repeating the phase reversal measurement 10 times, constructing a density matrix for each repetition, with an associated Bell state fidelity, and calculating 2σ, where σ is the standard deviation of the 10 resultant fidelity values. As discussed in section 4.3.4, measurement imperfections can result in the estimated density matrix not representing a physical density matrix. To find the nearest physical density matrix to the estimated matrix, $\hat{\rho}$, we therefore used a Nelder-Mead optimisation algorithm in python to optimise the parameters t_n in the following lower triangular matrix

$$T = \begin{pmatrix} t_1 & 0 & 0 & 0 \\ 0 & t_5 & 0 & 0 \\ 0 & 0 & t_6 & 0 \\ t_2 + it_3 & 0 & 0 & t_4 \end{pmatrix}, \tag{5.6}$$

The cost function to be minimised was given by the overlap between $\hat{\sigma}$ and the measured density matrix $\hat{\rho}$, where

$$\hat{\sigma} = \frac{T^{\dagger}(t)T(t)}{Tr(T^{\dagger}(t)T(t))}. \tag{5.7}$$

Figure 7.2 shows the individual iterations of the optimisation algorithm for both the density matrix with (Fig. 7.2, a) and without (Fig. 7.2, b) SPAM extracted. The t_n values converge to optimal values within 175 iterations of the optimisation algorithm in both cases, rendering a final overlap between the measured and estimated density matrices of 100.0% with SPAM error and 99.79% for the density matrix with SPAM extracted.

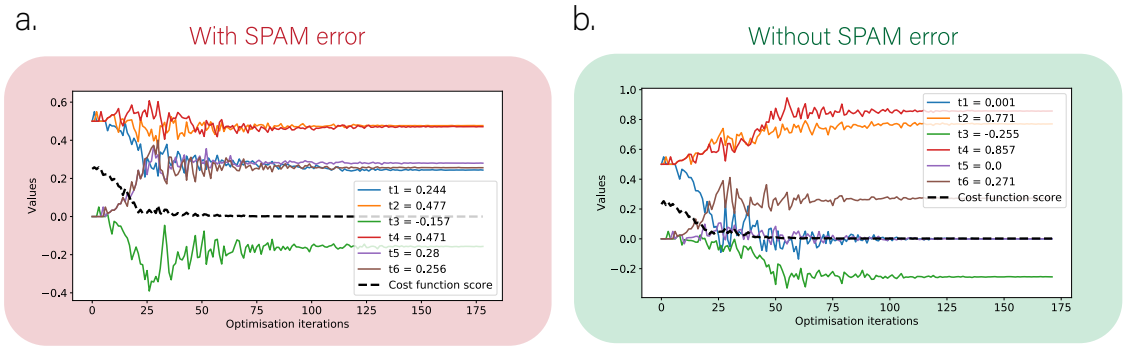

Figure 5.12: **Nelder-Mead estimation of density matrix elements. a.** Plot showing 175 iterations of the Nelder-Mead optimisation algorithm to find the nearest physical density matrix to the measured matrix. The values t_n are seen to converge to their optimal value. **b.** Plot of the same Nelder-Mead algorithm run on the density matrix with SPAM error extracted.

We extracted SPAM error by performing two Rabi oscillations, both with two-qubit readout. One Rabi was performed on Q2, between the states $|\downarrow\downarrow\rangle$ and $\widetilde{|\downarrow\uparrow\rangle}$ and one was performed on Q1, between the states $\widetilde{|\downarrow\uparrow\rangle}$ and $|\uparrow\uparrow\rangle$. The amplitude of the Rabi oscillation is dictated by a combination of initialisation, I_{ψ} and readout, R_{ψ}, error, where $\psi = \{\downarrow\downarrow, \downarrow\uparrow, \uparrow\downarrow, \uparrow\uparrow\}$ denotes the state being initialised or read out. The amplitudes of each of the four Rabi oscillations, as shown in Figure 5.13, can therefore be written as the following:

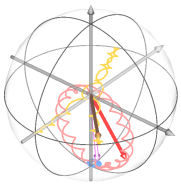

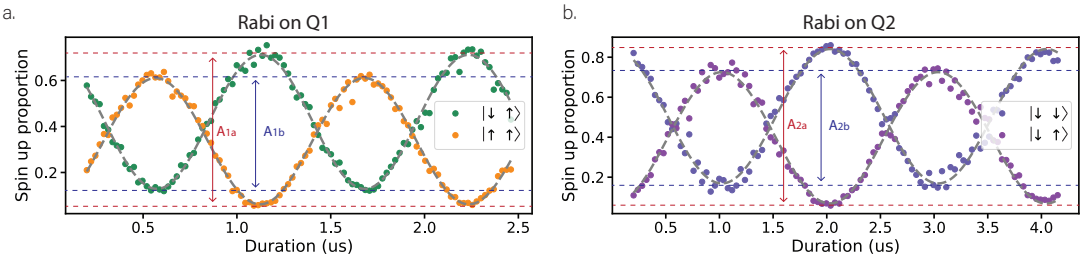

Figure 5.13: **Phase reversal tomography SPAM extraction. a.** Rabi oscillation with two-qubit readout performed on Q1. A_{1a} represents the amplitude of the oscillation of the $|\downarrow\uparrow\rangle$ state while A_{1b} represents the amplitude of the oscillation of the $|\uparrow\uparrow\rangle$ state. These amplitudes provide a scaling factor for the phase reversal oscillations and direct Bell state measurement, allowing for the extraction of SPAM error from the results. **b.** Rabi oscillation with two-qubit readout performed on Q2. A_{2a} represents the amplitude of the oscillation of the $|\downarrow\downarrow\rangle$ state while A_{2b} represents the amplitude of the oscillation of the $|\downarrow\uparrow\rangle$ state.

$$A_{1a} = I_{\downarrow\uparrow} \times R_{\downarrow\uparrow}, \tag{5.8}$$

$$A_{1b} = I_{\downarrow\uparrow} \times R_{\uparrow\uparrow}, \tag{5.9}$$

$$A_{2a} = I_{\downarrow\downarrow} \times R_{\downarrow\downarrow}, \tag{5.10}$$

$$A_{2b} = I_{\downarrow\downarrow} \times R_{\downarrow\uparrow}, \tag{5.11}$$

$$\tag{5.12}$$

In order to extract the SPAM from our phase reversal measurement, we require the information $I_{\downarrow\downarrow} \times R_{\downarrow\downarrow}$ and $I_{\downarrow\downarrow} \times R_{\uparrow\uparrow}$. The value of $I_{\downarrow\downarrow} \times R_{\downarrow\downarrow}$ is obtained directly from the amplitude A_{2a} (see Fig. 5.13), while $I_{\downarrow\downarrow} \times R_{\uparrow\uparrow}$ can be obtained with the following expression:

$$I_{\downarrow\downarrow} \times R_{\uparrow\uparrow} = \frac{I_{\downarrow\uparrow} \times R_{\uparrow\uparrow} \times I_{\downarrow\downarrow} \times R_{\downarrow\uparrow}}{I_{\downarrow\uparrow} \times R_{\downarrow\uparrow}} \tag{5.13}$$

$$= \frac{A_{1b} \times A_{2b}}{A_{1a}} \tag{5.14}$$

These values are then used as a scaling factor for the Bell state measurements.

As discussed in section 4.3.2.2, one useful metric for quantifying entanglement is concur-

rence, which represents the overlap between a state $|\Phi\rangle$ and a state that is diametrically opposite to $|\Phi\rangle$ on the Bloch sphere. A concurrence value of 0.91 ± 0.08 was obtained from the SPAM excluded, physical density matrix, indicating a high degree of entanglement between Q1 and Q2.

5.7 Further mechanisms associated with a reduction in two-qubit fidelity

5.7.1 AC Zeeman shift

In order to obtain high-fidelity two-qubit operations, we must account for off-resonant driving effects, such as AC Zeeman shift, as discussed in section 2.7. Although the resonance frequency shift induced by the AC Zeeman shift for a given pulse can be calculated theoretically, it is often beneficial to corroborate the theoretical results experimentally. Figure 5.14 shows the shift in resonance frequency caused by the AC Zeeman shift, as a function of frequency detuning between the applied magnetic field and the resonance frequency of the system, as well as power of the applied pulse. This information can be used to mitigate the effect of AC Zeeman shift during a two-qubit experiment, by performing a virtual Z gate after each pulse, through an additional phase added to the subsequent control pulses. The amount of phase added by the virtual gate can be extracted for each pulse by calculating the expected AC Zeeman shift for a given frequency detuning and pulse power (see equation 2.67 in section 2.7). Using these virtual-Z gates we can mitigate the effects of AC Zeeman shift in the system.

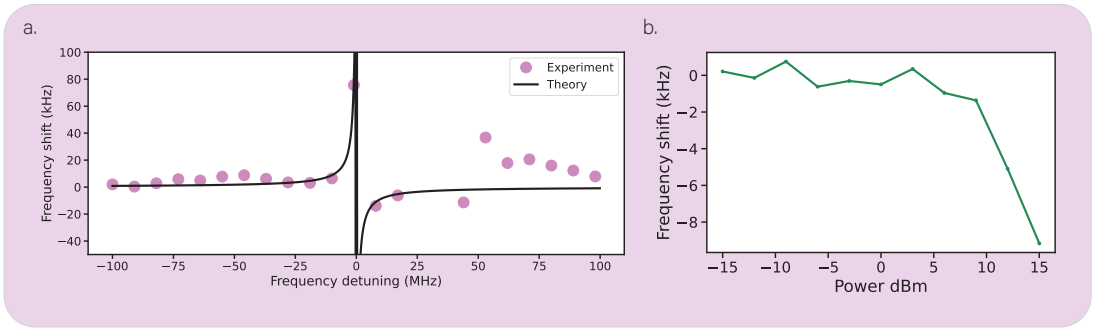

Figure 5.14: **Experimental AC Zeeman shift. a.** Measured vs theoretical frequency shift from the AC Zeeman effect, as a function of frequency detuning between the resonance frequency and the frequency of the magnetic AC driving field. **b.** Measured frequency shift as a function of the power of the AC drive.

5.7.2 Beating in spin precession

Another potential source of reduction in two-qubit fidelity in this device was a beating observed in the spin precession of electron Q2. Figure 5.15 shows a Ramsey measurement performed on electron Q2, with a destruction in the coherence of the Ramsey fringes observed at a wait time of approximately 15 μs, followed by a subsequent revival of the coherence fringes. Additionally, this beating in the coherence oscillations was observed in the two-electron Bell state. To probe this, we performed a modified version of the phase reversal tomography measurement discussed in section 5.6, whereby we introduced a wait time in between the Bell state preparation and reversal pulses; the duration of which was incrementally swept. This allowed us to measure the coherence time of the Bell state. As with the Ramsey measurement performed on a Q2, we observed a beating in the coherence of the Bell state, with the same period as that observed in the Ramsey measurement. Figure 5.16 shows this beating in the coherence of the Bell state for the case of the $\frac{1}{\sqrt{2}}(|\uparrow\downarrow\rangle + |\downarrow\uparrow\rangle)$ Bell state.

This beating was not however, observed in a Hahn echo measurement performed on electron Q2, as shown in Figure 5.15, indicating that the source of the beating is refocused during a Hahn echo measurement.

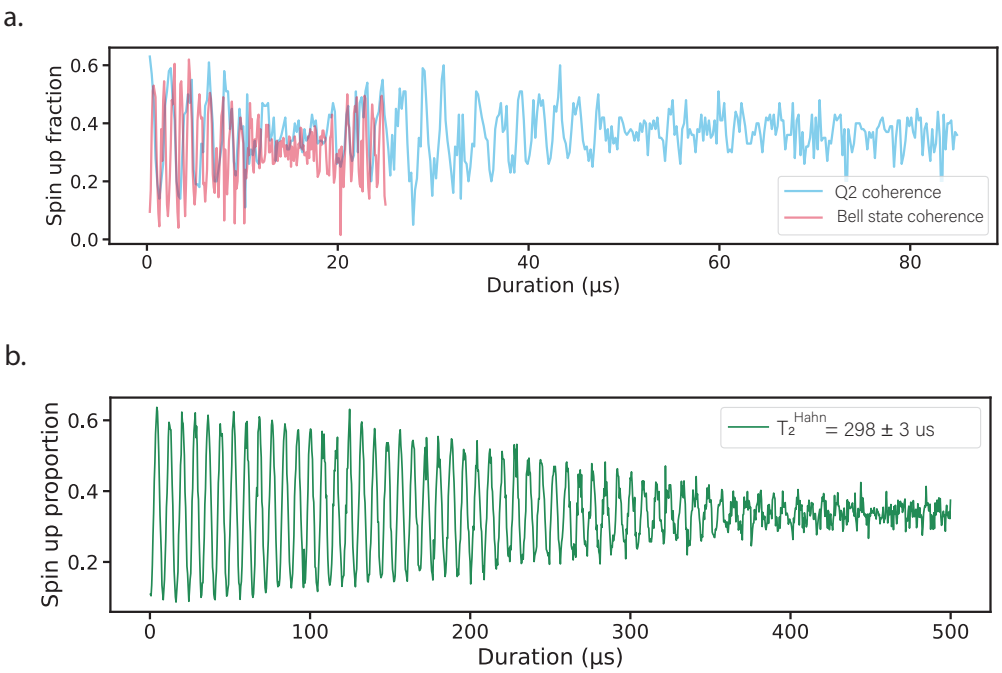

Figure 5.15: **Beating in Ramsey coherence. a.** Ramsey measurement performed on electron Q2 (blue line) and phase reversal tomography of a Bell state between the electrons (pink line), with a wait time introduced between the preparation and reversal pulses. A destruction of coherence is observed in both measurements at a wait time of approximately 15μs, which we denote as a beating in the coherence. **b.** Hahn echo measurement performed on electron Q2, which does not show any beating, indicating that the source of the beating has been refocused in this measurement.

One potential mechanism for this beating in the coherence of electron Q2 is as a result of a switching in the precession frequency of the electron, caused by the loading and unloading of a nearby charge trap in the vicinity of the donor. To test this, we performed a Ramsey measurement on Q2, while sweeping the voltage applied to the gate PL during the electron loading phase. We observed that the period of the beating observed in the Ramsey oscillation did not change as a function of gate voltage. This makes it unlikely that the ESR frequency switching is caused by a switching charge trap, because such traps typically switch only within narrow regions of gate space, whereas they are frozen

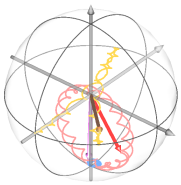

(polarized) by tuning them away from their charge resonance condition.

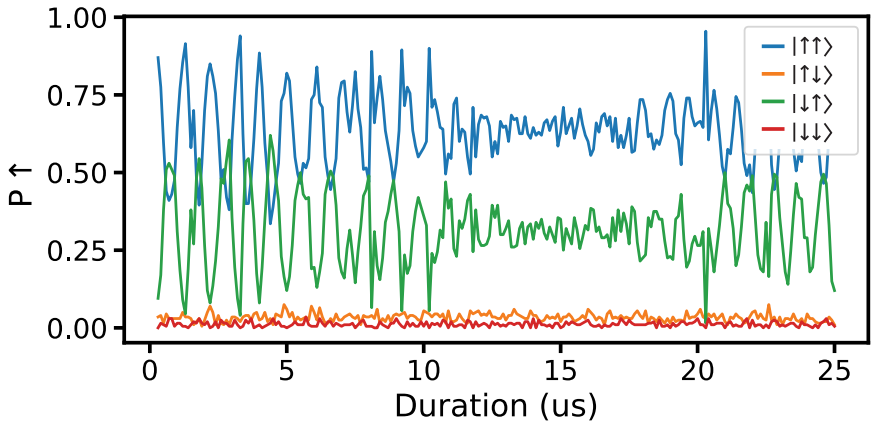

Figure 5.16: **Beating in the Bell state coherence.** In this measurement we first prepare the bell state $\frac{1}{\sqrt{2}}(|\uparrow\downarrow\rangle + |\downarrow\uparrow\rangle)$ with a $\frac{\pi}{2}$ on Q1 and a CROT on Q2. We then apply these pulses in reverse, while sweeping the phase of the reversal pulses. Additionally, we introduce a wait time between the Bell state preparation and reversal pulses, which is also swept. The duration along the x-axis of the plot represents the duration of the wait time between the Bell state preparation and reversal pulses. In this way we can therefore measure the coherence time of the prepared electron Bell state, revealing a beating in the coherence.

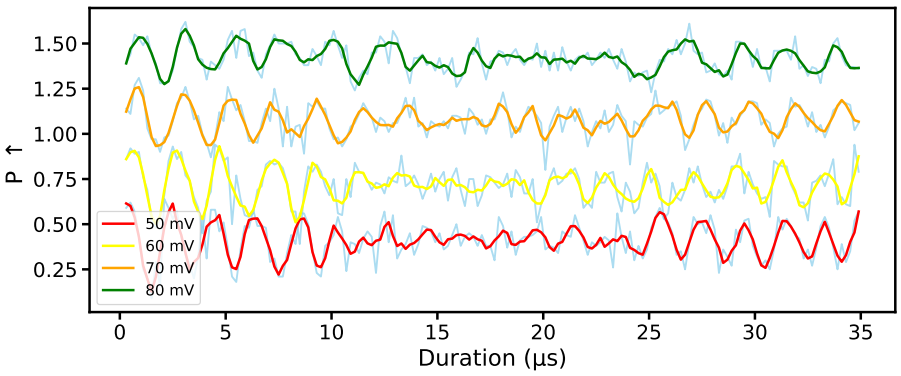

Figure 5.17: **Ramsey measurement on electron Q2 for varying loading voltages.** Beating observed in the Ramsey oscillation as a function of voltage applied to the PL gate at the 'load' tuning point of the electron (see section 3.9.3 for information on the 'load' tuning point).

5.8 Tuning the exchange interaction

The exact value of the exchange interaction between two exchange-coupled electrons depends upon the overlap of their wavefunctions, which in turn can be influenced by the voltages applied to the gates fabricated on the surface of the device. In order to test the tunability of the exchange interaction with the applied gate voltages, we initialised the nuclei in an anti-parallel spin configuration of $|\Uparrow\Downarrow\rangle$, before performing two Ramsey measurements, one on Q2 conditional on Q1 being in the $|\downarrow\rangle$ state ($f_{2\downarrow}$) and one on Q2 conditional on Q1 being in the $|\uparrow\rangle$ state ($f_{2\uparrow}$). These Ramsey measurements were performed while sweeping the voltage applied to one of the gates. Any frequency shift as a function of gate voltage, that shifts both $f_{2\downarrow}$ and $f_{2\uparrow}$ together can be explained by DC Stark shift of both the hyperfine interaction and g-factor. However, the frequency difference $|f_{2\downarrow} - f_{2\uparrow}|$ depends only on the exchange interaction between Q1 and Q2 and hence any change in $|f_{2\downarrow} - f_{2\uparrow}|$ represents a change in the magnitude of the exchange interaction between the electrons.

For a change in voltage of ≈ 70 mV we observed a DC Stark shift of ≈ 40 kHz and a shift in exchange coupling of ≈ 400 kHz. This translates to a tunability of the exchange coupling of $\frac{dJ}{dV_G} = 5.7$ MHz/V. This low tunability, indicates that we may be in a plateau region of electric sensitivity. This is also corroborated by the low noise in J-coupling measured by comparing the coherence times of the electrons with and without the exchange coupling present (see section 5.3).

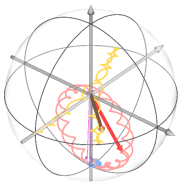

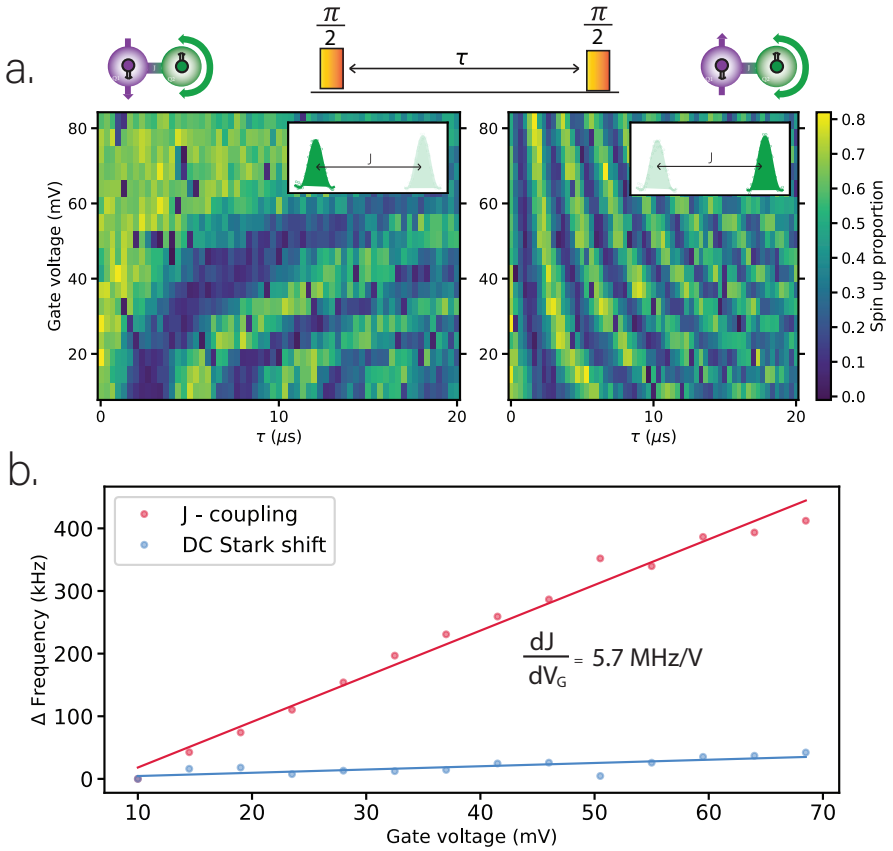

Figure 5.18: **Tuning the exchange coupling. a.** Ramsey measurements performed on the electron Q2 with electron Q1 either in the $|\downarrow\rangle$ state (left plot) or $|\uparrow\rangle$ state (right plot) as a function of the loading voltage of the electron. Each Ramsey was fitted and the frequency of the Ramsey oscillations as a function of voltage was extracted. **b.** DC Stark shift as a function of gate voltages, extracted with $\frac{\bar{\nu}}{\Delta V}$ where ΔV is the change in voltage and $\bar{\nu} = \frac{\nu_1+\nu_2}{2}$. ν_1 is the frequency of the Ramsey oscillation conditional on Q1 in the $|\downarrow\rangle$ state and ν_2 is the frequency of the Ramsey oscillation conditional on Q1 in the $|\uparrow\rangle$ state. The change in exchange interaction as a function of gate voltage was calculated with $\frac{\Delta\nu}{\Delta V}$ where $\Delta\nu = \nu_2 - \nu_1$.

5.9 Limitations of QND readout of the electron

As discussed in section 3.11.2, a condition that must be fulfilled in order for a measurement to be truly QND in nature is that the qubit Hamiltonian, $\hat{H}_Q$ must commute with the interaction $\hat{H}_C$ [109]

$$[\hat{H}_Q, \hat{H}_C] = 0. \tag{5.15}$$

For the case of $J \ll A$ the exchange interaction is only approximately of Ising type and thus for this system $[\hat{H}_Q, \hat{H}_C] \neq 0$, resulting in the readout of the electron Q2 being not fully QND in nature. As a consequence of this, the exchange interaction acts to weakly entangle the two electrons, resulting in the eigenstates of the system becoming hybridised. These hybridised eigenstates can be written as follows

$$\widetilde{|\uparrow_A\downarrow_D\rangle} = c\,|\uparrow_A\downarrow_D\rangle - s\,|\downarrow_A\uparrow_D\rangle\,, \tag{5.16}$$

$$\widetilde{|\downarrow_A\uparrow_D\rangle} = c\,|\downarrow_A\uparrow_D\rangle - s\,|\uparrow_A\downarrow_D\rangle\,, \tag{5.17}$$

where the subscript D denotes the state of the data electron being read out (Q2 in the case of this thesis) and A denotes the state of the ancillary electron being used to read out the data qubit (Q1 in this case). $c = \cos(\theta)$ and $s = \sin(\theta)$, $\tan(2\theta) = \frac{J}{\Delta}$. where $\Delta = \bar{A}$ for the case of the anti-parallel nuclei. This hybridisation of states leads to a small probability of flipping the data electron during the QND readout process. To understand the origin of this we must determine the tunnelling rates associated with the QND readout process. We can start by restricting our analysis to the case in which the temperature $T = 0$ [138].

There are two main contributions to the tunnel rates in this system. The first contribution is from the amplitudes of the transition matrix elements coupling the one-particle (1P) and two-particle (2P) states, where the 1P states consist of the donor qubit states $|\downarrow_D\rangle$ and $|\uparrow_D\rangle$, while the 2P states consist of the two-electron states $|\uparrow_A\uparrow_D\rangle\,, \widetilde{|\uparrow_A\downarrow_D\rangle}, \widetilde{|\downarrow_A\uparrow_D\rangle}, |\downarrow_A\downarrow_D\rangle$. These amplitudes are given by

$$M_{1P,2P} = |\,\langle 1P|\,\hat{a}_\uparrow + \hat{a}_\downarrow\,|2P\rangle\,|^2, \tag{5.18}$$

where $\hat{a}^\dagger_\downarrow(\hat{a}^\dagger_\uparrow)$ creates a spin $\downarrow$ ($\uparrow$) particle on the ancilla. A value of $M_{1P,2P} = 0$ for a given transition, indicates that this transition is forbidden.

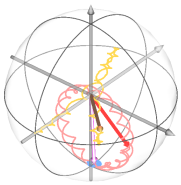

The second contribution to the tunnel rates is the selection through energy occurring as a result of the relative positioning of the chemical potentials of each energy level with respect to the SET electrochemical potential, μ_{SET}. In this system, there are three chemical potentials that lie above the electrochemical potential of the SET: $\mu_{\widetilde{\uparrow_A\downarrow_D}\leftrightarrow\downarrow_D}$, $\mu_{\uparrow_A\uparrow_D\leftrightarrow\uparrow_D}$, $\mu_{\widetilde{\downarrow_A\uparrow_D}\leftrightarrow\downarrow_D}$ and three chemical potentials that lie below the electrochemical potential of the SET: $\mu_{\widetilde{\uparrow_A\downarrow_D}\leftrightarrow\uparrow_D}$, $\mu_{\downarrow_A\downarrow_D\leftrightarrow\downarrow_D}$, $\mu_{\widetilde{\downarrow_A\uparrow_D}\leftrightarrow\uparrow_D}$. Making the assumption that the density of states in the SET is approximately constant over the relevant energy scales and that the Fermi distribution of the SET, $f(E)$, is approximately the same for all the cases of an $\uparrow$ electron tunnelling and all the cases of a $\downarrow$ electron tunnelling we can define the following tunnel rates

$$\Gamma_{\uparrow}^{\text{in}} = \Gamma_0 f(\mu_{\uparrow}), \tag{5.19}$$

$$\Gamma_{\uparrow}^{\text{out}} = \Gamma_0 f(1-\mu_{\uparrow}), \tag{5.20}$$

$$\Gamma_{\downarrow}^{\text{in}} = \Gamma_0 f(\mu_{\downarrow}), \tag{5.21}$$

$$\Gamma_{\downarrow}^{\text{out}} = \Gamma_0 f(1-\mu_{\downarrow}), \tag{5.22}$$

where $\mu_{\downarrow}(\mu_{\uparrow})$ represent the low (high) chemical potentials and $\Gamma_0 = |t_0|^2 n(\mu)$ is the bare tunnelling rate, where $n(\mu)$ is a constant. For the case in which $T = 0$ only the tunnel rates $\Gamma_{\downarrow}^{\text{in}}$ and $\Gamma_{\uparrow}^{\text{out}}$ are non-zero.

We can first consider the case for which an ancilla electron is loaded while the data qubit is in the $\uparrow_D$ state. In this case the relevant transition rates are given by the following

$$\Gamma^{\text{in}}_{\uparrow_D\leftrightarrow\widetilde{\uparrow_A\downarrow_D}} = \Gamma^{\text{in}}_{\downarrow} M_{\uparrow_D,\widetilde{\uparrow_A\downarrow_D}} = \Gamma^{\text{in}}_{\downarrow} s^2, \tag{5.23}$$

$$\Gamma^{\text{in}}_{\uparrow_D\leftrightarrow\widetilde{\downarrow_A\uparrow_D}} = \Gamma^{\text{in}}_{\downarrow} M_{\uparrow_D,\widetilde{\downarrow_A\uparrow_D}} = \Gamma^{\text{in}}_{\downarrow} c^2. \tag{5.24}$$

$$\tag{5.25}$$

For these three states the time evolution of the system can then be calculated using the following rate equations [138]

$$\begin{pmatrix} \dot{\rho}_{\widetilde{\uparrow_A\downarrow_D}} \\ \dot{\rho}_{\widetilde{\downarrow_A\uparrow_D}} \\ \dot{\rho}_{\uparrow_D} \end{pmatrix} = \begin{pmatrix} 0 & 0 & \Gamma_{\downarrow}^{\text{in}} s^2 \\ 0 & 0 & \Gamma_{\downarrow}^{\text{in}} c^2 \\ 0 & 0 & -\Gamma_{\downarrow}^{\text{in}} \end{pmatrix} \begin{pmatrix} \rho_{\widetilde{\uparrow_A\downarrow_D}} \\ \rho_{\widetilde{\downarrow_A\uparrow_D}} \\ \rho_{\uparrow_D} \end{pmatrix}. \tag{5.26}$$

For the case of an initial $\uparrow_D$ state of the data qubit the 2P state probabilities as a function of time are the following

$$\rho_{\widetilde{\uparrow_A\downarrow_D}}(t) = s^2(1 - e^{-\Gamma_{\downarrow}^{\text{in}} t}) \rightarrow^{t\rightarrow\infty} s^2, \tag{5.27}$$

$$\rho_{\widetilde{\downarrow_A\uparrow_D}}(t) = c^2(1 - e^{-\Gamma_{\downarrow}^{\text{in}} t}) \rightarrow^{t\rightarrow\infty} c^2. \tag{5.28}$$

The implications of this are that as the tunneling time $t \rightarrow \infty$ there exists a non-zero probability, even at $T = 0$, to flip the data qubit upon loading the ancilla, purely as a result of the weak entanglement between the ancilla and target electron. The probability of flipping the data qubit from $\uparrow_D \leftrightarrow \downarrow_D$ upon loading the ancilla is given by s^2. In the system described in this thesis, where $J \approx 12$ MHz and $\Delta = \bar{A} \approx 112$ MHz, $s^2 \approx 2.8 \times 10^{-3}$. For the case of $T = 0$, the probability of flipping the data qubit from $\downarrow_D \leftrightarrow \uparrow_D$ is 0 due to the fact that this requires the tunnel rates $\Gamma_{\uparrow}^{\text{in}}$ and $\Gamma_{\downarrow}^{\text{out}}$ to be non-zero.

For the case of $T > 0$ however, the Fermi distribution of the SET is broadened and hence

$$\Gamma_{\downarrow}^{\text{in}} = \Gamma_{\uparrow}^{\text{out}} = \Gamma_0(1 - f), \tag{5.29}$$

$$\Gamma_{\uparrow}^{\text{in}} = \Gamma_{\downarrow}^{\text{out}} = \Gamma_0 f. \tag{5.30}$$

where we assume that the chemical potential is centred perfectly between $\mu_{\uparrow}$ and $\mu_{\downarrow}$ and hence $f = f(\mu_{\uparrow}) = 1 - f(\mu_{\downarrow})$. For electrons in a magnetic field of approximately 1 T, $\mu_{\uparrow} - \mu_{\downarrow} \approx 27.97$ GHz and hence $f \approx 0.03$.

Simulating this tunnelling process, we find that the the probability of flipping the data qubit from $\downarrow_D \rightarrow \uparrow_D$ increases and then saturates at a flipping rate of 1.2×10^{-2} [109]. This saturation is as a result of two competing processes which converge to an equilibrium,

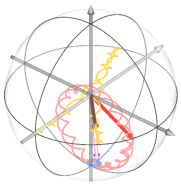

due to the fact that, when the data qubit is flipped to the $\uparrow_D$ state, then the processes described above act to flip this spin back to the $\downarrow_D$ state. The point at which this equilibrium converges depends upon the ratio of the 'fast' tunneling events: $\Gamma_{\downarrow}^{\text{in}}$, $\Gamma_{\uparrow}^{\text{out}}$ (which are non-zero even at $T = 0$) and the 'slow' tunnelling events: $\Gamma_{\uparrow}^{\text{in}}$, $\Gamma_{\downarrow}^{\text{out}}$ (which come about as a result of thermal broadening of the SET island for $T > 0$).

Interestingly, this equilibrium point also depends on which conditional resonance is used to flip the ancilla electron: the conditional resonance to flip the ancilla dependent on the data qubit being in the $\downarrow_D$ state (CR($\downarrow_D$)) or the conditional resonance to flip the ancilla dependent on the data qubit being in the $\uparrow_D$ state (CR($\uparrow_D$)). To understand the reason behind this we can break down the process involved in a spin flip of the data qubit from $\downarrow_D$ to $\uparrow_D$, for the case of driving either CR($\downarrow_D$) or CR($\uparrow_D$), as shown in Figure 5.19. This reveals that, for the case of driving CR($\downarrow_D$), both a slow and a fast tunnelling process are required in order to flip the data qubit from $\downarrow_D$ to $\uparrow_D$. For the case of driving CR($\uparrow_D$) on the other hand, the only tunnelling processes involved are slow tunnelling processes. Consequently, the flipping rate of the data qubit is slower for the case of driving the CR($\uparrow_D$) resonance.

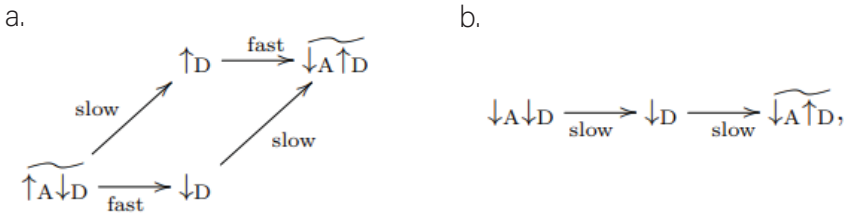

Figure 5.19: **Errors in the QND process.a.** Shows the tunnelling processes involved in flipping the data qubit from $\downarrow_D$ to $\uparrow_D$ for the case of reading out the resonance CR($\downarrow_D$) revealing that this flipping mechanism relies on both fast and slow tunnelling mechanisms. **b.** Shows the tunnelling processes involved in flipping the data qubit from $\downarrow_D$ to $\uparrow_D$ for the case of reading out the resonance CR($\uparrow_D$). In this case only slow tunnelling processes are involved in the flipping process, resulting in a slower flipping rate of the data qubit from $\downarrow_D$ to $\uparrow_D$ for the case of driving the CR($\uparrow_D$) resonance.

In order to best describe the true situation of QND readout in a two-donor exchange coupled electron system we input experimentally informed tunnelling rates into this QND model, as well as relaxing both the assumption that the density of states of the SET is constant [85] and that the electrochemical potential of the SET is perfectly centred between the $\mu_{\downarrow}$ and $\mu_{\uparrow}$ states. With these experimentally informed parameters, the simulations of the QND measurement process with an initial state of the data qubit of $\downarrow_D$, and driving the conditional rotation CR($\uparrow_D$) is shown in Figure 5.20. In this case, the ratio $\Gamma_{\downarrow}^{\text{in}}/\Gamma_{\uparrow}^{\text{in}} = 2$ and hence there is a much higher probability of erroneously loading a spin $\uparrow_A$ ancilla spin. This hence increases the likelihood of the process $\downarrow_D \rightarrow \widetilde{\downarrow_A\uparrow_D}$ and hence the probability of flipping the data qubit from $\downarrow_D$ to $\uparrow_D$.

These error mechanisms associated with imperfections in the QND readout process represent the dominant source of erroneous flipping of the data qubit compared to the natural relaxation of the electron spin [109].

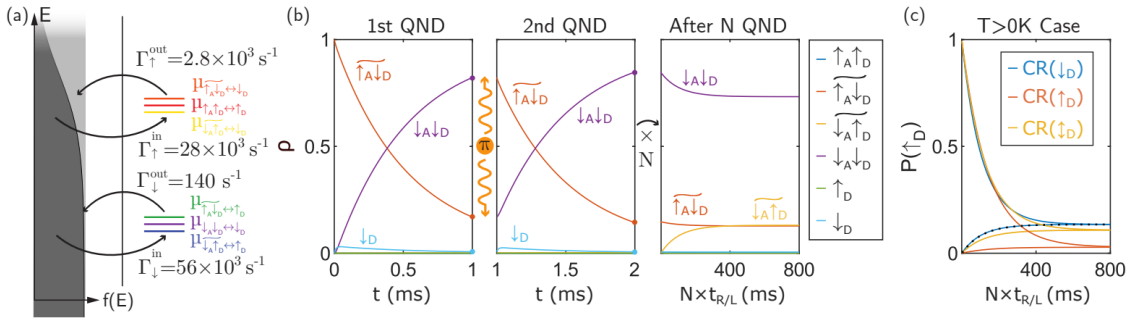

Figure 5.20: **Error channels in the QND measurement of exchange-coupled spins with experimental parameters. a.** Chemical potentials with respect to a Fermi distribution in the lead for an off-centered read/load tuning representing the given set of experimentally-informed spin-dependent tunnel rates. **b.** Simulations of the QND measurement with an initial state of the data qubit of $|\downarrow\rangle$, and driving a conditional rotation on the ancilla dependent on the data being spin $|\downarrow\rangle$ state. N represents the number of QND repetitions.**c.** Probability of finding the data in the spin $|\uparrow\rangle$ state after repeated QND measurements as a function of time for different conditional rotations (CR) on the ancillate qubit. The case of conditionally rotating the ancilla depending on the data qubit being in the $|\downarrow\rangle$ state, with an initial spin $|\downarrow\rangle$ data electron is highlighted by the black dotted line. Figure taken from [109].

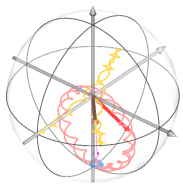

5.10 Operation and readout of electrons in the parallel nuclear regime of a J-coupled system

In the previous sections we have focused primarily on the operation and readout of the electrons in an exchange-coupled donor pair, for the case in which the two donor nuclei are initialised in an anti-parallel spin orientation of either $|\Downarrow\Uparrow\rangle$ or $|\Uparrow\Downarrow\rangle$. In this anti-parallel configuration, the detuning, Δ, between the two electrons is given by $\Delta = \bar{A}$, where $\bar{A} = \frac{A_1+A_2}{2}$ is typically $\approx$ 117 MHz. In the following sections we will consider the readout and operation of the electrons in an exchange-coupled donor pair, when the nuclei are instead initialised in a parallel spin orientation of either $|\Downarrow\Downarrow\rangle$ or $|\Uparrow\Uparrow\rangle$. When the nuclei are in a parallel orientation, the detuning between the electrons is given by $\Delta = \Delta A = |A_1 - A_2|$, which is typically of order $\approx$ a few MHz. Consequently, for the cases in which $\Delta A < J < \bar{A}$, as is the case for the device measured in this thesis with $\bar{A} \approx 112$ MHz, $\Delta A \approx 2$ MHz and $J \approx 12$ MHz, flipping the nuclei from an anti-parallel to a parallel spin orientation allows us to transition from the $J << \Delta$ to the $J > \Delta$ regime.

5.10.1 Operation

As discussed in section 4.2.2, when the nuclei are initialised in a parallel spin orientation of either $|\Downarrow\Downarrow\rangle$ or $|\Uparrow\Uparrow\rangle$ the electron transitions frequencies are the following

$$\nu_\beta = T_- \longleftrightarrow \widetilde{S}, \tag{5.31}$$

$$\nu_\alpha = T_- \longleftrightarrow T_0, T_0 \longleftrightarrow T_+, \tag{5.32}$$

$$\nu_\gamma = \widetilde{S} \longleftrightarrow T_+, \tag{5.33}$$

where $\widetilde{S}$ is a hybridised singlet-like state, introduced in section 4.2.2. Fig.5.21,a and b show a schematic representation of these resonance frequencies in the regime of $J > \Delta = \Delta A$. The transition α is comprised of two transitions, one from $T_- \longleftrightarrow T_0$ and one from $T_0 \longleftrightarrow T_+$, which differ in frequency by an amount ΔA in the limit of low J ($J < \bar{A}$). For the case in which $2\nu_R >> \Delta A$, where ν_R is the Rabi frequency of the electron, the AC driving field will overlap with both transition frequencies and thus drive both transitions

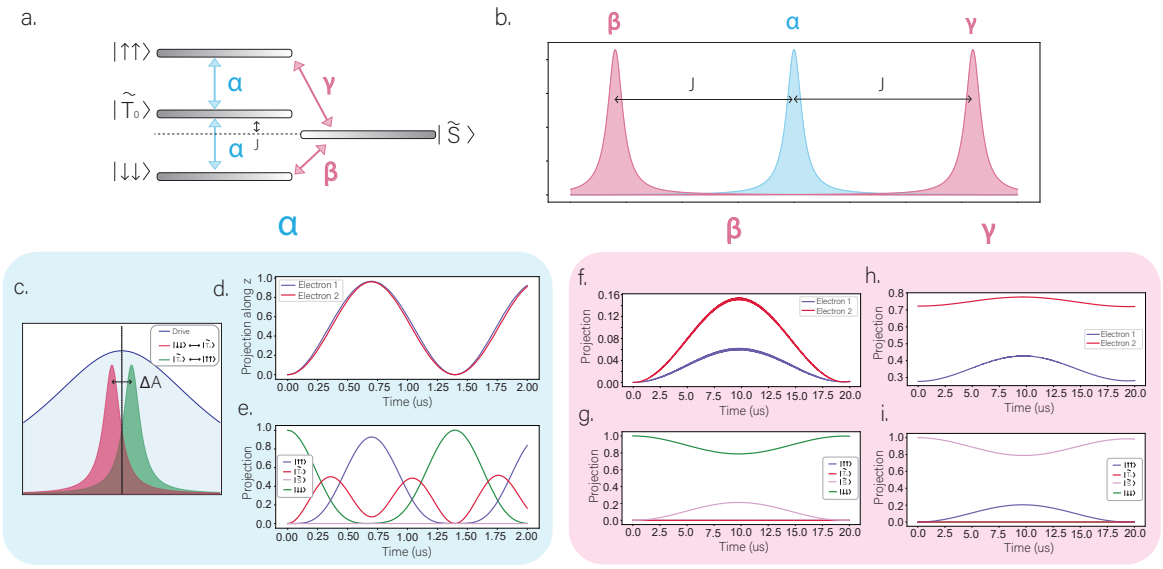

Figure 5.21: **Operation of the electrons for the case of parallel nuclear spins. a.** Energy eigenstates of the electrons in parallel nuclei regime. T_-,T_0 and T_+ represent the three triplet states, while $\tilde{S}$ represents a hybridised 'singlet-like' state. **b.** Schematic of the expected ESR transitions present in the parallel nuclear regime. **c.** Simulation of the driving of the α transition, at a frequency centred between the $T_- \leftrightarrow T_0$ transition and $T_0 \leftrightarrow T_+$ transition, which differ due to a different hyperfine between the two donors. The simulation was carried out with $J = 12$ MHz and $\Delta A = 2$ MHz. **d.** Simulation of the β and γ transitions for $J = 12$ MHz and $\Delta A = 10$ MHz. A higher value of ΔA was chosen in order to amplify the amplitude of the $\tilde{S}$ occupation.

simultaneously. This is shown schematically in Fig.5.21,c, which shows a driving field, applied at the centre of the two frequencies representing the transitions $T_- \longleftrightarrow T_0$ and $T_0 \longleftrightarrow T_+$, where the the linewidth of the driving field, $2\nu_R > \Delta A$ and hence the field drives both transitions simultaneously. The result of driving both transitions simultaneously is shown in the simulation in Fig 5.21 d and e. In this simulation, an AC driving field, with a Rabi frequency $2\nu_R > \Delta A$ is applied for a varying duration of time at a frequency centred between the frequency of the two transitions $T_- \longleftrightarrow T_0$ and $T_0 \longleftrightarrow T_+$. Plotting the projection of both electrons on the z-axis of the Bloch sphere (Fig 5.21 d), we see that both electrons oscillate between the $|\downarrow\rangle$ and $|\uparrow\rangle$ state. If we plot the projection of the electron states on the triplet and singlet states however (Fig 5.21 e), we see that the electrons oscillate between the T_- state and a state comprised primarily of the T_+ state,

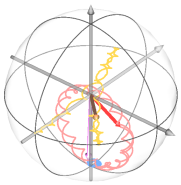

with a small contribution from the T_0 state. By extracting the $\frac{\pi}{2}$ pulse duration from Fig 5.21 d, we see that upon applying a $\frac{\pi}{2}$ pulse at the resonance ν_α we do not prepare the T_0 state but instead prepare a mixture of T_-, T_0 and T_+ state.

Fig. 5.21 f-i, shows the simulation of an AC driving field applied at either the resonance ν_β (Fig.5.21 f,g) or ν_γ (Fig.5.21 h,i). Although a pure singlet state possesses a total spin of zero, resonances β and γ are addressable via ESR, as a result of the singlet state becoming hybridised, in the energy regime for which $J \approx \Delta A$. This hybridised singlet-like state, $\tilde{S}$, thus no longer possess a spin of zero, allowing it to be addressed with ESR. As $J \to \infty$ however, this state approaches a pure singlet state and hence the β and γ transitions become forbidden in this energy regime. A characteristic behaviour of a weakly J coupled system is therefore the observation of two ESR transitions that always occur simultaneously when the electrons are initialised in the T_- state, corresponding to the α and β transitions, as shown in Figure 5.22. The difference in frequency between these transitions is given by J. In order to observe the γ transition, a pre-pulse at a frequency β must first be applied, in order to initialise the electrons into the $\tilde{S}$ state.

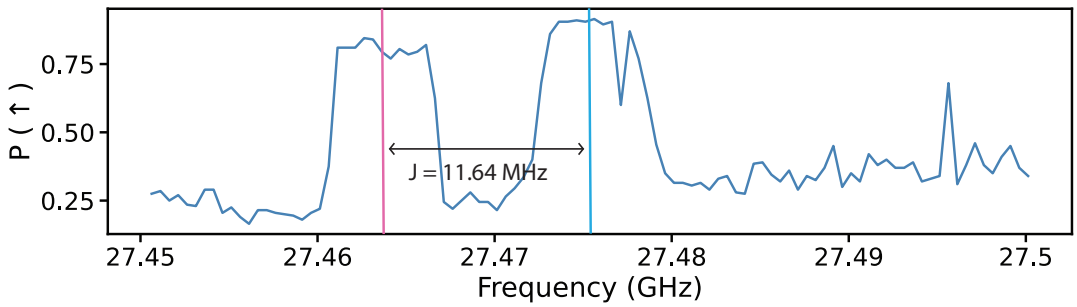

Figure 5.22: **Adiabatic ESR transitions in a parallel nuclear configuration.** Adiabatic ESR spectrum with the nuclei initialised in the $|\Downarrow\Downarrow\rangle$ state. Left peak centred around the pink line indicates the $T_- \leftrightarrow \tilde{S}$ transition, while the right peak centred around the blue line indicates the $T_- \leftrightarrow T_+$ transition. The two transition frequencies are separated by the exchange coupling strength $J = 11.64$ MHz and are simultaneously active when the nuclei are initialised in a parallel orientation.

5.10.1.1 Readout

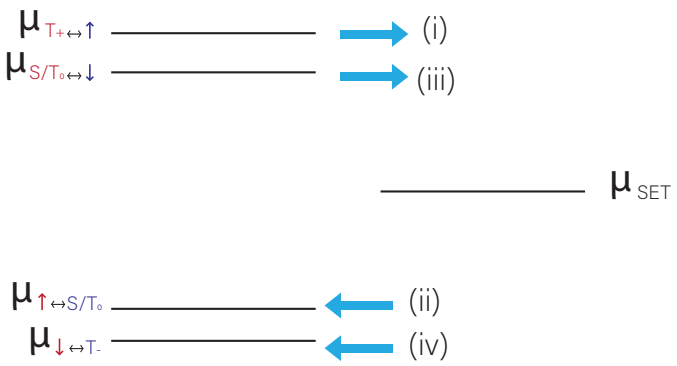

Figure 5.23: **Tunnelling to the SET in the parallel nuclear regime.** Two-electron energy levels with respect to the electrochemical potential of the SET, μ_{SET}. Labels (i - iv) depict the numbered steps associated with the electron readout process for the case of the nuclei in a parallel spin orientation. The subscripts for each of the two-electron energy levels depict the initial (red) and final (blue) states following a tunnelling event. Following the preparation of a T_+ state, in step (i) electron 1 tunnels onto the SET island, leaving behind a spin $|\uparrow\rangle$ electron on donor 2. In step (ii) a spin $|\downarrow\rangle$ electron tunnels onto the donor into a T_0/S state. The T_0 and S state energy levels have not been differentiated in this diagram as the energy level splitting between these states (given by J) is very small compared to the splitting between the spin $|\downarrow\rangle$ and spin $|\uparrow\rangle$ states (given by the Zeeman splitting). In step (iii) a spin $|\uparrow\rangle$ electron tunnels from the T_0/S state onto the SET island, leaving behind a spin $|\downarrow\rangle$ electron on donor 2. Finally, in step (iv), a spin $|\downarrow\rangle$ electron tunnels from the SET island, into the T_- state, resulting in further tunnelling to the SET being prohibited.

In a weakly J coupled donor system, the electron readout contrast is increased when the nuclei are in a parallel spin orientation, compared to an anti-parallel spin orientation, when the electrons are read out via spin dependent tunnelling to an SET [30]. We believe this to be attributed to the fact that a spin $|\uparrow\rangle$ electron will result in two tunnelling events to the SET island for the case of the nuclei being in a parallel state, compared to a single tunnelling event for the case of the nuclei being in an anti-parallel state. This extra tunnelling event presents an additional opportunity to identify a current blip, thus reducing the instances of missed current blips and the subsequent mis-identification of a spin $|\uparrow\rangle$ electron as a spin $|\downarrow\rangle$.

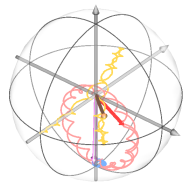

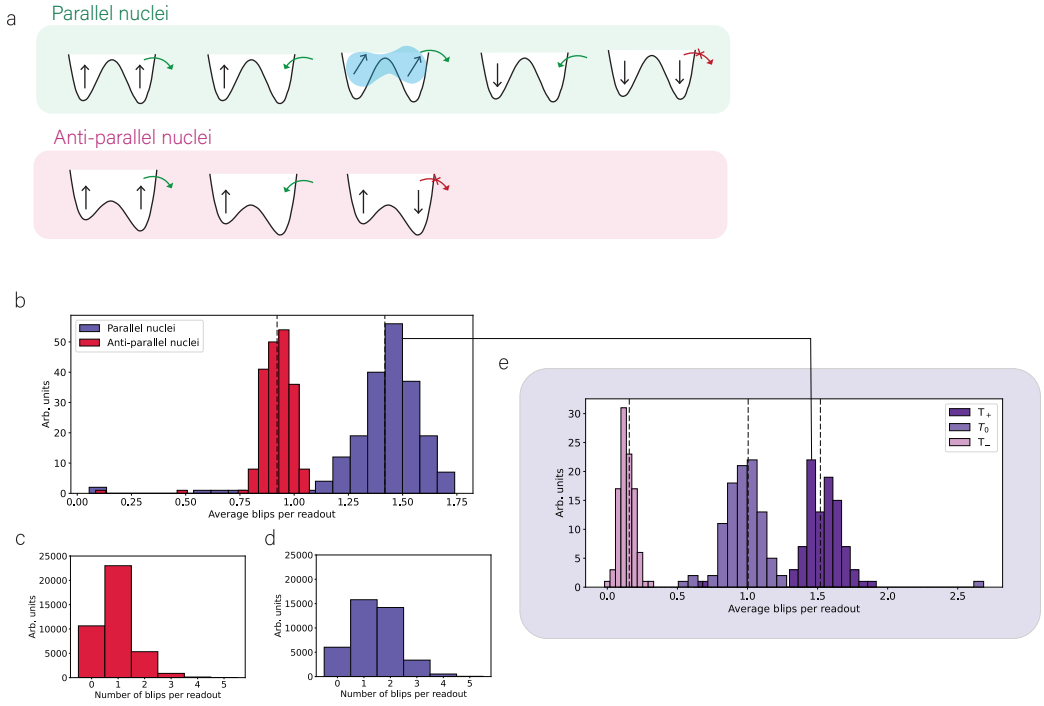

Figure 5.24: **Readout of the electron in the parallel nuclear regime.a.** Readout schematic of the electrons in the regime of parallel nuclear spins (top, green box) and the anti-parallel nuclear regime (bottom, pink box). **b** Histogram of 10,000 repetitions of T_+ readout for the anti-parallel and parallel nuclear configurations. **c** Histogram of 10,000 repetitions of the T_-, $\widetilde{T_0}$ and T_+ readout for the parallel nuclear state.

The process behind this double tunnelling event is outlined in Figure 5.23, where only electron 1 is read out via spin dependent tunnelling to the SET. In the case of a parallel nuclear orientation, as the eigenstates of the two electrons consist of highly entangled T_0 and S states, we must consider the combined, two-electron energy levels of the system in order to understand the tunnelling behaviour of electron 1. When the nuclei are in a parallel spin configuration, upon initialising the electrons into the T_+ state and moving to the readout position, the spin $|\uparrow_1\rangle$ electron 1 will tunnel off of the donor, resulting in a blip of current and leaving behind a spin $|\uparrow_2\rangle$ electron on donor 2. Remaining at the readout position, a spin $|\downarrow_1\rangle$ electron will eventually tunnel back onto the ionised donor 1. As the electron must tunnel into an eigenstate of the system, and the other electron of the pair is in the $|\uparrow_2\rangle$ state, the most energetically favourable state for the electron to tunnel into

is either the T_0 and S state. Both the T_0 and S state have an associated tunneling time to the SET, which is typically smaller then the readout duration. This therefore presents an additional opportunity, during the same readout window, for electron 1 to once again tunnel from the donor onto the SET island as a spin $|\uparrow_1\rangle$ electron, this time leaving behind a spin $|\downarrow_2\rangle$ electron on the donor 2.

For the case of the anti-parallel nuclei on the other hand, in the energy regime for which $\Delta A < J < \bar{A}$, the eigenstates of the electrons consist of, to a good approximation, separable product states between the spin states of electron 1 and electron 2 (see section 4.2.2). Therefore, when considering the tunnelling of electron 1, in the case of the nuclei in an anti-parallel spin orientation, the pertinent energy levels to consider are the single-electron energy levels belonging to electron 1. In this case the readout situation is exactly the same as the standard electron readout detailed in section 3.9.3, whereby a spin $|\uparrow_1\rangle$ electron tunnels from the donor onto the SET island, resulting in a blip of current. After some time a spin $|\downarrow_1\rangle$ electron tunnels from the SET and thus any further tunnelling events to the SET during the read period are prohibited.

Figure 5.24 shows the experimental results of 10,000 read periods of the T_+ state for the case of both the nuclei initialised in the parallel $|\Downarrow\Downarrow\rangle$ or the anti-parallel $|\Uparrow\Downarrow\rangle$ spin state. A histogram is plotted of the average number of current blips per read period, showing that for the case of the anti-parallel nuclear state, the average number of blips per read period is centred just below 1, compared to around 1.5 for the case of the anti-parallel nuclei. Similarly, for the case of the parallel nuclei, 10,000 read periods were measured for the initialisation of both the T_-, T_0 state and T_+ state. It is important to note that the T_0 state was prepared by performing a $\frac{\pi}{2}$ pulse on the transition between the T_- and T_+ state and thus the state does not constitute a pure T_0 state as discussed above (Fig. 5.21, e). For the case of the T_- state, the histogram of average blips per readout period is close to 0, for the T_0 state the histogram is centred around an average number of blips per read period of 1 and for the T_+ state this histogram is centred around 1.5. The reason

why this value for T_+ is not closer to 2 is likely as a result of missed current blips, which result in a misattributiung of the readout traces with two tunnelling events as a readout trace with only a single tunnelling event. These results corroborate the theory that the T_+ state results in multiple tunnelling events for the case of the parallel nuclei, explaining the increased electron readout observed for this nuclear configuration.

5.11 Conclusion

Here we have demonstrated a two-qubit gate between two exchange-coupled electrons by exploiting the hyperfine interaction to provide a natural source of detuning, $\Delta B_z = \pm\bar{A}$, between the two qubits. The major benefit of this method of two-qubit operation is that it is robust against the exact placement of the donors and hence relaxes the accuracy requirements of donor positioning and gate fabrication. In addition, the smaller value of J results in a lower sensitivity to electric noise. Consequently, the coupling does not introduce any signficant decoherence channels to the qubits. The ability to perform high fidelity two-qubit operations over the larger length scales, compared to electron sharing, offered by the exchange interaction opens the path towards scaling arrays of distant donor nuclei, coupled together via a weak exchange interaction. Additionally we have shown the principles behind the operation and readout of the electrons in the parallel nuclear regime, revealing that for the case of the parallel nuclei, the electron readout contrast is increased as a result of multiple tunnelling events to the SET island during a single read period.

6.
Two-qubit nuclear geometric controlled-Z gates in a J-coupled system

For a successful technology, reality must take precedence over public relations, for Nature cannot be fooled.

Richard Feynman

This chapter contain results that will form the basis of the following publication in preparation:

H. G. Stemp, S. Asaad, M. A. I. Johnson, M. T. Mądzik, A. J. A. Heskes, H.R. Firgau, Y.Su, A. Laucht, K. M. Rudinger, R. Blume-Kohout, F. E. Hudson, A. S. Dzurak, K. M. Itoh, A. M. Jakob, B.C. Johnson, D. N. Jamieson, and A. Morello, "Universal nuclear two-qubit logic operations in an exchange-coupled donor system"

6.1 Introduction

The DiVincenzo criteria for realising a scalable quantum computer demands that the constituent qubits must demonstrate long coherence times, be capable of performing a universal set of quantum gates and must be initialised and read out with sufficient fidelity [154]. Nuclear spins in silicon represent a qubit candidate that meets the entirety of these conditions, with measured coherence times of over 30 seconds [34], a universal set of quantum gates exceeding 99.4% fidelity [29] and initialisation and measurement fidelity exceeding 99.8% [19]. However, the weak coupling of such nuclei with each other and with external fields, although leading to long coherence times, also presents a challenge for coupling donor nuclei over the length scales required when scaling up these physical systems for large-scale quantum computation applications. Fortunately, donor nuclei in silicon have the additional resource of an electron bound by the Coulomb potential of the nucleus, which can be used as a mechanism of coupling nuclei over larger distances. Previously however, this mechanism has relied on utilising the hyperfine coupling between two nuclei to a shared electron, limiting the range over which the nuclei can be coupled to $\lessapprox$ 10 nm [29].

Here we present a system of two nuclei, each possessing their own bound electron, which are coupled to one another via the exchange interaction. By performing a 2π rotation on one of the electrons conditional on the state of the two nuclei, we impart a geometric phase of π on the nuclei, thus implementing a nuclear, geometric controlled-Z (CZ) gate [29].

6.2 Operation of the two nuclear processor

The system discussed in this chapter is the same system as that discussed in Chapter 5. The ^{31}P nuclei have a spin of $I = \frac{1}{2}$, with basis states $|\Downarrow\rangle$ and $|\Uparrow\rangle$. Similarly, the spin of the electrons is given by $S = \frac{1}{2}$, with the basis states $|\downarrow\rangle$ and $|\uparrow\rangle$. In this experiment however, we now utilise the spin of the ^{31}P nuclei as the qubits and thus refer to the two

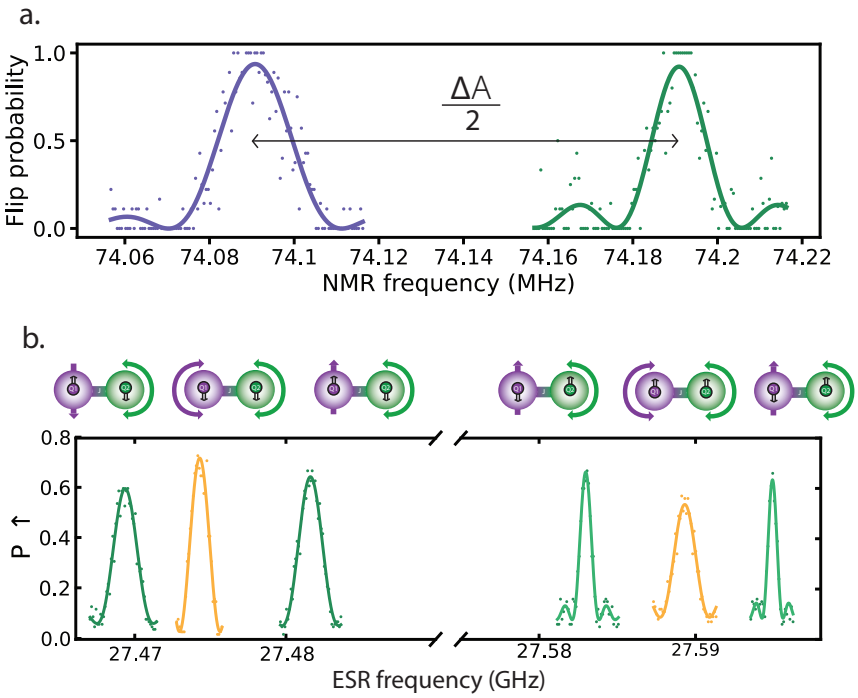

Figure 6.1: **Operation of the two nuclei quantum processor. a.** Nuclear magnetic resonance (NMR) spectrum showing the neutral NMR frequency of nucleus 1 and nucleus 2. These resonance frequencies are separated by the difference in hyperfine between the two donors, $\frac{\Delta A}{2}$. **b.** Elecron spin resonance (ESR) spectrum showing the ESR resonances present for electron 2 in the J-coupled system, with each resonance representing a frequency to flip the electron conditional on the state of the two nuclei, Q1 and Q2. The frequency difference between the ESR resonances conditional on the nuclei in the state $|\Downarrow\Downarrow\rangle$ and $|\Uparrow\Downarrow\rangle$ is different to the frequency difference between the ESR conditional on the nuclei in the $|\Uparrow\Uparrow\rangle$ and $|\Downarrow\Uparrow\rangle$ as a result of a ^{29}Si nucleus coupled with a hyperfine coupling of 2 MHz, which flipped between the frequency spectra.

nuclei as Q1 and Q2 respectively.

Denoting with $\mathbf{S_{1,2}}, \mathbf{I_{1,2}}$ the vector spin operators for each electron and nucleus, and $A_{1,2}$ the electron-nuclear hyperfine couplings on each atom, the Hamiltonian of the system (in frequency units) is:

$$\begin{aligned} H =&(\mu_B/h)B_0(g_1S_{z1} + g_2S_{z2})+ \\ &\gamma_n B_0(I_{z1} + I_{z2})+ \\ &A_1\mathbf{S_1}\cdot\mathbf{I_1} + A_2\mathbf{S_2}\cdot\mathbf{I_2}+ \\ &J(\mathbf{S_1}\cdot\mathbf{S_2}), \end{aligned} \tag{6.1}$$

where μ_B is the Bohr magneton, h is Planck's constant, $g_{1,2} \approx 1.9985$ the Landé g-factors of each electron spin, $g\mu_B/h \approx 27.97$ GHz/T and $\gamma_n \approx 17.23$ MHz/T is the ^{31}P nuclear gyromagnetic ratio.

Fig.6.1,c shows the nuclear magnetic resonance (NMR) frequency spectrum of Q1 and Q2 when both nuclei are in the neutral state, with an electron bound to each donor. As a result of the hyperfine coupling, A, between the donor nucleus and the electron, there exists two resonance frequencies for the neutral nucleus: one conditional on the electron being in the spin $|\downarrow\rangle$ state, with an associated resonance frequency given by $\nu_\alpha = \frac{A}{2} + \gamma_\mathrm{n}B_0$, and one conditional on the electron being in the spin $|\uparrow\rangle$ state, with associated frequency $\nu_\beta = \frac{A}{2} - \gamma_\mathrm{n}B_0$. As the electron is typically initialised in the $|\downarrow\rangle$ state before applying an NMR pulse, for the entirity of this work, when referring to the neutral NMR frequency for either Q1 or Q2, we are referring to the frequency ν_α for either nucleus (this is also the resonance frequency shown for both Q1 and Q2 in Fig.6.1,c). The two nuclei Q1 and Q2 are individually addressable when in the neutral charge state as a result of both donors possessing a slightly different hyperfine coupling strength, $\Delta A > 2\nu_{R,n}$, where $\Delta A = |A_1 - A_2|$ and $\nu_{R,n}$ is the nuclear Rabi frequency.

Fig.6.1,d, shows the electron spin resonance (ESR) frequency spectrum for the electron bound to donor Q2, as introduced in Chapter 5. The key property of this spectrum, pertinent to the work discussed in this chapter, is that, in the presence of the weak exchange interaction, there exists a resonance to flip the electron conditional on each of the four possible two-nuclear states: $|\Downarrow\Downarrow\rangle$, $|\Downarrow\Uparrow\rangle$, $|\Uparrow\Downarrow\rangle$, $|\Uparrow\Uparrow\rangle$.

The spins of the two nuclei and electrons in this system are initialised and read out using the same processes described in Chapter 4.

6.3 One-qubit gates

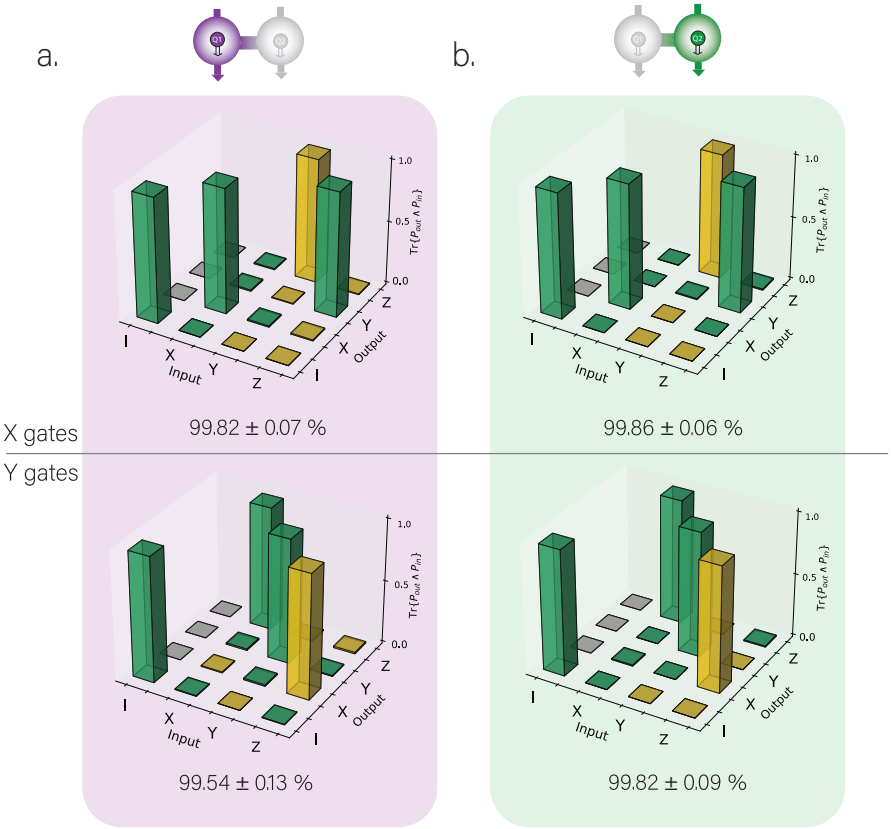

Figure 6.2: **One-qubit GST on the nuclei. a.** Process matrices estimated by single-qubit gate set tomography (GST) for the X $\frac{\pi}{2}$ (top) and Y $\frac{\pi}{2}$ (bottom) gates performed on nucleus Q1 in the neutral charge state. **b.** Process matrices estimated by single-qubit gate set tomography (GST) for the X $\frac{\pi}{2}$ (top) and Y $\frac{\pi}{2}$ (bottom) gates performed on nucleus Q2 in the neutral charge state. The corresponding estimated gate fidelities are shown beneath each process matrix.

Single qubit operations on Q1 and Q2 are trivially implemented, by applying an NMR pulse at one of the frequencies shown in Fig.6.1,c. In order to benchmark these single qubit

operations we performed single-qubit GST on each nucleus, on a gate set consisting of an $X_{\frac{\pi}{2}}$ and $Y_{\frac{\pi}{2}}$ rotation, along with an idle. Fig.6.2 shows the estimated process matrices and gate fidelities for the $X_{\frac{\pi}{2}}$ and $Y_{\frac{\pi}{2}}$ gates performed on Q1 and Q2, with the single-qubit fidelities exceeding 99.82 ± 0.09% and 99.5 ± 0.1% for Q1 and Q2 respectively.

6.4 Two-qubit gates

In order to implement a two-qubit gate between Q1 and Q2, we can utilise the geometric phase imparted by an electron onto the two nuclei of the J-coupled system, upon being driven around the Bloch sphere, in order to perform a two-qubit geometric CZ gate [29]. This CZ gate is performed by first initialising one of the nuclei into an eigenstate, such as the $|\Downarrow\rangle$ state and the other nucleus in a superposition state, such as $\frac{1}{\sqrt{2}}(|\Downarrow\rangle + |\Uparrow\rangle)$. For the case of these example initial states, the resulting two-qubit nuclear state is the following

$$|\Downarrow\rangle \otimes \frac{1}{\sqrt{2}}(|\Downarrow\rangle + |\Uparrow\rangle) = \frac{1}{\sqrt{2}}(|\Downarrow\Downarrow\rangle + |\Downarrow\Uparrow\rangle), \tag{6.2}$$

which represents a superposition between the two nuclear states $|\Downarrow\Downarrow\rangle$ and $|\Downarrow\Uparrow\rangle$. By performing a 2π rotation on one of the electrons, conditional on one of the nuclear states that make up the superposition (either $|\Downarrow\Downarrow\rangle$ or $|\Downarrow\Uparrow\rangle$ in this case), a geometric phase of π, equal to half the solid angle traversed on the Bloch sphere by the electron, is induced on the nuclear state upon which the electron rotation was conditioned (for a more thorough discussion on geometric phase, see section 2.8). For example, for the nuclear state described in equation 6.2, a 2π rotation of the electron bound to either Q1 or Q2, conditional on the nuclear state $|\Downarrow\Uparrow\rangle$, will result in the following

$$\frac{1}{\sqrt{2}}(|\Downarrow\Downarrow\rangle + |\Downarrow\Uparrow\rangle) \rightarrow^{2\pi} \frac{1}{\sqrt{2}}(|\Downarrow\Downarrow\rangle - |\Downarrow\Uparrow\rangle) = |\Downarrow\rangle \otimes \frac{1}{\sqrt{2}}(|\Downarrow\rangle - |\Uparrow\rangle). \tag{6.3}$$

The negative sign added to the nuclear superposition represents a rotation of the nucleus in a superposition state by 180^{o} around the XY plane of the Bloch sphere.

If however, the nucleus in an eigenstate was instead initialised in the spin $|\Uparrow\rangle$ state, rather than the spin $|\Downarrow\rangle$ as before, and we performed the same 2π rotation of the electron conditional on the state $|\Downarrow\Uparrow\rangle$, then the following would happen

$$\frac{1}{\sqrt{2}}(|\Uparrow\Downarrow\rangle + |\Uparrow\Uparrow\rangle) \rightarrow^{2\pi} \frac{1}{\sqrt{2}}(|\Uparrow\Downarrow\rangle + |\Uparrow\Uparrow\rangle). \tag{6.4}$$

In this case the $|\Downarrow\Uparrow\rangle$ state is not part of the nuclear superposition, and thus the ESR pulse is far off-resonant such that the electron does not undergo any rotation and thus no geometric phase is imparted on the nuclei. This conditional geometric phase of π imparted on one nucleus conditional on the state of the other nucleus thus constitutes a two-qubit nuclear CZ gate.

The magnitude of the geometric phase imparted by the electron on the nuclei, depends on the solid angle traversed by the electron on the Bloch sphere, which in turn depends on the frequency detuning $\Delta = \nu_0 - \nu_{MW}$, where ν_0 is the electron resonance frequency and ν_{MW} is the frequency of the AC field used to drive the electron. Fig.6.3 shows the path traversed by an electron on the Bloch sphere, for various magnitudes of frequency detuning, Δ, illustrating that the electron traverses a smaller cone on the Bloch sphere as Δ is increased. However, the solid angle ultimately traversed by the spin depends not only on the area of the cone enclosed by the path of the electron on the Bloch sphere but also on how many times the electron performs a rotation about this cone during the duration of the ESR pulse. As Δ increases, and thus the area of the cone about which the electron traverses decreases, although the electron traverses a smaller cone on the Bloch sphere, the electron is able to perform many more rotations about this smaller area for a given pulse duration, compared to the larger cone traversed for smaller values of Δ. The amount of geometric phase imparted on the nuclei therefore depends non-trivially on a combination of both these factors.

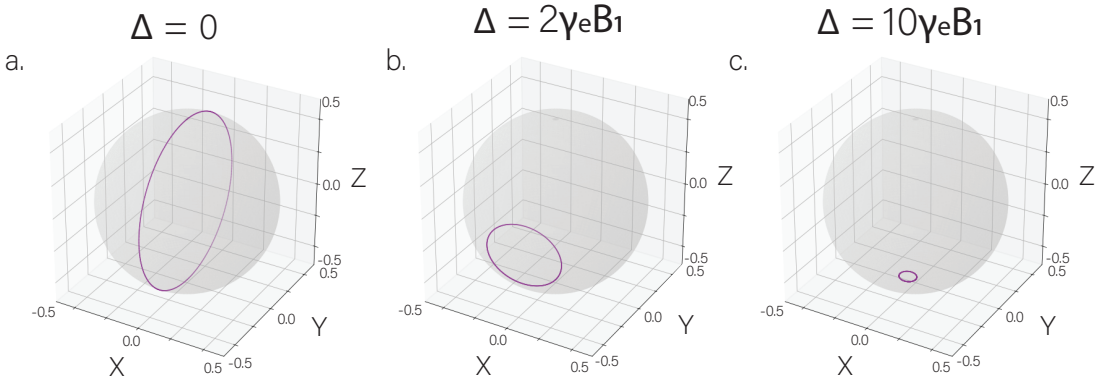

Figure 6.3: **Electron rotation with a frequency detuning. a.** Simulation of the expectation values of the path traversed by an electron on the Bloch sphere with the application of an AC driving field with a detuning $\Delta = \nu_0 - \nu_{MW} = 0$, where ν_0 is the electron resonance frequency and ν_{MW} is the frequency of the AC field used to drive the electron. **b.** Simulation of the expectation values of the path traversed by an electron on the Bloch sphere with the application of an AC driving field with a detuning $\Delta = 2\gamma_e B_1$ where $\gamma_e = 28.025$ GHz/T and B_1 is the amplitude of the AC driving field in units of T. **c.** Simulation of the expectation values of the path traversed by an electron on the Bloch sphere with the application of an AC driving field with a detuning $\Delta = 10\gamma_e B_1$. It should be noted that, in the case of a detuned AC driving field, where the cone traversed on the Bloch sphere is smaller, for the same duration of the application of an AC driving field, the electron will perform more full rotations about this smaller cone, increasing the solid angle traversed.

Fig.6.4b and c show a simulation and corresponding experimental results from a measurement designed to investigate the geometric phase incurred by the rotation of an electron in the J-coupled system. In this measurement the nucleus Q1 was first initialised in the spin $|\Downarrow\rangle$ state, while the nucleus Q2 was initialised in the superposition state $\frac{1}{\sqrt{2}}(|\Downarrow\rangle + |\Uparrow\rangle)$. The nuclei were hence in the following two-qubit state

$$|\psi\rangle = \frac{1}{\sqrt{2}}(|\Downarrow\Downarrow\rangle + |\Downarrow\Uparrow\rangle). \tag{6.5}$$

An AC driving field was then applied to the electron bound to Q1, with the frequency of the driving field being swept from $\frac{\nu_{|\Downarrow\Uparrow\rangle}+\nu_{|\Downarrow\Downarrow\rangle}}{2}$ - 10 MHz to $\frac{\nu_{|\Downarrow\Uparrow\rangle}+\nu_{|\Downarrow\Downarrow\rangle}}{2}$ + 10 MHz, where $\nu_{|\Downarrow\Uparrow\rangle}$ represents the ESR frequency to flip the electron bound to Q1 conditional on the

$|\Downarrow\Uparrow\rangle$ state and $\nu_{|\Downarrow\Downarrow\rangle}$ represents the frequency to flip the electron bound to Q1 conditional on the $|\Downarrow\Downarrow\rangle$ nuclear state. The duration of the AC driving field was also swept, from 0 - 20 μs. It should be noted that the π pulse duration for the electron bound to Q1 at the AC driving field power used in this experiment was ≈ 1 μs. A final $\frac{\pi}{2}$ pulse was then applied to nucleus Q2, in order to project the information along the equator of the Bloch sphere of Q2 onto the Z-axis of the Bloch sphere, which could then be subsequently read out (see section 3.11.2). Fig.6.4,c shows the results of the nuclear readout of Q2.

There are three key results of interest that should be highlighted from Fig.6.4. The first, is that a two-qubit nuclear CZ gate is performed whenever the electron traverses a solid angle of 2π around the Bloch sphere. When a geometric phase of π is added to the nuclei, the two-qubit nuclear state becomes $|\psi\rangle = \frac{1}{\sqrt{2}}(|\Downarrow\Downarrow\rangle - |\Downarrow\Uparrow\rangle)$ following the rotation of the electron. Therefore, the final $\frac{\pi}{2}$ pulse on the nucleus rotates Q2 into the $|\Downarrow\rangle$ state, as indicated by the regions of the plot for which the NMR flip probability drops to 0 (see section 3.11.2 for information on NMR flip probability). Conversely, if no geometric phase is added to the nuclei then the nuclear two-qubit state will remain as $|\psi\rangle = \frac{1}{\sqrt{2}}(|\Downarrow\Downarrow\rangle + |\Downarrow\Uparrow\rangle)$ following the rotation of the electron and thus the final $\frac{\pi}{2}$ pulse will rotate Q2 to the $|\Uparrow\rangle$ state, as indicated by the regions of the plot for which the NMR flip probability of Q2 is 1.

The second point to highlight is that whenever the electron traverses a solid angle of π on the Bloch sphere, a two qubit entangled state is created between the nucleus Q2 and the electron bound to nucleus Q1. This is due to the fact that, whenever the electron traverses an angle of π, the electron is flipped conditionally on the state of the two nuclei. As nucleus Q2 is in a superposition state, this results in the electron becoming entangled with Q2. For example, in the case for which the AC driving field is applied at the resonance to flip the electron conditional on Q2 being in the $|\Uparrow\rangle$ state (i.e. the resonance $|\Downarrow\Uparrow\rangle$ in Fig.6.4) for such a duration that the electron is flipped by an angle π on the Bloch sphere, then this leads to the following

$$\frac{1}{\sqrt{2}}(|\downarrow_{e1}\Downarrow_{Q2}\rangle + |\downarrow_{e1}\Uparrow_{Q2}\rangle \rightarrow \frac{1}{\sqrt{2}}(|\downarrow_{e1}\Downarrow_{Q2}\rangle + |\uparrow_{e1}\Uparrow_{Q2}\rangle), \tag{6.6}$$

where $|\downarrow_{e1}\rangle$ ($|\uparrow_{e1}\rangle$) represents the state of the electron bound to Q1 and $|\Downarrow_{Q2}\rangle$ ($|\Uparrow_{Q2}\rangle$) represents the state of nucleus Q2. As $\frac{1}{\sqrt{2}}(|\downarrow_{e1}\Downarrow_{Q2}\rangle + |\uparrow_{e1}\Uparrow_{Q2}\rangle)$ represents a fully entangled state, rotating the electron by an angle π thus entangles the electron with the nucleus Q2. This is also shown in Fig.6.4a, which depicts the simulated path of the electron bound to Q1 when an AC driving field is applied at a frequency denoted by the purple vertical line in Fig.6.4b. When the electron traverses a solid angle of π on the Bloch sphere, and hence the two spins become entangled, the vectors representing the two spins are seen to shrink towards the centre of the Bloch sphere.

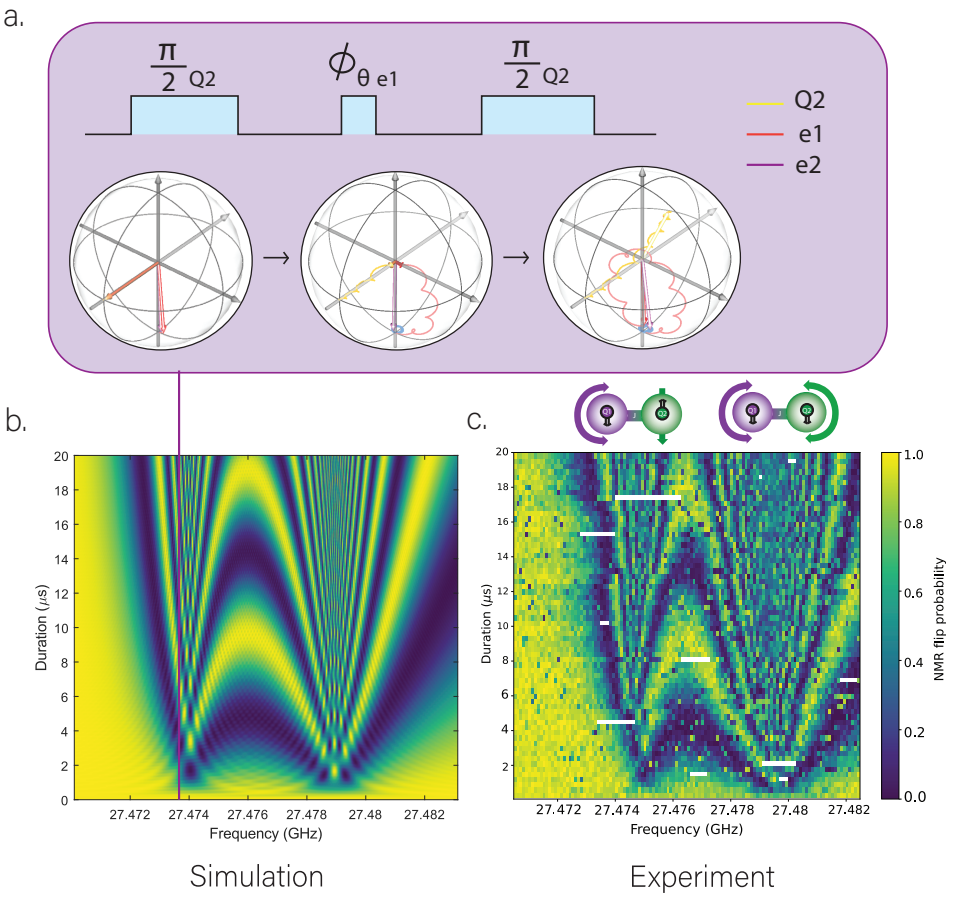

Figure 6.4: **Controlled-Z (CZ) gate in a J-coupled system.** Simulation (**b.**) and experimental results (**c.**) showing the geometric phase imparted by the electron onto the nuclei. Q2 is initialised into a superposition state before applying a pulse of varying frequency and duration to electron 1, to impart a varying geometric phase to Q2. A final $\frac{\pi}{2}$ pulse then projects the information along the XY plane onto the Z-axis of the Bloch sphere. The schematics above **c.** show which nuclear states ($|\Downarrow\Uparrow\rangle$ or $|\Downarrow\Downarrow\rangle$) are responsible for the two resonances observed for electron e1. **a.** Simulated trajectory on the Bloch sphere of the two electrons (denoted e1 and e2) and the nucleus Q2. The simulation was performed at a frequency denoted by the vertical purple line in **b.**, which corresponds to a frequency detuned slightly from the resonance to flip the electron e1 conditional on the nuclei being in the $|\Downarrow\Uparrow\rangle$ state. The leftmost Bloch sphere is a snapshot taken from the start of the simulation, at time $t = 0$, showing the nucleus Q2 initialised in a superposition state along the XY plane and electrons e1 and e2 pointing along the -Z direction. The middle Bloch sphere shows a snapshot of the simulation taken from a time $t = \pi_{e1}$ where π_{e1} is the π time for electron e1. At this time the electron e1 and the nucleus Q2 become entangled, as indicated by the spins shrinking towards the centre of the Bloch sphere. The electron e2 remains in -Z, as the AC field frequency is far detuned from the resonance frequency of this electron. The rightmost Bloch sphere is taken from a snapshot of the simulation at time $t = 2\pi_{e1}$. At this time, the electron e1 has returned to the -Z state, while the nucleus Q2 has been rotated almost 180^o around the XY plane as a result of the geometric phase imparted by the electron.

Finally, when the electron is rotated by an angle of π on the Bloch sphere, at the resonance frequency conditional on the nuclear $|\Downarrow\Downarrow\rangle$ state, a three qubit entangled state is created between the two electrons and the nucleus Q2. As discussed in section 4.2.2, when the nuclei are in a parallel orientation, the detuning between the two electrons in the J coupled system is given by ΔA. For the case in which $\Delta A < 2\nu_{R,e}$, where $\nu_{R,e}$ represents the Rabi frequency of the electron, this results in an AC driving field rotating both electrons simultaneously. Consequently, for the cases in Fig.6.4,b,c in which the electron is rotated at the resonance conditional on the nuclei being in the parallel orientation, $|\Downarrow\Downarrow\rangle$, both electrons are simultaneously driven. Thus, at this resonance frequency, when the electrons traverse an angle of π on the Bloch sphere, then both electrons are flipped conditional on the state of the nucleus Q2, which is in a superposition state, thus resulting in a three-qubit entangled state between the two electrons and the nucleus. Fig.6.5,d shows the simulation of electron e2 during this measurement revealing that, when the AC driving field is on resonance with the ESR frequency conditional on the parallel nuclear $|\Downarrow\Downarrow\rangle$ state then electron e2 is also driven. Plotting $\sqrt{x^2+y^2+z^2}$, where x, y and z are the projections along the X,Y and Z axis on the Bloch sphere, we see from Fig.6.5b,c and d that the spins for nucleus Q2 and electrons e1 and e2 all shrink to the middle of the Bloch sphere (indicated by $\sqrt{x^2+y^2+z^2}=0$) when the AC driving field is on resonance with the ESR resonance conditional on the $|\Downarrow\Downarrow\rangle$ state, indicating that we have prepared a three-qubit entangled state.

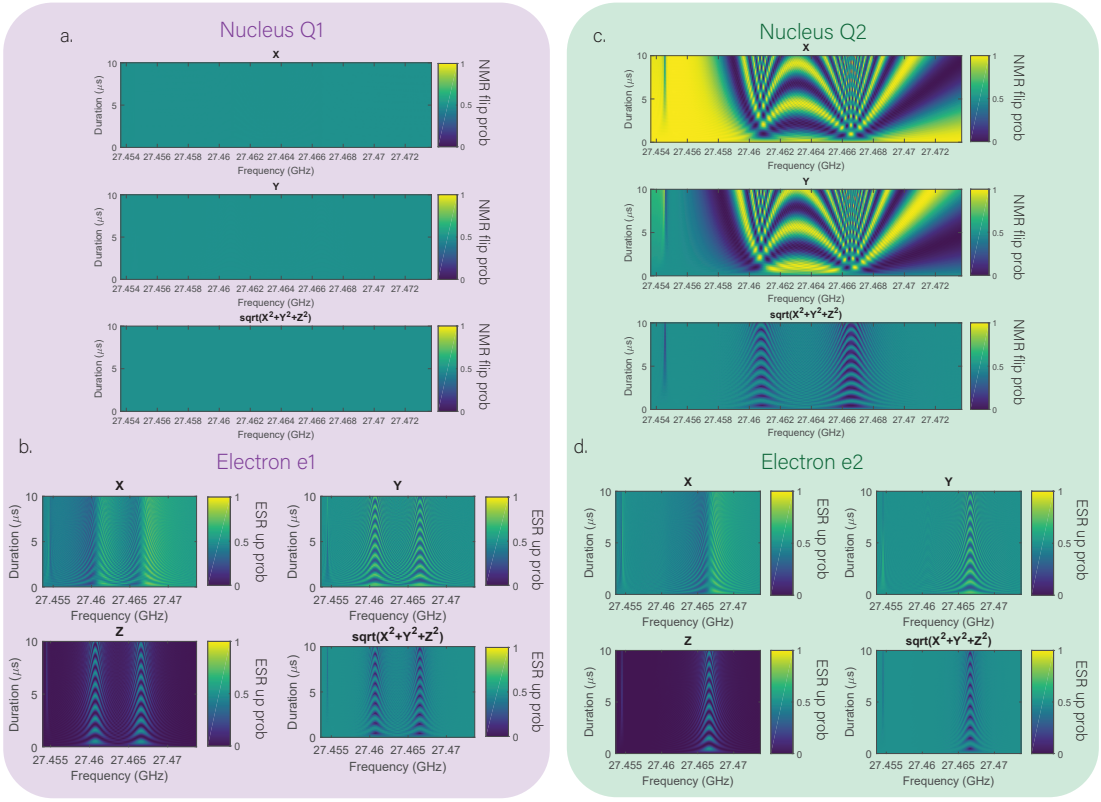

Figure 6.5: **Simulation of geometric phase in a four-qubit system.** The measurement simultaed involves first initialising Q1 in the spin $|\Downarrow\rangle$ state, Q2 along the +X direction of the Bloch sphere and both electrons e1 and e2 in the $|\downarrow\rangle$ state. An AC driving field is then applied, with the frequency swept between $\frac{\nu_{|\Downarrow\Uparrow\rangle}+\nu_{|\Downarrow\Downarrow\rangle}}{2}$ - 10 MHz to $\frac{\nu_{|\Downarrow\Uparrow\rangle}+\nu_{|\Downarrow\Downarrow\rangle}}{2}$ + 10 MHz, where $\nu_{|\Downarrow\Uparrow\rangle}$ represents the ESR frequency to flip the e1 conditional on the $|\Downarrow\Uparrow\rangle$ state and $\nu_{|\Downarrow\Downarrow\rangle}$ represents the frequency to flip the e1 and e2 conditional on the $|\Downarrow\Downarrow\rangle$ nuclear state (the two electrons are effectively degenerate for this nuclear orientation). The duration of the AC driving field is swept from 0-10 μs. **a.** Projection along the X and Y axis of the Bloch sphere for nucleus Q1. The total spin projection $\sqrt{x^2+y^2+z^2}$ is also plotted. This nucleus is not driven and hence remains in the $|\Downarrow\rangle$ state for the duration of the simulation. **b.** Projection along the X and Y axis of the Bloch sphere and the total spin projection for nucleus Q2. This nucleus is rotated about the XY plane of the Bloch sphere depending on the geometric phase imparted by the electrons. **c.** Projection along the X and Y axis of the Bloch sphere and the total spin projection for electron e1. This electron is rotated around the Bloch sphere when the AC driving field is close to or on resonance with the ESR resonances conditional on the nuclear $|\Downarrow\Uparrow\rangle$ and $|\Downarrow\Downarrow\rangle$ state. **d.** Projection along the X and Y axis of the Bloch sphere and the total spin projection for electron e2. This electron is only rotated around the Bloch sphere when the AC driving field is close to or on resonance with the ESR resonances conditional on the nuclear $|\Downarrow\Downarrow\rangle$ state.

6.5 Pulse-induced resonance shifts

As a result of the geometric phase imparted by the electrons being very sensitive to the frequency detuning, Δ, in order to impart a geometric phase of exactly π on the nuclei, and hence perform a high fidelity nuclear geometric CZ gate, it is crucial that the rotation of the electron is applied at exactly the resonance frequency. One phenomenon that can therefore result in the reduction of the CZ gate fidelity is the observation of a shift in the electron resonance frequency upon the application of an AC driving field, which we refer to as a pulse-induced resonance shift (PIRS). There are a number of characteristics of PIRS which clearly differentiate this effect from the AC Zeeman shift discussed in section 2.7. These characteristics include:

1. The electron resonance frequency does not shift instantaneously upon switching on the AC driving field but instead drifts over a timescale of $\approx 100\mu$s, before saturating at a new frequency approximately 100 kHz from the original resonance frequency. Similarly, upon switching off the AC driving field, the electron resonance drifts back to its original resonance frequency over the same timescale.

2. The shift in the electron resonance frequency does not depend on the frequency of the AC driving field but rather the power and duration for which it is applied. This results in a shift in the resonance frequency of the electrons occurring when an NMR pulse is applied, despite the NMR pulse frequency being detuned from the ESR resonance by ≈ 27 GHz.

PIRS is not an effect unique to this device, or even the donor system more generally; with the effect being reported in a number of different semiconductor qubit devices with a variety of architectures and material platforms [121,155–158]. Operating the devices at higher temperatures has been found to help mitigate this effect, suggesting that the resonance shift is caused by a heating of the device from the AC driving field [158]. Although the microscopic physics underpinning this effect is still unknown, it has been suggested that

it may be related to two-level systems in the qubit's environment [159].

In order to minimise the impact of PIRS on the CZ gate performance, we performed a 'saturation pulse' before the CZ gate. This pulse consists of an off-resonant NMR pulse that is applied for a sufficient duration to saturate the frequency shift of the electron induced by PIRS. As an AC driving field is continuously applied during the performance of the CZ gate, the saturation pulse ensures that the frequency of the electron remains stable throughout the implementation of the CZ gate.

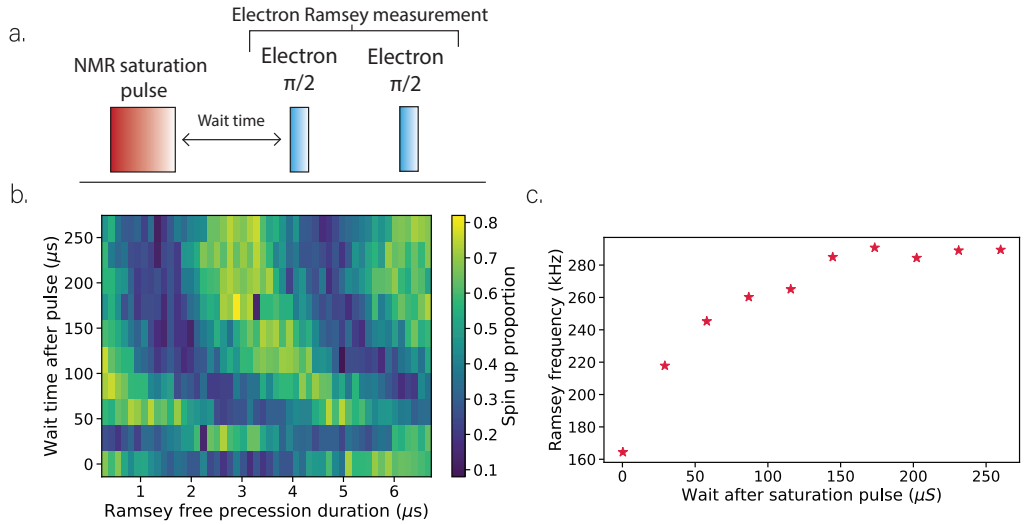

Figure 6.6: **a.** Schematic of the pulse sequence used in this experiment consisting of a long ($\approx 5\pi_{Q2}$, where π_{Q2} is the π time for the nucleus Q2) off-resonant NMR pulse used to saturate the pulse-induced frequency shift of the electron. This pulse is followed by a wait time, the duration of which is swept. A Ramsey measurement is then performed on the electron e1.**b.** Ramsey fringes as a function of the wait time after the NMR saturation pulse. The change in frequency of the Ramsey fringes is as a result of the resonance frequency of the electron drifting. **c.** Frequency extracted from the fit of the Ramsey fringes as a function of the wait time after the saturation pulse, revealing that the resonance frequency of the electron returns to its original resonance frequency (in the absence of any AC driving field) after ≈ 150 μs.

Fig.6.6c, shows the resonance frequency of the electron, as measured by a Ramsey exper-

iment, as a function of the wait time after the saturation pulse. A shift in the electron resonance of ≈ 120 kHz is observed over a time period following the saturation pulse of ≈ 150 μs. We therefore apply the saturation pulse for > 150 μs before implementing the CZ gate in order to ensure the resonance frequency of the electron is at this saturation point.

6.6 Conclusion

Here we have benchmarked the fidelity of operations on the nuclei of a J-coupled donor pair. We have demonstrated the implentation of a nuclear geometric CZ gate, achieved by utilising the exchange interaction between the donor-bound electrons. Work is currently underway to use this two-qubit CZ gate to generate an entangled state between the two nuclei.

In previous work, the hyperfine interaction between two nuclei and a shared electron was utilised as the coupling mechanism for the nuclear geometric CZ gate, limiting the maximum inter-donor distance over which this gate can be performed to $\lessapprox 10$ nm. In this work, with an exchange interaction strength of 12 MHz, we estimate the distance between the two nuclei of the exchange-coupled donor system to be ≈ 18 nm [138]. Utilising the exchange interaction to perform the nuclear CZ gate thus offers the possibility to entangle nuclei over larger distances then previously achievable.

7.
Conclusion and Future Directions

As for the future, your task is not to foresee it, but to enable it.

Antoine de Saint Exupery

In this work, we have presented the first experimental demonstration of exchange-based, entangling 2-qubit logic gates between electrons bound to individual ^{31}P donors in silicon. In the presence of the weak exchange interaction, each resonance frequency on the electron represents a native two-qubit CROT gate, to rotate one electron conditional on the state of the other electron. We have performed careful tomography of these native CROT gates in a one-qubit subspace using gate set tomography (GST), obtaining fidelities above 99.63 $\pm$ 0.07% for both qubits in the exchange-coupled pair. Using phase reversal tomography, we have benchmarked the fidelity of the entangling operations between the two electrons, obtaining a Bell state fidelity of 93 $\pm$ 9 %, with SPAM error extracted. Additionally, by comparing the coherence times of the electrons both with and without the presence of the exchange-interaction, we have shown that, in the regime of weak exchange, the presence of the coupling has no influence on the coherence of the individual spins.

Furthermore, we have utilised the weak exchange interaction to perform two-qubit gates between nuclei, over greater distances than previously achievable using the hyperfine interaction to mediate the coupling. The presence of the weak exchange interaction between the two electrons, results in each electron resonance being conditional on the state of both nuclei in the donor pair. Consequently, by initialising one of the nuclei into a superposition state and performing a 2π rotation on the electron conditional on a given state of the two nuclei, a geometric phase of π is incurred on the nuclear state upon which the electron rotation was conditioned. This therefore represents the implementation of a two-qubit CZ gate between the two nuclei of the exchange-coupled donor pair.

The appeal of this scheme of coupling nuclei is that the only requirement for its viability, is that there exists distinct ESR resonances to rotate an electron conditional on each of the two-qubit nuclear states $|\Downarrow\Downarrow\rangle$, $|\Downarrow\Uparrow\rangle$, $|\Uparrow\Downarrow\rangle$, $|\Uparrow\Uparrow\rangle$. Fig.7.1 shows an ESR spectrum for one of the electrons in an exchange-coupled donor pair for three regimes of exchange, J: $J \ll \Delta A, \Delta A < J < \bar{A}$ and $J \gg \bar{A}$ where $\Delta A = |A_1 - A_2|$ and $\bar{A} = \frac{A_1+A_2}{2}$ and A_1 and A_2 are the hyperfine coupling strengths for donor 1 and donor 2 respectively. It can be

seen that in the regime for which $\Delta A < J < \bar{A}$ there exists ESR resonances to rotate the electron conditional on each of the four two-qubit nuclear states. Consequently, the coupling of nuclei in an exchange-coupled system using the nuclear CZ gate is agnostic to the exact value of J, provided that it is within this energy regime. This optimal range of J corresponds to a range of possible inter-donor distances of approximately 10-24 nm [138].

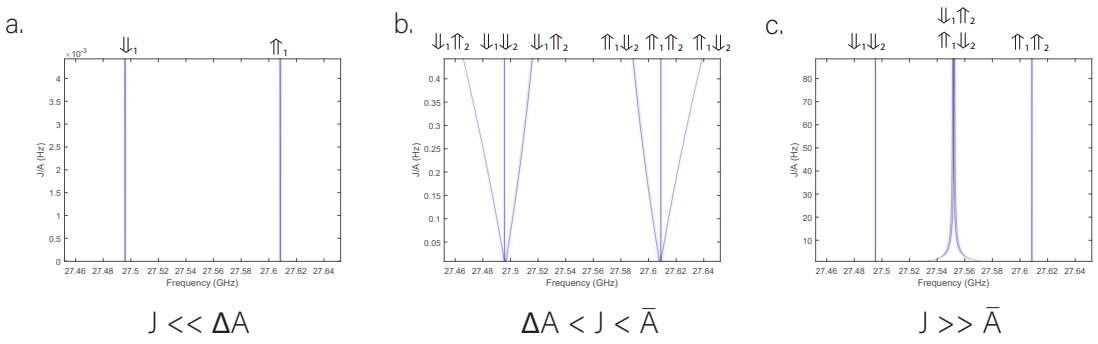

Figure 7.1: **ESR spectrum in different exchange-coupling regimes. a.** Simulated ESR frequency spectrum in the regime of $J \ll \Delta A$. In this regime there exists two resonance frequencies for the electron, one conditional on the nucleus to which the electron is bound being in the $|\Downarrow\rangle$ state and one conditional on this nucleus being in the $|\Uparrow\rangle$ state. **b.** Simulated ESR frequency spectrum for the regime for which $\Delta A < J < \bar{A}$. In this regime there exists ESR resonances to flip the electron conditional on each of the four nuclear states for the two nuclei: $|\Downarrow\Downarrow\rangle$, $|\Downarrow\Uparrow\rangle$, $|\Uparrow\Downarrow\rangle$ and $|\Uparrow\Uparrow\rangle$. **c.** Simulated ESR spectrum for the regime in which $J \gg \bar{A}$. In this regime the ESR resonances for the nuclear states $|\Downarrow\Uparrow\rangle$ and $|\Uparrow\Downarrow\rangle$ are split by ΔA. If $\Delta A > 2\nu_R$ where ν_R is the electron Rabi frequency then the electron is no longer able to be driven conditionally on each of the distinct two-qubit nuclear states, when in this energy regime. Simulations were performed using simulation code written by Dr Rachpon Kalra during his time at the University of New South Wales [114].

Having coupling mechanisms that do not rely on an exact value of J is crucial as they allow the coupling scheme to be robust against the uncertainty in donor placement inherent to the donor-implantation process. Using ion-implantation to introduce the donor atoms to the silicon lattice is beneficial as it allows these devices to retain compatibility with standard metal- oxide-semiconductor manufacturing processes [147], which represents a significant advantage when attempting to address the immense technological challenge of scaling up these systems. The uncertainty in lateral donor placement during the ion-

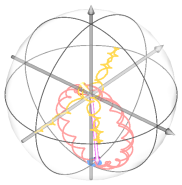

implantation process has reached unprecedented levels of precision, as a result of utilising an atomic-force microscope (AFM) nanostencil tip, with an aperture through which the the ion-beam can pass, to increase the localisation of the donor implantation site [37]. Using this procedure, the uncertainty in lateral donor placement depends on a number of factors, including: the lateral straggle of the donor as it is implanted in the lattice ($\approx$ 9 nm for a P ion implanted at a mean implantation depth of 20 nm and $\approx$ 5 nm for an Sb ion implanted at the same mean depth) the uncertainty in nanostencil aperature size ($\approx$ 5 nm for an aperature size of 10 um) and the uncertainty in AFM positioning ($\approx$ 0.5 nm). Combining these factors gives a rough estimate for the lateral uncertainty in donor placement of $\approx \pm 14.5$ nm for a phosphorus donor and $\approx \pm 10.5$ nm for an antimony donor [76]. This lateral uncertainty in donor placement achievable with ion-implantation techniques is therefore compatible with the range of viable distances for the optimal value of J for donor coupling.

Looking to the future, the fact that this operating regime is contingent only on the presence of conditional resonances to flip an electron depending on the state of two nuclei, allows for the possibility of introducing new mechanisms to mediate the exchange coupling between neighbouring donor atoms and thus further extend the range over which we can couple neighbouring donor atoms. One example of this exchange-mediating mechanism, is the jellybean quantum dot [31]. Jellybean quantum dots are elongated, gate defined quantum dots, which can act as mediating couplers of the exchange interaction [160,161], potentially extending the range of exchange interaction to $>$ 100 nm. As long as the mediated exchange is $J < A$ and larger than the ESR linewidth, the same geometric nuclear CZ gate demonstrated in chapter 6, for directly-coupled donors, can be extended to donors that are indirectly coupled through the jellybean dot. This scheme has two major benefits. The first, is that the increased distance between the donors helps to alleviate some of the crowding associated with integrating classical control electrons on-chip [162]. Secondly, this scheme allows us to benefit from the extremely long coherence times of the donor nuclei ($>$ 30 seconds), whilst still being able to perform two-qubit operations on the nuclei in the much faster time required to perform a rotation on the electrons compared to the nuclei

(1 us, compared to approximately 100 us). These considerations offer exciting promise to the potential of utilising donor atoms as the foundation of a scalable quantum processor.

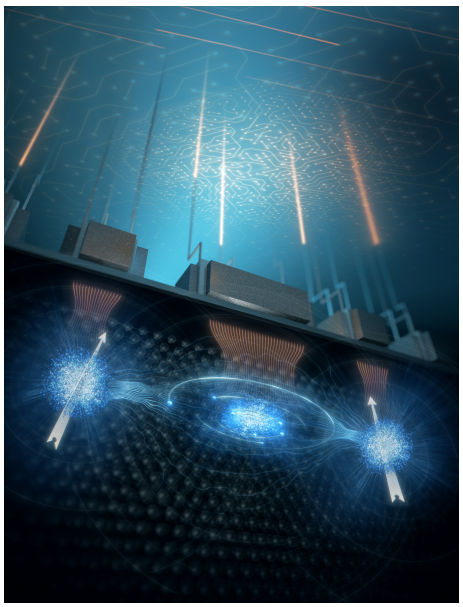

Figure 7.2: **Jellybean quantum dot.** Schematic depicting the concept of an elongated quantum dot being used as a mechanism of mediating the exchange-interaction between neighbouring spins. Image was taken from the cover art for the Advanced Materials publication in [31].

References

[1] A. Ramdas and S. Rodriguez, "Spectroscopy of the solid-state analogues of the hydrogen atom: donors and acceptors in semiconductors," *Reports on Progress in Physics*, vol. 44, no. 12, p. 1297, 1981.

[2] G. Feher, "Electron spin resonance experiments on donors in silicon. i. electronic structure of donors by the electron nuclear double resonance technique," *Physical Review*, vol. 114, no. 5, p. 1219, 1959.

[3] N. Stone, "Table of nuclear magnetic dipole and electric quadrupole moments," *Atomic Data and Nuclear Data Tables*, vol. 90, no. 1, pp. 75–176, 2005.

[4] A. Einstein *et al.*, "On the electrodynamics of moving bodies," *Annalen der physik*, vol. 17, no. 10, pp. 891–921, 1905.

[5] A. Einstein, "The field equations of gravitation," *Sitzungsber. Preuss. Akad. Wiss. Berlin (Math. Phys.)*, vol. 1915, pp. 844–847, 1915.

[6] M. Planck, "On the law of distribution of energy in the normal spectrum," *Annalen der physik*, vol. 4, no. 553, p. 1, 1901.

[7] N. Bohr, "I. on the constitution of atoms and molecules," *The London, Edinburgh, and Dublin Philosophical Magazine and Journal of Science*, vol. 26, no. 151, pp. 1–25, 1913.

[8] W. Heisenberg, "Über den anschaulichen inhalt der quantentheoretischen kinematik und mechanik," *Zeitschrift für Physik*, vol. 43, no. 3-4, pp. 172–198, 1927.

[9] E. Schrödinger, "An undulatory theory of the mechanics of atoms and molecules," *Physical review*, vol. 28, no. 6, p. 1049, 1926.

[10] P. A. M. Dirac, "The quantum theory of the electron," *Proceedings of the Royal Society of London. Series A, Containing Papers of a Mathematical and Physical Character*, vol. 117, no. 778, pp. 610–624, 1928.

[11] Y. Manin, "Computable and uncomputable," *Sovetskoye Radio, Moscow*, vol. 128, p. 28, 1980.

[12] R. P. Feynman *et al.*, "Simulating physics with computers," *Int. j. Theor. phys*, vol. 21, no. 6/7, 2018.

[13] H.-L. Huang, D. Wu, D. Fan, and X. Zhu, "Superconducting quantum computing: a review," *Science China Information Sciences*, vol. 63, pp. 1–32, 2020.

[14] C. D. Bruzewicz, J. Chiaverini, R. McConnell, and J. M. Sage, "Trapped-ion quantum computing: Progress and challenges," *Applied Physics Reviews*, vol. 6, no. 2, 2019.

[15] T. C. Ralph and G. J. Pryde, "Optical quantum computation," in *Progress in optics*. Elsevier, 2010, vol. 54, pp. 209–269.

[16] D. Loss and D. P. DiVincenzo, "Quantum computation with quantum dots," *Physical Review A*, vol. 57, no. 1, p. 120, 1998.

[17] C. Kloeffel and D. Loss, "Prospects for spin-based quantum computing in quantum dots," *Annu. Rev. Condens. Matter Phys.*, vol. 4, no. 1, pp. 51–81, 2013.

[18] L. M. Vandersypen and I. L. Chuang, "Nmr techniques for quantum control and computation," *Reviews of modern physics*, vol. 76, no. 4, p. 1037, 2005.

[19] J. J. Pla, K. Y. Tan, J. P. Dehollain, W. H. Lim, J. J. Morton, F. A. Zwanenburg, D. N. Jamieson, A. S. Dzurak, and A. Morello, "High-fidelity readout and control of a nuclear spin qubit in silicon," *Nature*, vol. 496, no. 7445, pp. 334–338, 2013.

[20] M. G. Dutt, L. Childress, L. Jiang, E. Togan, J. Maze, F. Jelezko, A. Zibrov, P. Hemmer, and M. Lukin, "Quantum register based on individual electronic and nuclear spin qubits in diamond," *Science*, vol. 316, no. 5829, pp. 1312–1316, 2007.

[21] R. Hanson, F. Mendoza, R. Epstein, and D. Awschalom, "Polarization and readout of coupled single spins in diamond," *Physical review letters*, vol. 97, no. 8, p. 087601, 2006.

[22] T. Gaebel, M. Domhan, I. Popa, C. Wittmann, P. Neumann, F. Jelezko, J. R. Rabeau, N. Stavrias, A. D. Greentree, S. Prawer *et al.*, "Room-temperature coherent coupling of single spins in diamond," *Nature Physics*, vol. 2, no. 6, pp. 408–413, 2006.

[23] C. Godfrin, A. Ferhat, R. Ballou, S. Klyatskaya, M. Ruben, W. Wernsdorfer, and F. Balestro, "Operating quantum states in single magnetic molecules: implementation of grover's quantum algorithm," *Physical review letters*, vol. 119, no. 18, p. 187702, 2017.

[24] F. J. Rueß, W. Pok, T. C. Reusch, M. J. Butcher, K. E. J. Goh, L. Oberbeck, G. Scappucci, A. R. Hamilton, and M. Y. Simmons, "Realization of atomically controlled dopant devices in silicon," *Small*, vol. 3, no. 4, pp. 563–567, 2007.

[25] B. E. Kane, "A silicon-based nuclear spin quantum computer," *nature*, vol. 393, no. 6681, pp. 133–137, 1998.

[26] J. J. Pla, K. Y. Tan, J. P. Dehollain, W. H. Lim, J. J. Morton, D. N. Jamieson, A. S. Dzurak, and A. Morello, "A single-atom electron spin qubit in silicon," *Nature*, vol. 489, no. 7417, pp. 541–545, 2012.

[27] D. P. DiVincenzo and D. Loss, "Quantum information is physical," *Superlattices and Microstructures*, vol. 23, no. 3-4, pp. 419–432, 1998.

[28] A. Laucht, J. T. Muhonen, F. A. Mohiyaddin, R. Kalra, J. P. Dehollain, S. Freer, F. E. Hudson, M. Veldhorst, R. Rahman, G. Klimeck *et al.*, "Electrically controlling single-spin qubits in a continuous microwave field," *Science advances*, vol. 1, no. 3, p. e1500022, 2015.

[29] M. T. Mądzik, S. Asaad, A. Youssry, B. Joecker, K. M. Rudinger, E. Nielsen, K. C. Young, T. J. Proctor, A. D. Baczewski, A. Laucht *et al.*, "Precision tomography of

a three-qubit donor quantum processor in silicon," *Nature*, vol. 601, no. 7893, pp. 348–353, 2022.

[30] M. T. Mądzik, A. Laucht, F. E. Hudson, A. M. Jakob, B. C. Johnson, D. N. Jamieson, K. M. Itoh, A. S. Dzurak, and A. Morello, "Conditional quantum operation of two exchange-coupled single-donor spin qubits in a mos-compatible silicon device," *Nature communications*, vol. 12, no. 1, p. 181, 2021.

[31] Z. Wang, M. Feng, S. Serrano, W. Gilbert, R. C. Leon, T. Tanttu, P. Mai, D. Liang, J. Y. Huang, Y. Su *et al.*, "Jellybean quantum dots in silicon for qubit coupling and on-chip quantum chemistry," *Advanced Materials*, p. 2208557, 2023.

[32] R. Savytskyy, T. Botzem, I. Fernandez de Fuentes, B. Joecker, J. J. Pla, F. E. Hudson, K. M. Itoh, A. M. Jakob, B. C. Johnson, D. N. Jamieson *et al.*, "An electrically driven single-atom "flip-flop" qubit," *Science Advances*, vol. 9, no. 6, p. eadd9408, 2023.

[33] J. Yoneda, W. Huang, M. Feng, C. H. Yang, K. W. Chan, T. Tanttu, W. Gilbert, R. Leon, F. Hudson, K. Itoh *et al.*, "Coherent spin qubit transport in silicon," *Nature communications*, vol. 12, no. 1, p. 4114, 2021.

[34] J. T. Muhonen, J. P. Dehollain, A. Laucht, F. E. Hudson, R. Kalra, T. Sekiguchi, K. M. Itoh, D. N. Jamieson, J. C. McCallum, A. S. Dzurak *et al.*, "Storing quantum information for 30 seconds in a nanoelectronic device," *Nature nanotechnology*, vol. 9, no. 12, pp. 986–991, 2014.

[35] J. T. Muhonen, A. Laucht, S. Simmons, J. P. Dehollain, R. Kalra, F. E. Hudson, S. Freer, K. M. Itoh, D. N. Jamieson, J. C. McCallum *et al.*, "Quantifying the quantum gate fidelity of single-atom spin qubits in silicon by randomized benchmarking," *Journal of Physics: Condensed Matter*, vol. 27, no. 15, p. 154205, 2015.

[36] J. P. Dehollain, S. Simmons, J. T. Muhonen, R. Kalra, A. Laucht, F. Hudson, K. M. Itoh, D. N. Jamieson, J. C. McCallum, A. S. Dzurak *et al.*, "Bell's inequality violation with spins in silicon," *Nature nanotechnology*, vol. 11, no. 3, pp. 242–246, 2016.

[37] A. M. Jakob, S. G. Robson, V. Schmitt, V. Mourik, M. Posselt, D. Spemann, B. C. Johnson, H. R. Firgau, E. Mayes, J. C. McCallum *et al.*, "Deterministic shallow dopant implantation in silicon with detection confidence upper-bound to 99.85% by ion–solid interactions," *Advanced Materials*, vol. 34, no. 3, p. 2103235, 2022.

[38] B. G. Streetman, S. Banerjee *et al.*, *Solid state electronic devices*. Prentice hall New Jersey, 2000, vol. 4.

[39] L. Zhang, "Silicon process and manufacturing technology evolution: An overview of advancements in chip making," *IEEE Consumer Electronics Magazine*, vol. 3, no. 3, pp. 44–48, 2014.

[40] S. Büttgenbach, I. Constantinou, A. Dietzel, and M. Leester-Schädel, *Case studies in micromechatronics. Chapter:Piezoresistive Pressure Sensors*. Springer, 2020.

[41] J. C. Bean, "Silicon-based semiconductor heterostructures: column iv bandgap engineering," *Proceedings of the IEEE*, vol. 80, no. 4, pp. 571–587, 1992.

[42] W. Gerlach and O. Stern, "Der experimentelle nachweis der richtungsquantelung im magnetfeld," *Zeitschrift für Physik*, vol. 9, no. 1, pp. 349–352, 1922.

[43] F. Weinert, "Wrong theory—right experiment: The significance of the stern-gerlach experiments," *Studies in History and Philosophy of Science Part B: Studies in History and Philosophy of Modern Physics*, vol. 26, no. 1, pp. 75–86, 1995.

[44] V. Meunier. (2020) Introduction to quantum mechanics, self-guided course. [Online]. Available: https://homepages.rpi.edu/~meuniv/IQM/index.html

[45] D. J. Griffiths and D. F. Schroeter, *Introduction to quantum mechanics*. Cambridge university press, 2018.

[46] P. Zeeman, "The effect of magnetisation on the nature of light emitted by a substance," *nature*, vol. 55, no. 1424, p. 347, 1897.

[47] A. Landé, "Über den anomalen zeemaneffekt (teil i)," *Zeitschrift für Physik*, vol. 5, no. 4, pp. 231–241, 1921.

[48] P. J. Mohr, D. B. Newell, and B. N. Taylor, "Codata recommended values of the fundamental physical constants: 2014," *Journal of Physical and Chemical Reference Data*, vol. 45, no. 4, p. 043102, 2016.

[49] A. Schweiger and G. Jeschke, *Principles of pulse electron paramagnetic resonance*. Oxford university press, 2001.

[50] W. Kutzelnigg, "Origin and meaning of the fermi contact interaction," *Theoretica chimica acta*, vol. 73, no. 2-3, pp. 173–200, 1988.

[51] P. Bracken, *Quantum Mechanics*. BoD–Books on Demand, 2020.

[52] J. Pla, A. Bienfait, G. Pica, J. Mansir, F. Mohiyaddin, Z. Zeng, Y.-M. Niquet, A. Morello, T. Schenkel, J. Morton *et al.*, "Strain-induced spin-resonance shifts in silicon devices," *Physical Review Applied*, vol. 9, no. 4, p. 044014, 2018.

[53] M. Steger, T. Sekiguchi, A. Yang, K. Saeedi, M. Hayden, M. Thewalt, K. M. Itoh, H. Riemann, N. Abrosimov, P. Becker *et al.*, "Optically-detected nmr of optically-hyperpolarized 31p neutral donors in 28si," *Journal of Applied Physics*, vol. 109, no. 10, p. 102411, 2011.

[54] C. P. Slichter, *Principles of magnetic resonance*. Springer Science & Business Media, 2013, vol. 1.

[55] C. Cohen-Tannoudji, B. Diu, and F. Laloe, "Quantum mechanics, volume 1," *Quantum Mechanics*, vol. 1, p. 898, 1986.

[56] F. Borgosano, "Studies of the influence of thermodynamical parameters on the production rate of hyperpolarised 129xe and the degree of hyperpolarisation," Ph.D. dissertation, 2012.

[57] Y. Wu and X. Yang, "Strong-coupling theory of periodically driven two-level systems," *Physical review letters*, vol. 98, no. 1, p. 013601, 2007.

[58] A. Laucht, S. Simmons, R. Kalra, G. Tosi, J. P. Dehollain, J. T. Muhonen, S. Freer, F. E. Hudson, K. M. Itoh, D. N. Jamieson *et al.*, "Breaking the rotating wave

approximation for a strongly driven dressed single-electron spin," *Physical Review B*, vol. 94, no. 16, p. 161302, 2016.

[59] N. F. Ramsey, "A molecular beam resonance method with separated oscillating fields," *Physical Review*, vol. 78, no. 6, p. 695, 1950.

[60] E. L. Hahn, "Spin echoes," *Physical review*, vol. 80, no. 4, p. 580, 1950.

[61] J. Bylander, S. Gustavsson, F. Yan, F. Yoshihara, K. Harrabi, G. Fitch, D. G. Cory, Y. Nakamura, J.-S. Tsai, and W. D. Oliver, "Noise spectroscopy through dynamical decoupling with a superconducting flux qubit," *Nature Physics*, vol. 7, no. 7, pp. 565–570, 2011.

[62] F. Yan, S. Gustavsson, A. Kamal, J. Birenbaum, A. P. Sears, D. Hover, T. J. Gudmundsen, D. Rosenberg, G. Samach, S. Weber *et al.*, "The flux qubit revisited to enhance coherence and reproducibility," *Nature communications*, vol. 7, no. 1, p. 12964, 2016.

[63] G. Ithier, E. Collin, P. Joyez, P. Meeson, D. Vion, D. Esteve, F. Chiarello, A. Shnirman, Y. Makhlin, J. Schriefl *et al.*, "Decoherence in a superconducting quantum bit circuit," *Physical Review B*, vol. 72, no. 13, p. 134519, 2005.

[64] B. Chen, *Fundamentals of Recoupling and Decoupling Techniques in Solid State NMR*. AIP Publishing LLC, 2020.

[65] L. Allen and J. H. Eberly, *Optical resonance and two-level atoms*. Courier Corporation, 1987, vol. 28.

[66] A. Blais, R.-S. Huang, A. Wallraff, S. M. Girvin, and R. J. Schoelkopf, "Cavity quantum electrodynamics for superconducting electrical circuits: An architecture for quantum computation," *Physical Review A*, vol. 69, no. 6, p. 062320, 2004.

[67] M. Boguslawski, M. Barrios, L. Xin, M. S. Chapman *et al.*, "Exploring non-abelian geometric phases in spin-1 ultracold atoms," *Physical Review Letters*, vol. 123, no. 17, p. 173202, 2019.

[68] J. C. Bardin, D. H. Slichter, and D. J. Reilly, "Microwaves in quantum computing," *IEEE journal of microwaves*, vol. 1, no. 1, pp. 403–427, 2021.

[69] L. Nietot, M. del Olmo, M. Santander *et al.*, "Aharonov-anandan geometric phase for spin-1/2 periodic hamiltonians," *Journal of Physics A: Mathematical and General*, vol. 25, no. 19, p. 5151, 1992.

[70] Y. Aharonov and J. Anandan, "Phase change during a cyclic quantum evolution," *Physical Review Letters*, vol. 58, no. 16, p. 1593, 1987.

[71] M. V. Berry, "Quantal phase factors accompanying adiabatic changes," *Proceedings of the Royal Society of London. A. Mathematical and Physical Sciences*, vol. 392, no. 1802, pp. 45–57, 1984.

[72] J. J. Pla, F. A. Mohiyaddin, K. Y. Tan, J. P. Dehollain, R. Rahman, G. Klimeck, D. N. Jamieson, A. S. Dzurak, and A. Morello, "Coherent control of a single si 29 nuclear spin qubit," *Physical review letters*, vol. 113, no. 24, p. 246801, 2014.

[73] P. A. De Groot, *Handbook of stable isotope analytical techniques*. Elsevier, 2004, vol. 1.

[74] K. M. Itoh, J. Kato, M. Uemura, A. K. Kaliteevskii, O. N. Godisov, G. G. Devyatych, A. D. Bulanov, A. V. Gusev, I. D. Kovalev, P. G. Sennikov *et al.*, "High purity isotopically enriched 29si and 30si single crystals: Isotope separation, purification, and growth," *Japanese Journal of Applied Physics*, vol. 42, no. 10R, p. 6248, 2003.

[75] D. Holmes, B. Johnson, C. Chua, B. Voisin, S. Kocsis, S. Rubanov, S. Robson, J. McCallum, D. McCamey, S. Rogge *et al.*, "Isotopic enrichment of silicon by high fluence 28 si- ion implantation," *Physical Review Materials*, vol. 5, no. 1, p. 014601, 2021.

[76] D. N. Jamieson, W. I. Lawrie, S. G. Robson, A. M. Jakob, B. C. Johnson, and J. C. McCallum, "Deterministic doping," *Materials Science in Semiconductor Processing*, vol. 62, pp. 23–30, 2017.

[77] J. Dehollain, J. Pla, E. Siew, K. Tan, A. Dzurak, and A. Morello, "Nanoscale broadband transmission lines for spin qubit control," *Nanotechnology*, vol. 24, no. 1, p. 015202, 2012.

[78] J. F. Ziegler. (2015) Interactions of ions with matter. [Online]. Available: http://www.srim.org/

[79] J. C. McCallum, D. N. Jamieson, C. Yang, A. D. Alves, B. C. Johnson, T. Hopf, S. C. Thompson, J. A. Van Donkelaar *et al.*, "Single-ion implantation for the development of si-based mosfet devices with quantum functionalities," *Advances in Materials Science and Engineering*, vol. 2012, 2012.

[80] D. Holmes, B. Wilhelm, A. M. Jakob, X. Yu, F. E. Hudson, K. M. Itoh, A. S. Dzurak, D. N. Jamieson, and A. Morello, "Improved placement precision of implanted donor spin qubits in silicon using molecule ions," *arXiv preprint arXiv:2308.04117*, 2023.

[81] R. Kalra, A. Laucht, J. P. Dehollain, D. Bar, S. Freer, S. Simmons, J. T. Muhonen, and A. Morello, "Vibration-induced electrical noise in a cryogen-free dilution refrigerator: Characterization, mitigation, and impact on qubit coherence," *Review of Scientific Instruments*, vol. 87, no. 7, 2016.

[82] M. Steer, *Microwave and RF Design: Radio Systems.* North Carolina State University, 2019.

[83] C. Adambukulam, V. Sewani, H. Stemp, S. Asaad, M. Mądzik, A. Morello, and A. Laucht, "An ultra-stable 1.5 t permanent magnet assembly for qubit experiments at cryogenic temperatures," *Review of Scientific Instruments*, vol. 92, no. 8, 2021.

[84] M. Möttönen, K. Y. Tan, K. W. Chan, F. A. Zwanenburg, W. H. Lim, C. C. Escott, J.-M. Pirkkalainen, A. Morello, C. Yang, J. A. Van Donkelaar *et al.*, "Probe and control of the reservoir density of states in single-electron devices," *Physical Review B*, vol. 81, no. 16, p. 161304, 2010.

[85] A. Morello, C. Escott, H. Huebl, L. W. Van Beveren, L. Hollenberg, D. Jamieson, A. Dzurak, and R. Clark, "Architecture for high-sensitivity single-shot readout and

control of the electron spin of individual donors in silicon," *Physical Review B*, vol. 80, no. 8, p. 081307, 2009.

[86] J. Elzerman, R. Hanson, L. Willems van Beveren, B. Witkamp, L. Vandersypen, and L. P. Kouwenhoven, "Single-shot read-out of an individual electron spin in a quantum dot," *nature*, vol. 430, no. 6998, pp. 431–435, 2004.

[87] H. Huebl, C. D. Nugroho, A. Morello, C. C. Escott, M. A. Eriksson, C. Yang, D. N. Jamieson, R. G. Clark, and A. S. Dzurak, "Electron tunnel rates in a donor-silicon single electron transistor hybrid," *Physical Review B*, vol. 81, no. 23, p. 235318, 2010.

[88] A. Morello, J. J. Pla, F. A. Zwanenburg, K. W. Chan, K. Y. Tan, H. Huebl, M. Möttönen, C. D. Nugroho, C. Yang, J. A. Van Donkelaar *et al.*, "Single-shot readout of an electron spin in silicon," *Nature*, vol. 467, no. 7316, pp. 687–691, 2010.

[89] R. De Sousa, "Dangling-bond spin relaxation and magnetic 1/ f noise from the amorphous-semiconductor/oxide interface: Theory," *Physical Review B*, vol. 76, no. 24, p. 245306, 2007.

[90] M. Weissman, "1 f noise and other slow, nonexponential kinetics in condensed matter," *Reviews of modern physics*, vol. 60, no. 2, p. 537, 1988.

[91] A. Mills, M. Feldman, C. Monical, P. Lewis, K. Larson, A. Mounce, and J. R. Petta, "Computer-automated tuning procedures for semiconductor quantum dot arrays," *Applied Physics Letters*, vol. 115, no. 11, 2019.

[92] S. Shankar, A. Tyryshkin, J. He, and S. Lyon, "Spin relaxation and coherence times for electrons at the si/sio 2 interface," *Physical Review B*, vol. 82, no. 19, p. 195323, 2010.

[93] A. Laucht, R. Kalra, J. T. Muhonen, J. P. Dehollain, F. A. Mohiyaddin, F. Hudson, J. C. McCallum, D. N. Jamieson, A. S. Dzurak, and A. Morello, "High-fidelity adiabatic inversion of a 31p electron spin qubit in natural silicon," *Applied Physics Letters*, vol. 104, no. 9, 2014.

[94] Y. Yang, H. H. Vallabhapurapu, V. K. Sewani, M. Isarov, H. R. Firgau, C. Adambukulam, B. C. Johnson, J. J. Pla, and A. Laucht, "Observing hyperfine interactions of nv- centers in diamond in an advanced quantum teaching lab," *American Journal of Physics*, vol. 90, no. 7, pp. 550–560, 2022.

[95] A. G. Fowler, M. Mariantoni, J. M. Martinis, and A. N. Cleland, "Surface codes: Towards practical large-scale quantum computation," *Physical Review A*, vol. 86, no. 3, p. 032324, 2012.

[96] D. Maradan, L. Casparis, T.-M. Liu, D. Biesinger, C. Scheller, D. Zumbühl, J. Zimmerman, and A. Gossard, "Gaas quantum dot thermometry using direct transport and charge sensing," *Journal of low temperature physics*, vol. 175, pp. 784–798, 2014.

[97] C. W. Beenakker, "Theory of coulomb-blockade oscillations in the conductance of a quantum dot," *Physical Review B*, vol. 44, no. 4, p. 1646, 1991.

[98] M. A. Johnson, M. T. Mądzik, F. E. Hudson, K. M. Itoh, A. M. Jakob, D. N. Jamieson, A. Dzurak, and A. Morello, "Beating the thermal limit of qubit initialization with a bayesian maxwell's demon," *Physical Review X*, vol. 12, no. 4, p. 041008, 2022.

[99] F. A. Zwanenburg, A. S. Dzurak, A. Morello, M. Y. Simmons, L. C. Hollenberg, G. Klimeck, S. Rogge, S. N. Coppersmith, and M. A. Eriksson, "Silicon quantum electronics," *Reviews of modern physics*, vol. 85, no. 3, p. 961, 2013.

[100] S. Asaad, *Electrical Control and Quantum Chaos with a High-Spin Nucleus in Silicon*. Springer Nature, 2021.

[101] J. A. Nelder and R. Mead, "A simplex method for function minimization," *The computer journal*, vol. 7, no. 4, pp. 308–313, 1965.

[102] F. Gao and L. Han, "Implementing the nelder-mead simplex algorithm with adaptive parameters," *Computational Optimization and Applications*, vol. 51, no. 1, pp. 259–277, 2012.

[103] J. C. Lagarias, J. A. Reeds, M. H. Wright, and P. E. Wright, "Convergence properties of the nelder–mead simplex method in low dimensions," *SIAM Journal on optimization*, vol. 9, no. 1, pp. 112–147, 1998.

[104] L. Han and M. Neumann, "Effect of dimensionality on the nelder–mead simplex method," *Optimization Methods and Software*, vol. 21, no. 1, pp. 1–16, 2006.

[105] Q-CTRL. (2023) Boulder opal. [Online]. Available: https://docs.q-ctrl.com/boulder-opal

[106] R. M. Dudley, "Real analysis and probability. wadsworth & brooks," *Cole, Pacific Groves, California*, vol. 8, p. 39, 1989.

[107] Q-CTRL. (2023) Boulder opal: Gaussian process initializer. [Online]. Available: https://docs.q-ctrl.com/references/qctrl/Types/closed_loop_optimization_step/GaussianProcessInitializer.html#qctrl.dynamic.types.closed_loop_optimization_step.GaussianProcessInitializer

[108] N. Ketkar and N. Ketkar, "Introduction to keras," *Deep learning with python: a hands-on introduction*, pp. 97–111, 2017.

[109] B. Joecker, H. G. Stemp, I. F. de Fuentes, M. A. Johnson, and A. Morello, "Error channels in quantum nondemolition measurements on spin systems," *arXiv preprint arXiv:2307.14103*, 2023.

[110] V. B. Braginsky and F. Y. Khalili, "Quantum nondemolition measurements: the route from toys to tools," *Reviews of Modern Physics*, vol. 68, no. 1, p. 1, 1996.

[111] R. Cook and D. H. Whiffen, "Electron nuclear double resonance study of a nitrogen centre in diamond," *Proceedings of the Royal Society of London. Series A. Mathematical and Physical Sciences*, vol. 295, no. 1441, pp. 99–106, 1966.

[112] C. Gemperle and A. Schweiger, "Pulsed electron-nuclear double resonance methodology," *Chemical reviews*, vol. 91, no. 7, pp. 1481–1505, 1991.

[113] S. Pribitzer, D. Mannikko, and S. Stoll, "Determining electron–nucleus distances and fermi contact couplings from endor spectra," *Physical Chemistry Chemical Physics*, vol. 23, no. 14, pp. 8326–8335, 2021.

[114] R. Kalra, A. Laucht, C. D. Hill, and A. Morello, "Robust two-qubit gates for donors in silicon controlled by hyperfine interactions," *Physical Review X*, vol. 4, no. 2, p. 021044, 2014.

[115] G. Burkard, T. D. Ladd, A. Pan, J. M. Nichol, and J. R. Petta, "Semiconductor spin qubits," *Reviews of Modern Physics*, vol. 95, no. 2, p. 025003, 2023.

[116] J. Levy, "Universal quantum computation with spin-1/2 pairs and heisenberg exchange," *Physical Review Letters*, vol. 89, no. 14, p. 147902, 2002.

[117] J. R. Petta, A. C. Johnson, J. M. Taylor, E. A. Laird, A. Yacoby, M. D. Lukin, C. M. Marcus, M. P. Hanson, and A. C. Gossard, "Coherent manipulation of coupled electron spins in semiconductor quantum dots," *Science*, vol. 309, no. 5744, pp. 2180–2184, 2005.

[118] K. Eng, T. D. Ladd, A. Smith, M. G. Borselli, A. A. Kiselev, B. H. Fong, K. S. Holabird, T. M. Hazard, B. Huang, P. W. Deelman *et al.*, "Isotopically enhanced triple-quantum-dot qubit," *Science advances*, vol. 1, no. 4, p. e1500214, 2015.

[119] K. Nowack, M. Shafiei, M. Laforest, G. Prawiroatmodjo, L. Schreiber, C. Reichl, W. Wegscheider, and L. Vandersypen, "Single-shot correlations and two-qubit gate of solid-state spins," *Science*, vol. 333, no. 6047, pp. 1269–1272, 2011.

[120] M. Veldhorst, C. Yang, J. Hwang, W. Huang, J. Dehollain, J. Muhonen, S. Simmons, A. Laucht, F. Hudson, K. M. Itoh *et al.*, "A two-qubit logic gate in silicon," *Nature*, vol. 526, no. 7573, pp. 410–414, 2015.

[121] T. Watson, S. Philips, E. Kawakami, D. Ward, P. Scarlino, M. Veldhorst, D. Savage, M. Lagally, M. Friesen, S. Coppersmith *et al.*, "A programmable two-qubit quantum processor in silicon," *nature*, vol. 555, no. 7698, pp. 633–637, 2018.

[122] D. M. Zajac, A. J. Sigillito, M. Russ, F. Borjans, J. M. Taylor, G. Burkard, and J. R. Petta, "Resonantly driven cnot gate for electron spins," *Science*, vol. 359, no. 6374, pp. 439–442, 2018.

[123] H. Bulou, L. Joly, J.-M. Mariot, and F. Scheurer, *Magnetism and Accelerator-Based Light Sources: Proceedings of the 7th International School "Synchrotron Radiation and Magnetism", Mittelwihr (France), 2018.* Springer Nature, 2021.

[124] W. Pauli, "Über den zusammenhang des abschlusses der elektronengruppen im atom mit der komplexstruktur der spektren," *Zeitschrift für Physik*, vol. 31, no. 1, pp. 765–783, 1925.

[125] T. Obata, M. Pioro-Ladrière, Y. Tokura, Y.-S. Shin, T. Kubo, K. Yoshida, T. Taniyama, and S. Tarucha, "Coherent manipulation of individual electron spin in a double quantum dot integrated with a micromagnet," *Physical Review B*, vol. 81, no. 8, p. 085317, 2010.

[126] S. Gorman, J. Keizer, and M. Simmons, "A two-qubit gate between phosphorus donor electrons in silicon," *Nature*, vol. 571, no. 7765, pp. 371–375, 2019.

[127] Y. Chong, "Quantum mechanics iii," *Nanyang Technological University.*

[128] W. K. Wootters, "Entanglement of formation and concurrence." *Quantum Inf. Comput.*, vol. 1, no. 1, pp. 27–44, 2001.

[129] H. Fan, K. Matsumoto, and H. Imai, "Quantify entanglement by concurrence hierarchy," *Journal of Physics A: Mathematical and General*, vol. 36, no. 14, p. 4151, 2003.

[130] S. A. Hill and W. K. Wootters, "Entanglement of a pair of quantum bits," *Physical review letters*, vol. 78, no. 26, p. 5022, 1997.

[131] D. F. James, P. G. Kwiat, W. J. Munro, and A. G. White, "Measurement of qubits," *Physical Review A*, vol. 64, no. 5, p. 052312, 2001.

[132] M. Mehring, J. Mende, and W. Scherer, "Entanglement between an electron and a nuclear spin 1 2," *Physical review letters*, vol. 90, no. 15, p. 153001, 2003.

[133] J. B. Altepeter, E. R. Jeffrey, and P. G. Kwiat, "Photonic state tomography," *Advances in atomic, molecular, and optical physics*, vol. 52, pp. 105–159, 2005.

[134] U. Fano, "A stokes-parameter technique for the treatment of polarization in quantum mechanics," *Physical Review*, vol. 93, no. 1, p. 121, 1954.

[135] C. A. Sackett, D. Kielpinski, B. E. King, C. Langer, V. Meyer, C. J. Myatt, M. Rowe, Q. Turchette, W. M. Itano, D. J. Wineland *et al.*, "Experimental entanglement of four particles," *Nature*, vol. 404, no. 6775, pp. 256–259, 2000.

[136] K. X. Wei, I. Lauer, S. Srinivasan, N. Sundaresan, D. T. McClure, D. Toyli, D. C. McKay, J. M. Gambetta, and S. Sheldon, "Verifying multipartite entangled greenberger-horne-zeilinger states via multiple quantum coherences," *Physical Review A*, vol. 101, no. 3, p. 032343, 2020.

[137] B. Koiller, X. Hu, and S. D. Sarma, "Exchange in silicon-based quantum computer architecture," *Physical review letters*, vol. 88, no. 2, p. 027903, 2001.

[138] B. Joecker, A. D. Baczewski, J. K. Gamble, A. Saraiva, and M. Andrea, "Full configuration interaction simulations of exchange-coupled donors in silicon using multi-valley effective mass theory," *New Journal of Physics*, vol. 23, 2021.

[139] B. M. Maune, M. G. Borselli, B. Huang, T. D. Ladd, P. W. Deelman, K. S. Holabird, A. A. Kiselev, I. Alvarado-Rodriguez, R. S. Ross, A. E. Schmitz *et al.*, "Coherent singlet-triplet oscillations in a silicon-based double quantum dot," *Nature*, vol. 481, no. 7381, pp. 344–347, 2012.

[140] H. Eenink, L. Petit, W. Lawrie, J. Clarke, L. Vandersypen, and M. Veldhorst, "Tunable coupling and isolation of single electrons in silicon metal-oxide-semiconductor quantum dots," *Nano letters*, vol. 19, no. 12, pp. 8653–8657, 2019.

[141] M. Nurizzo, B. Jadot, P.-A. Mortemousque, V. Thiney, E. Chanrion, M. Dartiailh, A. Ludwig, A. D. Wieck, C. Bäuerle, M. Urdampilleta *et al.*, "Controlled quantum dot array segmentation via highly tunable interdot tunnel coupling," *Applied Physics Letters*, vol. 121, no. 8, 2022.

[142] M. Reed, B. Maune, R. Andrews, M. Borselli, K. Eng, M. Jura, A. Kiselev, T. Ladd, S. Merkel, I. Milosavljevic *et al.*, "Reduced sensitivity to charge noise in semiconductor spin qubits via symmetric operation," *Physical review letters*, vol. 116, no. 11, p. 110402, 2016.

[143] F. Martins, F. K. Malinowski, P. D. Nissen, E. Barnes, S. Fallahi, G. C. Gardner, M. J. Manfra, C. M. Marcus, and F. Kuemmeth, "Noise suppression using symmetric exchange gates in spin qubits," *Physical review letters*, vol. 116, no. 11, p. 116801, 2016.

[144] J. P. Dehollain, J. T. Muhonen, R. Blume-Kohout, K. M. Rudinger, J. K. Gamble, E. Nielsen, A. Laucht, S. Simmons, R. Kalra, A. S. Dzurak *et al.*, "Optimization of a solid-state electron spin qubit using gate set tomography," *New Journal of Physics*, vol. 18, no. 10, p. 103018, 2016.

[145] B. Voisin, J. Bocquel, A. Tankasala, M. Usman, J. Salfi, R. Rahman, M. Simmons, L. Hollenberg, and S. Rogge, "Valley interference and spin exchange at the atomic scale in silicon," *Nature communications*, vol. 11, no. 1, p. 6124, 2020.

[146] A. Morello, J. J. Pla, P. Bertet, and D. N. Jamieson, "Donor spins in silicon for quantum technologies," *Advanced Quantum Technologies*, vol. 3, no. 11, p. 2000005, 2020.

[147] R. Pillarisetty, N. Thomas, H. George, K. Singh, J. Roberts, L. Lampert, P. Amin, T. Watson, G. Zheng, J. Torres *et al.*, "Qubit device integration using advanced semiconductor manufacturing process technology," in *2018 IEEE International Electron Devices Meeting (IEDM)*. IEEE, 2018, pp. 6–3.

[148] T. Nakajima, A. Noiri, J. Yoneda, M. R. Delbecq, P. Stano, T. Otsuka, K. Takeda, S. Amaha, G. Allison, K. Kawasaki *et al.*, "Quantum non-demolition measurement of an electron spin qubit," *Nature nanotechnology*, vol. 14, no. 6, pp. 555–560, 2019.

[149] X. Xue, B. D'Anjou, T. F. Watson, D. R. Ward, D. E. Savage, M. G. Lagally, M. Friesen, S. N. Coppersmith, M. A. Eriksson, W. A. Coish *et al.*, "Repetitive

quantum nondemolition measurement and soft decoding of a silicon spin qubit," *Physical Review X*, vol. 10, no. 2, p. 021006, 2020.

[150] A. M. Tyryshkin, J. J. Morton, A. Ardavan, and S. Lyon, "Davies electron-nuclear double resonance revisited: Enhanced sensitivity and nuclear spin relaxation," *The Journal of chemical physics*, vol. 124, no. 23, 2006.

[151] M. T. Madzik, T. D. Ladd, F. E. Hudson, K. M. Itoh, A. M. Jakob, B. C. Johnson, J. C. McCallum, D. N. Jamieson, A. S. Dzurak, A. Laucht, and A. Morello, "Controllable freezing of the nuclear spin bath in a single-atom spin qubit," *Science Advances*, vol. 6, no. 27, 2020.

[152] W. Huang, C. Yang, K. Chan, T. Tanttu, B. Hensen, R. Leon, M. Fogarty, J. Hwang, F. Hudson, K. M. Itoh *et al.*, "Fidelity benchmarks for two-qubit gates in silicon," *Nature*, vol. 569, no. 7757, pp. 532–536, 2019.

[153] E. Nielsen, J. K. Gamble, K. Rudinger, T. Scholten, K. Young, and R. Blume-Kohout, "Gate set tomography," *Quantum*, vol. 5, p. 557, 2021.

[154] D. P. DiVincenzo, "The physical implementation of quantum computation," *Fortschritte der Physik: Progress of Physics*, vol. 48, no. 9-11, pp. 771–783, 2000.

[155] A. Zwerver, T. Krähenmann, T. Watson, L. Lampert, H. C. George, R. Pillarisetty, S. Bojarski, P. Amin, S. Amitonov, J. Boter *et al.*, "Qubits made by advanced semiconductor manufacturing," *Nature Electronics*, vol. 5, no. 3, pp. 184–190, 2022.

[156] K. Takeda, J. Kamioka, T. Otsuka, J. Yoneda, T. Nakajima, M. R. Delbecq, S. Amaha, G. Allison, T. Kodera, S. Oda *et al.*, "A fault-tolerant addressable spin qubit in a natural silicon quantum dot," *Science advances*, vol. 2, no. 8, p. e1600694, 2016.

[157] S. G. Philips, M. T. Mądzik, S. V. Amitonov, S. L. de Snoo, M. Russ, N. Kalhor, C. Volk, W. I. Lawrie, D. Brousse, L. Tryputen *et al.*, "Universal control of a six-qubit quantum processor in silicon," *Nature*, vol. 609, no. 7929, pp. 919–924, 2022.

[158] B. Undseth, O. Pietx-Casas, E. Raymenants, M. Mehmandoost, M. T. Madzik, S. G. Philips, S. L. de Snoo, D. J. Michalak, S. V. Amitonov, L. Tryputen *et al.*, "Hotter is easier: unexpected temperature dependence of spin qubit frequencies," *arXiv preprint arXiv:2304.12984*, 2023.

[159] Y. Choi and R. Joynt, "Interacting random-field dipole defect model for heating in semiconductor-based qubit devices," *arXiv preprint arXiv:2308.00711*, 2023.

[160] V. Srinivasa, H. Xu, and J. M. Taylor, "Tunable spin-qubit coupling mediated by a multielectron quantum dot," *Physical review letters*, vol. 114, no. 22, p. 226803, 2015.

[161] F. K. Malinowski, F. Martins, T. B. Smith, S. D. Bartlett, A. C. Doherty, P. D. Nissen, S. Fallahi, G. C. Gardner, M. J. Manfra, C. M. Marcus *et al.*, "Fast spin exchange across a multielectron mediator," *Nature communications*, vol. 10, no. 1, p. 1196, 2019.

[162] L. Geck, A. Kruth, H. Bluhm, S. van Waasen, and S. Heinen, "Control electronics for semiconductor spin qubits," *Quantum science and technology*, vol. 5, no. 1, p. 015004, 2019.